

D I P L O M A R B E I T
M A S T E R ' S T H E S I S

**A multi-surface plasticity model
with strain softening
for failure mechanisms of clear spruce wood
under plain biaxial stress conditions and
stabilization of its numerical implementation
for large characteristic lengths**

ausgeführt zum Zwecke der Erlangung des akademischen
Grades eines Diplom-Ingenieurs

unter der Anleitung von

Univ. Doz. Dipl.-Ing. Dr. techn. **Peter Mackenzie-Helnwein**
Research Assistant Professor
Department of Civil and Environmental Engineering
University of Washington, Seattle

und

Univ. Prof. Dipl.-Ing. Dr. techn. **Josef Eberhardsteiner**
Institut für Mechanik der Werkstoffe und Strukturen
der Technischen Universität Wien

eingereicht an der Technischen Universität Wien
Fakultät für Bauingenieurwesen

von

Christoph Kohlhauser

Matr.Nr.: 98 25 700

Steg 4

A - 4817 St.Konrad

Wien, im Jänner 2005

Phantasie ist wichtiger als Wissen.
Wissen ist begrenzt.
Albert Einstein

Imagination is more important than knowledge.
Knowledge is limited.
Albert Einstein

Danksagung – Acknowledgment

Diese Diplomarbeit markiert den Abschluss meines Grundstudiums an der Technischen Universität Wien. An dieser Stelle möchte ich mich bei allen bedanken, die dazu beigetragen haben und auch einige namentlich erwähnen, ohne die ich dieses Ziel nicht erreicht hätte.

Mein aufrichtiger Dank gilt meiner Familie, ohne deren Unterstützung ein Studium nicht möglich gewesen wäre.

Ganz besonders danke ich meinem Vater Johann. Er hat mir meine Ausbildung und ein sorgenfreies Studium ermöglicht. Für seine stetige Unterstützung bin ich überaus dankbar.

Meiner Mutter Monika bin ich von ganzem Herzen dafür dankbar, dass sie meine Entscheidung zu Studieren immer mitgetragen und mich all die Jahre unterstützt hat.

Meinem Stiefvater Herbert danke ich aufrichtig dafür, dass er mich in jungen Jahren auf den richtigen Weg gebracht hat und auch jetzt noch immer für mich da ist.

Meinen Freunden sei gedankt, dass sie während meiner Studienzeit an der Technischen Universität Wien und an der University of Washington stets zu mir hielten, auch wenn über längere Zeit wenig Kontakt zueinander bestand. Besonders bei meiner Freundin Mariana bedanke ich mich von ganzem Herzen für ihr stetiges Verständnis, wenn während der Erstellung dieser Arbeit meine Freizeit sehr begrenzt war. Sie war in Seattle und Wien immer für mich da.

Bei den Studienkollegen an der Technischen Universität Wien bedanke ich mich für die kollegiale Zusammenarbeit und Hilfe während des Studiums.

Besonders herzlicher Dank gebührt Herrn Prof. Dipl.-Ing. Dr. techn. Peter Mackenzie-Helnwein für die hervorragende Betreuung bei der Erstellung dieser Arbeit. Er ließ mir diese nicht nur während meines Auslandsaufenthaltes an der University of Washington, sondern auch danach in Wien, als die Kommunikation sehr schwierig war, zukommen. Seine Unterstützung und Hilfe überstieg das übliche Maß bei weitem.

Herrn Univ. Prof. Dipl.-Ing. Dr. techn. Josef Eberhardsteiner danke ich ebenso recht herzlich für die ausgezeichnete Betreuung. Er stand mir jederzeit bei Fragen zur Verfügung und gab mir wertvolle Hinweise die zum Gelingen dieser Arbeit wesentlich beitrugen.

Auch den Assistenten am Institut für Mechanik der Werkstoffe und Strukturen sei gedankt. Sie standen mir jederzeit mit Rat und Tat zur Verfügung. Im Speziellen danke ich Christian Schranz und Karin Hofstetter für ihre fachliche Hilfe und ihre aufmunternden Worte in schwierigen Zeiten während der Erstellung dieser Arbeit.

From the Department of Civil and Environmental Engineering at the University of Washington I want to thank especially the Professors Dr. Gregory R. Miller and Dr. Pedro Arduino. They provided the foundation for this work and supported me during my studies at the University of Washington.

I thank my study colleagues at the University of Washington for the help with difficulties in adapting to a new environment.

I am very grateful to my friends from all around the world who have been a great help during my stay in Seattle.

Abstract

Wood is used in many applications in civil engineering but due to its complex hierarchical structure was this organic orthotropic material, neglected in research. Even though the behavior and properties of wood for uniaxial loading states were known in great detail for a long time, the research necessity regarding the biaxial behavior of the material remain comprehensive.

The lack of knowledge of biaxial strength properties led to simplified assumptions in design codes, which did not account for the complex biaxial interaction. With the emerging of numerical methods like the finite element method and the resulting ability of computing more complex structures, material models for wood and several other materials were required, to apply these methods to structures subjected to multi-axial stress states such as shells or structural details.

Based on biaxial experiments on clear spruce wood in the LR-plane, an orthotropic single-surface material model for wood under plane stress states was developed. The missing identification of failure modes by this model led to the description of the biaxial material behavior by a multi-surface constitutive model by Mackenzie-Helnwein et al. This model incorporates four state-surfaces, each of which includes modes for the description of post failure behavior.

This thesis presents this multi-surface material model and its numerical implementation in finite element programs in a detailed form. Before elucidating the mathematical and constitutive basic modules needed for this purpose, a short overview on the anatomy and structure of wood, as well as on the experiments identifying failure modes is given. The latter are the basis for the model and provide deeper insight in the material and its behavior.

Subsequently, the four state-surfaces and their softening and/or hardening behavior are discussed. The surfaces for tension both in fiber and in radial direction are characterized by a brittle failure. The latter surface is a mixed mode tension-shear model. The compression state-surfaces are characterized by non-linear hardening in radial direction and minor softening behavior in fiber direction.

The aim of this work is to reveal and resolve problems regarding stability of the numerical implementation of the multi-surface plasticity model. The identification of the characteristic length as the mathematical cause for some computational instabilities leads to the development of new algorithms for the description of softening behavior at large values of this model parameter. These algorithms at hands, the computational stability can be enhanced. Furthermore, independence of the numerical stability of an implementation from the characteristic length is an indispensable prerequisite for the applicability of a material model for large engineering structures.

A stable material model for plane stressed wood with its numerical stability widely unaffected by variations of material parameters is an important component for a technically more sophisticated and economic use of the material wood. Hence it will help to increase its range of applicability as a building material.

Kurzfassung

Holz wird im Bauingenieurwesen in vielen Anwendungen eingesetzt. Aufgrund des komplexen hierarchischen Aufbaus wurde dieses organische orthotrope Material in der modernen Wissenschaft vernachlässigt. Obwohl die wesentlichen Eigenschaften und das Verhalten von Holz unter einaxialen Belastungszuständen seit langer Zeit detailliert bekannt sind, gibt es noch einen erstaunlich hohen Forschungsbedarf über die biaxialen Eigenschaften.

Der Mangel an Wissen über die biaxiale Materialeigenschaften führte zu vereinfachten Annahmen in Normen, die die komplexe biaxiale Interaktion nicht berücksichtigen. Mit dem Aufkommen numerischer Methoden wie der Finiten Element Methode und den daraus resultierenden Möglichkeiten komplexere Konstruktionen zu berechnen, wurden Materialmodelle für Holz und andere Materialien notwendig. Diese sind erforderlich um diese Methoden für Konstruktionen unter mehr-axialen Spannungszuständen, wie Schalen oder Konstruktionsdetails, einsetzen zu können.

Ein orthotropes Einflächenmodell für Holz unter ebenen Spannungszuständen wurde von biaxialen Experimenten an reinem Fichtenholz in der LR-Ebene wurde am Institut für Mechanik der Werkstoffe und Strukturen abgeleitet. Die fehlende Möglichkeit der Identifikation von Versagensmechanismen mittels dieses Modells führte zur Beschreibung des biaxialen Materialverhaltens mit einem mehrflächen Plastizitätsmodell von Mackenzie-Helnwein et.al. Dieses Modell beinhaltet vier Zustandsflächen, die von den jeweiligen Versagenstypen abgeleitet wurden.

Diese Diplomarbeit beschreibt dieses orthotrope mehrflächen Plastizitätsmodell und die numerische Implementierung in einem Finite Elemente Programm in detaillierter Form. Bevor die mathematischen und konstitutiven Grundbausteine für diesen Zweck erläutert werden, gibt eine kurze Übersicht über die Anatomie und Struktur von Holz sowie die Experimente mit den beobachteten Versagensmechanismen einen genaueren Einblick in das Material und sein Verhalten.

Anschliessend werden die vier Zustandsflächen und deren Entfestigungs- bzw. Verfestigungsverhalten beschrieben. Die Flächen für Zugbeanspruchung in und normal zur Faserrichtung beschreiben sprödes Zugversagen. Jene normal zur Faser beschreibt ein kombiniertes Zug- und Schubmodell. Die Druck-Zustandsflächen sind durch eine nicht-lineare Verfestigung in radialer Richtung und eine geringe Entfestigung in Faserrichtung gekennzeichnet.

Das Ziel dieser Arbeit ist Probleme in der numerischen Implementierung des mehrflächen Plastizitätsmodells zu identifizieren und weitestgehend zu beheben. Die Identifikation der charakteristischen Länge als den mathematischen Grund für einige Instabilitäten bei FE-Berechnungen führte zur Entwicklung von neuen Algorithmen zur Berechnung der Entfestigung für große Werte dieses Modellparameters.

Mit diesen Algorithmen kann die Stabilität von Berechnungen deutlich verbessert werden. Weiters ist die Unabhängigkeit der Stabilität der numerischen Implementierung von der charakteristischen Länge eine Voraussetzung für die Anwendung des Materialmodells auf, im Bauingenieurwesen übliche, große Strukturen.

Ein von Modellparametern weitgehend unabhängig stabiles Materialmodell für Holz ist eine nützliche Komponente für eine technisch anspruchsvolle und wirtschaftliche Nutzung des Materials Holz und daher ein Schritt zur weiteren Verbreitung als Baumaterial.

Contents

1	Introduction	1
1.1	Wood as a material	1
1.2	Wood in structures	2
1.3	Motivation	2
1.4	Scope of work	4
2	Anatomy of wood	5
2.1	The tree - macroscale	5
2.2	The wood cell - microscale	6
2.3	The cell wall - nanoscale	9
2.4	The microfibril - molecularscale	11
3	Biaxial experiments	13
3.1	Equipment and test procedure	14
3.2	Experimental implementation	16
3.3	Test results	17
3.4	Failure modes	19
4	Material modeling	23
4.1	Orthotropy	23
4.1.1	Mathematical characterization	24
4.1.2	Structural tensors	27
4.1.3	Orthotropic invariants	31
4.2	Elasticity tensor	33
4.2.1	Isotropic elasticity tensor	34
4.2.2	Orthotropic elastic tensor	35
4.3	Theory of plasticity	37
4.3.1	Elastic stress-strain relationships	38
4.3.2	Yield criterion and elastic domain	39
4.3.3	Flow rule	40
4.3.4	Hardening and softening rule	40
4.3.5	Loading and unloading conditions	41
4.3.6	Consistency condition	41
4.3.7	Elasto-plastic tangent tensor	42
4.4	Multi-surface plasticity	43

5	Multi-surface plasticity model for wood	46
5.1	Generic constitutive functions	46
5.1.1	Generic formulation of orthotropic state-surfaces	46
5.1.2	Generic flow and softening/hardening rule	48
5.2	Fiber-tension surface	50
5.3	Fiber-compression surface	53
5.4	Radial-compression surface	57
5.5	Radial-tension and mixed mode surface	62
5.6	Visualization	72
5.7	Comparison of material models	75
6	Numerical implementation	78
6.1	Numerical integration – incremental formulation	78
6.2	Return mapping algorithm for a single orthotropic state surface	80
6.3	Specialization of the return mapping algorithm for two and more state surfaces	86
6.4	Corner-projection in multi-surface plasticity	91
6.5	Algorithmic tangent	92
6.6	Approximation of the algorithmic tangent	95
6.7	Residuum	95
6.8	Interdependency of return mapping algorithm and FE-computation	96
7	Stabilizing numerical algorithms for unstable cracks	98
7.1	Description of the problem for one dimension	98
7.1.1	Determination of softening coefficient k	100
7.1.2	Critical characteristical length	102
7.1.3	Maximum softening	105
7.2	Solution and implementation for biaxial stress states	105
7.2.1	Altering the start values of the return map algorithm	105
7.2.2	Algorithm for fiber tension and compression	107
7.2.3	Algorithm for radial tension - stress space	108
7.2.4	Algorithm for radial tension - strain space	112
7.2.5	Convergence study for large ℓ_c	114
7.2.6	Mixed mode example	118
7.2.7	Start values for return mapping algorithm in edges and corners . . .	119
7.3	Problem on structural-level	120
7.3.1	One-dimensional example	120
7.3.2	Convergence study for a biaxial stress state	123
8	Summary and conclusions	127
8.1	Summary	127
8.2	Conclusions	128
8.3	Future developments	128

Chapter 1

Introduction

1.1 Wood as a material

Wood is an indispensable material in the development of mankind and it is the most important sustainable mass raw material available. It has been used by man as building material since the rise of civilization and even before this time as energy resource and for tools. Newer applications use wood as a chemical raw material, such as paper, or as a raw material for wood composites or other bio-materials.

The extensive use of wood since the beginning of mans history is mainly due to its vast occurrence, but also to its easy availability and mechanical properties.

Forests occupy approximately one third of the earth's land area, which makes wood a natural resource that is worldwide available and regenerates itself constantly in the forests, faster than it is deforested. Moreover, the primary energy demand for extraction, transport, manufacturing and processing of wood products is very low.

In two aspects wood can be considered as an intelligent material, first due to

- its ability to detect its mechanical environment and adapt its structure to changing of stresses (adaptive growth) and second
- as a composite material on the nano structural level.

The material wood can be described as a fiber-composite cellular material with a hierarchical structure. It is optimized on all levels from the nano scale up to the scale of a whole tree. The cell walls structural skeleton contains cellulose fibers embedded in an amorphous matrix of hemicellulose and lignin.

The fact that wood is a naturally grown material does not have only positive sides. Nature is non-linear and not regular. Branches, existent in every tree, lead to inhomogeneities in the structure of wood. The appearance of knots in wood is irregular and can not be predicted. Knots lead to stress concentrations and weaken the material in general. Besides this inhomogeneity there are several other defects that may occur. Some of this

wood defects are growing anomalies like pressure wood, cracks in the raw material, distortions, curvatures, insect attack and fungal decay. Correct treatment and processing as well as a proper usage of wood in constructions can minimize the risk of many of this wood disadvantages.

1.2 Wood in structures

The origin for the vast use of timber in all kinds of constructions are also its mechanical properties. The high strength, $f_{t,0,\parallel} \approx 70 - 100 \text{ N/mm}^2$ for spruce wood (*Picea abies*), and low density, $\rho \approx 0.45 \text{ g/cm}^3$, result in one of the lowest strength/density ratios for commonly used materials in civil engineering.

Even though wood is one of the oldest materials used by man it is still of interest for scientists to analyze and investigate its structure and characteristics. Because of the fact that wood is a traditional material and is used in everyday life, one tends to overlook its importance for the future.

Besides the need for a better knowledge of the bodywork of wood to be used in material science, new cognitions about its mechanical properties are required for evaluating the possibility of wood usage in different engineering applications.

The use of wood for construction purposes changed and increased significantly with time and so have the methods to determine the best way of using the material wood in accordance with its unique (material) properties. As with all building materials the cost of materials strongly increased in the last centuries, while the cost of labor constantly dropped. This made a more accurate estimation of the bearing capacity of wood necessary.

The application of numerical calculation methods such as Finite-Element-Method (FEM) in structural engineering was one of the latest developments to determine structural responses to extraneous causes. The FEM can be used to assess the stiffness and strength performance of complicated wood structures close to reality.

In order to use the possibilities of calculating two and three dimensional structures like plates and shells or to improve structural details, and not depend on one-dimensional models or one-dimensional approximations, numerical simulation methods made the availability of an appropriate material model necessary.

For the most common construction materials in civil engineering this models exist already in several variants. Due to its hierarchical structure and its orthotropic behavior, material models for wood are more complicated than those for isotropic materials like concrete and steel. Moreover, the complexity of the needed tests to determine the two- or even three-dimensional behavior of wood was so high, that only recently some work was done to develop a 2-D material model for a plane stress state.

1.3 Motivation

The orthotropic behavior of wood is characterized by distinctive difference in the material properties in the material directions. Mechanical properties like the elastic stiffness as well as the strength, exhibit a high ratio of their values in grain direction with respect to the values in radial direction. The difference of the values between tangential (T) and radial

(R) direction is marginal in comparison to the large difference between the radial and the grain or longitudinal (L) direction. Not only the material orientation, given here with respect to the stem of a tree, also the loading direction is essential for the performance of wood. Tensile and compression strength in general show a large difference in their maximal values.

Due to this complex behavior, multi-axial experiments are difficult to perform. Tests for uniaxial states of stress have been performed in a wide range of different setups, but hardly any test under two- or even three-dimensional loading were accomplished.

The lack of knowledge concerning the biaxial behavior was reduced in the mid eighties when the first tests were performed by Spengler [41], Ehlbeck and Hemmer [10] and Hemmer [20]. A much more detailed insight in the behavior of wood under plane stress conditions was given in the nineties by Eberhardsteiner [7], Eberhardsteiner et al. [8, 9] and Gingerl [17].

They performed more than 400 individual tests with clear spruce wood specimens and loaded them in the LR-plane with 70 different biaxial stress states. The stress as well as the strain history was measured for all tests, leading to stress-strain relationships for biaxially stressed orthotropic material wood. Also in the post-failure regime the stress-strain behavior was recorded.

The lack of data concerning the interaction of different loading directions led to the use of the one-dimensional failure strengths, tensile and compressive, for the grain and radial direction in almost all codes, to define failure in the according direction for two dimensional stress states. Shear failure was defined as the maximum strength of the according plane. This failure values are equivalent to a cuboid as failure surface in the stress space. This box-like failure criterion was used in the works of Francois and Morlier [15] and Adalian and Morlier [1].

The elliptic failure surface developed by Tsai and Wu [42] for anisotropic materials fits the failure locations of the biaxial strength tests, as Eberhardsteiner [7] showed. Helnwein et al. [29] used a two-surface model to fit the same data, by adding a second surface for compression failure in radial direction. This allowed a better representation of failure in radial compression direction by implementing a hardening behavior.

A single-surface material model using the failure criterion of Tsai and Wu and implementing softening behavior for four different failure modes was suggested by Mackenzie-Helnwein et al. in [33]. A single-surface model is incapable of distinguishing between different failure modes. To accomplish a description of the softening for each mode, the single-surface was approximated to a multi-surface model. This multi-surface plasticity surface was developed by Mackenzie-Helnwein [30, 31] and comprises one surface for each failure mode observed in the biaxial strength tests. It is also based on the experimental data by Eberhardsteiner [7] and thus takes the coupling effects, observed in this tests, into account. The identification of a specific failure mode is possible with this model.

This work will perpetuate this four-surface failure model for clear spruce wood under plane stress conditions with the main focus on the softening model. The non-linear post-failure behavior was identified for four different failure modes and, with considerations of microscopic effects, macromechanically interpreted [30]. The detailed description of the softening behavior and its implementation with regard to a realistic finite-element discretization are the motivation for this thesis.

1.4 Scope of work

A general description as well as the mathematical formulation and computational implementation of the multi-surface failure model developed by Mackenzie-Helnwein [30, 31] is the content of this work. The emphasis is put on the post-failure behavior of this model, by focusing on unstable crack initialization. The last chapter is attended to solutions for numeric algorithms using the softening model.

After this short introduction on wood and its mechanical modeling a short overview of the anatomy and structure of wood is given in Chapter 2.

Chapter 3 presents the experiments by Eberhardsteiner [7] and the four failure modes with the micromechanically motivated explanation for their occurrence.

The mathematical tools for the description of the multi-surface model are presented in Chapter 4. An introduction on mathematical characterization of orthotropy is followed by the description of material stiffness and plasticity in this chapter. An individual section on multi-surface plasticity is the last part of this chapter on material modeling.

The material model with its four state surfaces is given in Chapter 5. After the introduction of a generic failure surface in the stress space and generic description of the softening/hardening state, each surface is described in detail. At the end of Chapter 5 a visualization of the multi-surface model in orthotropic stress space and a comparison with other models is given.

In Chapter 6 the numerical implementation in a finite-element program is described. The implementation of an individual surface, as well as the complete set of surfaces, including the accompanying problems at intersections, are shown in different sections. Besides the numerical formulation of the algorithmic tangent, an approximation for it is also given.

The last Chapter 7 deals with the problems of the numerical implementation of the softening model. A description for one-dimension is included, to present the problem in a concise way. The local and global effects in softening are shown theoretically and by several computations of different examples.

A summary of this work and a view on future developments can be found in Chapter 8.

Chapter 2

Anatomy of wood

Wood is an organic material with a complex hierarchical structure. It can be defined as the tissue which results from the secondary growth in the cambium of a living tree (see Section 2.1). The material can be described as a cellular composite structure. The walls of its cells are built up with cellulose fibrils, which are embedded in an amorphous matrix of hemicellulose and lignin.

The hierarchical structure of wood is optimized on each level. The shape of the whole tree, the cellular structure, and the construction of the cell wall are examples for this optimization process of nature.

This chapter contains a short introduction to the anatomy of wood. In the four sections are four different levels of observation discussed. Starting with the macroscale, the tree and its structure are described, followed by a description of the wood cell on the microscale and the nano structure of the cell wall. The last section concerns the molecular structure of the microfibrils.

The material model described in this work was developed for clear spruce wood, therefore the main focus is put on Norwegian spruce (*Picea abies*). This species is preferably growing in a climate with high humidity. Its appearance shows slim, tall and straight trees with a general height of 30 to 50 m and an average diameter of the stem of maximum 1.2 m. In Europe, especially in Austria, it is one of the most common conifer species. Due to its fast growth spruce is widely cultivated and used as building material in this region. Other common conifer trees in Austria are pine (*Pinus*) and larch (*Larix*).

Relevant literature on the topic of the anatomy of wood is e.g. [12, 14, 43], whereas a short overview can be found in [21, 25].

2.1 The tree - macroscale

In this section the structure of wood at the macroscale, i.e. in the range of 10^{-3} to 10^{-1} meters, is described.

The natural tasks of the structure that supports the trees greenery are mechanical

stability, transport and storage of water and minerals. The wood tissue of the tree fulfills these functions with a radial structure of different layers. The shape of a tree is optimized to transmit the external loadings in the best possible way to the underground. If the loading or the underground changes, e.g. after a slope gliding of the soil, the shape is adapted to the new requirements.

A tree is growing in every part, the stem, the branches and the roots. The origin of this growth is the cambial zone, which is located between the outer peel of the tree (bark) and the inner wood tissue. In the cambium, cells in two directions are developed due to growth. Toward the outside the *phloem* or bark cells are created, whereas toward the center the *xylem* or wood is built. The latter is called the secondary growth. The radial growing advance in the phloem is smaller than in the xylem.

In the following the components of a stem cross-section are described from the outer to the inner layer.

- The protective outer layer of the tree is the **bark**, which is divided into inner bark (living phloem) and outer bark (dead phloem).
- The **cambium** is a microscopic layer of living cells, that is not visible to the naked eye. Cells of the cambium subdivide and thus lead to growth in both, in inward direction and in outward direction.
- One part of the xylem is the **latewood**, which grows in summer and provides the main strength to the tree. It has a high density and is mostly dark.
- The **earlywood**, the other part of the xylem, is built in spring with lower density and light color. It provides the main water transport for the tree.
- The **pith** marks the center of a tree. It has a diameter of a few millimeters and represents the first cells grown in a tree. In early stages the pith stores and supports water in its cells for the germs, later the pith stores nutrients or it dies off.

Latewood and earlywood make up for the better part of the stem. They form an *annual* or *growth ring*. In trees that grow in regions with pronounced seasonal climate these rings are clearly distinguishable. In winter the growth stops completely, until the next annual ring with earlywood and latewood is added in the following year. This structure adds up and forms the wood structure, which does not change, once it is grown. The number of annual rings leads to the age of a tree, whereas by its thickness and structure information on environmental influences, like climate, is provided.

In old trees heartwood or corewood with its darker and sapwood with a lighter color can sometimes be distinguished. For spruce the color difference is marginal and thus corewood and sapwood can not be distinguished with the naked eye. The color of spruce wood is yellow-white.

2.2 The wood cell - microscale

In the dimension of millimeters down to micrometers the wood structure displays its cellular formation. Cellular solids are preferred to all-solids in nature and biology not only because of the lower density. The resulting voids of cellular solids can be used for several purposes.

In order to fulfill the three tasks mentioned in the beginning of Section 2.1, the cellular structure is essential for a tree because it provides high strength, while requiring less material. Moreover, the cells form a sophisticated system for the controlled interchange of water and minerals and they store nutrients.

The wood cells are mostly oriented parallel to the stem. The shape of the cells can be described as hollow tubes with closed ends. A wood cell can just about be seen by the naked eye, but a clear distinction is only possible with optical help.

The major two different kinds of trees, coniferous and deciduous trees, have generally different cellular structures, named with the wood types softwood and hardwood, respectively.

The biogenetically younger deciduous trees exhibit a more complex structure with several cell types. The main types are fibers, vessels and parenchyma cells. Fibers are long and slender cells and they mainly contribute to the mechanical strength. The main water transport takes place in vessels, which are long tubes with open ends to allow flow of the water. Parenchyma cells store nutrients. All cell types appear in various forms. The most obvious difference in comparison to softwood are the vessels, which are a magnitude of order bigger than other cells and thus influence the more or less uniform structure.

Coniferous trees are evolutionally older, nevertheless their anatomy is considerably simpler and more regular. Spruce wood is ranked among softwoods and serves as basis of this work.

Softwood consists of only two different wood cell types, which are tracheids and parenchyma cells.

Tracheids

Tracheids (prosenchymatic cells) are long and slender tubular cells with tapered ends and a lumen enclosed. Their cross-section is nearly rectangular or hexagonal.

Tracheids make up approximately 95 % of the total volume of spruce wood, with similar amounts in other softwoods. Their average length in spruce wood is 2.9 mm and the diameter varies from 7 to 32 μm depending on the location in the growth ring. Earlywood tracheids have thinner walls and a large mostly quadratic lumen. The cells become smaller in radial direction until reaching the annual ring border, where an abrupt stop indicates the complete growth pause in autumn and winter. This latewood tracheids have thicker cell walls and thus a smaller lumen. The transition between earlywood and latewood cells is more or less continuous.

The functions of tracheids are mechanical support and water transport. The spacious earlywood tracheids are best suited for the transport of water, whereas the latewood of the annual rings with the thick walls of the tracheids provides strength and mechanically support the tree. Prosenchymatic cells also exist in radial direction. These ray tracheids form in combination with the longitudinal tracheids a sophisticated conduction system for the interchange of water and minerals in the whole tree.

Softwood does not have continuous vessels for the water transport as hardwood does. Thus the water runs vertical in tracheids and, because prosenchymatic cells are closed volumina, needs to pass through the cell wall to the adjacent cell, where it continues vertically. To allow this penetration the cell walls are equipped with bordered pits. Most

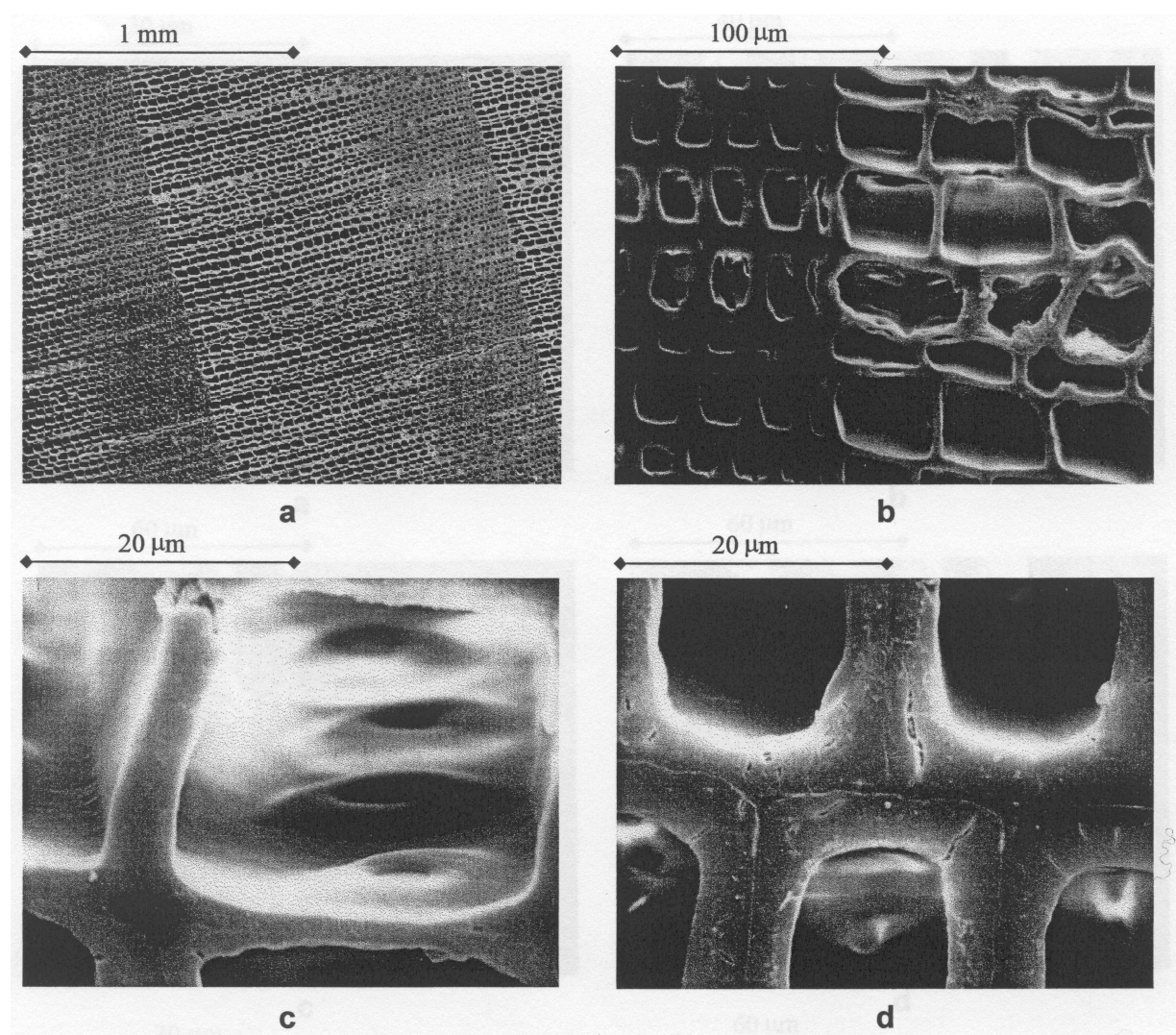


Figure 2.1: Cross-section of spruce wood tracheids: (a) two annual rings, (b) annual ring border, (c) earlywood tracheids with bordered pits and (d) latewood tracheids [25].

of the pits are located in the radial cell walls and especially more in earlywood tracheids, whereas the tangential walls have little or no pits.

The pits are pathways or gaps in the secondary cell wall. A membrane, which is located between the two cells, consists of the middle lamella and the primary cell walls (see Section 2.3). The influence of the pits on the mechanical properties of the cell wall is unknown. In bordered pits the secondary wall is separated from the primary wall and vaulted as a spherical shell to form the pit chamber. This shell, the *porus*, has a hole in the top part, where water can enter into the pit chamber and penetrate through the pit membrane. The pit membrane in coniferous trees is thickened in the center, forming the *torus*. Interchange of liquids takes place in the *margo*, which is the thin membrane around the torus.

In case of a high pressure difference between two adjacent cells the bordered pits serve as a valve and may close the pit irreversibly. Through stretching of the margo, the torus is pressed against the porus, thus closing the pit.

Figure 2.1 shows micrographs of a cross-section of spruce wood tracheid cells in different scales from 1 mm down to 20 μm obtained by Scanning Electron Microscopy (SEM). In Figures 2.1(a) and (b) the different sizes of cells in the earlywood and latewood as part of a growth ring are visible. Figures 2.1(c) and (d) show the pits in the cell walls of earlywood and latewood cells, respectively. In comparison to hardwood the more or less uniform anatomy of softwood becomes visible from this pictures.

Contrary to other softwood species, spruce wood shows a relatively regular cellular structure. The cells are aligned in regular lines. The cross-sections of its tracheids are nearly perfectly rectangular and show rounded edges.

Parenchyma cells

Parenchyma cells are short cells with a more or less flat end and thin wall. They form a tissue arranged like bricks and are the only living cells in a tree. All other cell types die soon after their formation. As prosenchymatic cells the parenchyma cells appear as longitudinal and radial cells in coniferous trees. The main function of ray and longitudinal parenchyma cells is storage of nutrients. Epithelia cells of vertical and horizontal resin canals are responsible for the secretion of elements. The wood rays, where parenchyma cells are agglomerated, seldom run continuously through the whole radius from pith to bark. More likely they split into single shorter rays.

Parenchyma cells also need pits for water conduction. These simple pits connect living parenchyma cells with each other. The secondary wall is recessed forming a small canal. The exchange of plasmatic material takes place at the membrane in this canal, consisting of the middle lamella and the primary cell wall on both sides.

A combination of bordered and simple pits exists in tracheids that cross radial wood rays. These half bordered pits are constructed as simple pits to the parenchyma cell's side and regular to the adjacent tracheid.

2.3 The cell wall - nanoscale

The cell wall can be described as a layered wall made of high-polymeric organic matter. The main macromolecular components are cellulose, polyoses or hemicelluloses, and lignin, which account for approximately 97 to 99 % of the wood structure. The term *macromolecular* states that the components consist of chains of molecules. The rest are low molecular weight substances like alcohols and aromatic compounds.

Cellulose is a polymer with a high molecular weight that is built up from only β -D-glucose and is one of the few natural compounds that maintains the same primary structure regardless of the organism it originates from, such as wood, cotton, grass or other plants. It is the main structural component of plant cell walls and accounts for 40 to 50 wt% of wood cell walls. The long cellulose chains form crystalline fibrils, as described in Section 2.4. A higher percentage can be found in tension wood of deciduous trees, where only a few percent lignin is contained in the cell walls.

Hemicellulose or **polyoses** also forms molecular chains, which are much shorter than in cellulose, due to side-groups or branches in the structure. The chemical structure depends on its origin, unlike cellulose. The content of polyoses in the cell wall is about 20 to 40 wt%. It is part of the matrix that surrounds the cellulose fibrils.

Lignin is a three-dimensional amorphous polymer. It is a major component of the cell wall giving it its final strength. It provides the compressive strength to the walls, thus the content of lignin in compression wood is higher. Lignin is also part of the matrix in which the fibrils are embedded.

In spruce the proportion of the three major components cellulose, hemicellulose and lignin is 40, 31 and 28 %, respectively. The matrix of hemicellulose and lignin is amorphous and softer than the cellulose fibrils, also called microfibrils. Therefore one can describe wood as stiff fibers embedded in a ductile matrix forming a natural fiber composite.

The layers of the cell wall mark the different steps in the process of the cell formation. The layers are arranged concentric and have different chemical compositions and different orientations of the structural components. In the following listing the different layers from the outer to the inner are described. This is equivalent to the direction of development of the layers.

- The **middle lamella** (ML) is the layer between two adjacent cells, gluing them together. It is very thin and nearly without cellulose. It consists mainly of hemicellulose and lignin.
- With the middle layer the form of the cells are defined. The cells now start growing the **primary wall** (P). The cellulose fibrils are spread in a random network over this layer. The primary wall allows an expansion of the cell, which is necessary in this state of cell growth.
- After the cell expansion has stopped, the secondary wall is built with either two or three layers. The fibrils in the first two layers are closely packed and parallel to each other. In the **secondary wall layer 1** (S1) the cellulose fibrils are wound around the lumen in a slight helical slope in several counter-running laminae.
- In the **secondary wall layer 2** (S2) the fibrils are also running in a helix form, but it is characterized by a steep angle. In latewood of spruce the average tilt angle of the fibrils with respect to the longitudinal cell axis, the so called *microfibril angle* (MFA), is about 20°, whereas in earlywood the MFA was found to be approximately 0°, i.e. the microfibrils are oriented vertical [26].
- The **secondary wall layer 3** (S3) exists only in parenchyma cells. The cellulose microfibrils are oriented randomly.
- In the last layer, the **tertiary wall** (T), the cellulose fibrils are oriented more or less randomly, but have a slightly helical shape.
- In some cells, such as parenchyma, the luminal surfaces, i.e. the inner part of the cell wall, is covered with warts, forming a **warty layer** (W).

In Table 2.1 the average thicknesses of the tracheid cell wall layers in spruce wood are given with the relative amount of the wall. The S2 layer is by far the prevailing layer of the cell wall, especially in cells which provide strength to the wood structure. Therefore the mechanical properties of the S2 layer are dominating the mechanical properties of wood. The microfibril angle is crucial for the mechanical behavior of the wood. It varies for different tree species and also within a tree. In compression wood of conifer trees and in the juvenile wood near the pith the MFA increases.

Table 2.1: Average thickness and percentage of the cell wall layers of spruce wood (*Picea abies*) tracheids [13].

layer	earlywood		latewood	
	[μm]	[%]	[μm]	[%]
ML/2+P	0.09	4.3	0.09	2.1
S1	0.26	12.4	0.38	8.8
S2	1.66	79.0	3.69	85.8
T	0.09	4.3	0.14	3.3
total	2.10	100.0	4.30	100.0

2.4 The microfibril - molecularscale

Wood is formed by mainly three chemical elements, namely carbon, oxygen and hydrogen. Because the cell wall accounts for nearly the whole wood material, the composition of the cell wall with approximately 50 wt% carbon, 43 wt% oxygen and 6 wt% hydrogen, can be assumed to represent the material wood. This composition is equivalent to 32 carbon, 21 oxygen and 47 hydrogen atoms per unit.

The most important component of wood is the **cellulose**, which forms the structural skeleton of nearly every cell wall layer.

Cellulose is a linear polymer with a uniform chain structure. This chain is built by **anhydroglucopyranose units**, which are bound together with β -(1 \rightarrow 4)-glycosidic linkages. One molecule of water is eliminated by the linkage of carbon 1 and carbon 4. Two anhydroglucopyranose units form a **cellobiose unit** with a length of 1.03 nm. These cellobiose units built up long cellulose chains, which are characteristic for wood. Only the β -glycosidic linkage with the β -position of the OH-group at carbon 1 allows the formation of elongated chains, whereas other glycosidic linkages would lead to different polymers.

The size of these cellulose chains is given by the ratio of the molecular weight of the chain to the molecular weight of the cellobiose unit and is defined as the *degree of polymerization*.

The **cellulose chains** are bound together and stabilized within itself by H-bonds at the OH-groups of each unit, hence forming a supramolecular structure. These H-bonds are responsible for the chemical and physical properties of cellulose. The two different types of H-bonds are the intramolecular and the intermolecular H-bonds. The first are bounds within a chain between two units and define the stiffness of the chain and the

orientation of the chain in the lattice of the crystallites. The latter connect the chains with each other and are the reason for the formation of fibrils and their crystalline structure.

The formed crystals are **native cellulose** or **cellulose I**. Its crystalline structure is constructed from monoclinic unit cells. A monoclinic cell of the crystal lattice has the form of a cube with one angle $\beta = 84^\circ$ not being a right angle. The dimensions of this cube are $a = 0.82$ nm, $b = 0.79$ nm and $c = 1.03$ nm, where the angle β is defined between a and b . The length c is oriented parallel to the longitudinal axis of a fibril.

An **elementary cellulose fibril** is built up by elongated cellulose chains, which form a crystal lattice. Its diameter is about 2.5 nm in spruce wood. The dimension of the crystalline region is with approximately 2.2 nm perpendicular to the fibril axis slightly smaller than the fibril diameter. The length of a crystal of about 11 nm is two or more orders of magnitude smaller than the length of a fibril.

The elementary cellulose fibril are combined to form a bundle of fibrils. This larger fibrils are the **microfibrils**, which are, embedded in a matrix, the basic module of the cell wall and hence the wood.

Chapter 3

Biaxial experiments

The material model for wood described in this work is based on biaxial experiments performed by Eberhardsteiner [7]. The goals of the research project conducted by Eberhardsteiner [7], Eberhardsteiner et al. [8, 9] and Gingerl [17] was to investigate the mechanical behavior of spruce wood under biaxial loading oblique to the fiber direction. The stress-strain relationship in the pre-failure domain and the failure location need to be known for arbitrary strain paths in order to develop a constitutive model.

For this type of loading there was a significant lack of knowledge, resulting in an insufficient variety of constitutive models for the orthotropic material wood. The orthotropic properties of wood arise from its hierarchical structure, as described in Chapter 2 and the resulting fiber alignment. The uniaxial mechanical behavior is also strongly influenced by the orthotropy, i.e. the grain angle.

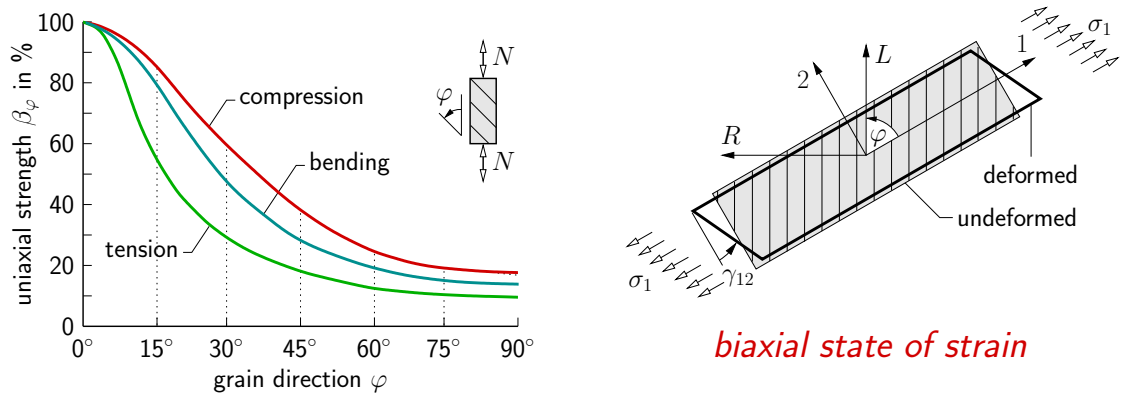


Figure 3.1: Uniaxial strength of wood [23] and biaxial strain state [7].

Figure 3.1 shows the decrease of uniaxial strength properties with increasing grain angle φ with respect to the loading direction. The appearance of shear deformation, that occurs at uniaxial loading of orthotropic materials oblique to the principal material directions is

also shown in this figure. The decrease of tensile strength of nearly 50 % in case of only 15° deviation of the fiber to the loading direction, is much more significant than the one of the compressive strength.

To investigate the behavior of wood under biaxial loading conditions 439 individual displacement-driven biaxial tests were performed on cruciform spruce wood specimens at the Institute for Mechanics of Materials and Structures of Vienna University of Technology. A special servo-hydraulic testing device for biaxial loading of anisotropic materials was used, which also measured the applied forces. The strain history was derived from analyses performed with a 3D Electronic Speckle Pattern Interferometer, with which three-dimensional contactless full-field deformation measurements were carried out.

This chapter gives an overview of these experiments and the obtained results. A detailed description and all test results can be found in [7]. In the last section the observed failure modes and their macroscopic interpretation are introduced.

3.1 Equipment and test procedure

Testing device

The used biaxial servo-hydraulic testing device was developed for this experiments. The specimens were mounted in the biaxial testing device by means of 12 steel bolts, which acted as points of application of the loads. Figure 3.2 shows the bolts of the testing device with the specimen attached to them. At each loading point two loading axis were attached with an angle of approximately 45° . Each of the 24 loading axes consists of a load cell, an inductive displacement transducer, a piston rod and a hydraulic cylinder.

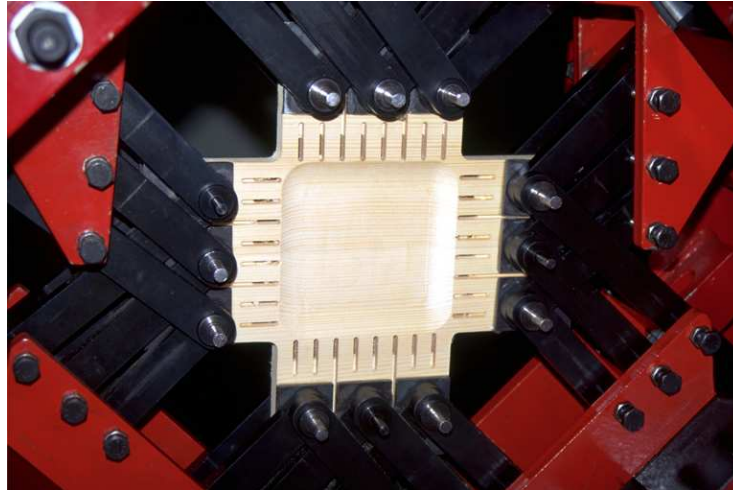


Figure 3.2: Spruce wood specimen in biaxial testing device [7].

Each hydraulic cylinder could apply a tensile or compressive force of ≈ 14 kN. The accuracy of the force measurement was 0.04 kN.

The testing machine featured, as mentioned above, a displacement-driven loading application. Each load application point is individually movable in two directions, thus in-plane

tensile and compression forces could be applied. The loading axes had a mobility of ± 5 mm, with an absolute positioning accuracy of $2.4 \mu\text{m}$.

Specimen

The shape of the specimen was determined and optimized by means of finite element analysis, to accomplish the requirements for a homogeneous strain and stress state within the measuring area. The specimen was a full symmetric cruciform plate as shown in Figure 3.3.

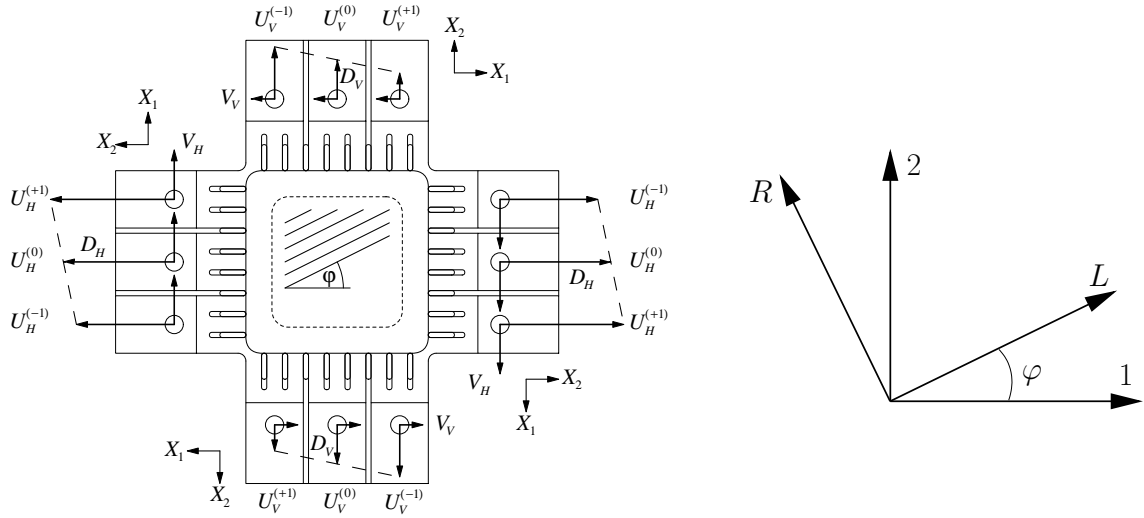


Figure 3.3: Cruciform specimen with applied displacements [7] and coordinate system $\{1;2\}$ and material coordinate system $\{L;R\}$.

At the loading points steel plates were glued to the wooden specimen to prevent fracture in these regions. The testing and measuring area was a wood area located in the middle of the specimen with a dimension of 140 mm times 140 mm and a thickness t of 4.5 mm. At this area the specimen was thinner, to ensure failure initiation there. For biaxial compression tests the testing area was slightly thicker with $t = 7.5 - 9.5$ mm to prevent buckling.

The principal directions of stress had to correspond with the horizontal and vertical direction of the specimen in order to avoid stress and strain concentrations in the corners of the measurement area. The specimen was antisymmetrically loaded at the loading points. A shear force was applied to achieve a principal stress state in the testing area.

In a material test the purpose of the specimen is the simulation of a infinitesimal element of the material wood. To accomplish this the specimen had to be technological homogeneous. This required constant distance of annual rings, parallel and straight annual rings, no inclusions, no defect- or rotary-growth and no knots or other failures. The obtained material is also called *clear* wood.

Deformation measurement

The deformation analysis system used for this experiments had to meet two major requirements. The mechanical homogeneity of the strain field needed to be controlled in the measuring field until failure was reached. Besides this qualitative requirement, the quantitative requirement was to measure the displacement and strain field until failure.

The used deformation measurement system was a 3D Electronic Speckle Pattern Interferometer (3D ESPI) system. The advantages of such a system are

- 3D measurement, i.e. all components of the deformation vector and not only a scalar value,
- full-field measurement in all points of the testing area, leading to a 2D displacement field,
- contactless measurement, i.e. without any mechanical interaction with the specimen,
- high accuracy, at least in the μm -range, and
- measurement in real-time; measuring time for every load increment only a few seconds.

Further details on this method and a description of the implementation for this testing configuration can be found in [17, 7].

3.2 Experimental implementation

As most used in uniaxial tests, the chosen material parameters of the investigated clear spruce wood were the density ρ and the moisture content u . After a test the volume and the mass of a special wood specimen were determined and the density was calculated. The specimens were stored in a climatic chamber at 20 °C and 65 % relative humidity, leading to a constant moisture content of $u = 12$ %. Keeping the moisture content constant keeps also the influence of this parameter on the strength properties constant. Therefore each test was performed within one hour.

The experimental parameters, loading direction (defined by φ) and loading ratio κ , varied for each test. The loading direction is defined by the grain angle φ , which is defined as the angle between the applied first principal stress direction and the fiber direction. Five different fiber directions were chosen for the experiments: $\varphi = 0^\circ, 7.5^\circ, 15^\circ, 30^\circ$, and 45° . The loading ratio κ describes the biaxial loading conditions. Its definition is $\kappa = D_h : D_v$, where D_h and D_v are the horizontal and the vertical displacements in certain loading points as shown in Figure 3.3. This ratio is approximately equivalent to the ratio of the normal components of the strain state, $\varepsilon_1 : \varepsilon_2$.

The specimen were loaded step-wise until failure was reached. The displacement increments varied between 4 and 10 μm . After reaching the load-plateau a deformation measurement was performed and the arose differences were analyzed.

Displacements and forces were measured and from these the strain and stress components computed. Numerical differentiation of the measured incremental displacements and summation over all load steps lead to the strain field.

It was assumed that when the testing area in the middle of the specimen was not under a homogeneous state of deformation, the influence of the loading zones was significant with respect to the observed forces at the loading points. Thus, failure was defined as the first extreme value of any of the two measured stress values σ_1 and σ_2 . It occurred in most tests approximately after 500-1000 displacements steps.

3.3 Test results

The main goal of the research project [7] was to describe the biaxial stress-strain relationship of clear spruce wood and to distinguish failure modes and their occurrence. To investigate the unloading behavior before reaching failure a small amount of the total number of proportional tests was performed with loading-unloading cycles at different load levels.

The data is given in terms of the independent variables σ_1 , σ_2 and φ . The coordinate system {1;2} in which the data is given, is aligned with the horizontal and vertical axes of the specimen (see Fig. 3.3). The formulation of the material model will be stated in terms of the stresses for the material directions longitudinal (L) or grain and radial (R). The transformation of stress components is given as

$$\begin{aligned}\sigma_L &= \sigma_1 \cos^2 \varphi + \sigma_2 \sin^2 \varphi, \\ \sigma_R &= \sigma_1 \sin^2 \varphi + \sigma_2 \cos^2 \varphi, \\ \tau_{LR} &= (\sigma_1 - \sigma_2) \sin \varphi \cos \varphi.\end{aligned}\tag{3.1}$$

For every test configuration $\{\varphi, \kappa\}$ six proportional tests were performed. Figure 3.4 shows the complete set of tests for grain angles $\varphi = 0^\circ$ and $\varphi = 45^\circ$. The axes aligned with the horizontal and vertical axis 1 and 2 of the cruciform specimen, as indicated in Figure 3.3. Their values are the principal stresses σ_1 and σ_2 .

The stress path of tests with tension in radial direction are linear, whereas wood under compression in radial direction shows a non-linear elastic stress-strain relation.

Each line represents the evolution of the principal stress ratio σ_2/σ_1 according the given loading ratio κ . Such charts were created for all five different fiber directions and are contained in [7]. The stress-strain relationship for every test were evaluated and documented in [7]. Four characteristic stress-strain relationships are shown in Figure 3.5.

In Figure 3.4 the material failure for each test is indicated with a symbol at the end of each line. This failure points form an ellipse in the stress space defined by the principal stress axes σ_1 and σ_2 . For different grain angles φ this ellipse rotates, as it can be seen by comparing the two graphs in Figure 3.4. This ellipses describe the strength of clear spruce wood.

Eberhardsteiner [7] used an ellipse described by a second order tensor polynomial according to Tsai and Wu [42] to fit this data. Figure 3.5 shows three elliptic failure envelopes. Each data point in Figure 3.5 indicates material failure of a test. The data points for $\varphi = 0^\circ$ are plotted in a $\sigma_L - \sigma_R$ graph, because for this grain angle the stresses in material direction σ_L and σ_R are equal to the principal stresses σ_1 and σ_2 , respectively. By transforming stress states with $\varphi \neq 0^\circ$ in material coordinates, these data points can be used for illustrations in a $\sigma_L - \sigma_R$ diagram. The blue failure envelope is based on the data points $\varphi = 0^\circ$, whereas for the red and green ellipses experimental data of all grain angles

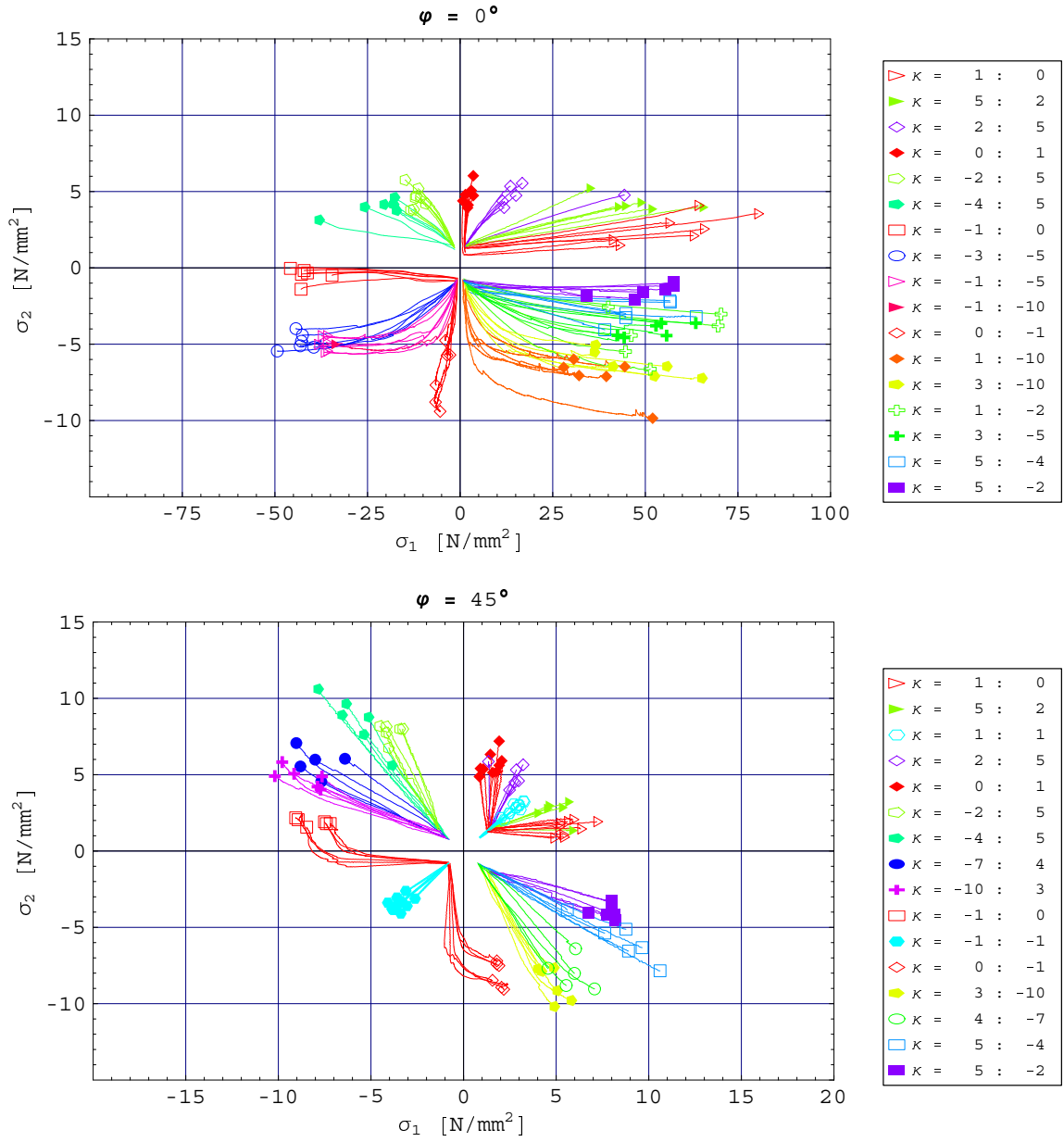


Figure 3.4: Biaxial stress-strain curves and failure positions for fiber directions $\varphi = 0^\circ$ and $\varphi = 45^\circ$ [7].

up to $\varphi = 45^\circ$ were considered. The green envelope was computed neglecting extreme values of each test configuration.

The scatter of the data points is only larger in the fiber tensile regime. The fiber compression regime with mixed loading shows very little scatter.

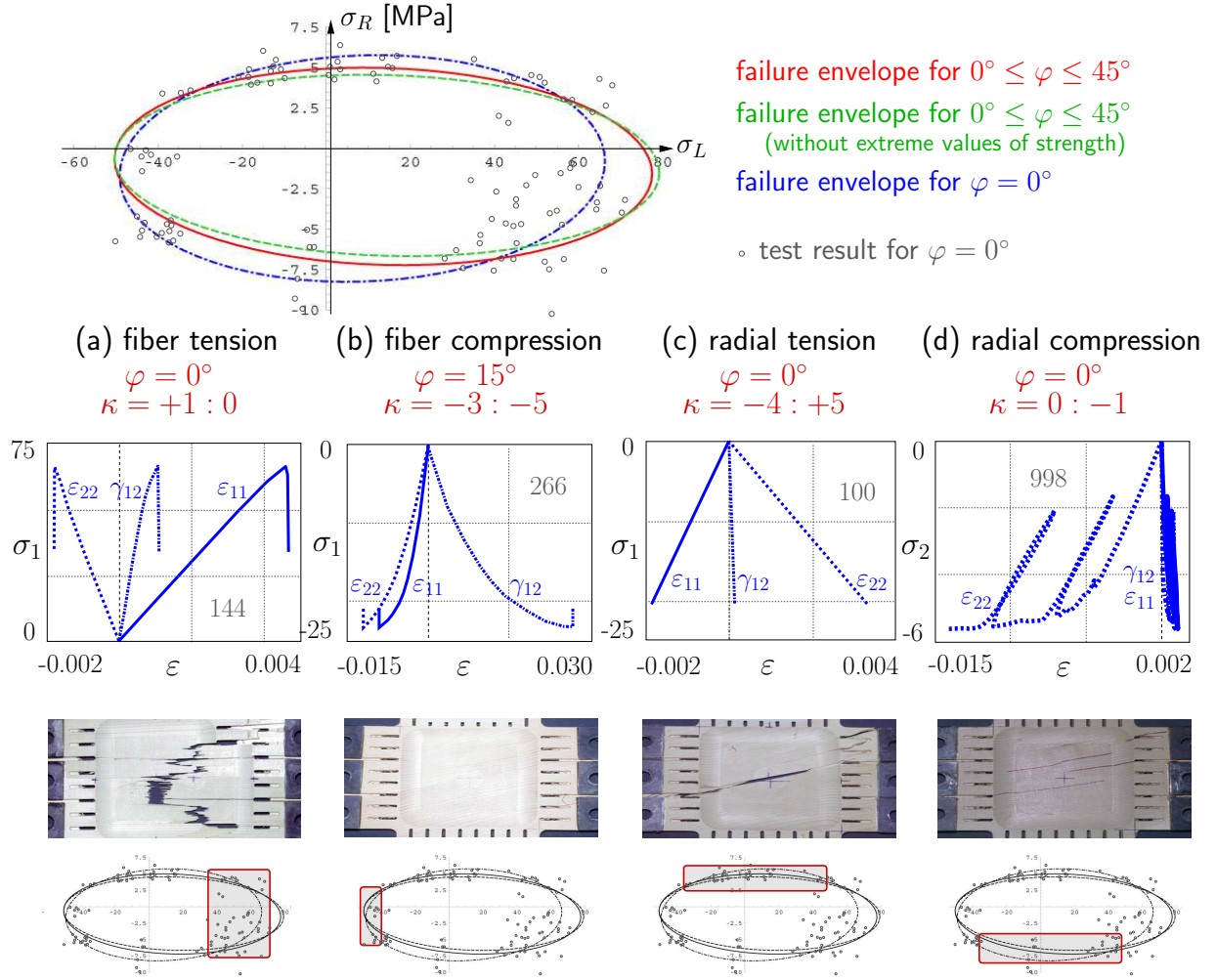


Figure 3.5: Elliptic failure envelopes and stress-strain curves with fracture type for characteristic loading types [30, 31].

3.4 Failure modes

Four different failure modes can be distinguished from the biaxial experiments. These failure modes occur in the tension and compression regime in the fiber and radial direction, respectively. Figure 3.5 shows a picture of the specimen after failure for every failure mode and a characteristic stress-strain relationship of a test exhibiting this behavior.

This section describes the four identified failure modes, their macroscopic characterization and a micromechanical explanation for their occurrence [30, 31]. The constitutive model, presented in detail in Chapter 5, describes these modes mathematically with four different failure surfaces.

(a) Fiber tension

This mode can be described as brittle tensile failure in fiber direction. As already mentioned above, the strength shows a large scatter for this mode, that only occurs for small grain

angles. This failure type is indicated by a cascading crack pattern on the macroscopic level. A reason for this crack pattern can be found on the microscopic scale in the strength of the cells [40].

The tensile strength of the fibers and the shear strength between the cells is approximately the same. After the rupture of the weakest fiber, the crack initially perpendicular to grain turns parallel to the fibers. Such a shear crack runs between the cells or within a cell wall. The shear crack evolves further until it reaches a weak cell and changes back to a crack in radial direction. This change between fiber rupture and inter-cell shear failure is indicated in Figure 3.6(a). The boundary between earlywood and latewood is most vulnerable to a shear crack.

The large scatter in the tensile strength can be explained with the statistical variation of the cell strength in the specimen and the importance of the weakest fiber for the evolution of the crack. The observed cascading crack pattern follows the weakest cell in a cell compound and combines shear failure with tensile failure of a fiber. Thus a description of this failure type on the macroscopic level is not directly possible.

The tensile tests in fiber direction described in this chapter show a brittle failure behavior with immediate loss of strength and without any softening, as observable in the left stress-strain relationship in Figure 3.5(a). On the contrary experiments on single cells or on cell compounds with a few fibers show a softening behavior [11]. Other tests on the micro scale show a dominant recovery mechanism that reforms the amorphous matrix between the cellulose microfibrils within the cell wall, maintaining its mechanical properties. This plastic response was found to be similar to that effected by moving dislocations in metals [22]. Due to the size of the specimen this effect is not visible on the macroscale.

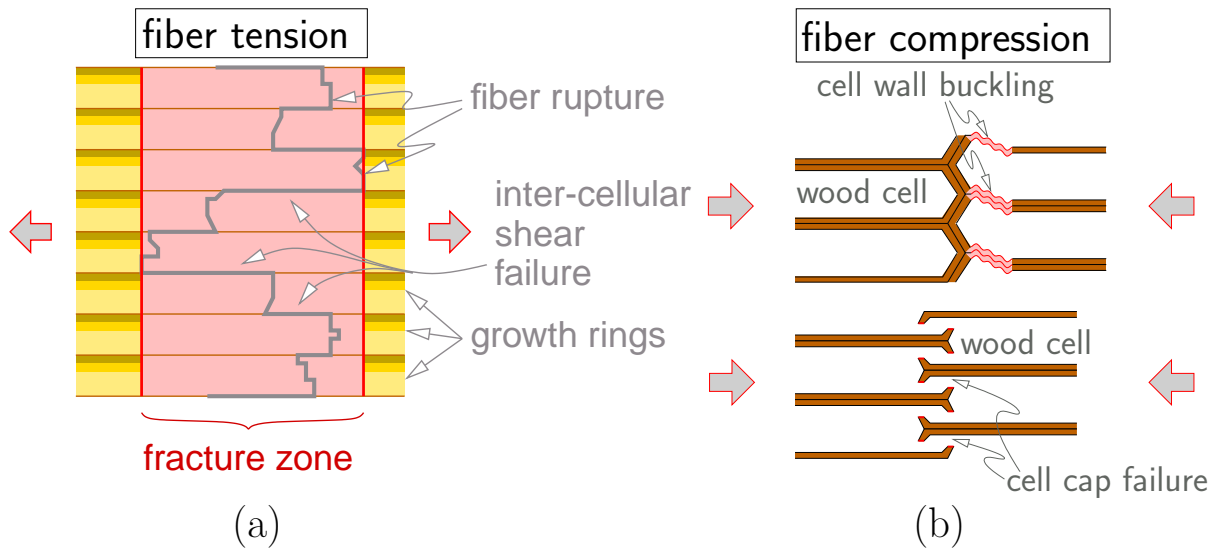


Figure 3.6: Tensile and compression failure modes in fiber direction.

(b) Fiber compression

Compression failure in fiber direction is signalized by the development of bands of damaged cells. This cell damage observed at a microscopic scale results from either inelastic cell wall buckling or brittle failure of the cell caps [16], as indicated in Figure 3.6(b). The combination with shear loading will more likely lead to cell wall buckling, but within a characteristic macroscopic reference volume a combination of these two failure types will be dominate. This is due to the variability of the micro structure, like different cell size and wall thickness, and chemistry.

The stress-strain curve for fiber compression in Figure 3.5(b) shows a minor non-linearity before failure and a softening after reaching the maximum strength. The initial strength drops off after failure, but stays at a strength plateau as observed in uniaxial tests. This strength degradation amounts to 20 to 30 % and it is not as strong as in the tensile regime. The strength degradation is caused by the before mentioned microscopic cell damage that occurs in a local region - the crushing band width - and is dependent on the fracture toughness.

At large compressive strains of about 50-60 % a sharp increase of the fiber compression strength occurs. This effect is called densification and leads to a significant increase in strength, while the material becomes nearly rigid. Densification causes a homogeneous deformation on a macroscopic level and is independent from the fracture toughness and the size of the crushing band width.

(c) Radial tension

The tensile failure perpendicular to grain and mixed mode failure is also brittle, as already described for fiber tension (see the stress-strain curve in Figure 3.5(c)). The failure pattern shows distinct straight cracks parallel to the fibers. The observed crack patterns showed a combination of mode I and mode II crack development. Loading at any grain angle may lead to this failure type.

If a developed crack is loaded with a compressive normal stress, shear stress can be transfered by friction over the two crack surfaces. This shear stress is smaller than the initial shear strength and decreases until it reached a residual value.

(d) Radial compression

The failure behavior for compressive loads perpendicular to the fiber direction can be described as ductile. A linear elastic behavior in unloading-reloading cycles and hardening plasticity can be observed in the right stress-strain relationship of Figure 3.5(d). The stiffness degradation in the different unloading-reloading cycles is negligible for the tested range of small strains.

The non-linear behavior, observable in the stress-strain curves, emanates from inelastic deformations during loading. The crushing of single cell rows, observed on the microscopic level, leads to homogeneous plastic deformations on the macroscopic scale. This is due to the repeated micro structure of the annual rings and the size of the specimen, which contains several annual rings.

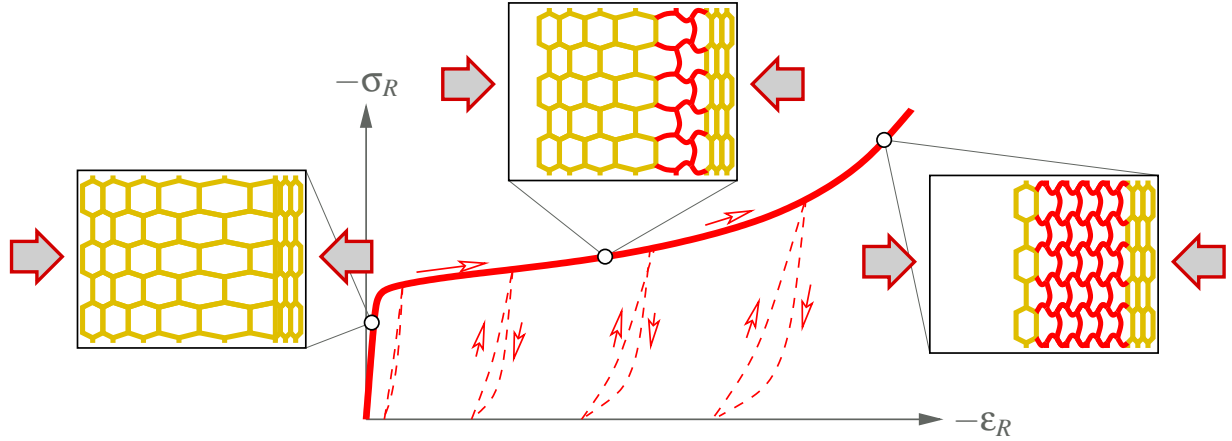


Figure 3.7: Failure mode for radial compression.

Thus this is the only mode where yielding-like deformations are observable. This effect can be seen in the stress-strain curve of Figure 3.5(d). It is similar to the saturation type hardening in metal plasticity.

Always a full cell row crushes with increasing plastic deformations, as indicated in Figure 3.7. The weakest rows are the ones in the early wood of the annual ring. Higher stress leads to the collapse of smaller and stronger cell rows until reaching the latewood rows. When the pore space has reached a minimum the compressive strength steeply increases [16]. The last phase is called densification and occurs as in the fiber direction at large compressive strains. The deformation process for radial compression is shown in Figure 3.7 for an elastic, a plastic and a point with densification.

Chapter 4

Material modeling

In this chapter, we will develop the basic ingredients for successful constitutive modeling of orthotropic materials. In the first section the mathematical description of orthotropy and the difference between the invariants of isotropic and the orthotropic tensors are given. Subsequently, the derivation of the elasticity tensors for isotropy and orthotropy, respectively, is elucidated. Finally, the theory of plasticity is discussed. Besides the main compounds of this theory for a single yield-surfaces, the foundations for multi-surface plasticity are given.

4.1 Orthotropy

The word *orthotropy* is a compound of the words *orthogonal* and *anisotropy*. A material is isotropic if it does not possess any distinct preferred directional behavior. Otherwise, it is orthogonal anisotropic. A special case of anisotropy is orthogonal anisotropy, or short, orthotropy. Orthotropic materials possess three mutually perpendicular symmetry planes. Examples for orthotropic materials are wood, ligaments, muscles or reinforced concrete plates.

The way how an orthotropic material behavior effects the solution strategy for a problem in theory of elasticity is illustrated in Figure 4.1. From a change $d\mathbf{u}$ of the global displacement field \mathbf{u} follows the local change $d\boldsymbol{\varepsilon}$ of the strain from the rate-kinematic relations. A constitutive law, that connects the internal strain $d\boldsymbol{\varepsilon}$ with the internal stress change $d\boldsymbol{\sigma}$, is obtained from material-tests. The material behavior, such as the orthotropy, are represented in the elastic stiffness tensor \mathbb{C} . By formulating the equilibrium of a system, the internal and external forces are to be balanced with each other. A free body diagram, the principal of virtual work, and the minimum of potential energy are the three possibilities of statics to formulate equilibrium conditions. From the kinematic relations, the equilibrium condition, and the constitutive law follows a set of equations to solve the problem. The change of the external forces $d\mathbf{f}$ and of the displacement field $d\mathbf{u}$ can be connected by the system stiffness matrix \mathbf{K} .

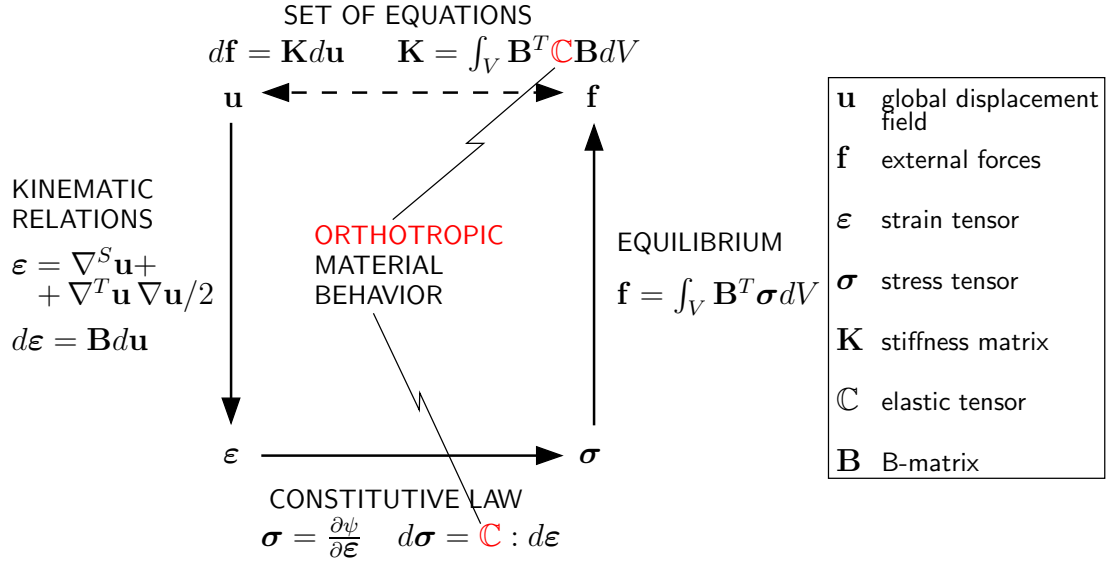


Figure 4.1: Effect of orthotropy in elasticity-theory.

4.1.1 Mathematical characterization

The mathematical characterization of orthotropy is based on the comparison of a deformed body, where parts of this body were subjected to a transformation \mathbf{Q} before the deformation.

Figure 4.2 shows an undeformed body \mathcal{U} . The material point \mathbf{X} is subjected to a transformation \mathbf{Q} . To define the properties of this transformation, the body undergoes a deformation \mathbf{u} in the transformed \mathcal{U}^* and initial condition \mathcal{U} . The acting forces along the interface of the material point in the deformed body \mathcal{D} are compared.

The mathematical definition of isotropy, illustrated by Figure 4.2, can be stated as

$$\mathbf{t} = \mathbf{t}^* \quad \forall \mathbf{X} \in \mathcal{U} \quad \text{or} \quad \forall \mathbf{x} \in \mathcal{D}, \quad (4.1)$$

where \mathbf{t}^* and \mathbf{t} are stress-vectors at the interface, that follow from Cauchy's formulas

$$\mathbf{t} = \mathbf{n} \boldsymbol{\sigma}, \quad (4.2)$$

in the same point, with and without a transformation \mathbf{Q} of a material part, respectively. \mathbf{n} is the normal vector in a point on the interface of this material part. A transformation is a symmetry transformation if condition (4.1) is satisfied. And, therefore does not change the properties of the material.

(4.1) holds when the material does not change its behavior, due to a transformation \mathbf{Q} . If (4.1) holds for

- any orthogonal transformation $\mathbf{Q} \in \mathcal{SO}(3) \Rightarrow$ material is **isotropic**
- only the *identity* transformation $\mathbf{Q} = \mathbf{1} \Rightarrow$ material is generally **anisotropic**
- certain transformations $\mathbf{Q} \in \mathcal{MO}(3) \in \mathcal{SO}(3) \Rightarrow$ mat. possesses **special anisotropy**.

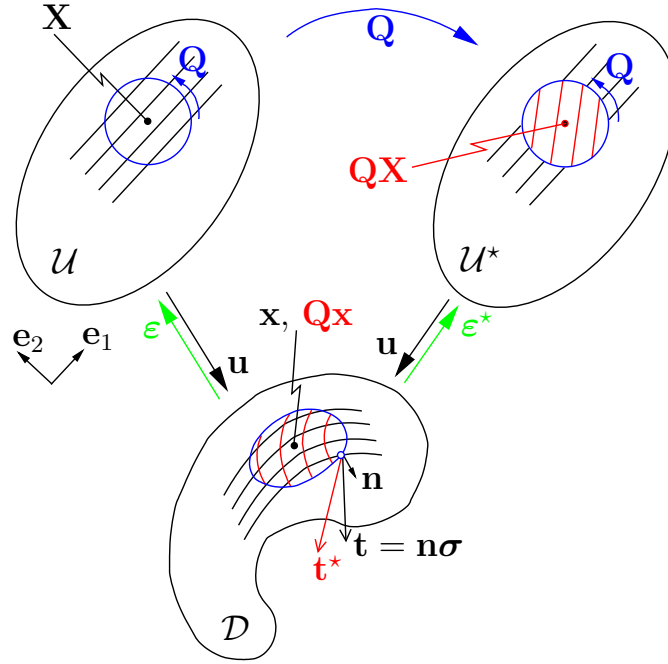


Figure 4.2: Illustration of the mathematical definition of isotropy and orthotropy.

The *material symmetry group* $\mathcal{SO}(3)$ or *isotropy group* of a material is defined as the group of transformations of the material coordinates which leave the constitutive equations invariant [32]. $\mathcal{MO}(3)$ is the material orthogonal group defining the type of anisotropy. For an orthotropic material, this group consists of rotations of 180° each about three mutually orthogonal axes defined by the unit normal vectors \mathbf{A}_1 , \mathbf{A}_2 and \mathbf{A}_3 .

The transformation of a vector \mathbf{A} , defined in an arbitrary observer coordinate system $\mathbf{e}_1, \mathbf{e}_2$, to a new orientation \mathbf{A}^* can be written

$$\mathbf{A}^* = \mathbf{Q}\mathbf{A}. \quad (4.3)$$

A transformation of a second order tensor $\mathbf{S} = \mathbf{A} \otimes \mathbf{A}$ yields from (4.3) as

$$\mathbf{S}^* = \mathbf{A}^* \otimes \mathbf{A}^* = (\mathbf{Q}\mathbf{A}) \otimes (\mathbf{Q}\mathbf{A}) = \mathbf{Q}(\mathbf{A} \otimes \mathbf{A})\mathbf{Q}^T = \mathbf{Q}\mathbf{S}\mathbf{Q}^T. \quad (4.4)$$

The last operations of (4.4) become more clear, when performed in index notation as follows:

$$S_{ij}^* = A_i^* A_j^* = Q_{ik} A_k Q_{jl} A_l = Q_{ik} A_k A_l Q_{lj}^T = Q_{ik} S_{kl} Q_{lj}^T. \quad (4.5)$$

Similar tensor definitions are used in Section 4.1.2 for the formulation of structural tensors.

To check if \mathbf{Q} is a symmetry transformation one needs to compute a potential function of the material, e.g. the Helmholtz free energy $\psi(\boldsymbol{\varepsilon})$. As indicated in Figure 4.2 this computation needs to be performed for the unaltered body \mathcal{U} and for the body \mathcal{U}^* , where parts have been subjected to a transformation. A deformation \mathbf{u} yields to strains $\boldsymbol{\varepsilon}$. The strain tensor $\boldsymbol{\varepsilon}^*$ after the transformation, e.g. a rotation, follows from the strain tensor $\boldsymbol{\varepsilon}$

$$\boldsymbol{\varepsilon}^* = \mathbf{Q}\boldsymbol{\varepsilon}\mathbf{Q}^T. \quad (4.6)$$

\mathbf{Q} is a *symmetry transformation* if the Helmholtz free energy $\psi(\boldsymbol{\varepsilon})$ does not change due to this transformation, i.e.

$$\psi(\boldsymbol{\varepsilon}) \equiv \psi(\boldsymbol{\varepsilon}^*). \quad (4.7)$$

Only for isotropic materials are all operations symmetry transformations. For the special anisotropy orthotropy (4.1) only holds for certain symmetry transformations $\mathbf{Q} \in \mathcal{MO}(3)$, which will be described subsequently for the two-dimensional case $\mathbf{Q} \in \mathcal{MO}(2)$.

The symmetry operation for an orthotropic material, in the two-dimensional, plane case, are shown in Figure 4.3. The vectors \mathbf{e}_1 and \mathbf{e}_2 define an arbitrary orthonormal coordinate system. The left figure in 4.3 shows the unit normal vectors \mathbf{A}_1 and \mathbf{A}_2 that are permanently attached to the orthogonal axis, that define the orthotropic directions of the material. A general position (red) with an angle Φ to the observer coordinate system and a special position (blue), where the vectors \mathbf{A}_1 and \mathbf{A}_2 are aligned with the observer coordinate system, is shown. Note, that the four material parts that were subjected to the symmetry transformations indicated in Figure 4.3, have the same alignment. This is an obvious requirement the symmetry of the transformation, because the body, i.e. material, must not change its mechanical properties and response.

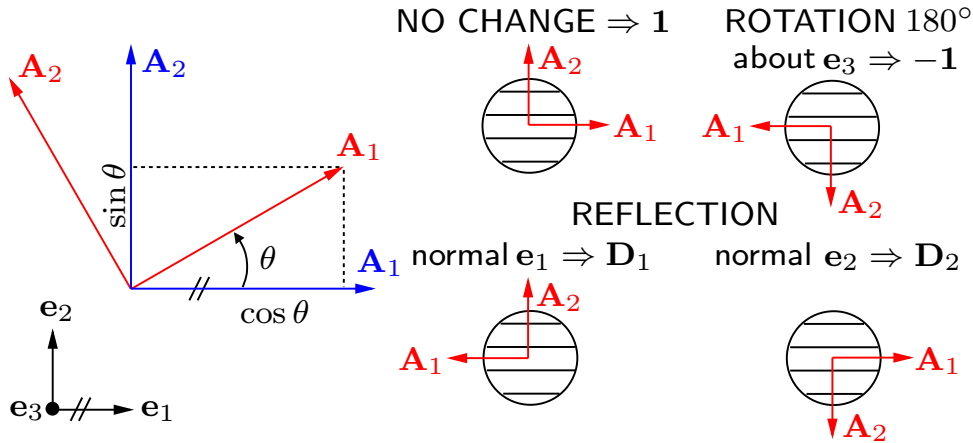


Figure 4.3: Symmetry transformations for 2D orthotropy.

If no change is observed for the material response, it is obviously a symmetry operation. Mathematically this is equivalent to

$$\mathbf{Q} = \mathbf{1}. \quad (4.8)$$

A rotation of 180° is also a symmetry operation and is equivalent to a sign change of the basis vectors. It can be written

$$\mathbf{Q} = -\mathbf{1}. \quad (4.9)$$

The fact that $\det \mathbf{1} = 1$ is positive, proves that the transformation (4.9) actually is a rotation. The symmetry operation reflection with normal \mathbf{e}_1 can be computed as

$$\mathbf{Q} = \mathbf{D}_1 = \mathbf{1} - 2\mathbf{M}_1, \quad (4.10)$$

where \mathbf{M}_1 is a structural tensor, which are laid out in detail in Section 4.1.2. The reflection with normal \mathbf{e}_2 is also a symmetry transformation, but it is a combination of other

symmetry transformations and hence depending on other transformations. A rotation of 180° and a reflection with normal \mathbf{e}_1 gives the same result

$$\mathbf{Q} = \mathbf{D}_2 = \mathbf{D}_1 \cdot (-\mathbf{1}). \quad (4.11)$$

Both transformations \mathbf{D}_1 and \mathbf{D}_2 have negative determinant, $\det \mathbf{D} = -1$, which proves that these actually are reflections.

The symmetry group for two dimensional orthotropy therefore is

$$\mathcal{MO}(2) = \{\mathbf{1}, -\mathbf{1}, \mathbf{D}_1\}, \quad (4.12)$$

where the symmetry transformation \mathbf{D}_2 is excluded, because it is not independent from the other members in the group. This transformations $\mathbf{Q} \in \mathcal{MO}(2)$ cause no change in the material behavior if applied to the whole structure or parts of it. Table 4.1 shows the matrix representation of the four symmetry transformations for two dimensional orthotropy for the special case that the observer coordinate system \mathbf{e}_1 and \mathbf{e}_2 is in accordance with the vectors \mathbf{A}_1 and \mathbf{A}_2 . The notation $\{\square_{ij}\}$ for the matrix-representation of a tensor was taken from [18]. In the three dimensional case, the orthotropic symmetry transformations are

$$\mathcal{MO}(3) = \{\mathbf{1}, -\mathbf{1}, \mathbf{R}_1, \mathbf{R}_2, \mathbf{R}_3\}, \quad (4.13)$$

where \mathbf{R}_1 , \mathbf{R}_2 and \mathbf{R}_3 are rotations of 180° about the three main material axes.

Table 4.1: Matrix representation of symmetry transformations for two dimensional orthotropy for the special coordinate-system $\mathbf{A}_1 = \mathbf{e}_1$ and $\mathbf{A}_2 = \mathbf{e}_2$.

$\mathcal{MO}(2)$	$\{\mathbf{1}_{ab}\}$	$-\{\mathbf{1}_{ab}\}$	$\{\mathbf{D}_{1ab}\}$	$\{\mathbf{D}_{2ab}\}$
$\{\mathbf{Q}_{ab}\}$	$\begin{bmatrix} 1 & 0 \\ 0 & 1 \end{bmatrix}$	$\begin{bmatrix} -1 & 0 \\ 0 & -1 \end{bmatrix}$	$\begin{bmatrix} -1 & 0 \\ 0 & 1 \end{bmatrix}$	$\begin{bmatrix} 1 & 0 \\ 0 & -1 \end{bmatrix}$

4.1.2 Structural tensors

The main directions of the tree are described by a ortho-normal system of three basis-vectors \mathbf{A}_i with $i \in 1, 2, 3$. These are not unique, because some transformations, e.g. a rotation of 180° about any of these directions, changes the sign of the two other basis vectors. As explained above, symmetry transformations must not change the behavior of orthotropic materials. Thus, the vectors \mathbf{A}_i are not directly suitable to describe orthotropic material behavior. The definition of structural tensors is used to allow for the formulation of tensor functions for an orthotropic material. They ensure that the material tensors and tensor functions are not changed by transformations, by applying changes according to the symmetry of the transformation in the coordinates (components) of the tensors. Tensors are coordinate-independent objects, hence this applies also to structural tensors. Transformations between different coordinate systems, e.g. from the coordinate system

used in the finite element computation to the material coordinate system, will only change the components in the particular coordinate system, with consideration of orthotropic symmetry transformation.

The structural tensors are constructed from unit normal vectors that are locally aligned with the L or grain (longitudinal), R or radial and T or tangential growth directions of the tree. This material vectors \mathbf{A}_L , \mathbf{A}_R and \mathbf{A}_T are shown in Figure 4.4.

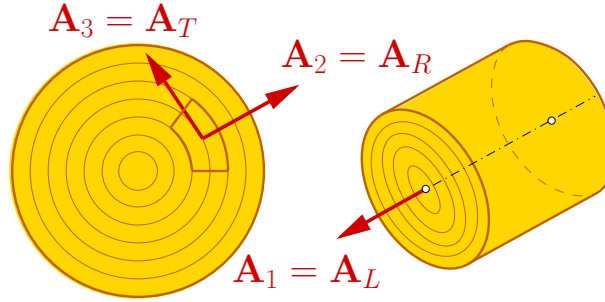


Figure 4.4: Definition of the material vectors aligned to the directions of the tree [30].

The structural tensors for three dimensions are [30]

$$\mathbf{M}_L = \mathbf{A}_L \otimes \mathbf{A}_L, \quad \mathbf{M}_R = \mathbf{A}_R \otimes \mathbf{A}_R, \quad \text{and} \quad \mathbf{M}_T = \mathbf{A}_T \otimes \mathbf{A}_T. \quad (4.14)$$

For the material model elucidated in this work, a plane state of stress in the LR -plane leads to a two dimensional problem. The last structural tensor of (4.14), \mathbf{M}_T , is therefore not needed for the formulation.

\mathbf{A}_i are aligned with and permanently attached to the main orthotropic material directions as shown in Figure 4.4. They are unique and independent of the (observer) coordinate system. Changing the observer coordinate system leads to an alteration of the components of \mathbf{A}_i , but not its orientation.

The left figure in 4.3 shows the base vectors \mathbf{A}_i inclined with an angle θ (red) and aligned (blue) with the observer coordinate system \mathbf{e}_1 and \mathbf{e}_2 . The general coordinate representation of the base vectors follow from simple geometric considerations to

$$\mathbf{A}_L = \begin{bmatrix} \cos \theta \\ \sin \theta \end{bmatrix} \quad \text{and} \quad \mathbf{A}_R = \begin{bmatrix} -\sin \theta \\ \cos \theta \end{bmatrix}, \quad (4.15)$$

where \mathbf{A}_L and \mathbf{A}_R are vectors with $\mathbf{A}_L \cdot \mathbf{A}_R = 0$, i.e. they are orthogonal. For a special coordinate system that is aligned with \mathbf{A}_i , i.e. $\theta = 0$, the coordinate representation changes using $\cos \theta = 1$ and $\sin \theta = 0$.

Computing the structural tensors

$$\mathbf{M}_i = \mathbf{A}_i \otimes \mathbf{A}_i = \mathbf{A}_i \mathbf{A}_i^T \quad (4.16)$$

is fairly easy in an arbitrary chosen observer coordinate system. They make the implementation of transformations better understandable. For the special case, that the observer

coordinate system \mathbf{e}_1 and \mathbf{e}_2 and \mathbf{e}_3 is identical to the vectors \mathbf{A}_L , \mathbf{A}_R and \mathbf{A}_T , the computation of \mathbf{M}_L according to (4.16) can be written for the

$$\{\mathbf{M}_{Lab}\} = \begin{bmatrix} 1 \\ 0 \end{bmatrix} \begin{bmatrix} 1 & 0 \end{bmatrix} = \begin{bmatrix} 1 & 0 \\ 0 & 0 \end{bmatrix}, \quad (4.17)$$

where $\{\square_{ij}\}$ indicates the matrix-representation of a tensor, which was taken from [18].

Table 4.2 shows the coordinate representation of the base vectors \mathbf{A}_i and the structural tensors \mathbf{M}_i for an observer coordinate system with $\theta = 0^\circ, 45^\circ, 90^\circ$ and 180° . The representations of the structural tensors for 0° and 180° are equal, which shows that the rotation of 180° is a symmetry transformation, for which the material must not change its behavior.

Table 4.2: Coordinate representation of material vectors and structural tensors for different angles θ .

θ	\mathbf{A}_L	\mathbf{A}_R	$\mathbf{M}_L = \mathbf{A}_L \otimes \mathbf{A}_L$	$\mathbf{M}_R = \mathbf{A}_R \otimes \mathbf{A}_R$
0°	$\begin{bmatrix} 1 \\ 0 \end{bmatrix}$	$\begin{bmatrix} 0 \\ 1 \end{bmatrix}$	$\begin{bmatrix} 1 & 0 \\ 0 & 0 \end{bmatrix}$	$\begin{bmatrix} 0 & 0 \\ 0 & 1 \end{bmatrix}$
45°	$\begin{bmatrix} 1/\sqrt{2} \\ 1/\sqrt{2} \end{bmatrix}$	$\begin{bmatrix} -1/\sqrt{2} \\ 1/\sqrt{2} \end{bmatrix}$	$\begin{bmatrix} 1/2 & 1/2 \\ 1/2 & 1/2 \end{bmatrix}$	$\begin{bmatrix} 1/2 & -1/2 \\ -1/2 & 1/2 \end{bmatrix}$
90°	$\begin{bmatrix} 0 \\ 1 \end{bmatrix} = \mathbf{A}_2$	$\begin{bmatrix} -1 \\ 0 \end{bmatrix} = -\mathbf{A}_1$	$\begin{bmatrix} 0 & 0 \\ 0 & 1 \end{bmatrix}$	$\begin{bmatrix} 1 & 0 \\ 0 & 0 \end{bmatrix}$
180°	$\begin{bmatrix} -1 \\ 0 \end{bmatrix} = -\mathbf{A}_1$	$\begin{bmatrix} 0 \\ -1 \end{bmatrix} = -\mathbf{A}_2$	$\begin{bmatrix} 1 & 0 \\ 0 & 0 \end{bmatrix}$	$\begin{bmatrix} 0 & 0 \\ 0 & 1 \end{bmatrix}$

The norm $\|\square\|$ of any vector \mathbf{A}_i must be one, since the structural tensors must be constructed from unit vectors. The sum of \mathbf{M}_L and \mathbf{M}_R in any coordinate system must be

$$\mathbf{1} = \mathbf{A}_L \otimes \mathbf{A}_L + \mathbf{A}_R \otimes \mathbf{A}_R = \mathbf{M}_L + \mathbf{M}_R \quad \Rightarrow \quad \{\mathbf{1}_{ab}\} = \begin{bmatrix} 1 & 0 \\ 0 & 1 \end{bmatrix} \quad (4.18)$$

for any θ , because the 2^{nd} order identity tensor is an *isotropic tensor*, which is invariant under *any* coordinate transformation.

The shear base tensor \mathbf{N}

An important abbreviation used in connection with the shear terms is the tensor

$$\mathbf{N} = \frac{1}{2} (\mathbf{A}_L \otimes \mathbf{A}_R + \mathbf{A}_R \otimes \mathbf{A}_L). \quad (4.19)$$

The matrix and vector representations of \mathbf{N} for a coordinate system aligned with \mathbf{A}_1 and \mathbf{A}_2 are

$$\{\mathbf{N}_{ab}\} = \begin{bmatrix} 0 & 1/2 \\ 1/2 & 0 \end{bmatrix}, \quad \{\mathbf{N}_a\} = \begin{bmatrix} 0 \\ 0 \\ 2 \cdot 1/2 = 1 \end{bmatrix} \quad \text{and} \quad \{\mathbf{N}^a\} = \begin{bmatrix} 0 \\ 0 \\ 1/2 \end{bmatrix}, \quad (4.20)$$

where $\{\mathbf{N}_a\}$ is the vector representation in covariant and $\{\mathbf{N}^a\}$ in contra-variant coordinates, respectively. \mathbf{N} according to (4.19) is no structural tensor, because its sign changes under symmetry transformation.

According to a general convention, the second order stress tensor $\boldsymbol{\sigma}$ is used in contra-variant coordinates

$$\boldsymbol{\sigma} = \begin{bmatrix} \sigma_{LL} & \tau_{LR} \\ \tau_{RL} & \sigma_{RR} \end{bmatrix} \quad \Rightarrow \quad \{\boldsymbol{\sigma}^a\} = \begin{bmatrix} \sigma_{LL} \\ \sigma_{RR} \\ \tau_{LR} \end{bmatrix}. \quad (4.21)$$

Symmetric tensors can be written with (4.19) as

$$\begin{aligned} \boldsymbol{\sigma} &= \sigma_{LL} \mathbf{A}_L \otimes \mathbf{A}_L + \sigma_{RR} \mathbf{A}_R \otimes \mathbf{A}_R + \tau_{LR} (\mathbf{A}_L \otimes \mathbf{A}_R + \mathbf{A}_R \otimes \mathbf{A}_L) = \\ &= \sigma_{LL} \mathbf{M}_L + \sigma_{RR} \mathbf{M}_R + 2\tau_{LR} \mathbf{N}. \end{aligned} \quad (4.22)$$

The strain tensor $\boldsymbol{\varepsilon}$ is commonly represented in covariant coordinates. Its matrix and vector representations, respectively, are

$$\boldsymbol{\varepsilon} = \begin{bmatrix} \varepsilon_{LL} & \varepsilon_{LR} \\ \varepsilon_{RL} & \varepsilon_{RR} \end{bmatrix} \quad \Rightarrow \quad \{\boldsymbol{\varepsilon}_a\} = \begin{bmatrix} \varepsilon_{LL} \\ \varepsilon_{RR} \\ 2\varepsilon_{LR} = \gamma_{LR} \end{bmatrix}, \quad (4.23)$$

where $\gamma_{LR} = 2\varepsilon_{LR}$ is the engineering strain. $\boldsymbol{\varepsilon}$ can be written, using the definition of \mathbf{N} according to (4.19), as

$$\begin{aligned} \boldsymbol{\varepsilon} &= \varepsilon_{LL} \mathbf{A}_L \otimes \mathbf{A}_L + \varepsilon_{RR} \mathbf{A}_R \otimes \mathbf{A}_R + \varepsilon_{LR} (\mathbf{A}_L \otimes \mathbf{A}_R + \mathbf{A}_R \otimes \mathbf{A}_L) = \\ &= \varepsilon_{LL} \mathbf{M}_L + \varepsilon_{RR} \mathbf{M}_R + \gamma_{LR} \mathbf{N}. \end{aligned} \quad (4.24)$$

Computing the double dot product or double contraction of a symmetric second order tensor and \mathbf{N} leads to the shear stress

$$\boldsymbol{\sigma} : \mathbf{N} = \frac{1}{2} \boldsymbol{\sigma} : (\mathbf{A}_L \otimes \mathbf{A}_R + \mathbf{A}_R \otimes \mathbf{A}_L) = \frac{1}{2} (\mathbf{A}_L \boldsymbol{\sigma} \mathbf{A}_R + \mathbf{A}_R \boldsymbol{\sigma} \mathbf{A}_L) = \frac{1}{2} (\tau_{LR} + \tau_{RL}) = \tau_{LR} \quad (4.25)$$

and for the strain tensor to the shear strain

$$\boldsymbol{\varepsilon} : \mathbf{N} = \frac{1}{2} (\varepsilon_{LR} + \varepsilon_{RL}) = \varepsilon_{LR} = \frac{\gamma_{LR}}{2}. \quad (4.26)$$

Both results (4.25) and (4.26) represent components which are almost identical to stress (strain) invariants except for they are carrying a sign while the invariants do not.

4.1.3 Orthotropic invariants

Physical values must not change if the coordinate system is changed. Both, stresses and strains are physical values, which are mathematically formulated in tensors $\boldsymbol{\sigma}$ and $\boldsymbol{\varepsilon}$, respectively. The orthotropic tensor functions used to describe the multi-surface material model need to be expressed in terms of invariants. These are scalar-values which are independent of any coordinate transformation. The mathematical description of an orthotropic tensor function is only complete if a complete set of linearly independent orthotropic invariants, the so-called integrity basis, is used for this description.

For the isotropic two-dimensional case, the invariants follow from the characteristic equation of the strain tensor $\boldsymbol{\varepsilon}$

$$\lambda^2 - \lambda \operatorname{tr} \boldsymbol{\varepsilon} + \det \boldsymbol{\varepsilon} = 0. \quad (4.27)$$

From the Hamilton-Cayley theorem, which states that a tensor satisfies *its own* characteristic equation, follows

$$\boldsymbol{\varepsilon}^2 - \boldsymbol{\varepsilon} \operatorname{tr} \boldsymbol{\varepsilon} + \mathbf{1} \det \boldsymbol{\varepsilon} = \mathbf{0}. \quad (4.28)$$

Double contraction of (4.28) with $\mathbf{1}$, which is equal to computing the trace of (4.28), leads to the scalar equation

$$\operatorname{tr} \boldsymbol{\varepsilon}^2 - \operatorname{tr} \boldsymbol{\varepsilon} \operatorname{tr} \boldsymbol{\varepsilon} + 2 \det \boldsymbol{\varepsilon} = 0, \quad (4.29)$$

which renders one of the invariant $\operatorname{tr} \boldsymbol{\varepsilon}$, $\operatorname{tr} \boldsymbol{\varepsilon}^2$, and $\det \boldsymbol{\varepsilon}$ redundant. Thus, two independent invariants for isotropy can be chosen from $\operatorname{tr} \boldsymbol{\varepsilon}^2$, $\operatorname{tr} \boldsymbol{\varepsilon}$ and, $\det \boldsymbol{\varepsilon}$, e.g.

$$I_{iso} = \operatorname{tr} \boldsymbol{\varepsilon} \quad \text{and} \quad II_{iso} = \det \boldsymbol{\varepsilon} = \frac{1}{2} [(\operatorname{tr} \boldsymbol{\varepsilon})^2 - \operatorname{tr} \boldsymbol{\varepsilon}^2]. \quad (4.30)$$

The orthotropic invariants are constructed as simultaneous invariants of a tensor and the structural tensors. The formulation as a combination of a tensor and a structural tensor can be found in [3, 47]. The invariants are formulated in terms of the structural tensors to encapsulate the material behavior, such an information is not necessary for isotropic materials. One suitable set of invariants for 2D isotropic problems can be obtained by rewriting the first isotropic invariant of the strain tensor $\boldsymbol{\varepsilon}$ using (4.18) as

$$I_{iso} = \operatorname{tr} \boldsymbol{\varepsilon} = \boldsymbol{\varepsilon} : \mathbf{1} = \boldsymbol{\varepsilon} : \mathbf{M}_L + \boldsymbol{\varepsilon} : \mathbf{M}_R = \varepsilon_{LL} + \varepsilon_{RR} \quad (4.31)$$

and the second one as

$$II_{iso} = \det \boldsymbol{\varepsilon} = \varepsilon_{LL} \varepsilon_{RR} - \varepsilon_{LR}^2. \quad (4.32)$$

One suitable set of independent invariants for 2D orthotropic problems is ε_{LL} , ε_{RR} , and ε_{LR}^2 . These values have to be formulated, such that they are independent to coordinate transformations. For this purpose structural tensors are used.

The square of the shear strain can be expressed using the structural tensors as follows:

$$\operatorname{tr} \boldsymbol{\varepsilon} \mathbf{M}_L \boldsymbol{\varepsilon} \mathbf{M}_R = \operatorname{tr} (\boldsymbol{\varepsilon} \cdot \mathbf{A}_L \otimes \underbrace{\mathbf{A}_L \cdot \boldsymbol{\varepsilon} \cdot \mathbf{A}_R}_{\varepsilon_{LR}} \otimes \mathbf{A}_R) = \varepsilon_{LR} \underbrace{(\boldsymbol{\varepsilon} \cdot \mathbf{A}_L \otimes \mathbf{A}_R) : \mathbf{1}}_{\varepsilon_{LR}} = \varepsilon_{LR}^2 = \frac{1}{4} \gamma_{LR}^2, \quad (4.33)$$

where the second simplification indicated by the under-brace becomes clear with $\mathbf{1} = \{\delta_{ij}\}$ and

$$(\boldsymbol{\varepsilon} \cdot \mathbf{A}_L \otimes \mathbf{A}_R) : \mathbf{1} = (\boldsymbol{\varepsilon}_{ij} \mathbf{A}_{L,j} \mathbf{A}_{R,k}) \delta_{ik} = \boldsymbol{\varepsilon}_{kj} \mathbf{A}_{L,j} \mathbf{A}_{R,k} = \mathbf{A}_{R,k} \boldsymbol{\varepsilon}_{kj} \mathbf{A}_{L,j} = \varepsilon_{RL} = \varepsilon_{LR}. \quad (4.34)$$

A general tensor M_{ij} can be partitioned as

$$M_{ij} = A_i \otimes A_j = \frac{1}{2}(A_i \otimes A_j + A_j \otimes A_i) + \frac{1}{2}(A_i \otimes A_j - A_j \otimes A_i), \quad (4.35)$$

where the first term is the symmetric part of the tensor and the second its antisymmetric part. When multiplying a symmetric tensor with a general tensor, the antisymmetric part of this tensor drops out of the computation. Using this property with the symmetric strain tensor $\boldsymbol{\varepsilon}$ and considering (4.35) the shear component may also be written,

$$\begin{aligned} 4\varepsilon_{LR}^2 &= \gamma_{LR}^2 = 4(\boldsymbol{\varepsilon} : \mathbf{A}_L \otimes \mathbf{A}_R)^2 = 4 \left[\boldsymbol{\varepsilon} : \frac{1}{2}(\mathbf{A}_L \otimes \mathbf{A}_R + \mathbf{A}_R \otimes \mathbf{A}_L) \right]^2 = 4[\boldsymbol{\varepsilon} : \mathbf{N}]^2 = \\ &= \boldsymbol{\varepsilon} : (\mathbf{A}_L \otimes \mathbf{A}_R + \mathbf{A}_R \otimes \mathbf{A}_L) \otimes (\mathbf{A}_L \otimes \mathbf{A}_R + \mathbf{A}_R \otimes \mathbf{A}_L) : \boldsymbol{\varepsilon} = \boldsymbol{\varepsilon} : \mathbb{M} : \boldsymbol{\varepsilon}, \end{aligned} \quad (4.36)$$

where \mathbb{M} is defined as

$$\mathbb{M} = (\mathbf{A}_L \otimes \mathbf{A}_R + \mathbf{A}_R \otimes \mathbf{A}_L) \otimes (\mathbf{A}_L \otimes \mathbf{A}_R + \mathbf{A}_R \otimes \mathbf{A}_L) = 4\mathbf{N} \otimes \mathbf{N} \quad (4.37)$$

and \mathbf{N} according to the definition (4.19) is the symmetric part of $\mathbf{A}_L \otimes \mathbf{A}_R$.

A complete set of linearly independent orthotropic invariants for a plane stress in the LR -plane is therefore

$$I_{ortho} = \varepsilon_{LL} = \text{tr } \boldsymbol{\varepsilon} \mathbf{M}_L = \boldsymbol{\varepsilon} : \mathbf{M}_L, \quad II_{ortho} = \varepsilon_{RR} = \text{tr } \boldsymbol{\varepsilon} \mathbf{M}_R = \boldsymbol{\varepsilon} : \mathbf{M}_R \quad (4.38)$$

and

$$III_{ortho} = \gamma_{LR}^2 = 4 \text{tr } \boldsymbol{\varepsilon} \mathbf{M}_L \boldsymbol{\varepsilon} \mathbf{M}_R = \boldsymbol{\varepsilon} : \mathbb{M} : \boldsymbol{\varepsilon}. \quad (4.39)$$

Instead of the shear strain, the engineering strain γ_{LR} is used to represent the third invariant. These invariants form an integrity basis for the tensors $\boldsymbol{\sigma}$, \mathbf{M}_L , and \mathbf{M}_R . Note, that in the orthotropic case, three invariants are necessary, whereas for isotropy only two invariants are needed. For three dimensional problems, a complete set of orthotropic invariants is [30]

$$\begin{aligned} \varepsilon_{LL} &= \text{tr } \boldsymbol{\varepsilon} \mathbf{M}_L, & \varepsilon_{RR} &= \text{tr } \boldsymbol{\varepsilon} \mathbf{M}_R, & \varepsilon_{TT} &= \text{tr } \boldsymbol{\varepsilon} \mathbf{M}_T, & III &= \det \boldsymbol{\varepsilon}, \\ \gamma_{LR}^2 &= 4 \text{tr } \boldsymbol{\varepsilon} \mathbf{M}_L \boldsymbol{\varepsilon} \mathbf{M}_R, & \gamma_{TL}^2 &= 4 \text{tr } \boldsymbol{\varepsilon} \mathbf{M}_T \boldsymbol{\varepsilon} \mathbf{M}_L, & \gamma_{RT}^2 &= 4 \text{tr } \boldsymbol{\varepsilon} \mathbf{M}_R \boldsymbol{\varepsilon} \mathbf{M}_T. \end{aligned} \quad (4.40)$$

The fact that the shear components are squared shows, that the sign of the shear strain is meaningless under orthotropic symmetry transformations. From this follows, that all orthotropic functions are symmetric with respect to the planes $\gamma_{LR} = 0$, $\gamma_{TL} = 0$ and $\gamma_{RT} = 0$. This applies also for the stress tensor, leading, e.g., to a symmetry of any yield function with respect to the $(\tau_{LR} = 0)$ -plane (see Chapter 5). The set of invariants for 2D problems can be deducted from (4.40) by means of the plane stress conditions in the LR -plane, $\sigma_{TT} = \tau_{TL} = \tau_{RT} = 0$, leading to $\gamma_{TL} = \gamma_{RT} = 0$.

For the stress tensor $\boldsymbol{\sigma}$, a set of invariants similar to those given in (4.38) and (4.39) can be obtained for 2D-problems as

$$\sigma_{LL} = \text{tr } \boldsymbol{\sigma} \mathbf{M}_L, \quad \sigma_{RR} = \text{tr } \boldsymbol{\sigma} \mathbf{M}_R \quad \text{and} \quad \tau_{LR}^2 = \text{tr } \boldsymbol{\sigma} \mathbf{M}_L \boldsymbol{\sigma} \mathbf{M}_R \quad (4.41)$$

or alternatively expressed as

$$\sigma_{LL} = \boldsymbol{\sigma} : \mathbf{M}_L, \quad \sigma_{RR} = \boldsymbol{\sigma} : \mathbf{M}_R \quad \text{and} \quad \tau_{LR}^2 = \frac{1}{4} \boldsymbol{\sigma} : \mathbb{M} : \boldsymbol{\sigma}. \quad (4.42)$$

With these two sets of invariants for the strain (4.38), (4.39) and stress tensor (4.41), respectively, all scalar valued orthotropic functions can be defined as polynomials. This is used for the description of all state functions

$$f_i = f_i(\boldsymbol{\sigma}) = f_i(\sigma_{LL}, \sigma_{RR}, \tau_{LR}^2), \quad (4.43)$$

which are defined in the orthotropic stress space, and also for the construction of the Helmholtz free energy function

$$\psi = \psi(\boldsymbol{\varepsilon}) = \psi(\varepsilon_{LL}, \varepsilon_{RR}, \gamma_{LR}^2), \quad (4.44)$$

which will be used to compute the orthotropic elastic tensor \mathbb{C} in Section 4.2. Details on state functions will be discussed in Chapter 5.

4.2 Elasticity tensor

The second law of thermodynamics for isothermal states, i.e. no change in temperature, is used for the derivation of the relationship between stresses and strains. The definition of the elasticity tensor is also connected to the second law of thermodynamics.

The second law of thermodynamics states that the dissipation power \mathcal{D} , defined as the difference between the input power \mathcal{P} into a system and the rate of change of the Helmholtz free energy ψ , must be greater or equal than zero. In mathematical terms, this can be expressed as

$$\mathcal{D} = \mathcal{P} - \dot{\psi}(\boldsymbol{\varepsilon}) \geq 0. \quad (4.45)$$

The input energy and the Helmholtz free energy are given to

$$\mathcal{P} = \boldsymbol{\sigma} \dot{\boldsymbol{\varepsilon}} \quad \text{and} \quad \dot{\psi} = \frac{\partial \psi}{\partial \boldsymbol{\varepsilon}} : \dot{\boldsymbol{\varepsilon}}, \quad (4.46)$$

so the dissipation can be written as

$$\mathcal{D} = \left(\boldsymbol{\sigma} - \frac{\partial \psi}{\partial \boldsymbol{\varepsilon}} \right) : \dot{\boldsymbol{\varepsilon}} \geq 0. \quad (4.47)$$

For elastic processes there is no dissipation regardless of the strain path $\dot{\boldsymbol{\varepsilon}}$. Thus, the equal sign must be valid in (4.47), yielding the elastic constitutive relation:

$$\boldsymbol{\sigma} = \frac{\partial \psi}{\partial \boldsymbol{\varepsilon}}. \quad (4.48)$$

Relation (4.48) is commonly assumed to be valid even for inelastic processes. For linear elastic materials the strain energy density is a quadratic function of the strain, e.g. $\psi = 1/2 \boldsymbol{\varepsilon} : \mathbb{C} : \boldsymbol{\varepsilon}$ with \mathbb{C} being a constant fourth-order tensor.

4.2.1 Isotropic elasticity tensor

The elasticity tensor is defined as the stiffness in the elastic regime, defined by

$$d\boldsymbol{\sigma} = \mathbb{C} : d\boldsymbol{\varepsilon} \quad (4.49)$$

Using (4.48) one can express (4.49) and obtains

$$d\boldsymbol{\sigma} = \frac{\partial^2 \psi}{\partial \boldsymbol{\varepsilon} \otimes \partial \boldsymbol{\varepsilon}} : d\boldsymbol{\varepsilon} = \mathbb{C} : d\boldsymbol{\varepsilon} \quad \Rightarrow \quad \mathbb{C} := \frac{\partial^2 \psi}{\partial \boldsymbol{\varepsilon} \otimes \partial \boldsymbol{\varepsilon}}. \quad (4.50)$$

For linear elastic materials, the Helmholtz free energy is a quadratic function. It can be written as a polynomial of the isotropic invariants (4.30) as

$$\psi(\boldsymbol{\varepsilon}) = \frac{1}{2} (\eta_1 I_{iso}^2 + \eta_2 II_{iso}), \quad (4.51)$$

where η_1 and η_2 are material parameters, which need to be determined. The second isotropic invariant II_{iso} can be rewritten using

$$\text{tr } \boldsymbol{\varepsilon}^2 = (\boldsymbol{\varepsilon} \cdot \boldsymbol{\varepsilon}) : \mathbf{1} = \varepsilon_{ik} \varepsilon_{kj} \delta_{ij} = \varepsilon_{ik} \varepsilon_{ki} = \varepsilon_{ik} \varepsilon_{ik} = \boldsymbol{\varepsilon} : \boldsymbol{\varepsilon} \quad (4.52)$$

as

$$II_{iso} = \frac{1}{2} [(\text{tr } \boldsymbol{\varepsilon})^2 - \text{tr } \boldsymbol{\varepsilon}^2] = \frac{1}{2} [\boldsymbol{\varepsilon} : \mathbf{1} \otimes \mathbf{1} : \boldsymbol{\varepsilon} - \boldsymbol{\varepsilon} : \boldsymbol{\varepsilon}]. \quad (4.53)$$

The stress tensor can be written based on the Helmholtz free energy and (4.48) as

$$\boldsymbol{\sigma} = \frac{\partial \psi}{\partial \boldsymbol{\varepsilon}} = \eta_1 I_{iso} \mathbf{1} + \eta_2 \frac{1}{2} \frac{\partial II_{iso}}{\partial \boldsymbol{\varepsilon}} = \eta_1 \boldsymbol{\varepsilon} : \mathbf{1} \otimes \mathbf{1} + \eta_2 \frac{1}{2} (\boldsymbol{\varepsilon} : \mathbf{1} \otimes \mathbf{1} - \boldsymbol{\varepsilon}). \quad (4.54)$$

where $\partial II_{iso} / \partial \boldsymbol{\varepsilon}$ is found from the differential dII_{iso} and the definition

$$\begin{aligned} dII_{iso} =: \frac{\partial II_{iso}}{\partial \boldsymbol{\varepsilon}} : d\boldsymbol{\varepsilon} &= \frac{1}{2} [d\boldsymbol{\varepsilon} : \mathbf{1} \otimes \mathbf{1} : \boldsymbol{\varepsilon} + \boldsymbol{\varepsilon} : \mathbf{1} \otimes \mathbf{1} : d\boldsymbol{\varepsilon} - d\boldsymbol{\varepsilon} : \boldsymbol{\varepsilon} - \boldsymbol{\varepsilon} : d\boldsymbol{\varepsilon}] = \\ &= [\boldsymbol{\varepsilon} : \mathbf{1} \otimes \mathbf{1} - \boldsymbol{\varepsilon}] : d\boldsymbol{\varepsilon}. \end{aligned} \quad (4.55)$$

Computing the differential of the stress tensor (4.54) requires the second partial derivative of the free energy,

$$\mathbb{C} = \frac{\partial^2 \psi}{\partial \boldsymbol{\varepsilon} \otimes \partial \boldsymbol{\varepsilon}} = \eta_1 \mathbf{1} \otimes \mathbf{1} + \eta_2 \frac{1}{2} (\mathbf{1} \otimes \mathbf{1} - \mathbb{I}) = \lambda \mathbf{1} \otimes \mathbf{1} + \mu \mathbb{I}. \quad (4.56)$$

\mathbb{C} connects the strain differential with the stress differential and thus leads to the elastic tensor for isotropic materials. The factors

$$\lambda = \eta_1 + \frac{1}{2} \eta_2 \quad \text{and} \quad \mu = -\frac{1}{2} \eta_2 \quad (4.57)$$

are called Lamé's constants [34]. Because \mathbb{C} (4.56) is constant, (4.49) can be integrated. Due to the convention for the stress and strain tensor expressed in (4.21) and (4.23), respectively, and the incremental form of Hooke's law

$$d\{\sigma^a\} = \{\mathbb{C}^{ab}\} \cdot d\{\varepsilon_b\} \quad (4.58)$$

the matrix representation of the elastic tensor has to be given in contra-variant coordinates. Thus, the matrix representations of the forth order tensor

$$(\mathbf{1} \otimes \mathbf{1})^{ijkl} = \delta^{ij} \delta^{kl} \quad \text{and} \quad \mathbb{I}^{ijkl} = \frac{1}{2}(\delta^{ik} \delta^{jl} + \delta^{il} \delta^{jk}) \quad (4.59)$$

for contra-variant coordinates are, respectively,

$$\{(\mathbf{1} \otimes \mathbf{1})^{ab}\} = \begin{bmatrix} 1 & 1 & 0 \\ 1 & 1 & 0 \\ 0 & 0 & 0 \end{bmatrix}, \quad \{\mathbb{I}^{ab}\} = \begin{bmatrix} 1 & 0 & 0 \\ 0 & 1 & 0 \\ 0 & 0 & 1/2 \end{bmatrix}. \quad (4.60)$$

The "shear component" or "mixed component" of \mathbb{I} follows from

$$\mathbb{I}^{33} = \frac{1}{4}(\mathbb{I}^{1212} + \mathbb{I}^{1221} + \mathbb{I}^{2112} + \mathbb{I}^{2121}) \quad (4.61)$$

and

$$\mathbb{I}^{ijkl} = \mathbb{I}^{1212} = \frac{1}{2}(\delta^{11} \delta^{22} + \delta^{12} \delta^{21}) = \frac{1}{2}(1 \cdot 1 + 0 \cdot 0) = \frac{1}{2}. \quad (4.62)$$

Thus, the matrix representation of \mathbb{C} (4.56) follows from (4.60) as

$$\{\mathbb{C}\}^{ab} = \begin{bmatrix} \eta_1 & \eta_1 + \frac{1}{2}\eta_2 & 0 \\ \eta_1 + \frac{1}{2}\eta_2 & \eta_1 & 0 \\ 0 & 0 & -\frac{1}{4}\eta_2 \end{bmatrix}. \quad (4.63)$$

Comparing (4.63) with Hooke's law for isotropic plane stress as given in [34], i.e.,

$$\mathbb{C} = (K - \frac{2}{3}G)\mathbf{1} \otimes \mathbf{1} + 2G\mathbb{I} = \frac{E}{1 - \nu^2} \begin{bmatrix} 1 & \nu & 0 \\ \nu & 1 & 0 \\ 0 & 0 & \frac{1-\nu}{2} \end{bmatrix}. \quad (4.64)$$

leads to the determination of the parameters η_1 and η_2 as

$$\eta_1 = \frac{E}{1 - \nu^2} \quad \text{and} \quad \eta_2 = \frac{-4E}{2(1 + \nu)} = -4G, \quad (4.65)$$

where E is Young's modulus, ν is Poisson's ratio, G the shear modulus, and K the bulk modulus.

4.2.2 Orthotropic elastic tensor

For the formulation of the Helmholtz free energy, the orthotropic invariants of the strain tensor ε_{LL} , ε_{RR} (4.38) and $(\gamma_{LR})^2 = 4\varepsilon_{LR}^2$ (4.39) are used to construct a complex second order polynomial

$$\psi(\boldsymbol{\varepsilon}) = \mu_1 \frac{1}{2}(\boldsymbol{\varepsilon} : \mathbf{M}_L)^2 + \mu_2 \frac{1}{2}(\boldsymbol{\varepsilon} : \mathbf{M}_R)^2 + \mu_3(\boldsymbol{\varepsilon} : \mathbf{M}_L)(\boldsymbol{\varepsilon} : \mathbf{M}_R) + \mu_4 \frac{1}{2}\boldsymbol{\varepsilon} : \mathbb{M} : \boldsymbol{\varepsilon} \quad (4.66)$$

To keep the formulation, according to the orthotropic material behavior, valid for all coordinate systems, the Helmholtz free energy for the orthotropic case is a polynomial with the structural (second order) tensors.

According to (4.48), the first derivative of (4.66) with respect to $\boldsymbol{\varepsilon}$ yields the stress as

$$\boldsymbol{\sigma} = \frac{\partial \psi}{\partial \boldsymbol{\varepsilon}} = \mu_1(\boldsymbol{\varepsilon} : \mathbf{M}_L)\mathbf{M}_L + \mu_2(\boldsymbol{\varepsilon} : \mathbf{M}_R)\mathbf{M}_R + \mu_3(\boldsymbol{\varepsilon} : \mathbf{M}_L)\mathbf{M}_R + \mu_3(\boldsymbol{\varepsilon} : \mathbf{M}_R)\mathbf{M}_L + \mu_4\mathbb{M} : \boldsymbol{\varepsilon}. \quad (4.67)$$

The stiffness tensor \mathbb{C} follows from (4.67) and (4.49) as

$$\mathbb{C} = \frac{\partial^2 \psi}{\partial \boldsymbol{\varepsilon} \otimes \partial \boldsymbol{\varepsilon}} = \mu_1\mathbf{M}_L \otimes \mathbf{M}_L + \mu_2\mathbf{M}_R \otimes \mathbf{M}_R + \mu_3(\mathbf{M}_L \otimes \mathbf{M}_R + \mathbf{M}_R \otimes \mathbf{M}_L) + \mu_4\mathbb{M}. \quad (4.68)$$

For a special coordinate system with $\mathbf{e}_1 = \mathbf{A}_L$ and $\mathbf{e}_2 = \mathbf{A}_R$, i.e. the material coordinate system coincides with the observer coordinate system, the matrix representation of (4.68) follows from (4.37) and (4.61) as

$$\{\mathbb{C}^{ab}\} = \begin{bmatrix} \mu_1 & \mu_3 & 0 \\ \mu_3 & \mu_2 & 0 \\ 0 & 0 & \mu_4 \end{bmatrix}. \quad (4.69)$$

Comparison with Hooke's law for orthotropic plane stress given in [34], i.e.,

$$\mathbb{C} = \mathbb{D}^{-1} = \frac{1}{\Delta} \begin{bmatrix} E_L & \nu_{LR}E_R & 0 \\ \nu_{LR}E_R & E_R & 0 \\ 0 & 0 & \Delta G_{LR} \end{bmatrix} \quad \text{with} \quad \Delta = 1 - \nu_{RL}\nu_{LR} = 1 - \nu_{LR}\frac{E_R}{E_L}, \quad (4.70)$$

where \mathbb{D} is the elastic compliance tensor, allows for identification of μ_1 to μ_4 in terms of Young's moduli and Poisson's ratios. The elastic stiffness tensor \mathbb{C} in (4.68) thus can be written as

$$\mathbb{C} = \frac{E_L}{\Delta}\mathbf{M}_L \otimes \mathbf{M}_L + \frac{E_R}{\Delta}\mathbf{M}_R \otimes \mathbf{M}_R + \frac{\nu_{LR}E_R}{\Delta}(\mathbf{M}_L \otimes \mathbf{M}_R + \mathbf{M}_R \otimes \mathbf{M}_L) + G_{LR}\mathbb{M}, \quad (4.71)$$

where E_L and E_R are the elasticity moduli in grain and radial direction, respectively, ν_{LR} and ν_{RL} are two Poisson's ratios and G_{LR} is the shear modulus in the LR -plane. The representation of \mathbb{C} in (4.71) is valid for any coordinate system, also for curved coordinate systems, and thus applicable for arbitrary spatial orientations of the wood.

Note that both the isotropic (4.56) and the orthotropic (4.71) material tensor are obtained as a linear combination of isotropic and orthotropic fourth-order tensor generators. \mathbb{I} and $\mathbf{1} \otimes \mathbf{1}$ are the (only) two isotropic fourth-order generators, whereas the orthotropic tensor generators are constructed from the structural tensors to $\mathbf{M}_i \otimes \mathbf{M}_j$ and \mathbb{M} . Another major difference is the fact that in the orthotropic case the shear stiffness is an independent variable, as are the elastic moduli. As for isotropy, the shear modulus can be expressed in terms of E and ν (see (4.65)), which is not possible for orthotropic materials.

Only four of the five material parameters E_L , E_R , ν_{LR} , ν_{RL} , and G_{LR} are independent and sufficient to describe an orthotropic material for plane stress states. In the three-dimensional case, nine independent material parameters are needed. These are three elastic moduli, three Poisson's ratios, and three shear moduli. Isotropic materials are fully characterized by two independent material parameters, e.g. E and ν , or G and K , both in two and three dimensions.

Table 4.3 gives an overview of the required independent invariants and material parameters for isotropic and orthotropic materials both in two and three dimensions. It should be noted, that there exists an infinite number of invariants but most of them can be expressed as polynomials of others by means of the Caley-Hamilton theorem.

Table 4.3: Number of independent invariants and material parameters for isotropic and orthotropic materials.

	isotropy	orthotropy
	independent invariants	
2D	2	3
3D	3	7
	material parameters	
2D	2	4
3D	2	9

4.3 Theory of plasticity

An introduction to the theory of plasticity can be found in [34], whereas a detailed discussion is given in [38] and [27].

In linear theory of elasticity the knowledge of the elastic tangent is enough to solve a problem with Hooke's law

$$\boldsymbol{\sigma} = \mathbb{C}\boldsymbol{\varepsilon}, \quad (4.72)$$

if the deformations are known. The theory of plasticity deals with the generation of permanent (irreversible) strain during a general deformation of a body. If this residual strain evolves in a rate-independent fashion, it is called plastic strain $\boldsymbol{\varepsilon}^p$. For small strains, an additive decomposition of the total strain into elastic and plastic parts is assumed. This can be expressed as

$$\boldsymbol{\varepsilon} = \boldsymbol{\varepsilon}^e + \boldsymbol{\varepsilon}^p. \quad (4.73)$$

where $\boldsymbol{\varepsilon}^e$ is the elastic strain. The theory of plasticity needs to be formulated in rate equations which are given in infinitesimal terms, because the deformation state is dependent on the loading history. With the existence of plastic strains there still is a unique relationship between stresses and strains. The evolution of plastic strain, however, depends on the loading path. Thus the problems must be solved incrementally. Time differentiation of (4.73) leads to its rate formulation

$$\frac{d\boldsymbol{\varepsilon}}{dt} = \dot{\boldsymbol{\varepsilon}} = \dot{\boldsymbol{\varepsilon}}^e + \dot{\boldsymbol{\varepsilon}}^p. \quad (4.74)$$

Only the elastic strain causes stresses. This is reflected in the Helmholtz free energy as

$$\psi = \hat{\psi}(\boldsymbol{\varepsilon}^e) = \hat{\psi}(\boldsymbol{\varepsilon} - \boldsymbol{\varepsilon}^p) \quad (4.75)$$

and subsequently in the constitutive relation

$$\boldsymbol{\sigma} = \frac{\partial \hat{\psi}}{\partial \boldsymbol{\varepsilon}} = \frac{\partial \hat{\psi}}{\partial \boldsymbol{\varepsilon}^e} : \frac{\partial \boldsymbol{\varepsilon}^e}{\partial \boldsymbol{\varepsilon}} = \frac{\partial \hat{\psi}}{\partial \boldsymbol{\varepsilon}^e} \quad (4.76)$$

and

$$\frac{\partial \hat{\psi}}{\partial \boldsymbol{\varepsilon}^p} = \frac{\partial \hat{\psi}}{\partial \boldsymbol{\varepsilon}^e} : \frac{\partial \boldsymbol{\varepsilon}^e}{\partial \boldsymbol{\varepsilon}^p} = -\frac{\partial \hat{\psi}}{\partial \boldsymbol{\varepsilon}^e} = -\boldsymbol{\sigma}. \quad (4.77)$$

Thus, for ideally plastic processes, the rate of the Helmholtz free energy is only a function of the elastic strain, yielding, using (4.77) and (4.76),

$$\dot{\psi}(\boldsymbol{\varepsilon}^e) = \dot{\psi}(\boldsymbol{\varepsilon} - \boldsymbol{\varepsilon}^p) = \frac{\partial \psi}{\partial \boldsymbol{\varepsilon}} : \dot{\boldsymbol{\varepsilon}} + \frac{\partial \psi}{\partial \boldsymbol{\varepsilon}^p} : \dot{\boldsymbol{\varepsilon}}^p = \frac{\partial \psi}{\partial \boldsymbol{\varepsilon}} : \dot{\boldsymbol{\varepsilon}} - \frac{\partial \psi}{\partial \boldsymbol{\varepsilon}} : \dot{\boldsymbol{\varepsilon}}^p = \frac{\partial \psi}{\partial \boldsymbol{\varepsilon}} (\dot{\boldsymbol{\varepsilon}} - \dot{\boldsymbol{\varepsilon}}^p), \quad (4.78)$$

leading, using the first equation of (4.46), to a dissipation power

$$\mathcal{D} = \mathcal{P} - \dot{\psi} = \left(\boldsymbol{\sigma} - \frac{\partial \psi}{\partial \boldsymbol{\varepsilon}} \right) : \dot{\boldsymbol{\varepsilon}} + \frac{\partial \psi}{\partial \boldsymbol{\varepsilon}} : \dot{\boldsymbol{\varepsilon}}^p \geq 0. \quad (4.79)$$

In the elastic range the plastic strain rate and therefore the dissipation vanishes, revealing once again (4.48). Assuming (4.48) remains valid even for inelastic processes, the expression for the plastic dissipation (4.79) becomes

$$\mathcal{D} = \frac{\partial \psi}{\partial \boldsymbol{\varepsilon}} : \dot{\boldsymbol{\varepsilon}}^p = - \frac{\partial \psi}{\partial \boldsymbol{\varepsilon}^p} : \dot{\boldsymbol{\varepsilon}}^p = \boldsymbol{\sigma} : \dot{\boldsymbol{\varepsilon}}^p \geq 0. \quad (4.80)$$

In addition to the elastic stress strain relationship (4.47) the following components are essential for a complete plasticity model:

- yield criterion to limit the elastic domain,
- plastic flow rule to identify $\dot{\boldsymbol{\varepsilon}}^p$,
- hardening and/or softening laws,
- the consistency condition, and
- the loading and unloading conditions.

These six components of the theory of plasticity are elucidated in detail in the subsequent subsections.

4.3.1 Elastic stress-strain relationships

The theory of elasticity is used as part of the hyperelastic theory of plasticity to evaluate the stress. The relations may be linear or non-linear. The additive decomposition (4.73) of the strain tensor is used to describe the elastic stress-strain relationships in the theory of plasticity. The constitutive equation or stress function

$$\boldsymbol{\sigma} = \frac{\partial \psi(\boldsymbol{\varepsilon} - \boldsymbol{\varepsilon}^p)}{\partial \boldsymbol{\varepsilon}} \quad (4.81)$$

follows from the second law of thermodynamics as laid out in the beginning of Section 4.2 and in (4.76). From the rate form of the stress function

$$\dot{\boldsymbol{\sigma}} = \frac{d}{dt} \left(\frac{\partial \psi(\boldsymbol{\varepsilon} - \boldsymbol{\varepsilon}^p)}{\partial \boldsymbol{\varepsilon}} \right) = \frac{\partial^2 \psi}{\partial \boldsymbol{\varepsilon} \otimes \partial \boldsymbol{\varepsilon}} : \dot{\boldsymbol{\varepsilon}} + \frac{\partial^2 \psi}{\partial \boldsymbol{\varepsilon} \otimes \partial \boldsymbol{\varepsilon}^p} : \dot{\boldsymbol{\varepsilon}}^p \quad (4.82)$$

yields the definition of the material stiffness tensor to

$$\mathbb{C} := \frac{\partial^2 \psi(\boldsymbol{\varepsilon} - \boldsymbol{\varepsilon}^p)}{\partial \boldsymbol{\varepsilon} \otimes \partial \boldsymbol{\varepsilon}}. \quad (4.83)$$

The second term of (4.82) can be written due to the additive decomposition as

$$\frac{\partial^2 \psi}{\partial \boldsymbol{\varepsilon} \otimes \partial \boldsymbol{\varepsilon}^p} = \frac{\partial^2 \psi}{\partial \boldsymbol{\varepsilon}^e \otimes \partial \boldsymbol{\varepsilon}^e} : \frac{\partial \boldsymbol{\varepsilon}^e}{\partial \boldsymbol{\varepsilon}^p} = -\frac{\partial^2 \psi}{\partial \boldsymbol{\varepsilon}^e \otimes \partial \boldsymbol{\varepsilon}^e} = -\mathbb{C}. \quad (4.84)$$

Thus the rate form of the stress function reads

$$\dot{\boldsymbol{\sigma}} = \mathbb{C}(\dot{\boldsymbol{\varepsilon}} - \dot{\boldsymbol{\varepsilon}}^p). \quad (4.85)$$

For a constant elasticity tensor \mathbb{C} a special form of (4.85) is

$$\boldsymbol{\sigma} = \mathbb{C}(\boldsymbol{\varepsilon} - \boldsymbol{\varepsilon}^p). \quad (4.86)$$

The general form of the elasticity tensor for orthotropic materials such as wood, for which a material model is described in this work, was given in Section 4.2.

4.3.2 Yield criterion and elastic domain

A criterion needs to be formulated to identify elastic and plastic states, respectively. This criterion is defined by means of a yield function $f(\boldsymbol{\sigma})$, which describes a surface in the stress-space. The values of the yield function then characterizes the state of the material as follows:

$$f(\boldsymbol{\sigma}) < 0 \quad \dots \quad \text{elastic material behavior (elastic loading, or unloading)} \quad (4.87)$$

$$f(\boldsymbol{\sigma}) = 0 \quad \dots \quad \text{plastic material behavior.} \quad (4.88)$$

$f(\boldsymbol{\sigma}) > 0$ is not possible for an elasto-plastic material. The stress-space for three dimensional isotropic problems is the Haigh-Westergaard stress-space, which coordinates are the principal stresses σ_1 , σ_2 and σ_3 . For plane stress states a two dimensional stress-space is sufficient for isotropic materials but a three dimensional one is necessary for orthotropic materials. The coordinate system is formed by the orthotropic invariants given in (4.41).

As mentioned above, stresses $\boldsymbol{\sigma}$, which would lead to $f(\boldsymbol{\sigma}) > 0$ are not admissible. Admissible stress states need to be within an admissible domain of elastic stresses. This elastic domain can be defined by a function $f : \mathbb{R}^3 \times \mathbb{R}^3 \times \mathbb{R}^n \rightarrow \mathbb{R}$ in the stress-space and an admissible states $\{\boldsymbol{\sigma}, \mathbf{q}\} \in \mathbb{R}^3 \times \mathbb{R}^3 \times \mathbb{R}^n$ as

$$\mathbb{E}_\sigma := \{(\boldsymbol{\sigma} \in \mathbb{R}^3 \times \mathbb{R}^3, \mathbf{q} \in \mathbb{R}^n) \in \mathbb{R}^3 \times \mathbb{R}^3 \times \mathbb{R}^n \mid f(\boldsymbol{\sigma}, \mathbf{q}) \leq 0\}, \quad (4.89)$$

where \mathbf{q} comprises a hardening behavior and the superscript n gives the number of components of the hardening stress \mathbf{q} . For perfect plasticity, $f(\boldsymbol{\sigma}, \mathbf{q}) = f(\boldsymbol{\sigma})$ only depends on the stress $\boldsymbol{\sigma}$. Any other kind of plasticity leads to hardening or softening and thus a general form $f(\boldsymbol{\sigma}, \mathbf{q})$. Hardening behavior will be described in more detail in Section 4.3.4. The boundary $\partial \mathbb{E}_\sigma$ of this admissible domain

$$\partial \mathbb{E}_\sigma := \{(\boldsymbol{\sigma}, \mathbf{q}) \in \mathbb{R}^3 \times \mathbb{R}^3 \times \mathbb{R}^n \mid f(\boldsymbol{\sigma}, \mathbf{q}) = 0\} \quad (4.90)$$

is the yield-surface f , which has to be a convex function [27].

The yield and failure criterion's used to define the multi-surface model in the stress-space will be introduced and discussed in Chapter 5.

4.3.3 Flow rule

To evaluate the plastic component $\boldsymbol{\varepsilon}^p$ of the total strain, the rate of change of the plastic strain tensor needs to be defined by the plastic flow rule

$$\dot{\boldsymbol{\varepsilon}}^p = \gamma \mathbf{r}(\boldsymbol{\sigma}, \mathbf{q}), \quad (4.91)$$

where the tensor valued function \mathbf{r} defines the direction of the plastic flow and γ is the positive semidefinite scalar consistency parameter, which defines the length (i.e., the norm) of $\dot{\boldsymbol{\varepsilon}}^p$ in stress-space. The flow rule describes the evolution of the plastic strains.

If the plastic flow direction \mathbf{r} is equal to the stress-gradient of the yield-function $f(\boldsymbol{\sigma}, \mathbf{q})$ at a point $\boldsymbol{\sigma}$, the flow rule is called *associative flow rule*, i.e.,

$$\dot{\boldsymbol{\varepsilon}}^p = \gamma \frac{\partial f}{\partial \boldsymbol{\sigma}}. \quad (4.92)$$

If the direction \mathbf{r} of the plastic flow $\dot{\boldsymbol{\varepsilon}}^p$ is not directly connected to the yield-surface, one speaks of a *non-associative flow rule*

$$\dot{\boldsymbol{\varepsilon}}^p = \gamma \frac{\partial g}{\partial \boldsymbol{\sigma}}, \quad (4.93)$$

where the function $g(\boldsymbol{\sigma}, \mathbf{q})$ is the plastic flow potential or load-function. The stress gradient of the plastic flow potential is used to describe the direction \mathbf{r} of the plastic flow $\dot{\boldsymbol{\varepsilon}}^p$. This may be necessary where tests show a behavior, which cannot be described by (4.92).

The consistency parameter γ needs to obey the condition

$$\gamma \geq 0, \quad (4.94)$$

where $\gamma > 0$ is true for plastic loading and $\gamma = 0$ holds for elastic loading or unloading.

4.3.4 Hardening and softening rule

With plastic deformation the material may harden or soften, which means it changes the state at which yielding occurs. This is equal to a movement of the yield-surfaces in the stress space. Adding a hardening/softening potential $\mathcal{H}(\boldsymbol{\alpha})$ to the Helmholtz free energy according to (4.66) leads to $\psi(\boldsymbol{\varepsilon}^e, \boldsymbol{\alpha})$. The (associative) hardening rule can be written as

$$\dot{\boldsymbol{\alpha}} = \gamma \mathbf{h}(\boldsymbol{\sigma}, \mathbf{q}) \quad \text{with} \quad \mathbf{q} = -\frac{\partial \psi(\boldsymbol{\varepsilon}^e, \boldsymbol{\alpha})}{\partial \boldsymbol{\alpha}} \quad \text{and} \quad \mathbf{h}(\boldsymbol{\sigma}, \mathbf{q}) = \frac{\partial f(\boldsymbol{\sigma}, \mathbf{q})}{\partial \mathbf{q}}, \quad (4.95)$$

where $\boldsymbol{\alpha}$ is a strain-like hardening variable and the function $\mathbf{h}(\boldsymbol{\sigma}, \mathbf{q})$ describes the type of hardening/softening. Besides perfect plasticity, i.e. no hardening, three different types of hardening may be distinguished:

- *Isotropic hardening* leads to growth (scaling) of the yield-surface, without translation of the surface in the stress-space.
- *Kinematic hardening* moves the yield-surface in stress-space, without changing size.
- *Mixed hardening* changes the shape and location of the yield-surface.

The hardening/softening rule describes the evolution of the hardening variable $\boldsymbol{\alpha}$, i.e., it controls the change of the yield-surface.

4.3.5 Loading and unloading conditions

The loading and unloading conditions are also called the *Kuhn-Tucker conditions*. From (4.87), (4.88) and (4.94) follow the conditions to distinguish between elastic loading and unloading, plastic loading or neutral loading as

- $f < 0$ and $\gamma = 0 \Rightarrow$ elastic loading or unloading,
- $f = 0$ and $\gamma = 0 \Rightarrow$ neutral loading,
- $f = 0$ and $\gamma > 0 \Rightarrow$ plastic loading.

From this three combinations follows $\gamma f = 0$. Together with the conditions (4.87), (4.88) and (4.94), we obtain the Kuhn-Tucker loading-unloading conditions

$$\gamma \geq 0, \quad f(\boldsymbol{\sigma}, \mathbf{q}) \leq 0 \quad \text{and} \quad \gamma f(\boldsymbol{\sigma}, \mathbf{q}) = 0. \quad (4.96)$$

4.3.6 Consistency condition

The yield-function and the consistency parameter need to satisfy the consistency condition

$$\gamma \dot{f}(\boldsymbol{\sigma}, \mathbf{q}) = 0. \quad (4.97)$$

The consistency condition assures admissibility of stress. This should be discussed for the two possible cases after yielding has occurred, i.e., for a point on the yield-surface:

- If both, f and \dot{f} are equal to zero, then a point on the yield-surface will stay on this surface, i.e. plastic loading occurs and $\gamma > 0$.
- For $f = 0$ and $\dot{f} < 0$, a point on the yield-surface will be moved into the elastic regime, i.e. elastic unloading occurs. Thus the rate of change of the plastic strain, $\dot{\boldsymbol{\epsilon}}^p$, must vanish. This is equivalent to $\gamma = 0$.

In both cases, the consistency condition (4.97) is satisfied.

An overview of the possible situations for states in plasticity is given in Table 4.4. If $f = 0$ the stress point is on the yield surface. Therefore, $\boldsymbol{\sigma} \in \partial \mathbb{E}_\sigma$. For $f < 0$, the stress point is positioned within the elastic regime, thus $\boldsymbol{\sigma} \in \mathbb{E}_\sigma$ see (4.89).

Table 4.4: Possible combinations of f , \dot{f} and γ and their loading state equivalence.

f	\dot{f}	γ	state
< 0	$-$	$= 0 \rightarrow$	elastic loading
$= 0$	< 0	$= 0 \rightarrow$	unloading
$= 0$	$= 0$	$= 0 \rightarrow$	neutral loading
$= 0$	$= 0$	$> 0 \rightarrow$	plastic loading

The case $f > 0$ is not possible since the stress point would be positioned in the outside the admissible domain. $\dot{f} > 0$ would lead for the stress point of the next time step to be projected into the non-admissible set $f > 0$.

4.3.7 Elasto-plastic tangent tensor

With plastic material behavior the stiffness changes with time, thus the linear elastic material behavior described by Hooke's law (4.72), must be replaced by a rate equation

$$\dot{\boldsymbol{\sigma}} = \mathbb{C}^{ep} \dot{\boldsymbol{\varepsilon}}. \quad (4.98)$$

to describe the elasto-plastic material. To compute the elasto-plastic tangent operator \mathbb{C}^{ep} one first needs to identify the consistency parameter γ .

From the consistency condition (4.97) follows

$$\dot{f} = \frac{\partial f}{\partial \boldsymbol{\sigma}} : \dot{\boldsymbol{\sigma}} + \frac{\partial f}{\partial \mathbf{q}} \cdot \dot{\mathbf{q}} = \partial_{\sigma} f : \dot{\boldsymbol{\sigma}} + \partial_q f \cdot \dot{\mathbf{q}} = 0. \quad (4.99)$$

Using the rate form of Hooke's law, (4.85), and the flow rule (4.91) leads to

$$\dot{\boldsymbol{\sigma}} = \mathbb{C} : (\dot{\boldsymbol{\varepsilon}} - \gamma \mathbf{r}). \quad (4.100)$$

Substituting $\dot{\boldsymbol{\sigma}}$ in (4.99) by (4.100) and using the hardening rule (4.95) yields

$$\dot{f} = \partial_{\sigma} f : \mathbb{C} : \dot{\boldsymbol{\varepsilon}} - \gamma (\partial_{\sigma} f : \mathbb{C} : \mathbf{r} + \partial_q f \cdot \mathbf{h}) = 0. \quad (4.101)$$

The consistency parameter, follows from (4.101) as

$$\gamma = \frac{\partial_{\sigma} f : \mathbb{C} : \dot{\boldsymbol{\varepsilon}}}{\partial_{\sigma} f : \mathbb{C} : \mathbf{r} + \partial_q f \cdot \mathbf{h}}. \quad (4.102)$$

For $f = \dot{f} = 0$ follows that $\gamma \geq 0$ and therefore that $\partial_{\sigma} f : \mathbb{C} : \dot{\boldsymbol{\varepsilon}} \geq 0$. This term can be used for the geometrical interpretation of the plastic loading condition. The angle Θ between the direction of the strain $\boldsymbol{\varepsilon}$ and the gradient of the yield-function $\partial_{\sigma} f$ in a point $\boldsymbol{\sigma}$ can be computed as

$$\cos \Theta = \frac{\partial_{\sigma} f : \mathbb{C} : \dot{\boldsymbol{\varepsilon}}}{(\partial_{\sigma} f : \mathbb{C} : \partial_{\sigma} f)^{1/2} (\dot{\boldsymbol{\varepsilon}} : \mathbb{C} : \dot{\boldsymbol{\varepsilon}})^{1/2}}. \quad (4.103)$$

For $\Theta < 90^\circ$ plastic loading occurs, whereas $\Theta = 90^\circ$ leads to neutral loading. $\Theta < 90^\circ$ indicates associative plasticity. In Figure 6.2 the angle Θ is shown.

To achieve a formula for the elasto-plastic tangent tensor, the consistency parameter γ according (4.102) is substituted in (4.100), leading to

$$\dot{\boldsymbol{\sigma}} = \left(\mathbb{C} - \frac{\mathbb{C} : \mathbf{r} \otimes \partial_{\sigma} f : \mathbb{C}}{\partial_{\sigma} f : \mathbb{C} : \mathbf{r} + \partial_q f \cdot \mathbf{h}} \right) : \dot{\boldsymbol{\varepsilon}}. \quad (4.104)$$

(4.104) has the same form as (4.98). Thus, the elasto-plastic tangent tensor follows to

$$\mathbb{C}^{ep} = \mathbb{C} - \frac{\mathbb{C} : \mathbf{r} \otimes \partial_{\sigma} f : \mathbb{C}}{\partial_{\sigma} f : \mathbb{C} : \mathbf{r} + \partial_q f \cdot \mathbf{h}}. \quad (4.105)$$

In the case of an associative flow rule, \mathbb{C}^{ep} is symmetric. However, in the general case of non-associative plasticity, \mathbb{C}^{ep} is not symmetric. Perfect plasticity is characterized by $\mathbf{h} = 0$, and thus has no effect on symmetry of \mathbb{C}^{ep} .

The elasto-plastic tangent tensor \mathbb{C}^{ep} can not be used in an iterative computational framework without loss of the quadratic rate of asymptotic convergence, the big advantage of the generalized Newton algorithm. The source of the problem is an inconsistency between the numerical time integration algorithm and the infinitesimal character of (4.104). Thus the algorithmic elasto-plastic tangent operator \mathbb{C}_{n+1}^{ep} must be determined. This will be elucidated in Section 6.5 for the cases of a single and for multiple yield-surfaces.

4.4 Multi-surface plasticity

In this section, the general framework for multi-surface plasticity will be discussed. The discussion given in Section 4.3 only refers to a single-surface plasticity model, i.e., an elastic domain $\mathbb{E}_{\boldsymbol{\sigma}}$ with smooth boundary $\partial\mathbb{E}_{\boldsymbol{\sigma}}$.

The orthotropic plasticity model for wood consists of multiple yield-surfaces combined defining a single convex elastic domain with piecewise smooth boundary. In case of the model described in this work, these are four different surfaces. The intersections of these surfaces, i.e. the edges and corners, are the reasons for the non-smooth elastic domain $\mathbb{E}_{\boldsymbol{\sigma}}$ of a multi-surface plasticity model. An extensive formulation for such a model is given in [38]. The edges and corners of the elastic domain are singular lines and points, respectively, and need special algorithmic treatment of the numerical implementation. Details on this algorithmic treatment will be given in 6.4.

The six essential components of a single-surface plasticity model as discussed in Subsections 4.3.1 to 4.3.6 do not lose general validity, but their formulation needs to be generalized for multiple yield-surfaces. The only exception are the equations for the elastic stress-strain relationships (4.83), (4.86) and (4.85), which do not change and are also valid for multi-surface plasticity. This is obvious, because the elastic response must not depend on the plastic behavior.

An index $\alpha \in \{1, 2, 3, 4\}$ is introduced, for the identification of individual yield-surfaces. In general, α is not limited to four surfaces. Note that in this chapter, the general Einstein summation convention for repeated indices is not used.

Yield criterion and elastic domain

The yield functions used in this work will be specified further in Chapter 5. Each of them describes a yield criterion with the same interpretation as discussed in Section 4.3.2, i.e. for each $\alpha \in \{1, 2, 3, 4\}$ one has to satisfy

$$f_{\alpha} \leq 0. \quad (4.106)$$

The non-smooth elastic domain can be formulated as a combination of all yield-surfaces to

$$\mathbb{E}_{\boldsymbol{\sigma}} := \{(\boldsymbol{\sigma}, \mathbf{q}) \in \mathbb{R}^3 \times \mathbb{R}^3 \times \mathbb{R}^n \mid f_{\alpha}(\boldsymbol{\sigma}, \mathbf{q}) \leq 0 \quad \forall \quad \alpha \in [1, \dots, m]\}, \quad (4.107)$$

where $m = 4$ is the total number of yield-surfaces. $m_{act} \leq m$ is the number of active constraints for a point on one or more yield-surfaces, i.e. $(\boldsymbol{\sigma}, \mathbf{q}) \in \partial\mathbb{E}_{\boldsymbol{\sigma}}$. The set of indices associated with the active constraints m_{act} is called \mathcal{J}_{act} .

In the case of independent constraints for each surface, $m_{act} > 1$ is possible only if the point $(\boldsymbol{\sigma}, \mathbf{q})$ is positioned on an edge or in a corner. In addition the number of active constraints in this case is limited with $m_{act} < m$, i.e. it is not possible that all yield-surfaces are active.

Flow rule and hardening/softening rule

The plastic flow tensor $\dot{\boldsymbol{\epsilon}}^p$ and the motion of the yield-surface in the stress space controlled by the hardening rule, are described by a tensor sum over $n < m$ active yield-surfaces f_{α} .

This general flow rule is

$$\dot{\boldsymbol{\varepsilon}}^p = \sum_{\alpha \in \mathcal{J}_{act}} \gamma^\alpha \mathbf{r}_\alpha(\boldsymbol{\sigma}, \mathbf{q}), \quad \text{with} \quad \mathcal{J}_{act} \subset \{1, 2, \dots, m\} \quad (4.108)$$

is the subset of active yield-surfaces and $\mathbf{r}_\alpha(\boldsymbol{\sigma}, \mathbf{q})$ is the respective direction of the plastic flow of the α -th yield-surface. \mathbf{r}_α is defined both for the associative and for the non-associative case as

$$\mathbf{r}_\alpha(\boldsymbol{\sigma}, \mathbf{q}) = \partial_\sigma f_\alpha(\boldsymbol{\sigma}, \mathbf{q}) \quad \text{and} \quad \mathbf{r}_\alpha(\boldsymbol{\sigma}, \mathbf{q}) = \partial_\sigma g_\alpha(\boldsymbol{\sigma}, \mathbf{q}), \quad (4.109)$$

respectively. The hardening or softening rule follows as

$$\dot{\boldsymbol{\alpha}} = \sum_{\alpha \in \mathcal{J}_{act}} \gamma^\alpha \mathbf{h}_\alpha(\boldsymbol{\sigma}, \mathbf{q}) \quad \text{with} \quad \mathbf{h}_\alpha = \frac{\partial f_\alpha(\boldsymbol{\sigma}, \mathbf{q})}{\partial \mathbf{q}}. \quad (4.110)$$

$\boldsymbol{\alpha}$ is a set of strain-type hardening variables.

Consistency and Kuhn-Tucker conditions

The $m \geq 1$ plastic consistency parameters γ^α need to satisfy the consistency condition

$$\gamma^\alpha \dot{f}_\alpha(\boldsymbol{\sigma}, \mathbf{q}) = 0 \quad (4.111)$$

and the loading and unloading conditions

$$\gamma^\alpha \geq 0, \quad f_\alpha(\boldsymbol{\sigma}, \mathbf{q}) \leq 0 \quad \text{and} \quad \gamma^\alpha f_\alpha(\boldsymbol{\sigma}, \mathbf{q}) = 0 \quad \forall \quad \alpha \in \{1, 2, \dots, m\}. \quad (4.112)$$

Elasto-plastic tangent moduli

The procedure to compute the elasto-plastic tangent moduli is similar to the one explained in detail in Section 4.3.7. The change of the yield-surface can be written using the chain rule as

$$\dot{f}_\alpha = \partial_\sigma f_\alpha : \dot{\boldsymbol{\sigma}} + \partial_q f_\alpha \cdot \dot{\mathbf{q}} = 0. \quad (4.113)$$

Using (4.85), and the flow rule (4.108) and hardening rules (4.110), \dot{f}_α can be expressed as

$$\dot{f}_\alpha = \partial_\sigma f_\alpha : \mathbb{C} : \dot{\boldsymbol{\varepsilon}} - \sum_{\beta \in \mathcal{J}_{act}} g_{\alpha\beta} \gamma^\beta = 0 \quad (4.114)$$

where

$$g_{\alpha\beta}(\boldsymbol{\sigma}, \mathbf{q}) = \partial_\sigma f_\alpha : \mathbb{C} : \mathbf{r}_\beta + \partial_q f_\alpha \cdot \mathbf{h}_\beta, \quad (4.115)$$

is the plastic metric of the corner region. From (4.114) and $\{g^{\alpha\beta}\} = \{g_{\alpha\beta}\}^{-1}$ or

$$\sum_{\beta \in \mathcal{J}_{act}} g^{\alpha\beta} g_{\beta\gamma} = \delta_\gamma^\alpha \quad (4.116)$$

follows the consistency parameter to

$$\begin{aligned} \gamma^\beta &= 0 & \forall \quad \beta \notin \mathcal{J}_{act} \\ \gamma^\alpha &= \sum_{\gamma \in \mathcal{J}_{act}} g^{\alpha\gamma} [\partial_\sigma f_\gamma : \mathbb{C} : \dot{\boldsymbol{\varepsilon}}] & \forall \quad \alpha \in \mathcal{J}_{act}. \end{aligned} \quad (4.117)$$

Plastic flow occurs if $\mathcal{J}_{act} \neq \{\}$. In this case $\partial_\sigma f_\alpha : \mathbb{C} : \dot{\boldsymbol{\varepsilon}} > 0$ and $\gamma^\alpha \geq 0$ for each active yield-surface.

The elasto-plastic tangent tensor for multiple yield-surfaces follows from in the same line of derivations as previously described in Subsection 4.3.7 as

$$\begin{aligned} \mathbb{C}^{ep} &= \mathbb{C} & \text{iff } \mathcal{J}_{act} &= \{\}, \\ \mathbb{C}^{ep} &= \mathbb{C} - \sum_{\alpha, \beta \in \mathcal{J}_{act}} g^{\alpha\beta} [\mathbb{C} : \mathbf{r}_\alpha] \otimes [\mathbb{C} : \partial_\sigma f_\beta] & \text{iff } \mathcal{J}_{act} &\neq \{\}. \end{aligned} \quad (4.118)$$

In the general case of non-associative plasticity \mathbb{C}^{ep} is unsymmetric, since $\mathbb{C}^{ep} + \mathbb{C}^{epT} \neq \mathbf{0}$. Associative plasticity for each yield-surface, i.e. $\mathbf{r}_\alpha = \partial_\sigma f_\alpha \quad \forall \quad \alpha \in \mathcal{J}_{act}$, leads to a symmetric \mathbb{C}^{ep} .

Multi-surface plasticity model for wood

In this chapter we will formulate the theoretical framework for a multi-surface constitutive model for wood. First, we present a generic state function, a generic flow rule, a generic hardening/softening law. Second, these three functions will be specified for each of the four surfaces used to define the multi-surface plasticity model. Furthermore, all necessary derivations of these functions will be given. These are required for a generic formulation of the return mapping algorithm and the algorithmic tangent, which both will be derived in Chapter 6.

The multi-surface plasticity model for clear spruce wood described in this chapter was first proposed and developed by Mackenzie-Helnwein et al. [30]. Some enhancements and changes will be applied to the description of the failure surfaces for fiber tension (see Section 5.2), and the mixed mode failure mode (see Section 5.5), as well as to the parameter identification for the radial compression model (see Section 5.4).

5.1 Generic constitutive functions

5.1.1 Generic formulation of orthotropic state-surfaces

The term *state surface* was chosen to capture the different character of surfaces for modeling either development of inelastic (plastic) deformations or failure mechanism of biaxially stressed clear spruce wood.

Mechanisms with softening behavior characterize material failure in a localized manner, i.e., by cracking. Respective state surfaces characterize the actual state of residual strength. That surface describing the initial strength of the virgin material is called the *failure surface*. Failure surface characterizes onset of failure. Thus it applies only to mechanisms possessing softening behavior.

Mechanisms with hardening-type behavior show homogeneous inelastic strains, very

similar to plastic yielding. Thus, respective surfaces will be denoted as *yield surface*. We are well aware that this does not mean that wood possesses the ability to yield as we know it from metals. The reference is to an analogy in the macroscopic deformation behavior only.

All state surfaces used to describe this orthotropic multi-surface model shall be characterized in a unified way in order to keep the mathematical description compact and easier understandable. They are constructed as scalar valued second-order (i.e. quadratic, no terms $\mathcal{O}(\sigma)^3$ or higher) tensor-polynomials. For orthotropic materials, such a polynomial $p(\sigma)$ can be expressed in terms of the orthotropic invariants defined in (4.41) as follows:

$$p(\sigma) = \tilde{p}(\sigma_{LL}, \sigma_{RR}, \tau_{LR}^2) = a_0 + a_1\sigma_{LL} + a_2\sigma_{RR} + a_3\sigma_{LL}^2 + a_4\sigma_{RR}^2 + a_5\sigma_{LL}\sigma_{RR} + a_6\tau_{LR}^2. \quad (5.1)$$

The stress invariants used in (5.1) can be expressed in terms of σ and the structural tensors \mathbf{M}_L and \mathbf{M}_R , and the tensor \mathbf{N} according to (4.19) as

$$\sigma_{LL} = \sigma : \mathbf{M}_L, \quad \sigma_{RR} = \sigma : \mathbf{M}_R, \quad \text{and} \quad \tau_{LR} = \sigma : \mathbf{N}. \quad (5.2)$$

Substituting (5.2) into (5.1) leads to

$$\begin{aligned} p(\sigma) &= a_0 + (a_1\mathbf{M}_L + a_2\mathbf{M}_R) : \sigma + \\ &+ \sigma : \left[a_3\mathbf{M}_L \otimes \mathbf{M}_L + a_4\mathbf{M}_R \otimes \mathbf{M}_R + \frac{1}{2}a_5(\mathbf{M}_L \otimes \mathbf{M}_R + \mathbf{M}_R \otimes \mathbf{M}_L) + \frac{1}{4}a_6\mathbb{M} \right] : \sigma \end{aligned} \quad (5.3)$$

with \mathbb{M} and \mathbf{N} as defined in (4.37) and (4.19), respectively. The expression within the first set of parenthesis defines a second-order tensor. A general two-dimensional second-order tensor \mathbf{a} can be written as

$$\mathbf{a} = a_{LL}\mathbf{A}_L \otimes \mathbf{A}_L + a_{RR}\mathbf{A}_R \otimes \mathbf{A}_R + a_{LR}\mathbf{A}_L \otimes \mathbf{A}_R + a_{RL}\mathbf{A}_R \otimes \mathbf{A}_L. \quad (5.4)$$

Comparing (5.4) with the first term in parenthesis in (5.3) leads to

$$\mathbf{a} = a_{LL}\mathbf{M}_L + a_{RR}\mathbf{M}_R \quad \text{with} \quad a_{LL} = a_1, \quad a_{RR} = a_2 \quad \text{and} \quad a_{LR} = a_{RL} = 0. \quad (5.5)$$

The last three equations in (5.5) could be derived directly from orthotropic symmetry conditions. The expression in brackets in (5.3) defines a fourth-order tensor

$$\mathbf{b} = b_{LLLL}\mathbf{M}_L \otimes \mathbf{M}_L + b_{RRRR}\mathbf{M}_R \otimes \mathbf{M}_R + b_{LLRR}(\mathbf{M}_L \otimes \mathbf{M}_R + \mathbf{M}_R \otimes \mathbf{M}_L) + b_{LRLR}\mathbb{M} \quad (5.6)$$

with

$$b_{LLLL} = a_3, \quad b_{RRRR} = a_4, \quad b_{LLRR} = \frac{1}{2}a_5 \quad \text{and} \quad b_{LRLR} = \frac{1}{4}a_6. \quad (5.7)$$

This tensor represents the most general form of a two-dimensional orthotropic fourth-order tensor.

Thus, using (5.3), (5.5), (5.6), and $a_0 = q - Y$, the second-order scalar valued tensor polynomial (5.1) can be written as

$$\begin{aligned} f(\sigma) &= a_{LL}\sigma_{LL} + a_{RR}\sigma_{RR} + b_{LLLL}\sigma_{LL}^2 + b_{RRRR}\sigma_{RR}^2 + \\ &+ 2b_{LLRR}\sigma_{LL}\sigma_{RR} + 4b_{LRLR}\tau_{LR}^2 + q - Y \\ &= \mathbf{a} : \sigma + \sigma : \mathbf{b} : \sigma + q - Y \end{aligned} \quad (5.8)$$

or in index notation

$$f(\sigma^{ij}) = a_{ij}\sigma^{ij} + \sigma^{ij}b_{ijkl}\sigma^{kl} + q - Y. \quad (5.9)$$

(5.8) is the generic representation of all state functions. This generic function utilizes two orthotropic tensors \mathbf{a} and \mathbf{b} which are of second and forth order, respectively, the hardening stress $q = \tilde{q}(\alpha)$ and the strength function $Y = \tilde{Y}(\alpha)$. It is obvious from (5.8) that only six independent material parameters are required to define the material tensors \mathbf{a} and \mathbf{b} . The index notation states that the parameter tensors \mathbf{a} and \mathbf{b} need to be expressed in covariant coordinates. The covariant matrix representation of \mathbf{a} is [18]

$$\{\mathbf{a}_a\} = \begin{bmatrix} a_{LL} \\ a_{RR} \\ a_{LR} \end{bmatrix}. \quad (5.10)$$

and that of \mathbf{b} is

$$\{\mathbf{b}_{ab}\} = \begin{bmatrix} b_{LLLL} & b_{LLRR} & 2b_{LLLR} \\ b_{RRLL} & b_{RRRR} & 2b_{RRLR} \\ 2b_{LRLL} & 2b_{LRRR} & 4b_{LRLR} \end{bmatrix}. \quad (5.11)$$

Computing the shear term in (5.8), and substituting b_{LRLR} by means of (5.7) results in

$$\tau_{LR} 4b_{LRLR} \tau_{LR} = a_6 \tau_{LR}^2, \quad (5.12)$$

which, in terms, is the shear term in (5.1). A distinction between lower and upper indices to represent covariant and contra-variant tensors is not necessary for most parts of this work. Only where needed for clarity, the matrix representation will be given with indices.

The construction of this generalized yield criterion allows for several types of surfaces in three dimensional stress space. Considering that the component b_{LRLR} needs to be positive in order to ensure positive shear strength, three generic shapes of the general orthotropic state surface are possible. Depending on sub determinant $S = b_{LLLL}b_{RRRR} - b_{LLRR}^2$, one can identify the following shapes

- $S > 0$... ellipsoidal surface (closed)
- $S = 0$... parabolic surface (open)
- $S < 0$... hyperbolic surface (open)

Only the ellipsoidal shape is closed. This is the only one which can be used for a single surface model. It is known as the Tsai-Wu failure criterion [42]. Both, parabolic and hyperbolic surfaces, are best suited for a multi-surface model due to their clear direction of the resulting plastic flow, and the fact that open surfaces allow for a clear distinction of tensile and compressive regimes. The multi-surface model described in this work uses three parabolic and one hyperbolic surfaces.

5.1.2 Generic flow and softening/hardening rule

The evolution law for the plastic strain can be defined in two ways, (i) as a tensor valued function and (ii) by means of the flow potential theory.

The orthotropic flow rule can be written as a second-order tensorial polynomial with forth order orthotropic tensors \mathbf{H}_0 , \mathbf{H}_1 and \mathbf{H}_2 as [3]

$$\dot{\epsilon}^p = (\mathbf{H}_0 : \mathbf{1} + \mathbf{H}_1 : \boldsymbol{\sigma} + \mathbf{H}_2 : \boldsymbol{\sigma}^2) \dot{\gamma}, \quad (5.13)$$

where the tensors \mathbf{H}_0 , \mathbf{H}_1 and \mathbf{H}_2 depend on the stress invariants and the structural tensors \mathbf{M}_α , and $\dot{\gamma}$ is the scalar positive semidefinite consistency parameter. Further details on the representation theory of tensor valued function can be found in the books [3, 4] by Betten, and in papers by Boehler [5] and Zheng [47].

Using the flow potential theory described by Lubliner, Malvern, and Simo and Hughes in [27, 32, 38], which introduces a scalar flow potential $g(\boldsymbol{\sigma})$, the plastic flow can be expressed as

$$\dot{\epsilon}^p = \dot{\gamma} \frac{\partial g(\boldsymbol{\sigma})}{\partial \boldsymbol{\sigma}} = \dot{\gamma} (\mathbf{A}^* + \mathbf{B}^* : \boldsymbol{\sigma} + \mathbf{C}^* : \boldsymbol{\sigma}^2). \quad (5.14)$$

$g(\boldsymbol{\sigma})$ can be written as a second-order scalar valued tensorial polynomial with the second-order orthotropic tensor \mathbf{A}^* and the fourth order orthotropic tensors \mathbf{B}^* and \mathbf{C}^* , respectively. Nevertheless, the definition (5.14) of the plastic flow in the flow potential theory is only first-order accurate, whereas (5.13) is exact, as proven by Betten in [4].

Using the flow potential $g(\boldsymbol{\sigma}) = \mathbf{A}^* : \boldsymbol{\sigma} + \boldsymbol{\sigma} : \mathbf{B}^* : \boldsymbol{\sigma} - 1$ with $\mathbf{A}^* \neq \mathbf{a}$ and $\mathbf{B}^* \neq \mathbf{b}$ leads to a non-associative flow rule. If the plastic flow is normal to the yield function, i.e. $g(\boldsymbol{\sigma}) = f(\boldsymbol{\sigma})$, one speaks of an associative flow rule. Computing the first partial derivation of generic yield function (5.8) with respect to $\boldsymbol{\sigma}$ yields

$$\frac{\partial f(\boldsymbol{\sigma})}{\partial \boldsymbol{\sigma}} = \mathbf{a} + 2\mathbf{b} : \boldsymbol{\sigma}. \quad (5.15)$$

The generic orthotropic plastic flow rule can be written as

$$\dot{\epsilon}^p = \dot{\gamma} \mathbf{r}, \quad (5.16)$$

where $\mathbf{r} = \partial f / \partial \boldsymbol{\sigma}$ for associative plasticity and $\mathbf{r} = \partial g / \partial \boldsymbol{\sigma}$ for non-associative plasticity. Formulation (5.15) shows that the orthotropic evolution law may be described only by a first-order tensor polynomial. Use of the flow potential theory thus results in a simplified orthotropic flow rule.

The generic evolution of a strain like hardening/softening parameter vector $\boldsymbol{\alpha}$ can be expressed as

$$\dot{\boldsymbol{\alpha}} = \dot{\gamma} \mathbf{s}, \quad (5.17)$$

where \mathbf{s} is a function of the plastic flow direction \mathbf{r} . The components of $\boldsymbol{\alpha}$ are positive semi-definite. If the rate of a component would be negative, i.e. during unloading, it will be zero, since unloading does not cause a softening behavior. This will be accomplished with the ramp function

$$\langle x \rangle = \frac{x + |x|}{2} = x \frac{1 + \text{sign}x}{2}. \quad (5.18)$$

5.2 Fiber-tension surface

The equal priority of the fiber rupture and inter-fiber shear failure (see in Chapter 3) leads to a constitutive assumption [33]. This constitutive assumption states that tensile failure under uniaxial loads occurs at the same level for both, tension in fiber direction and uniaxial tension close to but not exactly in the grain direction.

This assumption leads to a parabolic failure surface in the stress space which predicts the same uniaxial tensile strength for small variations of the grain angle from the fiber direction. This model was first proposed by Mackenzie-Helnwein [33]. A suitable set of parameters for the generic polynomial failure criterion without hardening,

$$f = \mathbf{a} : \boldsymbol{\sigma} + \boldsymbol{\sigma} : \mathbf{b} : \boldsymbol{\sigma} - Y \leq 0, \quad (5.19)$$

is defined by

$$\mathbf{a} = a_{LL} \mathbf{M}_L \quad \Rightarrow \quad \{\mathbf{a}_a\} = \begin{bmatrix} a_{LL} \\ 0 \\ 0 \end{bmatrix} \quad (5.20)$$

and

$$\mathbf{b} = b_{RRRR} \mathbf{M}_R \otimes \mathbf{M}_R + b_{LRLR} \mathbb{M} \quad \Rightarrow \quad \{\mathbf{b}_{ab}\} = \begin{bmatrix} 0 & 0 & 0 \\ 0 & b_{RRRR} & 0 \\ 0 & 0 & 4b_{LRLR} \end{bmatrix} \quad (5.21)$$

with

$$a_{LL} = \frac{1}{\beta_{t,L}^0}, \quad b_{RRRR} = \frac{1}{\beta_{t,L}^0{}^2}, \quad b_{LRLR} = \frac{1}{4\beta_{t,L}^0{}^2}, \quad \text{and} \quad Y = \frac{\beta_{t,L}}{\beta_{t,L}^0}. \quad (5.22)$$

$\beta_{t,L}^0$ is the initial tensile strength in fiber direction and $\beta_{t,L}$ the residual tensile strength after crack initiation. It is described by the softening rule

$$\beta_{t,L} = \beta_{t,L}^0 \exp(-k_{t,L} \alpha_{t,L}), \quad (5.23)$$

where $\alpha_{t,L}$ is a strain like softening parameter, which is equivalent to a crack opening of a single discrete crack perpendicular to grain divided by the characteristic length, the model parameter ℓ_c , i.e. $\alpha_{t,L} = w/\ell_c$.

$\{\mathbf{a}_a\}$ and $\{\mathbf{b}_{ab}\}$ are the matrix representations of the tensors \mathbf{a} and \mathbf{b} , given for the special case of a coordinate system aligned the material coordinate system L-R (see Section 4.1). All matrix representations of second- and fourth-order tensors in the subsequent sections will be given for the same specialization. If this representation is used for the implementation instead of the general form, the stress tensor and the strain tensor need to be transformed into the special coordinate system (see Chapter 6 for details). The general strength parameters (5.22) are not tensor components except for this very special coordinate system. However, they are material parameters and as such independent of coordinate transformations. The tensor component b_{1212} , e.g., is almost always never equal to b_{LRLR} .

Using the equality in (5.19) defines a parabolic surface with its axis parallel to the σ_L -axis. It can be written either as

$$f_{t,L} = a_{LL}\sigma_{LL} + b_{RRRR}\sigma_{RR}^2 + 4b_{LRLR}\tau_{LR}^2 - Y \leq 0 \quad (5.24)$$

or as

$$f_{t,L} = \frac{\sigma_{LL}}{\beta_{t,L}^0} + \frac{\sigma_{RR}^2}{\beta_{t,L}^0} + \frac{\tau_{LR}^2}{\beta_{t,L}^0} - \frac{\beta_{t,L}}{\beta_{t,L}^0} \leq 0. \quad (5.25)$$

It is clear from (5.25) that the yield-function $f_{t,L}$ is dimensionless. This simplifies combination of various state surfaces.

The softening parameter $\alpha_{t,L}$ is controlled by the evolution law for the plastic strain,

$$\dot{\epsilon}^p = \dot{\gamma}_{t,L} \frac{\partial f_{t,L}}{\partial \sigma} = \dot{\gamma}_{t,L} \mathbf{r}_{t,L}, \quad (5.26)$$

and the non-associative softening rule as

$$\dot{\alpha}_{t,L} = \langle \mathbf{M}_L : \dot{\epsilon}^p \rangle = \dot{\gamma}_{t,L} \underbrace{\langle \mathbf{M}_L : \mathbf{r}_{t,L} \rangle}_{=: s_{t,L}} = \dot{\gamma}_{t,L} s_{t,L}. \quad (5.27)$$

This softening rule is obviously a non-associative one because

$$\dot{\alpha}_{t,L} \neq \dot{\gamma}_{t,L} \frac{\partial f}{\partial q} = -\dot{\gamma}_{t,L} \frac{\partial f}{\partial Y} = \dot{\gamma}_{t,L}. \quad (5.28)$$

The dimensionless factor

$$k_{t,L} = \frac{\beta_{t,L}^0 \ell_{c,L}}{G_{f,L}^I} \quad (5.29)$$

is a function of the material parameters initial strength $\beta_{t,L}^0$, mode I fracture toughness of the fibers $G_{f,L}^I$ and the model parameter characteristic length $\ell_{c,L}$. This relation follows from equivalent dissipated energy for full crack development (i.e., rupture). The latter material parameter defines the width of a crack zone. The cascading crack pattern described in Chapter 3 evolves in this crack zone.

ℓ_c has significant influence in the macroscopic behavior of the model. The post-failure behavior as described by (5.23), is shown in Fig. 5.1 for $\ell_c = 1, 5, 10$ and 100 mm. Fig. 5.1(a) shows the strength function $\beta(\alpha_{t,L})$ over the strain-like parameter $\alpha_{t,L}$. The strength drops faster as ℓ_c increases. The strength remains uniquely defined for each $\alpha_{t,L}$ regardless of the size of ℓ_c . Fig. 5.1(b) shows the corresponding stress-strain relation. Again the stress drops faster as ℓ_c increases. However, for $\ell_c = 10$ mm and $\ell_c = 100$ mm, the stress-strain relations are no longer unique. This is the source of numerical instabilities and convergence problems, which will be addressed in Chapter 7.

Controlled by (5.23), the state surface moves along the σ_L -axis until it reaches the origin, which is tantamount to a complete loss of strength. Due to the exponential design of the softening function, this will happen at $\alpha_{t,L} = \infty$, but most of the fracture energy $G_{f,L}^I$ is already lost much earlier. Softening only influences the strength function Y in (5.19). The surface therefore experiences translation along the σ_{LL} -axis, but no change in curvature.

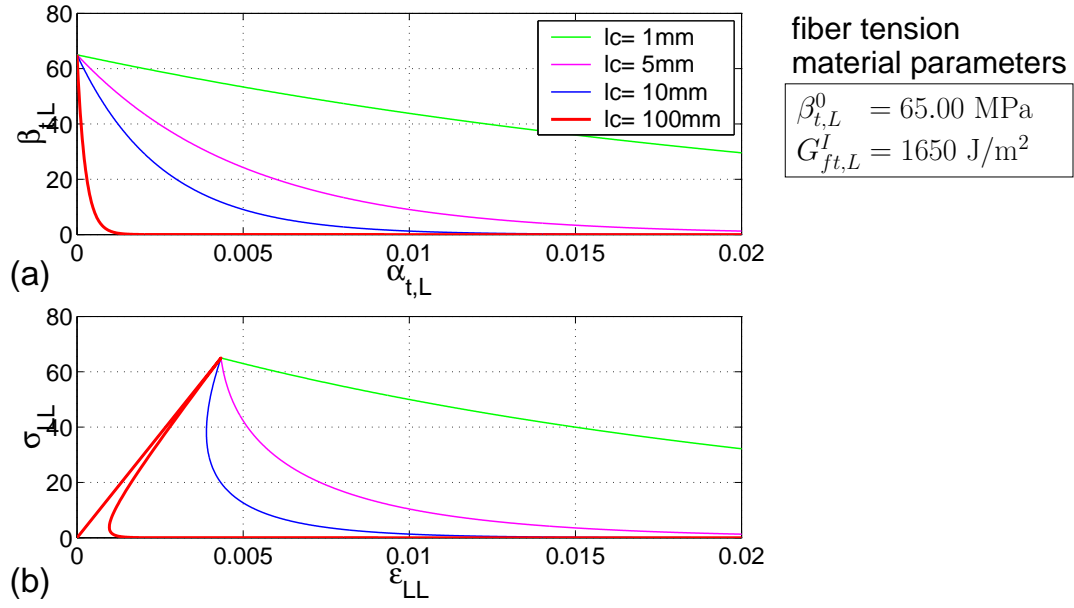


Figure 5.1: Post-failure behavior for uniaxial tension according to the fiber tension model (5.25)

Characteristic stages of the post failure behavior of the fiber tension model are shown in Figure 5.2. The characteristic length of $\ell_{c,L} = 1 \text{ mm}$ was chosen to show the motion of the surface in the stress space. A fraction zone width of this size is physically implausible and also difficult to model because a finite element mesh with all elements smaller than

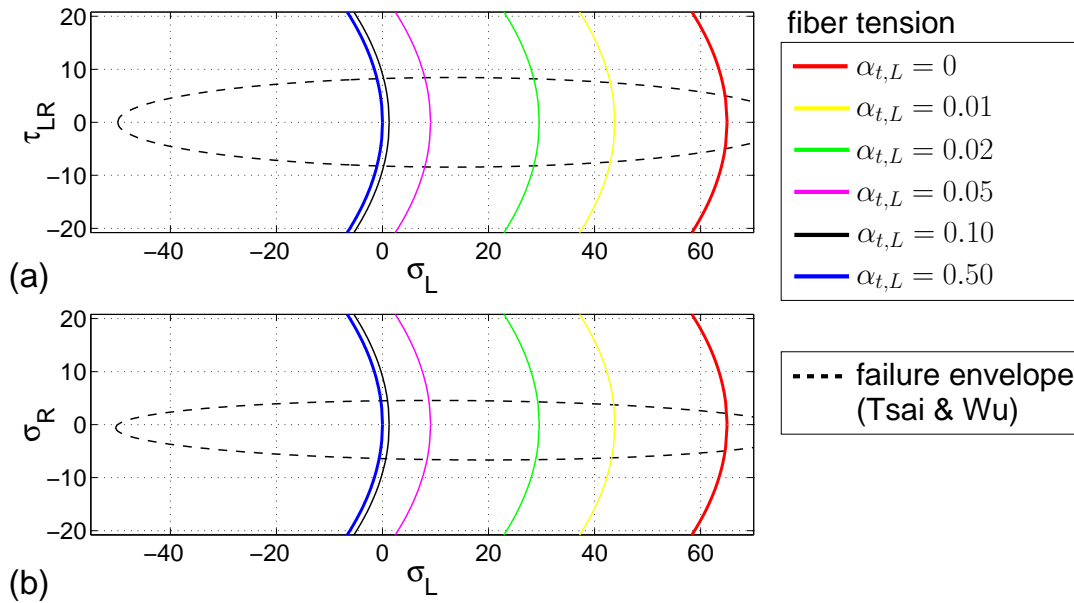


Figure 5.2: Motion of the fiber tension surface in the cross-sections (a) $\sigma_{RR} = 0$ and (b) $\tau_{RL} = 0$ for $\ell_c = 1 \text{ mm}$.

1 mm edge length is not possible for large structures. High values of $\ell_{c,L}$, i.e. high values of $k_{t,L}$, lead to abrupt loss of strength.

The plastic flow direction for this failure mechanism is computed from the yield function as

$$\mathbf{r}_{t,L} = \frac{\partial f}{\partial \boldsymbol{\sigma}} = \mathbf{a} + 2\mathbf{b} : \boldsymbol{\sigma} = \frac{1}{\beta_{t,L}^0} \mathbf{M}_L + 2 \frac{\sigma_{RR}}{\beta_{t,L}^0{}^2} \mathbf{M}_R + 2 \frac{\tau_{LR}}{\beta_{t,L}^0{}^2} \mathbf{N}. \quad (5.30)$$

(5.30) indicates use of the associative flow rule. Other derivatives and their matrix representations needed for the development of the return mapping algorithm in Section 6 are

$$\frac{\partial f}{\partial \alpha} = k_{t,L} Y = k_{t,L} \frac{\beta_{t,L}}{\beta_{t,L}^0}, \quad (5.31)$$

$$\frac{\partial^2 g}{\partial \boldsymbol{\sigma} \otimes \partial \boldsymbol{\sigma}} = \frac{\partial^2 f}{\partial \boldsymbol{\sigma} \otimes \partial \boldsymbol{\sigma}} = 2\mathbf{b} \quad \Rightarrow \quad \left\{ \left(\frac{\partial^2 g}{\partial \boldsymbol{\sigma} \otimes \partial \boldsymbol{\sigma}} \right)_{ab} \right\} = \frac{2}{\beta_{t,L}^0{}^2} \begin{bmatrix} 0 & 0 & 0 \\ 0 & 1 & 0 \\ 0 & 0 & 1 \end{bmatrix} \quad (5.32)$$

and

$$\frac{\partial^2 g}{\partial \boldsymbol{\sigma} \otimes \partial \boldsymbol{\alpha}} = \frac{\partial \mathbf{r}_{t,L}}{\partial \boldsymbol{\alpha}} = \mathbf{0}. \quad (5.33)$$

The derivative of the softening rule (5.27) yields

$$\frac{\partial \tilde{s}_{t,R}}{\partial \mathbf{r}_{t,L}} = \mathbf{M}_L \frac{\langle \mathbf{M}_L : \mathbf{r}_{t,L} \rangle}{\mathbf{M}_L : \mathbf{r}_{t,L}} \quad (5.34)$$

$\partial \tilde{s}_{t,R} / \partial \mathbf{r}_{t,L} = \mathbf{M}_L$ can be simplified because the plastic flow $\mathbf{r}_{t,L}$ just appears in the calculation if the fiber tension surface is active and

$$s_{t,L} = \tilde{s}_{t,L}(\mathbf{r}_{t,L}) := \langle \mathbf{M}_L : \mathbf{r}_{t,L} \rangle = r_{LL} = \begin{cases} \frac{1}{\beta_{t,L}^0} > 0 & \text{if } f_{c,L} \text{ is active} \\ 0 & \text{if } f_{c,L} \text{ is inactive} \end{cases} \quad (5.35)$$

is always positive and, thus the ramp-function in (5.34) is always positive.

5.3 Fiber-compression surface

The micro-mechanical behavior of compressive failure in fiber direction is not yet completely understood. The failure description with the single surface model according to Tsai and Wu [42] in combination with those parameters identified by Eberhardsteiner [7] provides good predictions for combined loading in the compressive regime. Therefore the failure envelope for fiber compression is associated with this model [30]. The compressive state surface is defined by a parabolic approximation of the single surface model proposed in [7].

Similar to the failure surface for tension in fiber direction, the state surface is constructed as a paraboloid with its axis parallel to the σ_L -axis. A direct interaction with the shear stress and the lateral normal stress σ_R has to be accounted for in this mode.

The latter was not necessary in the tensile region. A parabolic approximation at $\min \sigma_L$ is achieved using the generic failure envelope

$$f = \mathbf{a} : \boldsymbol{\sigma} + \boldsymbol{\sigma} : \mathbf{b} : \boldsymbol{\sigma} + q - Y \leq 0 \quad (5.36)$$

with constant material tensors

$$\mathbf{a} = a_{LL}\mathbf{M}_L + a_{RR}\mathbf{M}_R \Rightarrow \{\mathbf{a}_a\} = \begin{bmatrix} a_{LL} \\ a_{RR} \\ 0 \end{bmatrix} \quad (5.37)$$

and

$$\mathbf{b} = b_{RRRR}\mathbf{M}_R \otimes \mathbf{M}_R + 4b_{LRLR}\mathbf{N} \otimes \mathbf{N} \Rightarrow \{\mathbf{b}_{ab}\} = \begin{bmatrix} 0 & 0 & 0 \\ 0 & b_{RRRR} & 0 \\ 0 & 0 & 4b_{LRLR} \end{bmatrix}, \quad (5.38)$$

where the material parameters are

$$a_{LL} = -\frac{1}{\beta_{c,L}^0}, \quad a_{RR} = \frac{A}{\beta_{c,L}^0}, \quad b_{RRRR} = \frac{B}{\beta_{c,L}^0{}^2} \quad \text{and} \quad b_{LRLR} = \frac{C}{4\beta_{c,L}^0{}^2}. \quad (5.39)$$

$\beta_{c,L}^0 = |\min \sigma_L|$ is the initial compressive strength in L-direction. The dimensionless parameters $A, B > 0$ and $C > 0$ are chosen such to fit the curvature of the single surface model at $\min \sigma_L$. The dimensionless character of (5.36) is apparent from its invariant representation

$$f_{c,L} = a_{LL}\sigma_{LL} + a_{RR}\sigma_{RR} + b_{RRRR}\sigma_{RR}^2 + 4b_{LRLR}\tau_{LR}^2 + q - Y \leq 0 \quad (5.40)$$

in combination with (5.39), leading to

$$f_{c,L} = -\frac{1}{\beta_{c,L}^0}\sigma_{LL} + \frac{A}{\beta_{c,L}^0}\sigma_{RR} + \frac{B}{\beta_{c,L}^0{}^2}\sigma_{RR}^2 + \frac{C}{\beta_{c,L}^0{}^2}\tau_{LR}^2 + q - Y \leq 0. \quad (5.41)$$

The strength function $Y = Y(\alpha_{c,L})$ and the hardening stress $q = q(\alpha_{c,L})$ describe the strength degradation and densification behavior, respectively. They are shown in Fig. 5.3. The strength degradation, i.e. the softening behavior, is not pronounced as strong as for the tensile regime, where the strength is lost nearly immediately as failure is induced. The functions $Y(\alpha_{c,L})$ and $q(\alpha_{c,L})$ were derived from uniaxial static tests by Adalian and Morlier [1] under the assumption of a linear elastic behavior prior to failure. The strength function is constructed as

$$Y = 1 - \frac{Y_1}{Y_0} [1 - \exp(-k_{c,L}\alpha_{c,L})] \quad (5.42)$$

where $Y_0 = \beta_{c,L}^0$ and Y_1 are strength parameters as indicated in Fig. 5.3. In analogy to (5.29), the softening rate is controlled by a parameter

$$k_{c,L} = \frac{\beta_{c,L}^0 \ell_{c,L}}{G_{fc,L}^I} \quad (5.43)$$

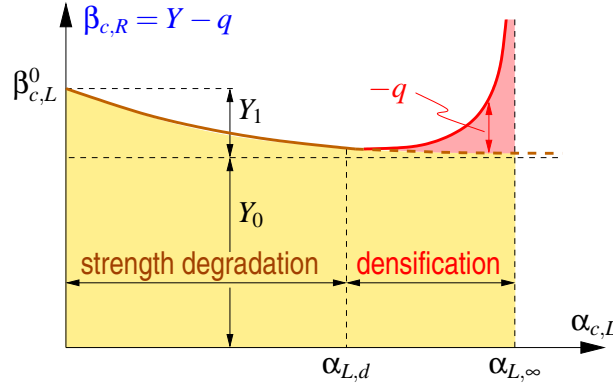


Figure 5.3: Parameters for strength function and hardening stress

and a strain-like state variable $\alpha_{c,L}$. The strength parameter $\beta_{c,L}^0$, the fracture toughness for compressive failure in fiber direction $G_{fc,L}^I$ (cell cap failure), and the fracture zone band width can be obtained from the fiber compression tests by Adalian and Morlier [1]. The characteristic length ℓ_c given by the finite element size is used to describe the fracture zone band width.

The second part of the post failure behavior, the densification, causes internal stresses which do not cause additional dissipation of fracture energy. Instead they cause an increase of effective compressive strength. This is modeled by the hardening stress

$$q(\alpha_{c,L}) = -\frac{H_{L,d}}{\beta_{c,L}^0} \frac{\langle \alpha_{c,L} - \alpha_{L,d} \rangle^2}{\alpha_{L,\infty} - \alpha_{c,L}}, \quad (5.44)$$

where $H_{L,d}$ is a hardening stiffness parameter, $\alpha_{L,d}$ marks the onset of densification, and $\alpha_{L,\infty}$ represents the maximum compaction strain. The magnitudes of the strain-like parameters $\alpha_{L,d}$ and $\alpha_{L,\infty}$ are already in the range of large strains and hence are beyond the validity of the discussed small strain model.

The evolution law for $\alpha_{c,L}$ is based on the associative flow rule

$$\dot{\epsilon}^p = \dot{\gamma}_{c,L} \frac{\partial f_{c,L}}{\partial \boldsymbol{\sigma}} = \dot{\gamma}_{c,L} \mathbf{r}_{c,L}, \quad (5.45)$$

and the non-associative softening rule

$$\dot{\alpha}_{c,L} := \langle \mathbf{M}_R : \dot{\epsilon}^p \rangle = \dot{\gamma}_{c,L} \langle \mathbf{M}_R : \mathbf{r}_{c,L} \rangle = \dot{\gamma}_{c,L} s_{c,L}. \quad (5.46)$$

The associative plastic flow direction $\mathbf{r}_{c,L}$ follows from (5.45) and (5.41) as

$$\mathbf{r}_{c,L} = \frac{\partial f}{\partial \boldsymbol{\sigma}} = \mathbf{a} + 2\mathbf{b} : \boldsymbol{\sigma} = -\frac{1}{\beta_{c,L}^0} \mathbf{M}_L + \left(\frac{A}{\beta_{c,L}^0} + \frac{2B}{\beta_{c,L}^0} \sigma_{RR} \right) \mathbf{M}_R + \frac{2C}{\beta_{c,L}^0} \tau_{LR} \mathbf{N} \quad (5.47)$$

with its vector representation

$$\{(\mathbf{r}_{c,L})_a\} = \frac{1}{\beta_{c,L}^0} \begin{bmatrix} -1 \\ A + \frac{2B}{\beta_{c,L}^0} \sigma_{RR} \\ \frac{2C}{\beta_{c,L}^0} \tau_{LR} \end{bmatrix}. \quad (5.48)$$

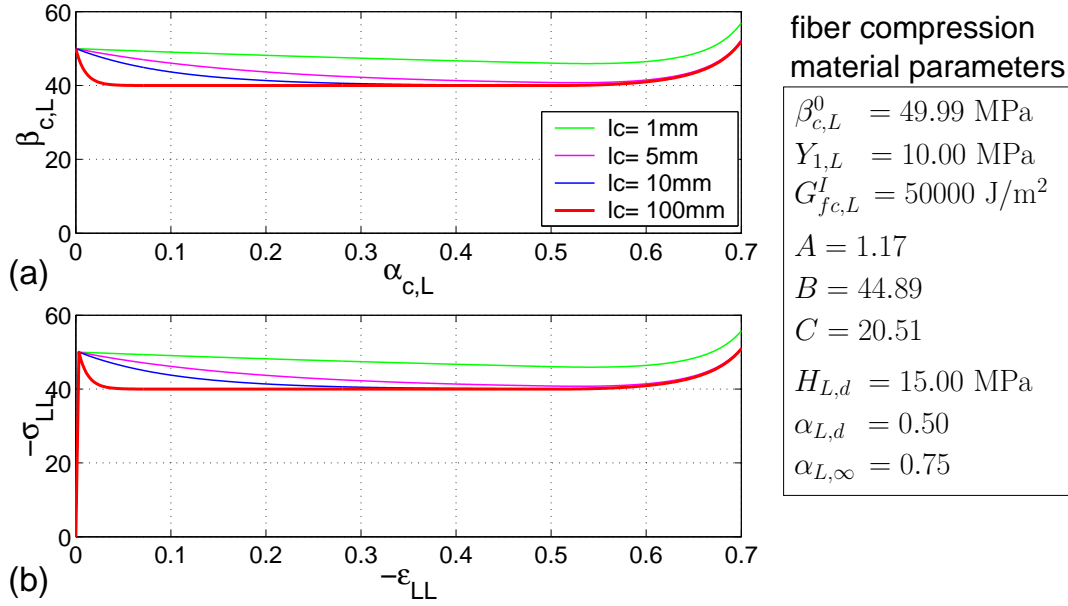


Figure 5.4: Post-failure behavior according to the fiber compression model (5.41).

The post failure behavior for the compressive regime according to (5.42) and (5.44) is shown in Figure 5.4 for $\ell_c = 1, 5, 10$ and 100 mm. Figure 5.4(a) shows the the strength function $\beta(\alpha_{c,L})$ over the $\alpha_{c,L}$. Figure 5.4(b) shows the corresponding stress-strain relationship of the stress $\sigma_{LL}(\alpha_{c,L})$ and the total strain ε_{LL} . All stress-strain relationships shown in Figure 5.4(b) are unique. The values of ℓ_c for which the stress-strain relationship is not unique are much higher than in the fiber tensile regime. It is clearly visible, that softening is not as pronounced as for the fiber tension behavior and that densification, described by (5.44), is an effect at large strains.

The good match of the initial fiber compression surface (red) with the failure surface by Tsai and Wu (dashed black) can be seen in Fig. 5.5. The softening behavior is also shown in Fig. 5.5 evaluated for $\ell_{c,L} = 100$ mm for various states of hardening $\alpha_{c,L} \in \{0.01, 0.02, 0.05, 0.5\}$ and densification $\alpha_{c,L} = 0.7$. The last shown position of the fiber compression surface at $\alpha_{c,L} = 0.7$ allows for higher compressive stresses than at the initial state. This behavior is typical for densification. Besides the translation, the state surface experiences a small change in curvature.

The hardening function $Y(\alpha_{c,L})$ and hardening stress $q(\alpha_{c,L})$ are the only terms in the yield-function (5.41) which depend on the strain-like variable $\alpha_{c,L}$, leading to

$$\frac{\partial f}{\partial \alpha} = \frac{\partial q}{\partial \alpha_{c,L}} - \frac{\partial Y}{\partial \alpha_{c,L}} \quad (5.49)$$

with

$$\frac{\partial q}{\partial \alpha_{c,L}} = -\frac{H_{L,d}}{\beta_{c,L}^0} \frac{\langle \alpha_{c,L} - \alpha_{L,d} \rangle}{(\alpha_{L,\infty} - \alpha_{c,L})^2} (2\alpha_{L,\infty} - \alpha_{c,L} - \alpha_{L,d}) = -\kappa_{L,d} \quad (5.50)$$

and

$$\frac{\partial Y}{\partial \alpha_{c,L}} = -k_{c,L} \frac{Y_1}{\beta_{c,L}^0} e^{-k_{c,L} \alpha_{c,L}} = \kappa_{L,Y}. \quad (5.51)$$

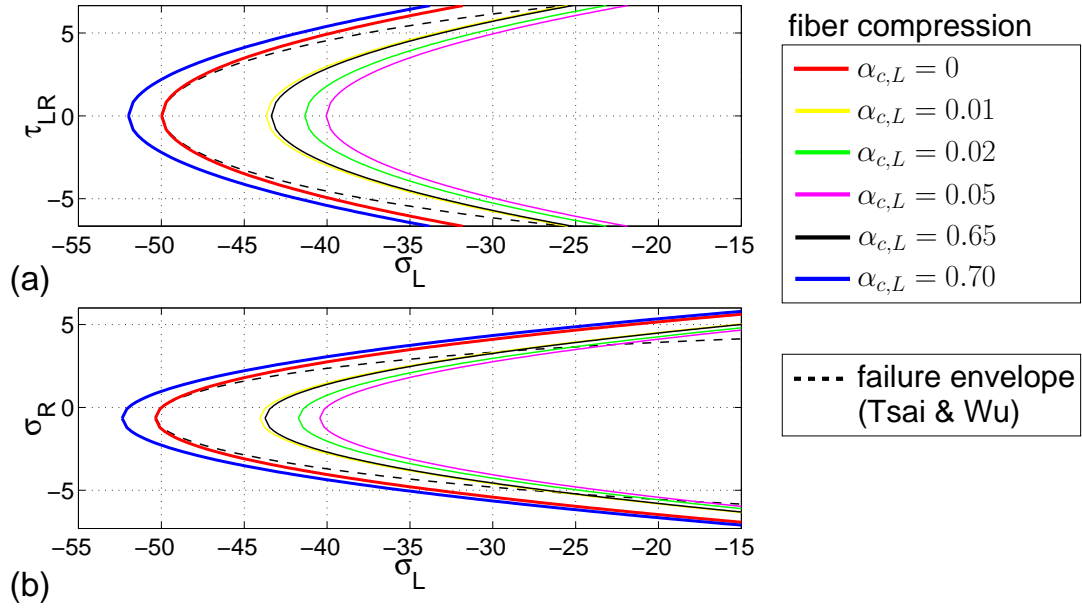


Figure 5.5: Motion of the fiber compression surface in the cross-sections (a) $\sigma_{RR} = 0$ and (b) $\tau_{RL} = 0$ for $\ell_c = 100$ mm.

Due to the associative flow rule, the derivatives

$$\frac{\partial^2 g}{\partial \boldsymbol{\sigma} \otimes \partial \boldsymbol{\sigma}} = \frac{\partial^2 f}{\partial \boldsymbol{\sigma} \otimes \partial \boldsymbol{\sigma}} = 2\mathbf{b} \quad \Rightarrow \quad \left\{ \left(\frac{\partial^2 g}{\partial \boldsymbol{\sigma} \otimes \partial \boldsymbol{\sigma}} \right)_{ab} \right\} = \frac{2}{\beta_{c,L}^0} \begin{bmatrix} 0 & 0 & 0 \\ 0 & B & 0 \\ 0 & 0 & C \end{bmatrix} \quad (5.52)$$

and

$$\frac{\partial^2 g}{\partial \boldsymbol{\sigma} \otimes \partial \boldsymbol{\alpha}} = \mathbf{0} \quad (5.53)$$

can be obtained directly from equation (5.41).

Substituting (5.47) into (5.46) yields

$$s_{c,L} = \tilde{s}_{c,L}(\mathbf{r}_{c,L}) := \langle -\mathbf{M}_L : \mathbf{r}_{c,L} \rangle = \begin{cases} \frac{1}{\beta_{c,L}^0} & \text{if } f_{c,L} \text{ is active} \\ 0 & \text{if } f_{c,L} \text{ is inactive} \end{cases}. \quad (5.54)$$

For an active state surface $f_{c,L}$, the derivative of $\tilde{s}_{c,L}$ with respect to $\mathbf{r}_{c,L}$ can be expressed as

$$\frac{\partial \tilde{s}_{c,L}}{\partial \mathbf{r}_{c,L}} = -\mathbf{M}_L \frac{\langle -\mathbf{M}_L : \mathbf{r}_{c,L} \rangle}{\mathbf{M}_L : \mathbf{r}_{c,L}} = -\mathbf{M}_L. \quad (5.55)$$

5.4 Radial-compression surface

The model used for this failure mode was first introduced by Mackenzie-Helnwein et al. in [19] and further developed in [30] and [33].

A dimensionless version of the formulation used in [30] and [33] is obtained by normalization with respect to the initial radial compressive strength $\beta_{c,R}^0$ as

$$f_{c,R} = -\frac{c}{\beta_{c,R}^0} \sigma_{LL} - \frac{1}{\beta_{c,R}^0} \sigma_{RR} + \frac{\mu}{\beta_{c,R}^0} \tau_{LR}^2 + q - Y \leq 0, \quad (5.56)$$

where c is a dimensionless material parameter, μ is a material parameter with dimension one over stress-unit. As in the compression model in fiber direction, $Y(\alpha_{c,R})$ is a strength function and $q(\alpha_{c,R})$ is the hardening stress function used for describing densification. Comparison of (5.56) with the general state function (5.8) yields the identification of the general strength parameters

$$a_{LL} = -\frac{c}{\beta_{c,R}^0}, \quad a_{RR} = -\frac{1}{\beta_{c,R}^0}, \quad \text{and} \quad b_{LRLR} = \frac{\mu}{4\beta_{c,R}^0}. \quad (5.57)$$

The parameter tensors and their respective matrix representation follow as

$$\mathbf{a} = a_{LL} \mathbf{M}_L + a_{RR} \mathbf{M}_R \Rightarrow \{\mathbf{a}_a\} = -\frac{1}{\beta_{c,R}^0} \begin{bmatrix} c \\ 1 \\ 0 \end{bmatrix} \quad (5.58)$$

and

$$\mathbf{b} = 4b_{LRLR} \mathbf{N} \otimes \mathbf{N} = b_{LRLR} \mathbb{M} \Rightarrow \{\mathbf{b}_{ab}\} = \frac{\mu}{\beta_{c,R}^0} \begin{bmatrix} 0 & 0 & 0 \\ 0 & 0 & 0 \\ 0 & 0 & 1 \end{bmatrix}. \quad (5.59)$$

The surface defined by (5.56) is a paraboloid with the σ_R -axis as its axis. As hardening progresses (i.e. cell crushing), the surfaces moves along the $-\sigma_R$ -axis away from the origin without changing its curvature.

Hardening at small strains is described by the strength function

$$Y(\alpha_{c,R}) = 1 + \frac{Y_1}{Y_0} [1 - e^{-k_{c,R} \alpha_{c,R}}], \quad (5.60)$$

where $Y_0 = \beta_{c,R}^0$ is the initial compressive strength, and $Y_0 + Y_1$ is the plateau strength, and $k_{c,R}$ is a dimensionless parameter controlling the slope of the strength function. $\alpha_{c,R}$ is a strain-like hardening parameter.

Like for both longitudinal-loading models an associative flow rule The softening parameter $\alpha_{c,R}$ is controlled by the evolution law for the plastic strain,

$$\dot{\boldsymbol{\epsilon}}^p = \dot{\gamma}_{c,R} \frac{\partial f}{\partial \boldsymbol{\sigma}} = \dot{\gamma}_{c,R} \mathbf{r}_{c,R} \quad (5.61)$$

and a non-associative softening rule as

$$\dot{\alpha}_{c,R} = \langle \mathbf{M}_R : \dot{\boldsymbol{\epsilon}}^p \rangle = \dot{\gamma}_{c,R} \langle \mathbf{M}_R : \mathbf{r}_{c,R} \rangle = \dot{\gamma}_{c,R} s_{c,R}. \quad (5.62)$$

Following same arguments as for fiber compression in Section 5.3, the densification is modeled by the hardening stress

$$q(\alpha_{c,R}) := -\frac{H_{R,d}}{\beta_{c,R}^0} \frac{\langle \alpha_{c,R} - \alpha_{R,d} \rangle^2}{\alpha_{R,\infty} - \alpha_{c,R}}, \quad (5.63)$$

with $H_{R,d}$ as hardening stiffness parameter and the material parameters $\alpha_{R,d}$ and $\alpha_{R,\infty}$, marking the onset and ultimate densification strain, respectively. The graphical interpretation of the strength function $Y(\alpha_{c,R})$ and the hardening stress $q(\alpha_{c,R})$ is shown in Figure 5.6.

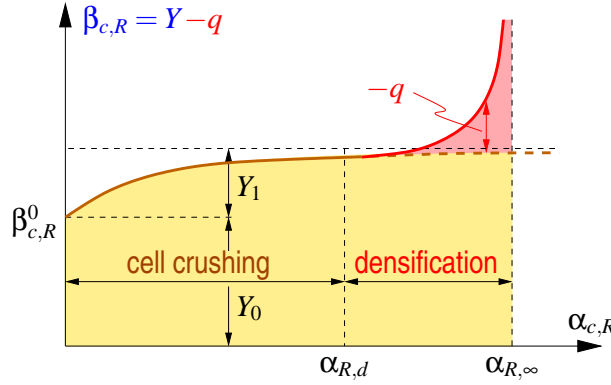


Figure 5.6: Definition of parameters for the strength- and densification functions.

From (5.56) and (5.61) the associative plastic flow direction follows as

$$\mathbf{r}_{c,R} = \frac{\partial f}{\partial \boldsymbol{\sigma}} = \mathbf{a} + 2\mathbf{b} : \boldsymbol{\sigma} = -\frac{c}{\beta_{c,R}^0} \mathbf{M}_L - \frac{1}{\beta_{c,R}^0} \mathbf{M}_R + \frac{2\mu}{\beta_{c,R}^0} \tau_{LR} \mathbf{N}. \quad (5.64)$$

According to (5.64) plastic flow occurs mainly, coinciding with experiments, as compaction in radial direction. Uniaxial compression tests insinuate plastic strain in fiber direction to be smaller than predicted by (5.64). This is modeled by using a non-associative flow potential

$$g = -\frac{\bar{c}}{\beta_{c,R}^0} \sigma_{LL} - \frac{1}{\beta_{c,R}^0} \sigma_{RR} + \frac{\mu}{\beta_{t,R}} \tau_{LR}^2 + q - Y \quad (5.65)$$

with $0 \leq \bar{c} < c$, leading to a non-associative flow direction $\tilde{\mathbf{r}}_{c,R}$

$$\tilde{\mathbf{r}}_{c,R} = \frac{\partial g}{\partial \boldsymbol{\sigma}} = \tilde{\mathbf{a}} + 2\tilde{\mathbf{b}} : \boldsymbol{\sigma} = -\frac{\bar{c}}{\beta_{c,R}^0} \mathbf{M}_L - \frac{1}{\beta_{c,R}^0} \mathbf{M}_R + \frac{2\mu}{\beta_{c,R}^0} \tau_{LR} \mathbf{N}. \quad (5.66)$$

where $\tilde{\mathbf{a}}$ and $\tilde{\mathbf{b}}$ are non-associative parameter tensors. $\tilde{\mathbf{r}}_{c,R}$ can be obtained by replacing the material parameter c in (5.64) by \bar{c} . This would have influence only on the tensor-parameter a_{LL} , leading to $\tilde{\mathbf{b}} = \mathbf{b}$, whereas

$$\tilde{\mathbf{a}} = \tilde{a}_{LL} \mathbf{M}_L + \tilde{a}_{RR} \mathbf{M}_R \quad \Rightarrow \quad \{\tilde{\mathbf{a}}_a\} = -\frac{1}{\beta_{c,R}^0} \begin{bmatrix} \bar{c} \\ 1 \\ 0 \end{bmatrix}. \quad (5.67)$$

The effect of hardening and densification on the post failure behavior for this mechanism is illustrated in Fig. 5.7. This is the only mode, where stable homogeneous inelastic deformations can be observed. Hence this is the only model which does not depend on the

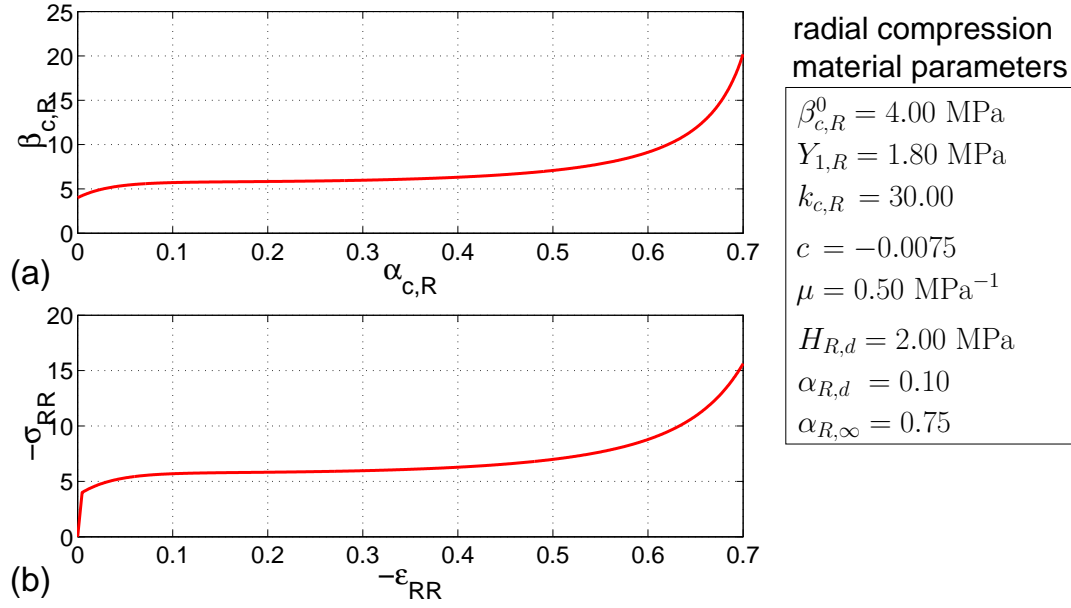


Figure 5.7: Post-failure behavior of the radial compression model (5.56).

characteristic length ℓ_c . Furthermore, the notion for this surface as a yield surface instead of a failure surface is reasonable.

Figure 5.8 illustrates hardening behavior of the radial compression model. The surface only moves along the σ_{RR} -axis and does not change its shape. Note that the initial surface

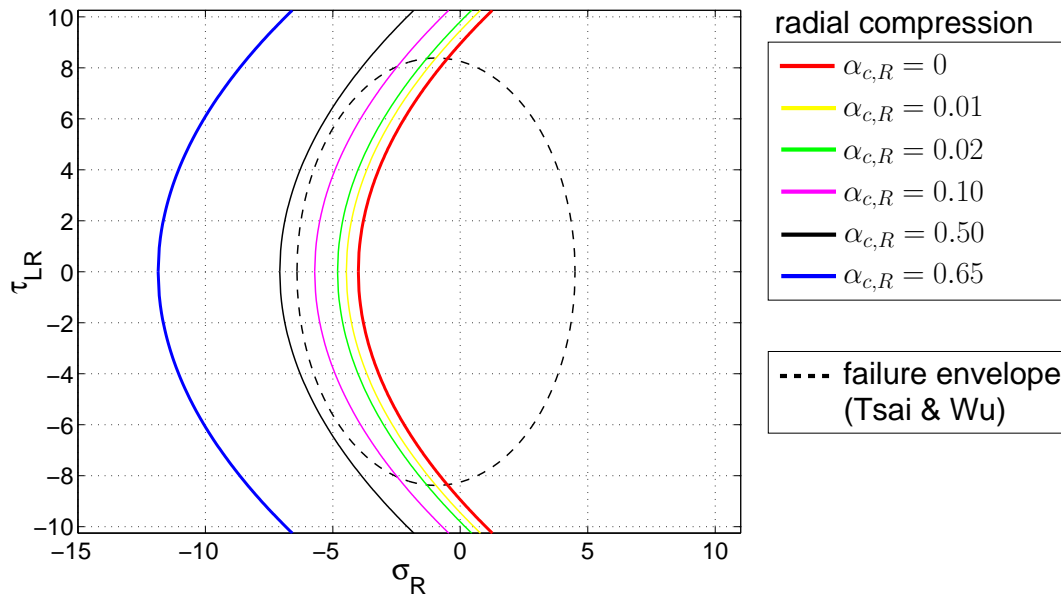


Figure 5.8: Motion of the radial compression surface in the cross-section $\sigma_{LL} = 0$ (ℓ_c without influence).

(red) shows the lowest compressive strength. Contrary to the fiber compression model, this surface can only move in the σ_{RR} -direction.

The surface used by Helnwein [30] for the numerical example intersects the plane $\sigma_{RR} = 0$ before the radial tension surface, meaning pure shear would activate the radial compression model. Test results for the exact behavior of wood under pure shear are not available, but it seems reasonable to activate the mixed mode radial tension surface instead. The material parameter μ describes the curvature of the radial compression surface. In this work μ is chosen, that this surface intersects the plane $\sigma_{RR} = 0$ first along the whole length of the plasticity envelope. This is visible in Figure 5.15. The parameter c influences the slope of the paraboloid to the plane $\sigma_{RR} = 0$.

If the associative flow rule is used, the derivations $\partial g / \partial \boldsymbol{\sigma} = \partial f / \partial \boldsymbol{\sigma} = \mathbf{r}_{c,R}$,

$$\frac{\partial^2 g}{\partial \boldsymbol{\sigma} \otimes \partial \boldsymbol{\sigma}} = \frac{\partial^2 f}{\partial \boldsymbol{\sigma} \otimes \partial \boldsymbol{\sigma}} = \frac{\partial \mathbf{r}_{c,R}}{\partial \boldsymbol{\sigma}} = 2\mathbf{b} \quad \Rightarrow \quad \left\{ \left(\frac{\partial^2 g}{\partial \boldsymbol{\sigma} \otimes \partial \boldsymbol{\sigma}} \right)_{ab} \right\} = \begin{bmatrix} 0 & 0 & 0 \\ 0 & 0 & 0 \\ 0 & 0 & 2\mu/\beta_{c,R}^0 \end{bmatrix} \quad (5.68)$$

and

$$\frac{\partial^2 g}{\partial \boldsymbol{\sigma} \otimes \partial \boldsymbol{\alpha}} = \mathbf{0} \quad (5.69)$$

can be obtained directly from (5.56). As in Section 5.3, the derivation of the yield-function (5.56) with respect to $\alpha_{c,R}$ is given by the sum of the derivatives

$$\frac{\partial f}{\partial \alpha} = \frac{\partial q}{\partial \alpha_{c,R}} - \frac{\partial Y}{\partial \alpha_{c,R}} = -(\kappa_{R,d} + \kappa_{R,Y}) \quad (5.70)$$

with

$$\frac{\partial q}{\partial \alpha_{c,R}} = -\frac{H_{R,d}}{\beta_{c,R}^0} \frac{\langle \alpha_{c,R} - \alpha_{R,d} \rangle}{(\alpha_{R,\infty} - \alpha_{c,R})^2} (2\alpha_{R,\infty} - \alpha_{c,R} - \alpha_{R,d}) = -\kappa_{R,d} \quad (5.71)$$

and

$$\frac{\partial Y}{\partial \alpha_{c,R}} = k_{c,R} \frac{Y_1}{\beta_{c,R}^0} e^{-k_{c,R} \alpha_{c,R}} = \kappa_{R,Y}. \quad (5.72)$$

Substituting (5.64) into (5.62) yields the hardening ratio as

$$s_{c,R} = \tilde{s}_{c,R}(\mathbf{r}_{c,R}) := \langle -\mathbf{M}_R : \mathbf{r}_{c,R} \rangle = \frac{1}{\beta_{c,R}^0}. \quad (5.73)$$

For an active yield surface $f_{c,R}$, the derivative of $\tilde{s}_{c,R}$ with respect to $\mathbf{r}_{c,R}$ can be written as

$$\frac{\partial \tilde{s}_{c,R}}{\partial \mathbf{r}_{c,R}} = -\mathbf{M}_R \frac{\langle -\mathbf{M}_R : \mathbf{r}_{c,R} \rangle}{\mathbf{M}_R : \mathbf{r}_{c,R}} = -\mathbf{M}_R, \quad (5.74)$$

following the same arguments as given in Section 5.2. Substituting (5.73) into (5.62) yields

$$\dot{\alpha}_{c,R} = \frac{\dot{\gamma}_{c,R}}{\beta_{c,R}^0}. \quad (5.75)$$

Disregarding the normation factor $\beta_{c,R}^0$ in (5.75), a similar expression could be acquired on the basis of associative plasticity as

$$\dot{\alpha}_{c,R} = \dot{\gamma}_{c,R} \frac{\partial f}{\partial q} = \dot{\gamma}_{c,R}. \quad (5.76)$$

But in such a formulation, the simple physical interpretation of $\alpha_{c,R}$ and ϵ^p from (5.62) would get lost.

5.5 Radial-tension and mixed mode surface

Mackenzie-Helnwein [30, 33] proposed a modified Mohr-Coulomb failure criterion for this mode, which is based on the model of Weihe [44, 45] and Kröplin & Weihe [24]. The latter was used by Lucena-Simon et al. [28] to describe the microscopic failure mechanism in the RT-plane of spruce wood. This work will present a slightly modified version of the model used in [33] by using a non-associative flow rule.

The model of Weihe was developed for frictional materials like soil. Cracked wood also displays frictional behavior between two adjacent surfaces of a crack, when subjected to compressive normal stress ($\sigma_R < 0$) and shear ($\tau_{LR} \neq 0$).

The state surface is obtained by specialization of the friction model by Kröplin & Weihe [24] for a crack in parallel to grain as follows

$$f_{t,RS} = \frac{1}{\beta_{t,R}^0 (\beta_{t,R}^0 + a_0)} \left[-(\sigma_{RR} - \beta_{t,R} - a)^2 + \frac{\tau_{LR}^2}{\tan^2 \phi} + a^2 \right] \leq 0. \quad (5.77)$$

$\beta_{t,R}$ is the current tensile strength perpendicular to grain direction, a is a stress-like parameter and $\tan \phi$ is the friction coefficient of the crack surface.

Equation (5.77) is normalized with a dominator containing the initial values of $\beta_{t,R}$ and a . The latter is obtained by using the equality in (5.77) and $\sigma_{RR} = 0$ as

$$a_0 = \frac{\beta_s^{02} - \beta_{t,R}^{02} \tan^2 \phi}{2\beta_{t,R}^0 \tan^2 \phi}, \quad (5.78)$$

where β_s^0 is the initial shear strength and $\beta_{t,R}^0$ is the initial tensile strength perpendicular to grain.

For a graphical interpretation of the parameters $\beta_{t,R}$, β_s^0 , a , and ϕ see Figure 5.9. The mixed mode radial tension model describes mode I and mode II cracks. Mode I leads to a translation of this surface toward $\sigma_{RR} = 0$. Mode II not only moves the surface toward the origin of the σ_{RR} axis, but also changes its shape. The limit state consists of two plane surfaces with a straight intersection at the σ_{LL} -axis ($\sigma_{RR} = 0$ and $\tau_{LR} = 0$). This so-called *friction cone* is equivalent to a coulomb friction material and applies to wood after it is fractured. ψ is the effective (initial or current) friction angle. The relation between shear and normal stress reads

$$|\tau_{LR}| = \sigma_{RR} \tan \psi. \quad (5.79)$$

From (5.79) follows that a reduction of the effective friction angle leads to smaller shear stresses in dependency of the normal stress σ_{RR} and the material parameters $\beta_{t,R}$ and

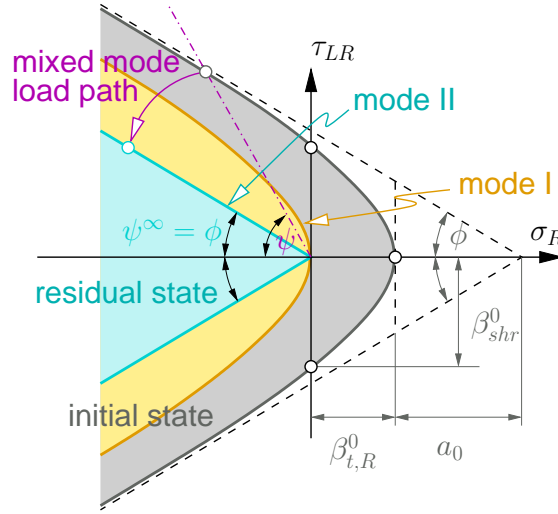


Figure 5.9: Failure surface of the radial tension model for a plane with $\sigma_{LL} = \text{const.}$

a. A reduction of the initial friction coefficient ($\tan \psi$) to an ultimate friction coefficient ($\tan \psi^\infty = \tan \phi$, the friction cone) can be explained by polishing effects on the crack surfaces due to relative slip. The ultimate friction angle $\psi^\infty = \phi$ is a material parameter and is independent from σ_{RR} and a .

To prevent numerical problems at $a = 0$, i.e. at the edge of the residual friction cone, a minimum value a_{\min} is introduced. If a_{\min} is chosen small enough, the accuracy of this model is not affected by this assumption.

Writing (5.77) in the form

$$f_{t,RS} = \frac{1}{D} \left[-2(\beta_{t,R} + a) \sigma_{RR} - \sigma_{RR}^2 + \frac{\tau_{LR}^2}{\tan^2 \phi} + \beta_{t,R}(\beta_{t,R} + 2a) \right] \leq 0 \quad (5.80)$$

with $D = \beta_{t,R}^0 (\beta_{t,R}^0 + a_0)$ and comparing it with the generic state surface (5.8) leads for $q = 0$ to the parameter tensors **a** and **b** and their respective matrix representation as

$$\mathbf{a} = a_{RR} \mathbf{M}_R \quad \Rightarrow \quad \{\mathbf{a}_a\} = \begin{bmatrix} 0 \\ a_{RR} \\ 0 \end{bmatrix} \quad (5.81)$$

and

$$\mathbf{b} = b_{RRRR} \mathbf{M}_R \otimes \mathbf{M}_R + b_{LRLR} \mathbb{M} \quad \Rightarrow \quad \{\mathbf{b}_{ab}\} = \begin{bmatrix} 0 & 0 & 0 \\ 0 & b_{RRRR} & 0 \\ 0 & 0 & 4b_{LRLR} \end{bmatrix} \quad (5.82)$$

with the tensor parameters

$$a_{RR} = \frac{2(\beta_{t,R} + a)}{D}, \quad b_{RRRR} = -\frac{1}{D}, \quad b_{LRLR} = \frac{1}{4D \tan^2 \phi} \quad (5.83)$$

and the strength function

$$Y = \frac{1}{D} \beta_{t,R} (\beta_{t,R} + 2a). \quad (5.84)$$

This criterion describes a hyperbolic surface in orthotropic stress space. Of the two half surfaces defined by (5.77), only the one satisfying $\sigma_R \leq \beta_{t,R}$ is of physical relevance. A special algorithm will be developed in Section 7.2 to ensure that any stress point violating (5.77) is projected to the correct surface.

Out of the four state surfaces of this multi-surface model, this is the only one using a non-associative plastic flow rule

$$\dot{\epsilon}^p = \dot{\gamma}_{t,RS} \frac{\partial g}{\partial \boldsymbol{\sigma}} = \dot{\gamma}_{t,RS} \tilde{\mathbf{r}}_{t,RS}. \quad (5.85)$$

An associative plastic flow direction defined as

$$\mathbf{r}_{t,RS} = \frac{\partial f}{\partial \boldsymbol{\sigma}} = \mathbf{a} + 2\mathbf{b} : \boldsymbol{\sigma} = \frac{2}{D} \left[(\beta_{t,R} + a - \sigma_{RR}) \mathbf{M}_R + \frac{\tau_{LR}}{\tan^2 \phi} \mathbf{N} \right] \quad (5.86)$$

would allow for plastic flow leading to volume increase due to shear strain, which contradicts experimental evidence. Stress states with shear component τ_{LR} and compression stress $\sigma_{RR} < 0$ show only a deviatoric part in the deformation and no increase of volume. Therefore, a non-associative plastic flow direction $\tilde{\mathbf{r}}_{t,R}$ is defined. It is constructed based on $\mathbf{r}_{t,R}$ according to (5.86), assuming that its shear component

$$\tilde{\mathbf{r}}^L = 2 \left(\frac{\partial f}{\partial \boldsymbol{\sigma}} : \mathbf{N} \right) \mathbf{N} = 2\mathbf{r}_{t,R} : \mathbf{N} \otimes \mathbf{N} = 8b_{LRLR}\tau_{LR}\mathbf{N} \quad (5.87)$$

remains valid but its normal component (responsible for volume change)

$$\tilde{\mathbf{r}}^R = \underbrace{\left(\frac{\partial f}{\partial \boldsymbol{\sigma}} : \mathbf{M}_R \right)}_{\text{length}} \underbrace{\mathbf{M}_R}_{\text{direction}} = \mathbf{r}_{t,R} : \mathbf{M}_R \otimes \mathbf{M}_R = (a_{RR} + 2b_{RRRR}\sigma_{RR}) \mathbf{M}_R \quad (5.88)$$

being the source of the contradiction, will be changed. $\tilde{\mathbf{r}}^R$ will be scaled by a factor

$$\kappa = \frac{\langle \sigma_{RR} - \beta_{t,R} + a \tan^2 \phi \rangle^2}{a^2 \tan^4 \phi}, \quad (5.89)$$

resulting in a non-associative flow direction

$$\tilde{\mathbf{r}}_{t,RS} = \tilde{\mathbf{r}}^R + \kappa \tilde{\mathbf{r}}^L = \frac{2}{D} \left[\kappa (\beta_{t,R} + a - \sigma_{RR}) \mathbf{M}_R + \frac{\tau_{LR}}{\tan^2 \phi} \mathbf{N} \right] \quad (5.90)$$

and its vector representation

$$\{(\tilde{\mathbf{r}}_{t,RS})_a\} = \frac{2}{D} \begin{bmatrix} 0 \\ \kappa (\beta_{t,R} + a - \sigma_{RR}) \\ \tau_{LR} / \tan^2 \phi \end{bmatrix}. \quad (5.91)$$

The flow potential g could be obtained by integrating (5.90), but it is not needed for (5.90).

If observed in an plane with $\sigma_{LL} = \text{const.}$, the the vector $\tilde{\mathbf{r}}_{t,RS}$ turns from the positive σ_{RR} -direction in the point ($\sigma_{RR} = \beta_{t,R}, \tau_{LR} = 0$) continuously until reaching the direction parallel to τ_{LR} in the points on the state surface with $\sigma_{RR} = -a \tan^2 \phi$. The point ($\sigma_{RR} = -a \tan^2 \phi, \tau_{LR} = 0$) is the point of curvature of the part of the hyperbolic surface, which is physically relevant for the state surface. In all points with $\sigma_{RR} < -a \tan^2 \phi$ the plastic flow direction is parallel to τ_{LR} .

To prevent problems in the numerical implementation κ is constructed such that a small normal part of the plastic flow direction $\tilde{\mathbf{r}}_{t,RS}$ for states that satisfy $(a \tan^2 \phi - \beta_{t,R}) < \sigma_R < 0$ remains, even though $\sigma_R < 0$ for this points.

A quadratic function was used for κ , leading to a smooth function κ and thus a continuous function for its derivation. The derivative of the ramp function (5.18), i.e.

$$\frac{\partial}{\partial x} \langle x \rangle = \frac{1 + \text{sign} x}{2}, \quad (5.92)$$

is not continuous, as can be verified by

$$\lim_{x \rightarrow 0^+} \frac{\langle x \rangle}{x} = 1 \quad \text{and} \quad \lim_{x \rightarrow 0^-} \frac{\langle x \rangle}{x} = 0. \quad (5.93)$$

(5.92) can also be expressed as

$$\frac{\partial}{\partial x} \langle x \rangle := \frac{\langle x \rangle}{x}. \quad (5.94)$$

To verify (5.94) one needs to compute the second derivative of the ramp function (5.18)

$$\frac{\partial^2}{\partial x^2} \langle x \rangle = \begin{cases} 0 & \dots & x \neq 0 \\ \text{undefined} & \dots & x = 0 \end{cases}. \quad (5.95)$$

Because $\lim_{x \rightarrow 0^+}$ of (5.95) is equal to zero as is $\lim_{x \rightarrow 0^-}$ of (5.95), one can define

$$\left. \frac{\partial^2}{\partial x^2} \langle x \rangle \right|_{x=0} := 0. \quad (5.96)$$

With (5.96) and the fact that x can not be zero for the radial tension state function, since the point of curvature $x = \sigma_{RR} - \beta_{t,R} + a \tan^2 \phi = 0$ is located with in the elastic domain \mathbb{E}_σ and not on its boundary $\partial \mathbb{E}_\sigma$. Thus, and because of (5.96), the definition (5.94) holds. Using (5.94), the derivation of the function $\langle x \rangle^2$ (used in κ (5.89)) leads to

$$\frac{\partial \langle x \rangle^2}{\partial x} = \frac{\langle x \rangle^2}{x}, \quad \text{thus} \quad \lim_{x \rightarrow 0^+} \frac{\langle x \rangle^2}{x} = \lim_{x \rightarrow 0^-} \frac{\langle x \rangle^2}{x} = 0. \quad (5.97)$$

From the second equation (5.97) follows that the derivative of κ (5.89) is continuous.

The softening functions, describing the stiffness degradation, are derived from Weihe's formulation [45]. They were originally defined as

$$\beta_{t,R} = \max(0, 1 - \xi_I - \xi_{II}) \beta_{t,R}^0 \quad \text{and} \quad a = (1 - \xi_{II}) a_0 \quad (5.98)$$

with two normalized state variables $\xi_I \in [0, 1]$ and $\xi_{II} \in [0, 1]$. They are defined by their evolution laws

$$\dot{\xi}_I = \frac{\ell_{c,R}}{G_{f,R}^I} \beta_{t,R} \dot{\alpha}_{t,R} \quad (5.99)$$

$$\dot{\xi}_{II} = \frac{\ell_{c,R}}{G_{f,R}^{II}} (|\tau_{LR}| - \langle -\sigma_R \tan \phi \rangle) \dot{\alpha}_s, \quad (5.100)$$

which describe the currently dissipated fraction of $G_{f,R}^I$ and $G_{f,R}^{II}$. $G_{f,R}^I$ and $G_{f,R}^{II}$ are the fracture toughnesses for mode I and mode II, respectively, $\ell_{c,R}$ is the characteristic length in radial direction, and

$$\boldsymbol{\alpha} = \left\{ \begin{array}{c} \dot{\alpha}_{t,R} \\ \dot{\alpha}_s \end{array} \right\} = \left\{ \begin{array}{c} \langle \mathbf{M}_R : \dot{\boldsymbol{\varepsilon}}^p \rangle \\ \sqrt{\dot{\boldsymbol{\varepsilon}}^p \mathbb{M} \dot{\boldsymbol{\varepsilon}}^p} \end{array} \right\} = \left\{ \begin{array}{c} \langle \dot{\boldsymbol{\varepsilon}}_{RR}^p \rangle \\ |\dot{\gamma}_{LR}^p| \end{array} \right\} \quad (5.101)$$

is the vector of inelastic interface strains ($\alpha_i \in [0, \infty)$). Substituting (5.85) into (5.101) yields to

$$\dot{\boldsymbol{\alpha}} = \dot{\gamma}_{t,RS} \left\{ \underbrace{\frac{\langle \mathbf{M}_R : \tilde{\mathbf{r}}_{t,RS} \rangle}{\sqrt{4tr(\mathbf{M}_R : \tilde{\mathbf{r}}_{t,RS} : \mathbf{M}_L : \tilde{\mathbf{r}}_{t,RS})}}}_{=: \mathbf{s}_{t,RS}} \right\} = \dot{\gamma}_{t,RS} \mathbf{s}_{t,RS}. \quad (5.102)$$

Specializing (5.98) to (5.101) for mode I only, i.e. for $\xi_{II} = 0$, yields

$$\dot{\xi}_I = (1 - \xi_I) \frac{\ell_{c,R}}{G_{f,R}^I} \beta_{t,R}^0 \dot{\alpha}_{t,R} = (1 - \xi_I) k_I \dot{\alpha}_{t,R} \quad (5.103)$$

with

$$k_I = \frac{\beta_{t,R}^0 \ell_{c,R}}{G_{f,R}^I}. \quad (5.104)$$

This may be rewritten in the standard form of a first order time-differential equation

$$\dot{\xi}_I + k_I \dot{\alpha}_{t,R} \xi_I = k_I \dot{\alpha}_{t,R}. \quad (5.105)$$

The homogeneous solution of (5.105) can be determined by writing (5.105) as

$$\frac{d\xi_I}{dt} + k_I \dot{\alpha}_{t,R} \xi_I = 0 \quad \Rightarrow \quad \frac{1}{\xi_I} d\xi_I = -k_I \dot{\alpha}_{t,R} dt. \quad (5.106)$$

Time integration of (5.106) with $t_0 = 0$ and $\xi_{I,0} = 0$

$$\int_{\xi_{I,0}}^{\xi_I} \frac{1}{\xi_I} d\xi_I = -k_I \dot{\alpha}_{t,R} \int_{t_0}^t dt \quad \Rightarrow \quad \ln \left(\frac{\xi_I}{A} \right) = -k_I \dot{\alpha}_{t,R} t \quad (5.107)$$

and subsequently

$$\xi_{I,h} = A \exp(-k_I \alpha_{t,R}) \quad \text{with} \quad A \in \mathbb{R}. \quad (5.108)$$

An attempt for the particular solution of (5.105) is, e.g. $\xi_{I,p} = B$. $B = 1$ can be verified by insertion of $\xi_{I,p} = B$ and $\dot{\xi}_{I,p} = \dot{B} = 0$ into (5.105). Adding the homogeneous (5.108) and particular solution yields the general solution of (5.105) as

$$\xi_I = \xi_{I,h} + \xi_{I,p} = 1 + A \exp(-k_I \alpha_{t,R}). \quad (5.109)$$

The constant A is obtained from the initial conditions $\alpha = 0 \rightarrow \xi_I = 0$ and follows $A = -B = -1$ and therefore

$$\xi_I = 1 - \exp(-k_I \alpha_{t,R}). \quad (5.110)$$

Backsubstitution of (5.110) and $\xi_{II} = 0$ in (5.98) yields

$$\beta_{t,R} = \beta_{t,R}^0 \exp(-k_I \alpha_{t,R}). \quad (5.111)$$

Mixed mode softening is modeled as an extension of (5.111) as

$$\beta_{t,R} = \beta_{t,R}^0 \exp(-k_I \alpha_{t,R}) \exp(-k_{II} \alpha_S) \quad (5.112)$$

and

$$a = a_0 \exp(-k_{II} \alpha_S) \quad \text{with} \quad k_{II} = \frac{\beta_S^0 \ell_{c,R}}{G_{f,R}^{II}}. \quad (5.113)$$

These formulas will be used instead of equations (5.98).

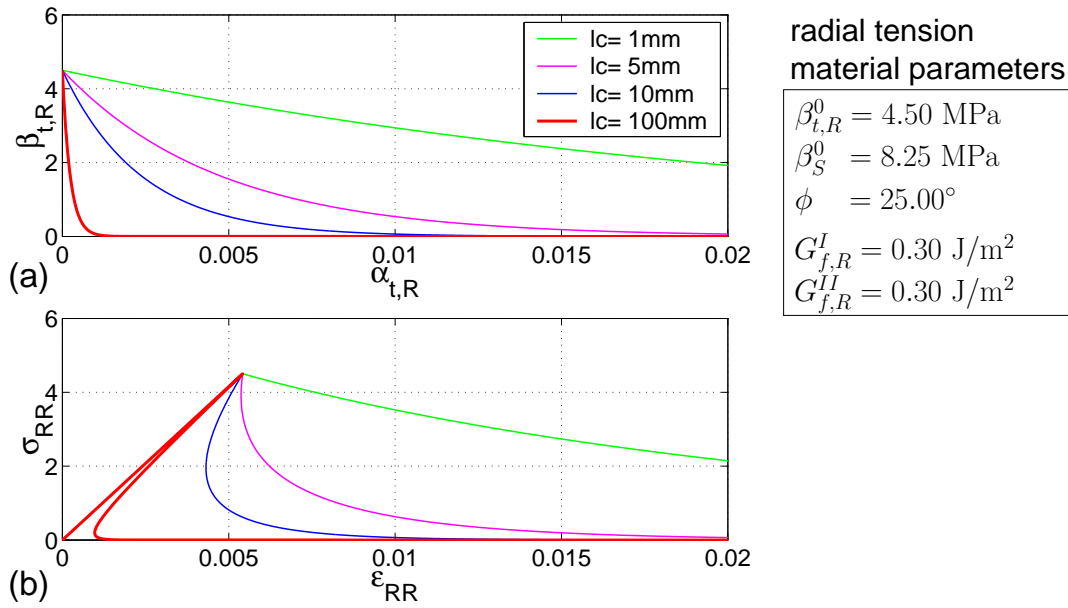


Figure 5.10: Modeled post-failure behavior for radial tension σ_{RR} (mode I).

The softening behavior for mode I according to (5.112) is shown in Figure 5.10(a) for $\ell_{c,R} = 1, 5, 10$, and 100 mm. It shows the strength function $\beta_{t,R}$ over the strain-like parameter $\alpha_{t,R}$. In Figure 5.10(b) the corresponding stress-strain relationships is shown.

Mode II softening behavior is illustrated for the same values of $\ell_{c,R}$ in Figure 5.11(a) and the the corresponding stress-strain relationships of the shear stress τ_{LR} and the shear deformation γ_{LR} in Figure 5.11(b). In Fig. 5.11(a) the strength function β_s , which was computed from (5.78) with a according to (5.113), is shown over α_S .

In both modes the strength drops faster with higher $\ell_{c,R}$ and the stress-strain relations are not unique for values of $\ell_{c,R}$ exceeding a certain length, which is $\ell_{c,R} \approx 5$ mm and $\ell_{c,R} \approx$

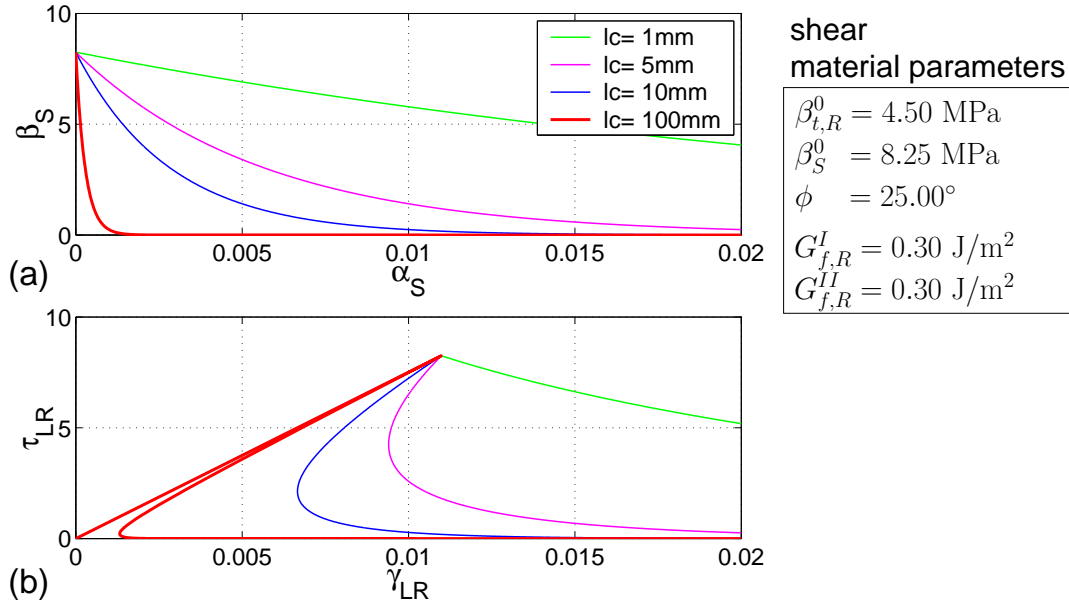


Figure 5.11: Modeled post-failure behavior for shear τ_{LR} (mode II).

2 mm for mode I and mode II, respectively. The fact that the stress-strain relationships are not always unique leads to numerical problems. This will be discussed in Chapter 7

Figure 5.12 shows the interaction surface between mode I and II. The same material parameters as given in the Figures 5.10 and 5.11 were used. The loss of strength (dimen-

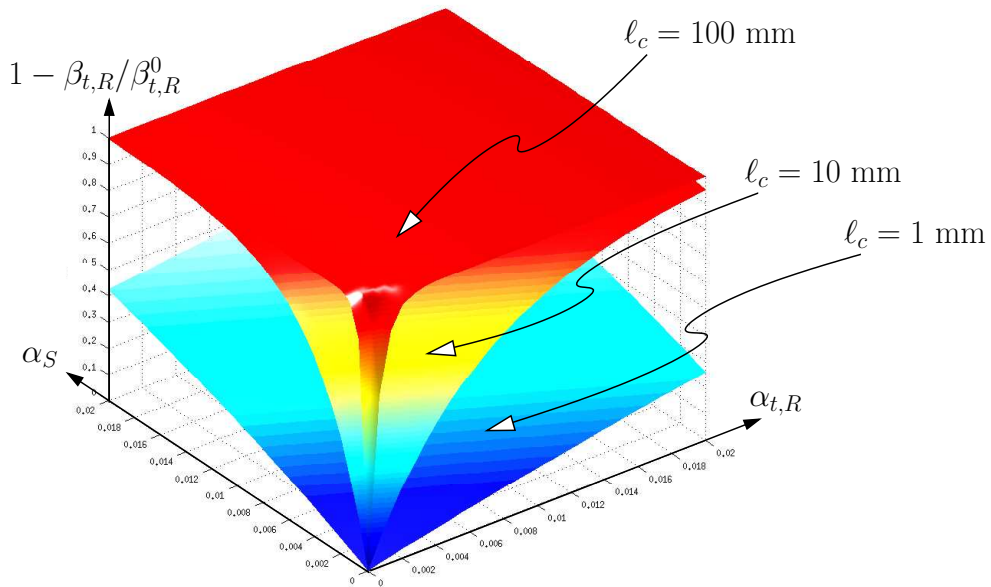


Figure 5.12: Strength degradation for mixed mode loading and $\ell_c = 1, 10$ and 100 mm.

sionless) is shown over the two strain-like parameters $\alpha_{t,R}$ and α_S for $\ell_{c,R} = 1, 10$, and 100 mm. The transition from a blue to a red colored interaction surface indicates decreasing strength. Red parts of the surface indicate states, where most of the initial strength is lost.

The second equation in (5.113) represents only an approximation for k_{II} . The precise form can be obtained by solving a set of ordinary differential equations

$$\dot{\mathbf{y}} = \begin{Bmatrix} \dot{\beta}_{t,R} \\ \dot{\beta}_S \\ \dot{a} \\ \dot{\alpha}_{t,R} \\ \dot{\alpha}_S \\ \dot{\mathcal{E}} \end{Bmatrix} = \mathbf{f}(\mathbf{y}), \quad (5.114)$$

which is necessary due to the actual coupling of mode I and mode II. $\mathbf{f}(\mathbf{y})$ is a set of function, which depend on the components of the vector \mathbf{y} . The last entry in \mathbf{y} is the rate of the dissipated mechanical energy \mathcal{E} . The differential equation (5.100) for plain mode II loading ($\sigma_{RR} = 0$) reads

$$\dot{\xi}_{II} = \frac{\ell_{c,R}}{G_{f,R}^{II}} |\tau_{LR}| \dot{\alpha}_S. \quad (5.115)$$

From (5.101) follows that the change of the strain like parameter $\dot{\alpha}_S$ equals the change of the plastic shear deformation $\dot{\gamma}_{LR}^p$. Using $\dot{\alpha}_S = \dot{\gamma}_{LR}^p$ and substituting the associative flow rule (5.86) with $\sigma_{RR} = 0$ into the second and first line of (5.102) yields

$$\dot{\gamma}_{t,RS} = \frac{\tan^2 \phi}{2|\tau_{LR}|} \dot{\gamma}_{LR}^p \quad \text{and} \quad \dot{\alpha}_{t,R} = 2(\beta_{t,R} + a) \dot{\gamma}_{t,RS} = \frac{\tan^2 \phi (\beta_{t,R} + a)}{|\tau_{LR}|} \dot{\gamma}_{LR}^p, \quad (5.116)$$

respectively. Time differentiation of (5.112) and (5.113) yields

$$\dot{\beta}_{t,R} = \frac{\partial \beta_{t,R}}{\partial \alpha_{t,R}} \dot{\alpha}_{t,R} + \frac{\partial \beta_{t,R}}{\partial \alpha_S} \dot{\alpha}_S \quad \text{and} \quad \dot{a} = \frac{\partial a}{\partial \alpha_S} \dot{\alpha}_S. \quad (5.117)$$

Using the equality in (5.77) with $\tau_{LR} = \beta_S$ yields

$$\beta_S = \sqrt{\beta_{t,R} (\beta_{t,R} + 2a) \tan^2 \phi}. \quad (5.118)$$

Time differentiation of (5.118)

$$\dot{\beta}_S = \frac{\partial \beta_S}{\partial \alpha_{t,R}} \dot{\alpha}_{t,R} + \frac{\partial \beta_S}{\partial \alpha_S} \dot{\alpha}_S. \quad (5.119)$$

Substituting

$$\frac{\partial \beta_{t,R}}{\partial \alpha_{t,R}} = k_I \beta_{t,R}, \quad \frac{\partial \beta_{t,R}}{\partial \alpha_S} = k_{II} \beta_{t,R} \quad \text{and} \quad \frac{\partial a}{\partial \alpha_S} = k_{II} a \quad (5.120)$$

into (5.117), the results into (5.119) and using (5.116) to express $\dot{\alpha}_{t,R}$ leads to the specific set of differential equations

$$\begin{Bmatrix} \dot{\beta}_{t,R} \\ \dot{\beta}_S \\ \dot{a} \\ \dot{\alpha}_{t,R} \\ \dot{\alpha}_S \\ \dot{\mathcal{E}} \end{Bmatrix} = \begin{Bmatrix} -\beta_{t,R} \left[(\beta_{t,R} + a) \frac{\tan^2 \phi}{|\beta_S|} k_I + k_{II} \right] \\ -\beta_{t,R} (\beta_{t,R} + a)^2 \frac{\tan^4 \phi}{\beta_S |\beta_S|} k_I - \beta_S k_{II} \\ -a k_{II} \\ (\beta_{t,R} + a) \frac{\tan^2 \phi}{|\beta_S|} \\ 1 \\ \ell_{c,R} \beta_S \end{Bmatrix} \dot{\gamma}_{LR}^p, \quad (5.121)$$

with $\dot{\gamma}_{LR}^p$ as only free variable which can be set one due to the rate independent plasticity. The dissipated energy \mathcal{E} must be identical for continuum mechanics with

$$\mathcal{E} = \int_{V^e} \mathcal{D} dV^e \quad (5.122)$$

and for fracture mechanics with

$$\mathcal{E} = \int_{A^e} G_{f,R}^{II} dA^e, \quad (5.123)$$

where V^e is the volume of a cracked element and A^e is the area of the actual crack through the very same element. Hence, the solution of (5.121) can be obtained as

$$G_{f,R}^{II}(k_{II}, \beta_S^0, \ell_{c,R}) = \ell_{c,R} \int_0^\infty \mathcal{D} dt. \quad (5.124)$$

In general this provides an implicit definition for k_{II} but no explicit expression can be given. Varying $\ell_{c,R}$ and solving (5.121) by numerical integration does affect the result for \mathcal{E} . Hence, (5.124) can be reduced to

$$\frac{G_{f,R}^{II}(k_{II}, \beta_S^0)}{\ell_{c,R}} = \int_0^\infty \mathcal{D} dt = \mathcal{E}. \quad (5.125)$$

This condition is violated by the second equation in (5.113), which is used as an approximation for (5.125).

Mode I (dashed lines) and mode II (solid lines) softening of the mixed mode radial tension model is shown in Figure 5.13 for $\ell_{c,R} = 1$ mm and different values of α . Problems with such small values of $\ell_{c,R}$ were discussed in Section 5.2. The transition from the hyperbolic surface to the friction cone with increasing α , as described in the beginning of this section, is nicely shown.

For the return map algorithm (to be described in Chapter 6), the computation of additional partial derivatives is necessary. An important part of these derivatives are partial derivatives of the non-associative scaling function κ according to (5.89). It is a

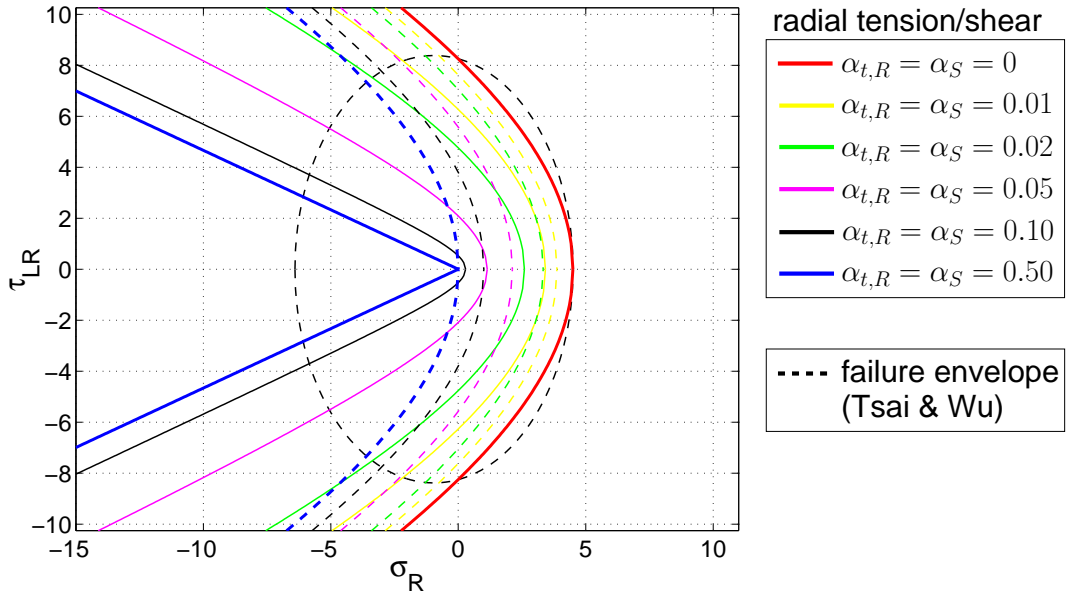


Figure 5.13: Motion of the radial tension surface in the cross-section $\sigma_{LL} = 0$ for $\ell_c = 1$ mm (only mode I: dashed lines, only mode II: solid lines).

function of σ_{RR} and both state variables $\alpha_{t,R}$ and α_S . Its derivatives with respect to these variables are

$$\frac{\partial \kappa}{\partial \sigma_{RR}} =: \kappa_{,\sigma} = \frac{2 \langle \sigma_{RR} - \beta_{t,R} + a \tan^2 \phi \rangle}{a^2 \tan^4 \phi}, \quad (5.126)$$

$$\frac{\partial \kappa}{\partial \alpha_{t,R}} =: \kappa_{,\alpha R} = k_I \beta_{t,R} \kappa_{,\sigma} \quad (5.127)$$

and

$$\frac{\partial \kappa}{\partial \alpha_S} =: \kappa_{,\alpha S} = k_{II} [\kappa_{,\sigma} (\beta_{t,R} - a \tan^2 \phi) + 2\kappa]. \quad (5.128)$$

The second partial derivative of the flow potential g with respect to $\boldsymbol{\sigma}$ can be derived from (5.90) and $d\tilde{\mathbf{r}}_{t,RS} = D_{\boldsymbol{\sigma}} \tilde{\mathbf{r}}_{t,RS} : d\boldsymbol{\sigma}$ as

$$\frac{\partial^2 g}{\partial \boldsymbol{\sigma} \otimes \partial \boldsymbol{\sigma}} := D_{\boldsymbol{\sigma}} \tilde{\mathbf{r}}_{t,RS} = \frac{2}{D} \left\{ [(\beta_{t,R} + a - \sigma_{RR}) \kappa_{,\sigma} - \kappa] \mathbf{M}_R \otimes \mathbf{M}_R + \frac{1}{\tan^2 \phi} \mathbf{N} \otimes \mathbf{N} \right\}. \quad (5.129)$$

The mixed partial derivative of g follows from (5.90) and with (5.120) to

$$\frac{\partial^2 g}{\partial \boldsymbol{\sigma} \otimes \partial \boldsymbol{\alpha}} = \left[\frac{\partial^2 g}{\partial \boldsymbol{\sigma} \otimes \partial \alpha_{t,R}} \quad \frac{\partial^2 g}{\partial \boldsymbol{\sigma} \otimes \partial \alpha_S} \right]^T \quad (5.130)$$

with

$$\frac{\partial^2 g}{\partial \boldsymbol{\sigma} \otimes \partial \alpha_{t,R}} = \frac{2k_I \beta_{t,R}}{D} [(\beta_{t,R} + a - \sigma_{RR}) \kappa_{,\sigma} - \kappa] \mathbf{M}_R \quad (5.131)$$

and

$$\frac{\partial^2 g}{\partial \boldsymbol{\sigma} \otimes \partial \alpha_S} = \frac{2}{D} [(\beta_{t,R} + a - \sigma_{RR}) \kappa_{,\sigma} - k_{II} (\beta_{t,R} + a) \kappa] \mathbf{M}_R. \quad (5.132)$$

The derivative of the yield function (5.77) with respect to $\boldsymbol{\alpha}$ is obtained as

$$\frac{\partial f}{\partial \boldsymbol{\alpha}} = \left[\frac{\partial f}{\partial \alpha_{t,R}} \quad \frac{\partial f}{\partial \alpha_S} \right]^T \quad (5.133)$$

with

$$\frac{\partial f}{\partial \alpha_{t,R}} = -\frac{2k_I \beta_{t,R}}{D} (\sigma_{RR} - \beta_{t,R} - a) \quad (5.134)$$

and

$$\frac{\partial f}{\partial \alpha_S} = -\frac{2k_{II}}{D} [\beta_{t,R} (\sigma_{RR} - \beta_{t,R} - a) + a (\sigma_{RR} - \beta_{t,R})]. \quad (5.135)$$

The ratios \mathbf{s} of $\tilde{\mathbf{r}}_{t,RS}$ relevant for softening thus can be written for an active state surface $f_{t,RS}$ as

$$\mathbf{s} = \begin{Bmatrix} s_{t,R} \\ s_S \end{Bmatrix} = \tilde{\mathbf{s}}(\tilde{\mathbf{r}}_{t,RS}) := \begin{Bmatrix} \frac{\langle \mathbf{M}_R : \tilde{\mathbf{r}}_{t,RS} \rangle}{\sqrt{\tilde{\mathbf{r}}_{t,RS} \mathbb{M} \tilde{\mathbf{r}}_{t,RS}}} \end{Bmatrix} = \frac{2}{D} \begin{Bmatrix} (\beta_{t,R} + a - \sigma_{RR}) \kappa \\ |\tau_{LR}| / \tan^2 \phi \end{Bmatrix} \quad (5.136)$$

and as $\mathbf{s} = \mathbf{0}$ if it is inactive. Its derivative with respect to the plastic flow direction $\tilde{\mathbf{r}}_{t,RS}$ is obtained as

$$\frac{\partial \tilde{\mathbf{s}}}{\partial \tilde{\mathbf{r}}_{t,RS}} = \left[\mathbf{M}_R \frac{\langle \mathbf{M}_R : \tilde{\mathbf{r}}_{t,RS} \rangle}{\mathbf{M}_R : \tilde{\mathbf{r}}_{t,RS}} \quad \frac{\mathbb{M} : \tilde{\mathbf{r}}_{t,RS}}{\sqrt{\tilde{\mathbf{r}}_{t,RS} : \mathbb{M} : \tilde{\mathbf{r}}_{t,RS}}} \right]. \quad (5.137)$$

A simplification for these components was developed in Section 5.2. It leads to

$$\frac{\partial \tilde{\mathbf{s}}}{\partial \tilde{\mathbf{r}}_{t,RS}} = \begin{bmatrix} \mathbf{M}_R & \text{sign}(\tau_{LR}) \mathbf{N} \end{bmatrix}. \quad (5.138)$$

5.6 Visualization

Four state surfaces for clear spruce wood under plane stress states were developed in Sections 5.2 to 5.5. Each surface covers one failure mode observed in the experiments by Eberhardsteiner [7].

One can imagine the orthotropic stress space with invariants (4.41) σ_{LL} , σ_{RR} , and τ_{RL}^2 as the main coordinate axes. This three-dimensional stress space is similar to the Haigh-Westergard stress space for isotropic materials. To obtain a visualization of the failure envelope which is easier to interpret, τ_{RL} will be used instead of τ_{RL}^2 . This results in symmetric pictures with respect to the plane $\tau_{RL} = 0$. Each of the state surfaces is only valid until it intersects another yield surface. The evolving multi-surface failure envelope is shown in its initial configuration in Figure 5.14.

The surfaces for radial compression and radial tension account for the highest portion of the whole model. Hence, the failure modes perpendicular to grain dominate the behavior of wood. The fiber tension mode has the least amount of influence with all possible plane stress states, but it accounts for those, possessing the highest strength values and thus is the preferred design mode. The fiber compression mode covers a larger domain than the fiber tension mode, due to its higher tolerance to changes of the grain angle φ .

Table 5.1 contains a composition of all material parameters used in this work to describe the failure envelope for clear spruce wood in the orthotropic stress space. Also the material

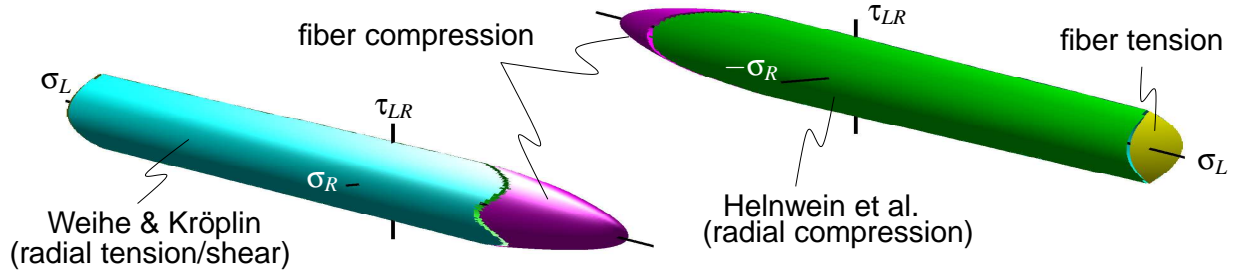


Figure 5.14: Multi-surface model in its initial state (failure envelope).

parameters for the elastic domain, i.e. for the orthotropic elasticity tensor \mathbb{C} (4.71), are given. All values are given in the units [MPa] and [mm]. This unified depiction enables the direct use of these values in the mathematical implementation of the multi-surface model. We are well aware that a sensible unit for the fracture toughness G_f is energy per area. The conversion to the before mentioned units is given as

$$[G_f] = 1 \frac{\text{J}}{\text{m}^2} = 1 \frac{\text{N} \cdot \text{m}}{\text{m}^2} = 1 \text{Pa} \cdot \text{m} = 10^{-3} \text{MPa} \cdot \text{mm}. \quad (5.139)$$

Table 5.1: Material parameters for the multi-surface plasticity model

<i>elastic domain</i>					
E_L	=	15000 MPa	G_{LR}	=	751 MPa
E_R	=	830 MPa	ν_{LR}	=	0.40
<i>fiber tension surface</i>					
$\beta_{t,L}^0$	=	65.00 MPa	$G_{ft,L}^I$	=	1.65 MPa·mm
<i>fiber compression surface</i>					
$\beta_{c,L}^0$	=	49.99 MPa	$Y_{1,L}$	=	10.00 MPa
A	=	1.17	B	=	44.89
$H_{L,d}$	=	15.00 MPa	$\alpha_{L,d}$	=	0.50
<i>radial compression surface</i>					
$\beta_{c,R}^0$	=	4.00 MPa	$Y_{1,R}$	=	1.80 MPa
c	=	-0.0075	μ	=	0.50 MPa ⁻¹
$H_{R,d}$	=	2.00 MPa	$\alpha_{R,d}$	=	0.10
<i>radial tension surface</i>					
$\beta_{t,R}^0$	=	4.50 MPa	$G_{f,R}^I$	=	0.30 MPa·mm
β_S^0	=	8.25 MPa	ϕ	=	25.00°
			$G_{f,R}^{II}$	=	0.30 MPa·mm

Figure 5.15 shows cross-sections through the planes $\sigma_{RR} = 0$ and $\tau_{RL} = 0$. One can recognize the parabolic shape of the fiber tension (magenta) and fiber compression (red) state surfaces in the cross-sections but not the shape of the radial surfaces. The latter are only visible as a straight line in these plots.

For comparison, the single-surface failure envelope on the basis of the Tsai and Wu criterion [42] with parameters identified by Eberhardsteiner [7] is shown as green dashed

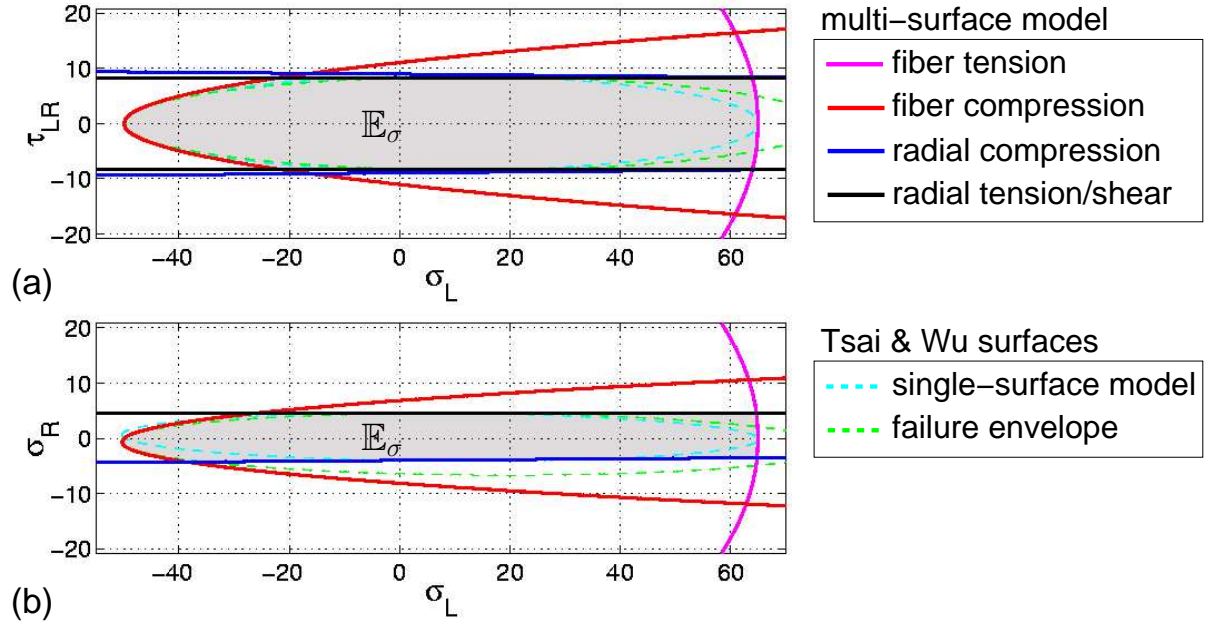


Figure 5.15: Cross-sections through planes (a) $\sigma_{RR} = 0$ and (b) $\tau_{RL} = 0$.

line in Figure 5.15. The parameters were determined according to the results of the experiments Eberhardsteiner [7] (see Chapter 3), with the definition of failure as the first (local) maximum any principal normal stress.

The single-surface model used in [35] is indicated by a dashed cyan line in Fig. 5.15. It describes the elastic domain for this model, which does not necessarily coincide with the points of failure as defined in [7]. This model also based on the Tsai and Wu criterion [42] but its parameters were fitted to the strength values of the multi-surface model. Due to the large scatter of the tensile strength in fiber direction, $\beta_{t,L}$ was chosen significantly smaller than the strength obtained by the failure envelope by Eberhardsteiner. This results in a shorter ellipse visible in the cross-sections in Fig. 5.15(a) and (b).

Figure 5.16 shows the cross-section for $\sigma_{LL} = 0$. The parabolic radial compression yield surface (blue) and the physically relevant branch of the hyperboloid representing the radial tension model (black) can be identified. The fiber compression surface (red) appears as an ellipse. One can clearly see that it is not relevant, since a stress path originating from within the elastic domain \mathbb{E}_σ (gray) would first reach one of the radial envelopes.

The significant difference of the failure envelope (dashed green) indicating the experimental results [7] and the multi-surface, as well as the single-surface model is due to the homogeneous inelastic strains in the radial compression regime. These strains lead to a material behavior that is no longer elastic. Failure according to the definition above is observed in the inelastic regime, resulting in a failure domain that is bigger than the elastic domain.

The ellipse representing the fiber tension surface is too large to be visible in this portion of the cross-section. The over and under estimations of the single-surface model (dashed cyan), accounted for by the multi-surface model (Gray elastic domain \mathbb{E}_σ), are clearly

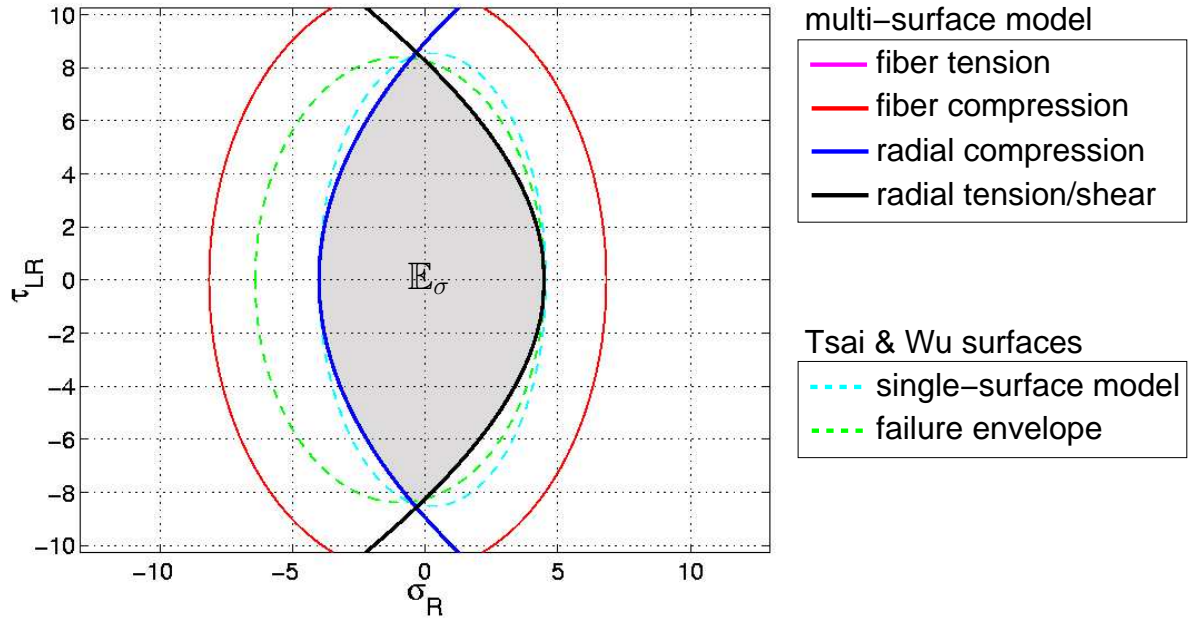


Figure 5.16: Cross-section through plane $\sigma_{LL} = 0$,

visible in the Figures 5.15 and 5.16.

Figure 5.17 shows a possible motion of all state surfaces in the $\tau_{RL} = 0$ plane. In this case all failure modes were activated. A motion of each surface individual or combined with others is obviously possible. The individual kinematics of each surface were shown in Figures 5.2 to 5.13 in the previous sections for constant ℓ_c and various values for the state variables α .

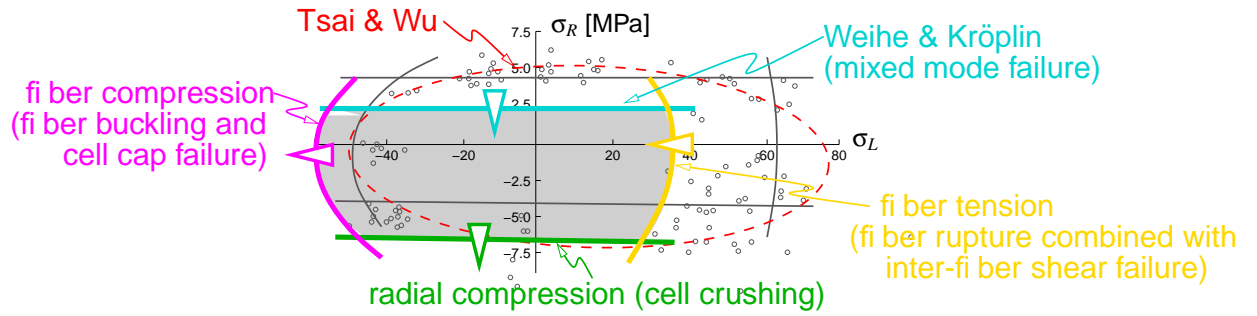


Figure 5.17: Possible motion of state surfaces in the plane $\tau_{RL} = 0$.

5.7 Comparison of material models

Besides the multi-surface failure model described in this chapter several other models exist that predict the material behavior of clear spruce wood. One is the single-surface model by Tsai and Wu [42] for orthotropic materials. Details on this model can be found in [33, 35].

A third model is the so called box-like failure model [1, 15], that is used in most design codes. This multi-surface model consists of four plane surfaces, each defined by the uniaxial strength in the respective main material direction. These surfaces describe a cube in the orthotropic stress space.

The uniaxial tensile and compressive strength is a good value to compare orthotropic material models with each other. This was done for the above mentioned failure models by Helnwein et al. [30]. A uniaxial stress state leads for a orthotropic material to a general plane stress state, thus an arbitrary stress state can be described by two values, uniaxial strength β_u and gain angle φ .

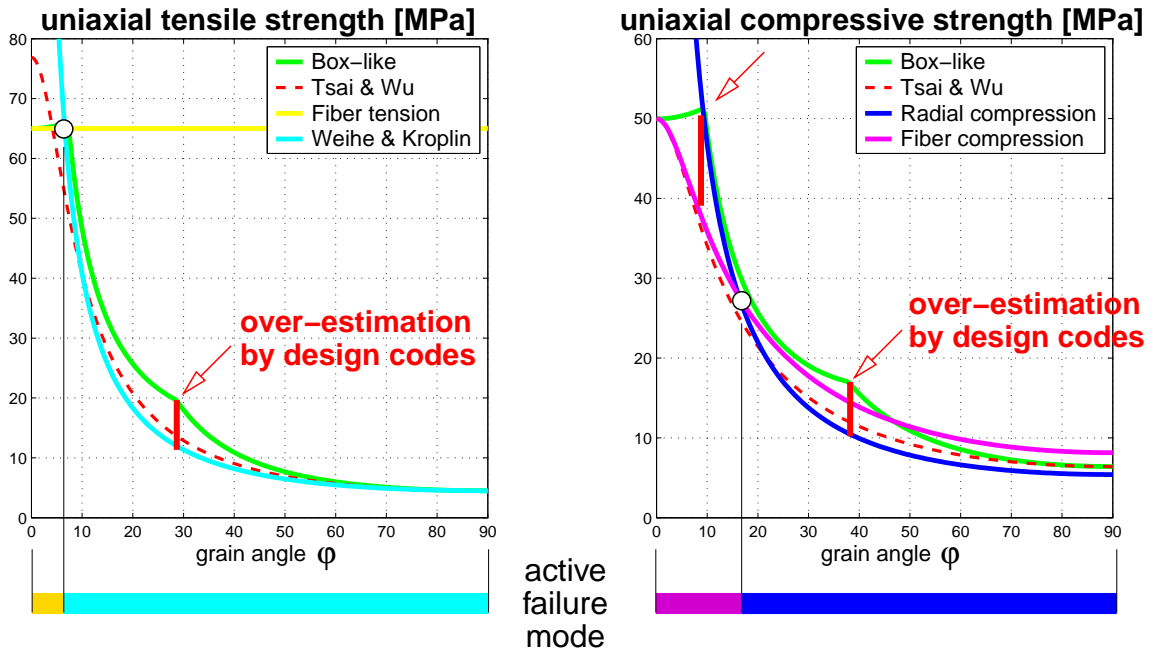


Figure 5.18: Uniaxial strength of clear spruce wood in dependency of the grain angle φ computed with different failure models [30].

The uniaxial stress state is defined by a single stress $\sigma_1 = \sigma$, a vanishing second principal stress $\sigma_2 = 0$ and a grain angle φ . Using this definition with the uniaxial strength $\sigma = \beta_u$ in (3.2) yields

$$\begin{aligned}\sigma_L &= \beta_u \cos^2 \varphi \\ \sigma_R &= \beta_u \sin^2 \varphi. \\ \tau_{LR} &= \beta_u \sin \varphi \cos \varphi\end{aligned}\tag{5.140}$$

Insertion of this values in the respective yield conditions for the each surface of the multi-surface (5.24), (5.40), (5.56) and (5.77) and the single-surface model leads to quadratic equations for β_u , which can be computed for each grain angle $0^\circ \leq \varphi \leq 90^\circ$. The uniaxial tensile and compressive strength for $\varphi = 0^\circ$ of the multi-surface model were used to fit the box-like model.

Figure 5.18 shows the result of this comparison. The tensile and compression uniaxial strength are shown in dependency of the grain angle φ . As already observed in Section 5.6,

the two surfaces for radial direction of the multi-surface model cover most of the possible loading types. The tension cut-off of the fiber tension surface and the fiber compression surface are only valid for small grain angles. The relevant range of grain angles for each surface of the multi-surface model is indicated at the bottom of Figure 5.18 by the respective color.

The over-estimation by design codes, which use the box-like model, is also indicated in the same figure. In the tensile regime the over-estimation is in the range of $\varphi = 10^\circ$ to 45° , whereas the strength of nearly the whole compression regime is overrated. The peak of approximately 60% strength over-estimation is reached for tensile loading at a grain angle of slightly under 30° and for compression stresses slightly under 40° . The reason for this misestimation is the missing coupling of the normal and shear stresses, that occurs in biaxial loading states, in the box-like model.

The Tsai and Wu model shows a good accordance with the multi-surface model, with only a small over-estimation of the tensile strength in grain direction, but does not allow the distinction of failure modes.

Chapter 6

Numerical implementation

The constitutive model for rate-independent plasticity of the orthotropic material clear spruce wood introduced in Chapter 4 and Chapter 5, is formulated as a set of rate equations. In general, no closed form integral can be obtained for these equation. A numerical time integration algorithm has to be employed. In this work the Euler backward algorithm will be used. It was first proposed by Simo and Taylor [39], and generalized by Simo and Hughes [38], both for isotropic elasto-plastic materials. Nevertheless, the algorithms in [38] can also be applied to orthotropic plasticity. The described algorithm involves an elastic predictor step and, if necessary, a plastic corrector step.

6.1 Numerical integration – incremental formulation

Any incremental form emanates from a known instance time t_n . All state variables are assumed known at t_n . The problem is to find a solution for all state variables after a given time increment Δt . The related time instance t_{n+1} is obtained as

$$t_{n+1} = t_n + \Delta t. \quad (6.1)$$

The update of state variables from t_n to t_{n+1} is performed by numerical integration of the rate equations given in Section 4.3 and Chapter 5.

Values of a variables at t_n are indicated by a subscript n . Values of a variables at t_{n+1} are indicated by a subscript $n + 1$. Following previous arguments, variables with subscript n are assumed known.

The numerical time integration algorithm works as follows:

- Obtain the total strain $\boldsymbol{\epsilon}_{n+1}$ from the global displacement field \mathbf{u}_{n+1} . Hence, the total strain is assumed known at t_{n+1} .
- Apply the Euler backward integration to both the flow rule and the hardening law to obtain $\boldsymbol{\epsilon}_n^p$ and $\boldsymbol{\alpha}_{n+1}$.

- Find total stress $\boldsymbol{\sigma}_{n+1}$, hardening stress \mathbf{q}_{n+1} , and current strength Y_{n+1} from respective hyperelastic relations.
- Enforce active yield conditions at t_{n+1} .

Therefore one speaks of a *strain-driven process* in which $\boldsymbol{\varepsilon}_{n+1}$ is the basic independent variable. This procedure is called the *return-mapping algorithm* with input variables $\boldsymbol{\varepsilon}_{n+1}$, $\boldsymbol{\varepsilon}_n^p$, $\boldsymbol{\alpha}_n$ and the output variables $\boldsymbol{\sigma}_{n+1}$, \mathbf{q}_{n+1} , Y_{n+1} , $\boldsymbol{\varepsilon}_{n+1}^p$ and $\boldsymbol{\alpha}_{n+1}$. The stress $\boldsymbol{\sigma}_{n+1}$ is a dependent variable following from the hyperelastic stress-strain relation (4.86).

In Chapter 5 the driving variable $\boldsymbol{\varepsilon}_{n+1}$ was defined in ordinary differential equation in the form

$$\dot{\boldsymbol{\varepsilon}}^p = \dot{\gamma}_\alpha \mathbf{r}_\alpha \quad \alpha \in \{1, 2, 3, 4\} \quad (6.2)$$

for each of the four state surfaces (indicated by the subscript α), where $\mathbf{r}_\alpha = \partial g_\alpha / \partial \boldsymbol{\sigma}$ with $g_\alpha = f_\alpha$ for some surfaces (see Chapter 5 for details). For the proposed state surfaces and flow rules, \mathbf{r}_α is linear with respect to the stress tensor $\boldsymbol{\sigma}$. Time integration of (6.2) yields

$$\boldsymbol{\varepsilon}_{n+1}^p = \boldsymbol{\varepsilon}_n^p + \int_{t_n}^{t_{n+1}} \dot{\boldsymbol{\varepsilon}}^p dt, \quad (6.3)$$

where $\boldsymbol{\varepsilon}_n^p$ is the know value of the plastic strain at time t_n and $\boldsymbol{\varepsilon}_{n+1}^p$ is the plastic strain at t_{n+1} . $\dot{\boldsymbol{\varepsilon}}^p$ depends on the load path during the interval $[t_n, t_{n+1}]$. A numerical approximation for the integral in (6.3) is obtained from the general implicit Euler integration rule as

$$\boldsymbol{\varepsilon}_{n+1}^p \approx \boldsymbol{\varepsilon}_n^p + \dot{\boldsymbol{\varepsilon}}_{n+\theta}^p \Delta t, \quad (6.4)$$

with time step $\Delta t = t_{n+1} - t_n$ and $\theta \in [0, 1]$ as shown in Figure 6.1.

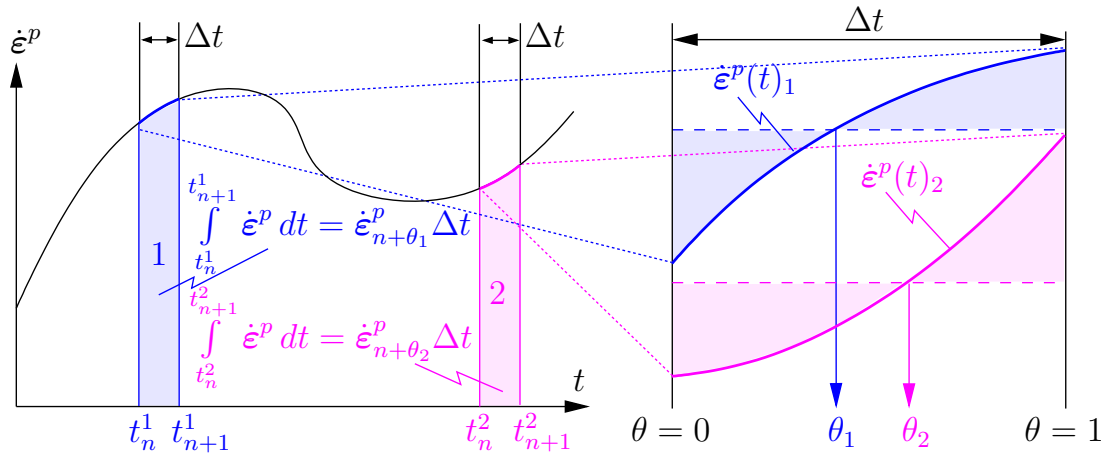


Figure 6.1: Geometrical interpretation of θ .

For every time step there exists one θ for which the exact solution is obtained for the area under the function $\dot{\boldsymbol{\varepsilon}}^p(t)$, but its value is not known a priori. See Figure 6.1 for an illustration. The right part of the figure shows two segments of the same function. One

θ can be found for each segment, but it depends on the location of the segment. This is shown for two different segments, indicated by the numbers 1 and 2. Assuming a value for θ leads to different numerical integration algorithms for (6.2). The most common integration algorithms are

- $\theta = 0$ \rightarrow forward or explicit Euler,
- $\theta = 1/2$ \rightarrow midpoint rule, and
- $\theta = 1$ \rightarrow backward or implicit Euler.

Only the midpoint rule leads to a second order accuracy. $\theta \geq 1/2$ leads to unconditional linearized stability [38]. Values of $\theta \geq 1/2$ always lead to stable solutions and convergence to a solution, thus these algorithms are unconditionally stable. For the integration of the elasto-plastic initial value problem the best suitable rule to use is the implicit backward Euler algorithm.

For $\theta = 1$, equation (6.4) yields under consideration of (6.2)

$$\boldsymbol{\varepsilon}_{n+1}^p \approx \boldsymbol{\varepsilon}_n^p + \dot{\boldsymbol{\varepsilon}}_{n+1}^p \Delta t = \boldsymbol{\varepsilon}_n^p + \mathbf{r}_{n+1} \underbrace{\dot{\gamma}_{n+1} \Delta t}_{=: \gamma_{n+1}} = \boldsymbol{\varepsilon}_n^p + \underbrace{\gamma_{n+1} \mathbf{r}_{n+1}}_{=: \Delta \boldsymbol{\varepsilon}^p} = \boldsymbol{\varepsilon}_n^p + \Delta \boldsymbol{\varepsilon}^p, \quad (6.5)$$

where $\gamma_{n+1} \geq 0$ is the algorithmic counterpart of the consistency parameter $\dot{\gamma}$. The solution is getting more accurate as the time step Δt decreases, but the computational effort increases.

Similar to (6.5) one can also integrate the general softening rule $\dot{\boldsymbol{\alpha}} = \dot{\gamma} \mathbf{s}$ as defined for each surface in 5.2 to 5.5 leading to

$$\boldsymbol{\alpha}_{n+1} = \boldsymbol{\alpha}_n + \gamma_{n+1} \mathbf{s}_{n+1} = \boldsymbol{\alpha}_n + \Delta \boldsymbol{\alpha}, \quad (6.6)$$

where $\boldsymbol{\alpha}_n$, $\boldsymbol{\alpha}_{n+1}$ and \mathbf{s}_{n+1} can be scalars or two component vectors, as e.g. for the radial tension model from Section 5.5.

The hyperelastic stress-strain relation (4.86) yields

$$\boldsymbol{\sigma}_{n+1} = \mathbb{C} : (\boldsymbol{\varepsilon}_{n+1} - \boldsymbol{\varepsilon}_{n+1}^p), \quad (6.7)$$

where the elastic material tensor \mathbb{C} is constant. The hardening stress q_{n+1} and the strength function Y_{n+1} follow from

$$q_{n+1} = q_{n+1}(\boldsymbol{\alpha}_{n+1}) \quad \text{and} \quad Y_{n+1} = Y_{n+1}(\boldsymbol{\alpha}_{n+1}), \quad (6.8)$$

respectively. The incremental consistency parameter γ_{n+1} is obtained from the algorithmic consistency condition

$$f_{n+1} = f_{n+1}(\boldsymbol{\sigma}_{n+1}, q_{n+1}) = 0. \quad (6.9)$$

6.2 Return mapping algorithm for a single orthotropic state surface

In this section the numerical solution will be specialized for a single orthotropic surface. This algorithm can be used to describe (i) a single failure mode, (ii) a single-surface model

with the appropriate parameters and derivatives, and (iii) a multi-surface model where only one surface is active. The latter saves computer time because the involved system of equations is smaller than for the full formulation for multiple active surfaces.

The implicit integration typically leads to an iterative procedure for solving the non-linear consistency condition $f_{n+1} = 0$. The result of this procedure is the incremental consistency parameter γ_{n+1} (see (6.5) and (6.6)).

The return mapping algorithm, the most common algorithm to solve problems in plasticity, consist of two main steps. The first step is the elastic predictor also called the trial state. This is computed assuming that the next step is elastic loading or unloading. If the trial state is outside the elastic domain, i.e. the yield surface, it is used as a starting point for the iteration to solve the plastic corrector. The plastic corrector is the second step of the return mapping algorithm and projects the trial state back on the yield surface. The elastic-plastic operator split of the return mapping algorithm can be written in rate-formulation as

$$\begin{array}{rclclcl}
 \text{Total} & = & \text{Elastic predictor} & + & \text{Plastic corrector} \\
 \hline
 \dot{\boldsymbol{\epsilon}} = \dot{\boldsymbol{\epsilon}} & & \dot{\boldsymbol{\epsilon}} = \dot{\boldsymbol{\epsilon}} & & \dot{\boldsymbol{\epsilon}} = \mathbf{0} \\
 \dot{\boldsymbol{\epsilon}}^p = \gamma \mathbf{r}(\boldsymbol{\sigma}, q) & = & \dot{\boldsymbol{\epsilon}}^p = \mathbf{0} & + & \dot{\boldsymbol{\epsilon}}^p = \gamma \mathbf{r}(\boldsymbol{\sigma}, q). \\
 \dot{\boldsymbol{\alpha}} = -\gamma \mathbf{s}(\boldsymbol{\sigma}, q) & & \dot{\boldsymbol{\alpha}} = \mathbf{0} & & \dot{\boldsymbol{\alpha}} = -\gamma \mathbf{s}(\boldsymbol{\sigma}, q)
 \end{array} \quad (6.10)$$

One needs to find a useful notion to defined the elastic predictor. As shown in [38] the Kuhn-Tucker conditions can be formulated in a different way based on plastic loading. Loading is characterized by the so-called *rate-of-trial elastic stress*

$$\dot{\boldsymbol{\sigma}}^{tr} := \mathbb{C} : \dot{\boldsymbol{\epsilon}} \quad (6.11)$$

and the conditions to define a plastic state such that

$$f(\boldsymbol{\sigma}, q) = 0 \quad \text{and} \quad \partial_{\boldsymbol{\sigma}} f(\boldsymbol{\sigma}, q) : \dot{\boldsymbol{\sigma}}^{tr} > 0. \quad (6.12)$$

This formulation can be used to distinguish between an instantaneous elastic process and an instantaneous plastic process. The equivalence of the rate of trial stress condition and the Kuhn-Tucker conditions (4.96) becomes obvious, when substituting (6.11) into (4.102), yielding

$$\gamma = \frac{\partial_{\boldsymbol{\sigma}} f : \dot{\boldsymbol{\sigma}}^{tr}}{\partial_{\boldsymbol{\sigma}} f : \mathbb{C} : \mathbf{r} + \partial_q f \cdot \mathbf{h}}. \quad (6.13)$$

For a point on the yield surface, $f = 0$, (6.13) leads to a positive value of γ , as (6.12) holds for a plastic state, and thus with (6.11) follows from (4.101) $\dot{f} = 0$. The advantage of this method is, that all values can be computed based on an elastic state.

Replacing the rates by finite increments in the rate-of-trial stress condition (6.11) and (6.12) leads to the trial state

$$\begin{array}{ll}
 \gamma_{n+1}^{tr} = 0, & \boldsymbol{\epsilon}_{n+1}^{p,tr} = \boldsymbol{\epsilon}_n^p + \gamma_{n+1}^{tr} \mathbf{r}_{n+1} = \boldsymbol{\epsilon}_n^p, \\
 \boldsymbol{\alpha}_{n+1}^{tr} = \boldsymbol{\alpha}_n, & q_{n+1}^{tr} = q_n, \quad \text{and} \quad Y_{n+1}^{tr} = Y_n.
 \end{array} \quad (6.14)$$

From the hyperelastic law follows

$$\boldsymbol{\sigma}_{n+1}^{tr} = \frac{\partial \psi}{\partial \boldsymbol{\epsilon}} \bigg|_{tr} = \mathbb{C} : \boldsymbol{\epsilon}_{n+1}^{e,tr} = \mathbb{C} : (\boldsymbol{\epsilon}_{n+1} - \boldsymbol{\epsilon}_{n+1}^{p,tr}) = \mathbb{C} : (\boldsymbol{\epsilon}_{n+1} - \boldsymbol{\epsilon}_n^p). \quad (6.15)$$

The trial state allows for a direct computational implementation of the incremental version of the Kuhn-Tucker loading/unloading conditions

$$\gamma_{n+1} \geq 0, \quad f_{n+1} \leq 0 \quad \text{and} \quad \gamma_{n+1} f_{n+1} = 0. \quad (6.16)$$

Freezing the plastic strain $\boldsymbol{\varepsilon}^p$ and the internal variables $\boldsymbol{\alpha}$ during a time step would be the physical explanation of the trial state. With the yield condition

$$f_{n+1}^{tr} = f(\boldsymbol{\sigma}_{n+1}^{tr}, q_{n+1}^{tr}, Y_{n+1}^{tr}) > 0 \quad (6.17)$$

it can be tested if the trial state is admissible. If this condition is not fulfilled, i.e. if the trial state is located outside the elastic domain, the plastic corrector step must be computed.

To solve the non-linear initial value problem defined by the rate-independent plasticity model given with the flow rule (6.5), the softening rule (6.6), the stress-strain relation (6.7), the definitions of the plastic flow direction \mathbf{r} and the softening ratio \mathbf{s} and the consistency condition (6.9), one can rephrase the equations in terms of residuums as

$$\mathbf{R}_{\sigma, n+1} = \mathbb{C}^{-1} : \boldsymbol{\sigma}_{n+1} - \boldsymbol{\varepsilon}_{n+1} + \boldsymbol{\varepsilon}_{n+1}^p = \mathbf{0}, \quad (6.18)$$

$$\mathbf{R}_{\varepsilon, n+1} = \boldsymbol{\varepsilon}_{n+1}^p - \boldsymbol{\varepsilon}_n^p - \gamma_{n+1} \mathbf{r}_{n+1} = \mathbf{0}, \quad (6.19)$$

$$\mathbf{R}_{r, n+1} = \mathbf{r}_{n+1} - \frac{\partial g_{n+1}}{\partial \boldsymbol{\sigma}_{n+1}} = \mathbf{0}, \quad (6.20)$$

$$\mathbf{R}_{\alpha, n+1} = \boldsymbol{\alpha}_{n+1} - \boldsymbol{\alpha}_n - \gamma_{n+1} \mathbf{s}_{n+1} = \mathbf{0}, \quad (6.21)$$

$$\mathbf{R}_{s, n+1} = \mathbf{s}_{n+1} - \tilde{\mathbf{s}}(\mathbf{r}_{n+1}) = \mathbf{0}, \quad (6.22)$$

and

$$R_{f, n+1} = f_{n+1} = 0. \quad (6.23)$$

The function $\tilde{\mathbf{s}}(\mathbf{r}_{n+1})$ in (6.22) extracts the hardening direction \mathbf{s}_{n+1} from the plastic flow direction \mathbf{r}_{n+1} . Each residuum presents a measure for the error of each equation, and hence a measure of the distance of any approximate state from its true solution. Combining these equations to a generalized residuum vector

$$\mathbf{R}_{n+1} = \{\mathbf{R}_{\sigma, n+1} \ \mathbf{R}_{\varepsilon, n+1} \ \mathbf{R}_{r, n+1} \ \mathbf{R}_{\alpha, n+1} \ \mathbf{R}_{s, n+1} \ R_{f, n+1}\}^T \quad (6.24)$$

and defining a generalized vector of independent unknowns

$$\mathbf{q}_{n+1} = \{\boldsymbol{\sigma}_{n+1} \ \boldsymbol{\varepsilon}_{n+1}^p \ \mathbf{r}_{n+1} \ \boldsymbol{\alpha}_{n+1} \ \mathbf{s}_{n+1} \ \gamma_{n+1}\}^T \quad (6.25)$$

allows for an easier formulation of the iterative procedure.

These equations can be solved using the generalized Newton-Raphson method. The series expansion of $\mathbf{R}_{n+1} = \mathbf{0}$ is

$$\mathbf{R}_{n+1}^{(k)} + D_q \mathbf{R}_{n+1}^{(k)} \bullet \Delta \mathbf{q}_{n+1} + D_{qq}^2 \mathbf{R}_{n+1}^{(k)} \bullet \Delta \mathbf{q}_{n+1} \otimes \Delta \mathbf{q}_{n+1} + \dots = \mathbf{0}. \quad (6.26)$$

The generalized Newton-Raphson method follows after the elimination of terms higher than first order in (6.26) (i.e. linearization) to

$$\mathbf{R}_{n+1}^{(k)} + D_q \mathbf{R}_{n+1}^{(k)} \bullet \Delta \mathbf{q}_{n+1} = \mathbf{0}, \quad (6.27)$$

where \bullet stands for the appropriate contraction operator (either a second order tensor product, a vector product, or a scalar product) according to the entry in $\Delta\mathbf{q}$. This method only requires a first-order tangent operator, because higher order terms are not used. The $(k+1)$ th-approximation of \mathbf{q}_{n+1} follows from (6.27) as

$$\mathbf{q}_{n+1}^{(k+1)} = \mathbf{q}_{n+1}^{(k)} + \Delta\mathbf{q}_{n+1} \quad (6.28)$$

with

$$\Delta\mathbf{q}_{n+1} = -(D_q\mathbf{R}_{n+1}^{(k)})^{-1} \bullet \mathbf{R}_{n+1}^{(k)}. \quad (6.29)$$

With $\mathbf{q}_{n+1}^{(k+1)}$ a new generalized residuum vector $\mathbf{R}_{n+1}^{(k+1)} = \mathbf{R}(\mathbf{q}_{n+1}^{(k+1)})$ can be computed. Steps (6.28) and (6.29) have to be repeated until

$$\|\mathbf{R}_{n+1}^{(k+1)}\| \leq \text{tolerance}, \quad (6.30)$$

with a tolerance value in the range of approximately $10 \cdot \varepsilon$, where ε stands for the accuracy of the used computer. The start value $\mathbf{q}_{n+1}^{(0)}$ for the iteration follows from the trial state defined in (6.14) and (6.15), and from the definition of the vector \mathbf{q}_{n+1} (6.25). It reads

$$\mathbf{q}_{n+1}^{(0)} = \mathbf{q}_{n+1}^{tr} = \{\boldsymbol{\sigma}_{n+1}^{tr} \boldsymbol{\varepsilon}_{n+1}^{p,tr} \mathbf{r}_{n+1}^{tr} \boldsymbol{\alpha}_{n+1}^{tr} \mathbf{s}_{n+1}^{tr} \gamma_{n+1}^{tr}\}^T. \quad (6.31)$$

The tangent operator for the Newton algorithm can be obtained from the differential

$$d\mathbf{R}_{n+1} = D_q\mathbf{R}_{n+1} \bullet d\mathbf{q}_{n+1} + D_\varepsilon\mathbf{R}_{n+1} : d\boldsymbol{\varepsilon}_{n+1}, \quad (6.32)$$

where $D_q\mathbf{R}_{n+1}$ is obtained for $\boldsymbol{\varepsilon}_{n+1} = \text{constant}$ and $D_\varepsilon\mathbf{R}_{n+1}$ is computed for $\mathbf{q}_{n+1} = \text{constant}$. The latter operator is not needed at this point but will be used for the computation of the consistent tangent operator in Section 6.5.

The differentials of equations (6.18) to (6.23) for independent variables in \mathbf{q}_{n+1} as defined in (6.25) and $\boldsymbol{\varepsilon}_{n+1} = \text{constant}$ are obtained as follows

$$d\mathbf{R}_\sigma = \mathbb{C}^{-1} : d\boldsymbol{\sigma}_{n+1} + d\boldsymbol{\varepsilon}_{n+1}^p, \quad (6.33)$$

$$d\mathbf{R}_\varepsilon = d\boldsymbol{\varepsilon}_{n+1}^p - d\gamma_{n+1} \mathbf{r}_{n+1} - \gamma_{n+1} d\mathbf{r}_{n+1}, \quad (6.34)$$

$$d\mathbf{R}_r = d\mathbf{r}_{n+1} - \frac{\partial^2 g_{n+1}}{\partial \boldsymbol{\sigma}_{n+1} \otimes \partial \boldsymbol{\sigma}_{n+1}} : d\boldsymbol{\sigma}_{n+1} - \frac{\partial^2 g_{n+1}}{\partial \boldsymbol{\sigma}_{n+1} \otimes \partial \boldsymbol{\alpha}_{n+1}} \cdot d\boldsymbol{\alpha}_{n+1}, \quad (6.35)$$

$$d\mathbf{R}_\alpha = d\boldsymbol{\alpha}_{n+1} - d\gamma_{n+1} \mathbf{s}_{n+1} - \gamma_{n+1} d\mathbf{s}_{n+1}, \quad (6.36)$$

$$d\mathbf{R}_s = d\mathbf{s}_{n+1} - \frac{\partial \tilde{\mathbf{s}}_{n+1}}{\partial \mathbf{r}_{n+1}} : d\mathbf{r}_{n+1}, \quad (6.37)$$

and

$$dR_f = \frac{\partial f_{n+1}}{\partial \boldsymbol{\sigma}_{n+1}} : d\boldsymbol{\sigma}_{n+1} + \frac{\partial f_{n+1}}{\partial q_{n+1}} \frac{\partial q_{n+1}}{\partial \boldsymbol{\alpha}_{n+1}} \cdot d\boldsymbol{\alpha}_{n+1} + \frac{\partial f_{n+1}}{\partial Y_{n+1}} \frac{\partial Y_{n+1}}{\partial \boldsymbol{\alpha}_{n+1}} \cdot d\boldsymbol{\alpha}_{n+1}. \quad (6.38)$$

The first and second-order partial derivatives in (6.35), (6.37) and (6.38) were defined for each state surface in Chapter 5. They will be abbreviated as “ $\partial_{\circ\circ}\square$ ”, where “ \square ” stands for the function to be differentiated and “ \circ ” for each partial derivative. Combining

equations (6.33) to (6.38) yields the differential $d\mathbf{R}_{n+1}$ according to (6.27). Using $d\mathbf{R}_{n+1} = D\mathbf{R}_{n+1} \bullet d\mathbf{q}_{n+1}$ uniquely defines the tangent operator $D_q\mathbf{R}_{n+1}$ as

$$D_q\mathbf{R}_{n+1} = \begin{bmatrix} \mathbb{C}^{-1} & \mathbb{I} & \mathbf{0} & \mathbf{0} & \mathbf{0} & \mathbf{0} \\ \mathbf{0} & \mathbb{I} & -\gamma_{n+1}\mathbb{I} & \mathbf{0} & \mathbf{0} & -\mathbf{r}_{n+1} \\ -\partial_{\sigma\sigma}g & \mathbf{0} & \mathbb{I} & -\partial_{\sigma\alpha}g & \mathbf{0} & \mathbf{0} \\ \mathbf{0} & \mathbf{0} & \mathbf{0} & \mathbb{I} & \gamma_{n+1} & -\mathbf{s}_{n+1} \\ \mathbf{0} & \mathbf{0} & -\partial_r\tilde{\mathbf{s}} & \mathbf{0} & \mathbb{I} & \mathbf{0} \\ \partial_\sigma f & \mathbf{0} & \mathbf{0} & \partial_\alpha f & \mathbf{0} & \mathbf{0} \end{bmatrix}. \quad (6.39)$$

Computation of the inverse of (6.39) poses a significant numerical effort. This effort can be reduced by solving (6.27) not directly but by means of a staggered scheme instead. A suitable staggered scheme is obtained by solving (6.27), one variable at a time, by using one row of (6.27) at a time. $D_q\mathbf{R}_{n+1}$, as needed in (6.27), was defined in (6.39). To prevent multiple usage of the same equation and to obtain a stable algorithm, the rows associated with $\Delta\sigma$ and $\Delta\alpha$, i.e. the 1st and 4th row of (6.27), are combined to one equation as

$$\begin{aligned} \begin{bmatrix} \mathbf{R}_{\sigma,n+1}^{(k)} \\ \mathbf{R}_{\alpha,n+1}^{(k)} \end{bmatrix} + \begin{bmatrix} \mathbb{C}^{-1} & \mathbf{0} \\ \mathbf{0} & \mathbb{I} \end{bmatrix} \begin{bmatrix} \Delta\sigma_{n+1}^{(k)} \\ \Delta\alpha_{n+1}^{(k)} \end{bmatrix} + \begin{bmatrix} \mathbb{I} \\ \mathbf{0} \end{bmatrix} : \Delta\epsilon_{n+1}^{p(k)} \\ + \begin{bmatrix} \mathbf{0} \\ -\gamma_{n+1}\mathbb{I} \end{bmatrix} \Delta\mathbf{s}_{n+1}^{(k)} + \begin{bmatrix} \mathbf{0} \\ -\mathbf{s}_{n+1} \end{bmatrix} \Delta\gamma_{n+1}^{(k)} = \mathbf{0}. \end{aligned} \quad (6.40)$$

From the 3rd row of (6.27) one obtains

$$\Delta\mathbf{r}_{n+1}^{(k)} = \begin{bmatrix} \partial_{\sigma\sigma}g & \partial_{\sigma\alpha}g \end{bmatrix} \begin{bmatrix} \Delta\sigma_{n+1}^{(k)} \\ \Delta\alpha_{n+1}^{(k)} \end{bmatrix} - \mathbf{R}_{r,n+1}^{(k)}. \quad (6.41)$$

Substituting (6.41) into the 2nd and 5th row of (6.27) yields

$$\Delta\epsilon_{n+1}^{p(k)} = \mathbf{r}_{n+1}^{(k)} \Delta\gamma_{n+1}^{(k)} + \gamma_{n+1}^{(k)} \begin{bmatrix} \partial_{\sigma\sigma}g & \partial_{\sigma\alpha}g \end{bmatrix} \begin{bmatrix} \Delta\sigma_{n+1}^{(k)} \\ \Delta\alpha_{n+1}^{(k)} \end{bmatrix} - \mathbf{R}_{1,n+1}^{(k)} \quad (6.42)$$

with

$$\mathbf{R}_{1,n+1}^{(k)} = \gamma_{n+1}^{(k)} \mathbf{R}_{r,n+1}^{(k)} + \mathbf{R}_{\epsilon,n+1}^{(k)}. \quad (6.43)$$

and

$$\Delta\mathbf{s}_{n+1}^{(k)} = \partial_r\tilde{\mathbf{s}} \begin{bmatrix} \partial_{\sigma\sigma}g & \partial_{\sigma\alpha}g \end{bmatrix} \begin{bmatrix} \Delta\sigma_{n+1}^{(k)} \\ \Delta\alpha_{n+1}^{(k)} \end{bmatrix} - \mathbf{R}_{2,n+1}^{(k)} \quad (6.44)$$

with

$$\mathbf{R}_{2,n+1}^{(k)} = \partial_r\tilde{\mathbf{s}} \mathbf{R}_{r,n+1}^{(k)} + \mathbf{R}_{s,n+1}^{(k)}, \quad (6.45)$$

respectively. With (6.42) and (6.44) in the two-vector equation (6.40) for $\Delta\sigma_{n+1}$ and $\Delta\alpha_{n+1}$ leads to

$$\begin{aligned} \begin{bmatrix} \mathbb{C}^{-1} + \gamma_{n+1}^{(k)} \partial_{\sigma\sigma}g & \gamma_{n+1}^{(k)} \partial_{\sigma\alpha}g \\ -\gamma_{n+1}^{(k)} \partial_r\tilde{\mathbf{s}} : \partial_{\sigma\sigma}g & \mathbb{I} - \gamma_{n+1}^{(k)} \partial_r\tilde{\mathbf{s}} : \partial_{\sigma\alpha}g \end{bmatrix} \begin{bmatrix} \Delta\sigma_{n+1}^{(k)} \\ \Delta\alpha_{n+1}^{(k)} \end{bmatrix} = \\ = \begin{bmatrix} -\mathbf{r}_{n+1}^{(k)} \\ \mathbf{s}_{n+1}^{(k)} \end{bmatrix} \Delta\gamma_{n+1}^{(k)} - \begin{bmatrix} \mathbf{R}_{\sigma,n+1}^{(k)} - \mathbf{R}_{1,n+1}^{(k)} \\ \mathbf{R}_{\alpha,n+1}^{(k)} + \gamma_{n+1}^{(k)} \mathbf{R}_{2,n+1}^{(k)} \end{bmatrix}. \end{aligned} \quad (6.46)$$

Solving (6.46) for $\{\Delta\boldsymbol{\sigma}_{n+1} \ \Delta\boldsymbol{\alpha}_{n+1}\}^T$ yields

$$\begin{bmatrix} \Delta\boldsymbol{\sigma}_{n+1}^{(k)} \\ \Delta\boldsymbol{\alpha}_{n+1}^{(k)} \end{bmatrix} = \Xi_{n+1}^{(k)} \begin{bmatrix} -\mathbf{r}_{n+1}^{(k)} \\ \mathbf{s}_{n+1}^{(k)} \end{bmatrix} \Delta\gamma_{n+1}^{(k)} - \begin{bmatrix} \mathbf{R}_{3,n+1}^{(k)} \\ \mathbf{R}_{4,n+1}^{(k)} \end{bmatrix} \quad (6.47)$$

with

$$\begin{bmatrix} \mathbf{R}_{3,n+1}^{(k)} \\ \mathbf{R}_{4,n+1}^{(k)} \end{bmatrix} = \Xi_{n+1}^{(k)} \begin{bmatrix} \mathbf{R}_{\sigma,n+1}^{(k)} - \mathbf{R}_{1,n+1}^{(k)} \\ \mathbf{R}_{\alpha,n+1}^{(k)} + \gamma_{n+1}^{(k)} \mathbf{R}_{2,n+1}^{(k)} \end{bmatrix} \quad (6.48)$$

and

$$\Xi_{n+1}^{(k)} = \begin{bmatrix} \mathbb{C}^{-1} + \gamma_{n+1}^{(k)} \partial_{\sigma\sigma} g & \gamma_{n+1}^{(k)} \partial_{\sigma\alpha} g \\ -\gamma_{n+1}^{(k)} \partial_r \tilde{\mathbf{s}} : \partial_{\sigma\sigma} g & \mathbb{I} - \gamma_{n+1}^{(k)} \partial_r \tilde{\mathbf{s}} : \partial_{\sigma\alpha} g \end{bmatrix}^{-1}. \quad (6.49)$$

Using (6.47) to reduce the 6th row of (6.27) yields

$$\underbrace{\begin{bmatrix} \partial_{\sigma} f & \partial_{\alpha} f \end{bmatrix} \Xi_{n+1}^{(k)} \bullet \begin{bmatrix} -\mathbf{r}_{n+1}^{(k)} \\ \mathbf{s}_{n+1}^{(k)} \end{bmatrix}}_{A_{\gamma}^{(k)}} \Delta\gamma_{n+1}^{(k)} = \underbrace{\begin{bmatrix} \partial_{\sigma} f & \partial_{\alpha} f \end{bmatrix} \begin{bmatrix} \mathbf{R}_{3,n+1}^{(k)} \\ \mathbf{R}_{4,n+1}^{(k)} \end{bmatrix}}_{R_{5,n+1}^{(k)}} - R_{f,n+1}^{(k)}, \quad (6.50)$$

which can be solved for $\Delta\gamma_{n+1}^{(k)}$ as

$$\Delta\gamma_{n+1}^{(k)} = \frac{R_{5,n+1}^{(k)}}{A_{\gamma}^{(k)}}. \quad (6.51)$$

Back substituting $\Delta\gamma_{n+1}^{(k)}$ according to (6.51) into (6.47) yields $\Delta\boldsymbol{\sigma}_{n+1}^{(k)}$ and $\Delta\boldsymbol{\alpha}_{n+1}^{(k)}$. Substituting $\{\Delta\boldsymbol{\sigma}_{n+1}^{(k)} \ \Delta\boldsymbol{\alpha}_{n+1}^{(k)}\}^T$ into (6.41) and (6.44) yields $\Delta\mathbf{r}_{n+1}^{(k)}$ and $\Delta\mathbf{s}_{n+1}^{(k)}$, respectively. Using the obtained results for $\Delta\gamma_{n+1}^{(k)}$ and $\{\Delta\boldsymbol{\sigma}_{n+1}^{(k)} \ \Delta\boldsymbol{\alpha}_{n+1}^{(k)}\}^T$ in (6.42) yields $\Delta\boldsymbol{\epsilon}_{n+1}^{p(k)}$. Thus all components of $\Delta\mathbf{q}_{n+1}^{(k)}$ are known.

The new and better approximation $\mathbf{q}_{n+1}^{(k+1)}$ for \mathbf{q}_{n+1} is obtained from (6.28) as

$$\mathbf{q}_{n+1}^{(k+1)} = \mathbf{q}_{n+1}^{(k)} + \begin{Bmatrix} \Delta\boldsymbol{\sigma}_{n+1}^{(k)} \\ \Delta\boldsymbol{\epsilon}_{n+1}^{p(k)} \\ \Delta\mathbf{r}_{n+1}^{(k)} \\ \Delta\boldsymbol{\alpha}_{n+1}^{(k)} \\ \Delta\mathbf{s}_{n+1}^{(k)} \\ \Delta\gamma_{n+1}^{(k)} \end{Bmatrix}. \quad (6.52)$$

The residuum $\mathbf{R}_{n+1}^{(k+1)} = \mathbf{R}_{n+1}(\mathbf{q}_{n+1}^{(k+1)})$ follows from (6.24). The vector \mathbf{R}_{n+1} is computed at every step throughout the iteration. This procedure is repeated until convergence criterion (6.30) is satisfied.

The return mapping algorithm can be viewed as back-projection of the trial state onto the yield surface, as illustrated in Figure 6.2. For the special case of associative plasticity, the return map represents the closest point projection for the \mathbb{C} -metric. The described procedure is part of the plastic corrector step in the two-step additive split of the elastic-plastic problem.

Figure 6.3 shows a corner projection in stress space. The figure illustrates a corner space defined by the base vectors $\mathbb{C} : \mathbf{r}_{i,n+1}$ of three state surfaces. The consistency parameters $\gamma_{i,n+1}$ are the coordinates in this system.

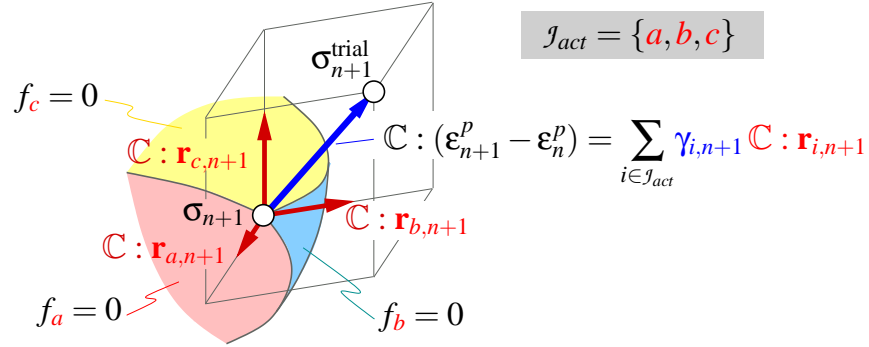


Figure 6.3: Combined projection of the trial stress onto active surfaces

Hardening and softening laws are formulated such that no coupling between various models occurs. This leads to decoupled integration equations and to the fact that it is impossible for more than three surfaces to be active. Time integration of the hardening-softening laws for each surface $i \in \mathcal{J}_{act}$ leads to

$$\boldsymbol{\alpha}_{i,n+1} = \boldsymbol{\alpha}_{i,n} + \gamma_{i,n+1} \mathbf{s}_{i,n+1}. \quad (6.55)$$

To make the implementation easier one can also combine all parameters $\boldsymbol{\alpha}_{i,n+1}$, $i = 1, 2, 3, 4$, into one large vector $\boldsymbol{\alpha}_{n+1}$ containing all hardening-softening variables. The softening ratios \mathbf{s}_i have to be written in vectors \mathbf{s}_i^* as

$$\mathbf{s}_{i,n+1}^* = \begin{Bmatrix} \vdots \\ \mathbf{s}_{i,n+1} \\ \vdots \end{Bmatrix} \quad (6.56)$$

Use of vectors $\mathbf{s}_{i,n+1}^*$ enables the description of the interactions between different softening modes. The i -th component of $\mathbf{s}_{i,n+1}^*$ is the softening ratio for the i -th state surface and the other components describe the coupling of the hardening and softening behavior with other surfaces. If the i -th component of $\mathbf{s}_{i,n+1}^*$ is the only non-zero entry no coupling effect is taken into account. If the j -th component, $j \neq i$, is non-zero, it describes the effect of the j -th mode on the i -th one.

The general form of (6.55) thus follows as

$$\boldsymbol{\alpha}_{n+1} = \boldsymbol{\alpha}_n + \sum_{i \in \mathcal{J}_{act}} \gamma_{i,n+1} \mathbf{s}_{i,n+1}^*. \quad (6.57)$$

This way there is only one vector containing l state variables, where $l = m_{act} + 1$ in case the radial tension surface is active and $l = m_{act}$ if that surface is inactive.

The approach with residuum equations used for single-surface plasticity can also be used for the non-linear initial value problem of multi-surface plasticity. The generalized

Newton-Raphson method (6.27) will also be used for multi-surface plasticity. The number of unknowns and the definition of the tangent operator $D_q \mathbf{R}_{n+1}$ will be adjusted for this purpose.

A single active surface in a multi-surface model yields to the same unknowns as a single-surface model. These six unknowns are the stress tensor $\boldsymbol{\sigma}$, the plastic strain $\boldsymbol{\varepsilon}^p$, a plastic flow direction \mathbf{r}_i , a softening parameter $\boldsymbol{\alpha}_i$, a softening ratio \mathbf{s}_i^* , and a consistency parameter γ_i . With every additional active surface four unknowns $(\mathbf{r}_i, \boldsymbol{\alpha}_i, \mathbf{s}_i^*, \gamma_i)$ are added to the system of equations.

The softening parameters $\boldsymbol{\alpha}_i$ are combined to a single vector $\boldsymbol{\alpha}$ according to (6.57) thus leading to one vectorial equation. For each active surface an equation for \mathbf{r}_i , \mathbf{s}_i^* , and γ_i is added in (6.27). Hence a vector of unknowns can be written

$$\mathbf{q}_{n+1} = \{\boldsymbol{\sigma}_{n+1} \ \boldsymbol{\varepsilon}_{n+1}^p \ \{\mathbf{r}_{i,n+1}\} \ \boldsymbol{\alpha}_{n+1} \ \{\mathbf{s}_{i,n+1}^*\} \ \{\gamma_{i,n+1}\}\}^T \quad (6.58)$$

with

$$\{\square_{i,n+1}\} = \left\{ \begin{array}{c} \square_{a,n+1} \\ \square_{b,n+1} \\ \vdots \end{array} \right\} \quad \mathcal{J}_{act} = \{a, b, \dots\}, \quad (6.59)$$

where \square stands for either \mathbf{r} , \mathbf{s}^* , or γ . The residuums equivalent to ones used in Section 6.2 follow for multi-surface plasticity as

$$\mathbf{R}_{\varepsilon,n+1} = \boldsymbol{\varepsilon}_{n+1}^p - \boldsymbol{\varepsilon}_n^p - \sum_{i \in \mathcal{J}_{act}} \gamma_{i,n+1} \mathbf{r}_{i,n+1} = \mathbf{0}, \quad (6.60)$$

$$\mathbf{R}_{r,i,n+1} = \mathbf{r}_{n+1} - \partial_{\sigma} g_i = \mathbf{0}, \quad (6.61)$$

$$\mathbf{R}_{\alpha,n+1} = \boldsymbol{\alpha}_{n+1} - \boldsymbol{\alpha}_n - \sum_{i \in \mathcal{J}_{act}} \gamma_{i,n+1} \mathbf{s}_{i,n+1}^* = \mathbf{0}, \quad (6.62)$$

$$\mathbf{R}_{s,i,n+1} = \mathbf{s}_{i,n+1}^* - \sum_{j \in \mathcal{J}_{act}} \tilde{\mathbf{s}}_i(\mathbf{r}_{j,n+1}) = \mathbf{0} \quad \forall \ i \in \mathcal{J}_{act}, \quad (6.63)$$

and

$$R_{f,i,n+1} = f_{i,n+1} = 0. \quad (6.64)$$

The residuum $\mathbf{R}_{\sigma,n+1}$ (6.18) of the return mapping algorithm for a single surface is also valid for multiple surfaces.

The differential of (6.63) follows as

$$d\mathbf{R}_{s,i} = d\mathbf{s}_{i,n+1}^* - \sum_{j \in \mathcal{J}_{act}} \frac{\partial \tilde{\mathbf{s}}_{i,n+1}}{\partial \mathbf{r}_{j,n+1}} d\mathbf{r}_{j,n+1} \quad \forall \ i \in \mathcal{J}_{act}. \quad (6.65)$$

If the softening modes of the state surfaces are uncoupled, several $\partial_{r_j} \tilde{\mathbf{s}}_i|_{n=1}$ become zero. For decoupled Harding/softening, equation (6.65) reduces to

$$d\mathbf{R}_{s,i} = d\mathbf{s}_{i,n+1}^* - \frac{\partial \tilde{\mathbf{s}}_{i,n+1}}{\partial \mathbf{r}_{i,n+1}} d\mathbf{r}_{i,n+1} \quad (6.66)$$

The summations in (6.60) and (6.62) can be rewritten using (6.59) as

$$\sum_{j \in \mathcal{J}_{act}} \square_{j,n+1} \Delta_{j,n+1} = \left\{ \begin{matrix} \square_{a,n+1} & \square_{b,n+1} & \dots \end{matrix} \right\} \bullet \left\{ \begin{matrix} \Delta_{a,n+1} \\ \Delta_{b,n+1} \\ \vdots \end{matrix} \right\} = \{\square_{j,n+1}\}^T \bullet \{\Delta_{j,n+1}\}, \quad (6.67)$$

where \square and Δ stands for the respective term in the sum.

The multi-surface equivalence to (6.27) is obtained from (6.18), (6.60), (6.61), (6.62), (6.66), and (6.64) as

$$\left\{ \begin{matrix} \mathbf{R}_\sigma \\ \mathbf{R}_\varepsilon \\ \{\mathbf{R}_{r,i}\} \\ \mathbf{R}_\alpha \\ \{\mathbf{R}_{s,i}\} \\ \{R_{f,i}\} \end{matrix} \right\} + \left[\begin{matrix} \mathbb{C}^{-1} & \mathbb{I} & \mathbf{0} & \mathbf{0} & \mathbf{0} & \mathbf{0} \\ \mathbf{0} & \mathbb{I} & -\{\mathbb{I}_{\gamma_i}\}^T & \mathbf{0} & \mathbf{0} & -\{\mathbf{r}_{i,n+1}\}^T \\ -\{\partial_{\sigma\sigma} g_i\} & \mathbf{0} & \mathbb{I} & -\{\partial_{\sigma\alpha} g_i\} & \mathbf{0} & \mathbf{0} \\ \mathbf{0} & \mathbf{0} & \mathbf{0} & \mathbb{I}_{ll} & \{\mathbb{I}_{ll,\gamma_i}\}^T & -\{\mathbf{s}_{i,n+1}^*\}^T \\ \mathbf{0} & \mathbf{0} & -\{\partial_{r_i} \tilde{\mathbf{s}}_i\} & \mathbf{0} & \mathbb{I}_{ll} & \mathbf{0} \\ \{\partial_\sigma f_i\} & \mathbf{0} & \mathbf{0} & \{\partial_\alpha f_i\} & \mathbf{0} & \mathbf{0} \end{matrix} \right] \bullet \left\{ \begin{matrix} \Delta\sigma \\ \Delta\varepsilon^p \\ \{\Delta\mathbf{r}_i\} \\ \Delta\alpha \\ \{\Delta\mathbf{s}_i^*\} \\ \{\Delta\gamma_i\} \end{matrix} \right\} = \mathbf{0}, \quad (6.68)$$

with

$$\mathbb{I}_{\gamma_i} = \gamma_{i,n+1} \mathbb{I}, \quad \mathbb{I}_{ll,\gamma_i} = \gamma_{i,n+1} \mathbb{I}_{ll}, \quad \text{and} \quad \{\mathbb{I}_{ll}\} = \begin{bmatrix} 1 & 0 & \dots \\ 0 & 1 & \dots \\ \vdots & \vdots & \ddots \end{bmatrix}_{l \times l}. \quad (6.69)$$

The index $n+1$ in (6.68) is suppressed.

This nonlinear system of equations will be solved in a similar way as described in Section 6.2 with a partitioned solution scheme for multiple state surfaces. The obtained solution scheme is given in Table 6.1. The index (k) that indicates the current approximation of the $(n+1)$ -values is suppressed in Table 6.1 Using the definition of \mathbf{q}_{n+1} (6.58) and (6.28) a new approximation $\mathbf{q}_{n+1}^{(k+1)}$ can be computed with $\Delta\mathbf{q}$ as

$$\mathbf{q}_{n+1}^{(k+1)} := \left\{ \begin{matrix} \sigma_{n+1}^{(k+1)} \\ \varepsilon_{n+1}^{p(k+1)} \\ \{\mathbf{r}_{i,n+1}^{(k+1)}\} \\ \alpha_{n+1}^{(k+1)} \\ \{\mathbf{s}_{i,n+1}^{*(k+1)}\} \\ \{\gamma_{i,n+1}^{(k+1)}\} \end{matrix} \right\} = \left\{ \begin{matrix} \sigma_{n+1}^{(k)} \\ \varepsilon_{n+1}^{p(k)} \\ \{\mathbf{r}_{i,n+1}^{(k)}\} \\ \alpha_{n+1}^{(k)} \\ \{\mathbf{s}_{i,n+1}^{*(k)}\} \\ \{\gamma_{i,n+1}^{(k)}\} \end{matrix} \right\} + \left\{ \begin{matrix} \Delta\sigma_{n+1}^{(k)} \\ \Delta\varepsilon_{n+1}^{p(k)} \\ \{\Delta\mathbf{r}_{i,n+1}^{(k)}\} \\ \Delta\alpha_{n+1}^{(k)} \\ \{\Delta\mathbf{s}_{i,n+1}^{*(k)}\} \\ \{\Delta\gamma_{i,n+1}^{(k)}\} \end{matrix} \right\}. \quad (6.70)$$

The components of $\Delta\mathbf{q}$ are given by equations (viii)-(xii) in Table 6.1.

With this approximation the updated values of the yield function and its derivatives for each surface can be obtained and the next approximation step given in Table 6.1 follows until (6.30) is satisfied.

The computation scheme of Table 6.1 can be compared to (6.29). Hence Table 6.1 is equivalent to $-(D_q \mathbf{R}_{n+1})^{-1}$ and a given residuum \mathbf{R}_{n+1} .

To maintain an overview of each tensor, vector and variable, Table 6.2 lists all variables with their dimensions used in the computation. For tensors the matrix and vector representations are given.

Table 6.1: Partitioned solution scheme for stress projection

- Residuum

$$\mathbf{R}_{n+1} = \begin{Bmatrix} \mathbf{R}_{\sigma,n+1} \\ \mathbf{R}_{\varepsilon,n+1} \\ \{\mathbf{R}_{r,i,n+1}\} \\ \mathbf{R}_{\alpha,n+1} \\ \{\mathbf{R}_{s,i,n+1}\} \\ \{R_{f,i,n+1}\} \end{Bmatrix} = \begin{Bmatrix} \mathbb{C}^{-1} : \boldsymbol{\sigma}_{n+1} - \boldsymbol{\varepsilon}_{n+1} + \boldsymbol{\varepsilon}_{n+1}^p \\ \boldsymbol{\varepsilon}_{n+1}^p - \boldsymbol{\varepsilon}_n^p - \sum_{i \in \mathcal{J}_{act}} \gamma_{i,n+1} \mathbf{r}_{i,n+1} \\ \{\mathbf{r}_{i,n+1}\} - \{\partial_{\sigma} g_i\} \\ \boldsymbol{\alpha}_{n+1} - \boldsymbol{\alpha}_n - \sum_{i \in \mathcal{J}_{act}} \gamma_{i,n+1} \mathbf{s}_{i,n+1}^* \\ \{\mathbf{s}_{i,n+1}^*\} - \{\tilde{\mathbf{s}}_i(\mathbf{r}_{i,n+1})\} \\ \{f_{i,n+1}\} \end{Bmatrix} \quad (\text{i})$$

- Ξ -matrix by inversion

$$\Xi_{n+1} = \begin{bmatrix} \mathbb{C}^{-1} + \sum_{i \in \mathcal{J}_{act}} \gamma_{i,n+1} \partial_{\sigma\sigma} g_i & \sum_{i \in \mathcal{J}_{act}} \gamma_{i,n+1} \partial_{\sigma\alpha} g_i \\ - \sum_{i \in \mathcal{J}_{act}} \gamma_{i,n+1} \partial_{r_i} \mathbf{s}_i \partial_{\sigma\sigma} g_i & \mathbb{I} - \sum_{i \in \mathcal{J}_{act}} \gamma_{i,n+1} \partial_{r_i} \tilde{\mathbf{s}}_i \partial_{\sigma\alpha} g_i \end{bmatrix}^{-1} \quad (\text{ii})$$

- Left- and right-hand sides

$$\mathbf{R}_{1,n+1} = \sum_{i \in \mathcal{J}_{act}} \gamma_{i,n+1} \mathbf{R}_{r,i,n+1} + \mathbf{R}_{\varepsilon,n+1} \quad (\text{iii})$$

$$\mathbf{R}_{2,i,n+1} = \partial_{r_i} \tilde{\mathbf{s}}_i \mathbf{R}_{r,i,n+1} + \mathbf{R}_{s,i,n+1} \quad \forall \quad i \in \mathcal{J}_{act} \quad (\text{iv})$$

$$\begin{bmatrix} \mathbf{R}_{3,n+1} \\ \mathbf{R}_{4,n+1} \end{bmatrix} = \Xi_{n+1} \begin{bmatrix} \mathbf{R}_{\sigma,n+1} - \mathbf{R}_{1,n+1} \\ \mathbf{R}_{\alpha,n+1} + \sum_{i \in \mathcal{J}_{act}} \gamma_{i,n+1} \mathbf{R}_{2,i,n+1} \end{bmatrix} \quad (\text{v})$$

$$\{R_{5,i,n+1}\} = \begin{bmatrix} \{\partial_{\sigma} f_i\} & \{\partial_{\alpha} f_i\} \end{bmatrix} \begin{bmatrix} \mathbf{R}_{3,n+1} \\ \mathbf{R}_{4,n+1} \end{bmatrix} - \{R_{f,i,n+1}\} \quad (\text{vi})$$

$$\{A_{\gamma,ij}\} = \begin{bmatrix} \{\partial_{\sigma} f_i\} & \{\partial_{\alpha} f_i\} \end{bmatrix} \Xi_{n+1} \begin{bmatrix} -\{\mathbf{r}_{j,n+1}\}^T \\ \{\mathbf{s}_{j,n+1}^*\}^T \end{bmatrix} \quad (\text{vii})$$

- Solve i -equations to compute $\{\Delta\gamma_j\}$ for each active surface $j \in \mathcal{J}_{act}$

$$\{A_{\gamma,ij}\} \{\Delta\gamma_{j,n+1}\} = \{R_{5,i,n+1}\} \quad (\text{viii})$$

- Compute correction factor for each component of $\Delta\mathbf{q}$

$$\begin{bmatrix} \Delta\boldsymbol{\sigma}_{n+1} \\ \Delta\boldsymbol{\alpha}_{n+1} \end{bmatrix} = \Xi_{n+1} \sum_{i \in \mathcal{J}_{act}} \begin{bmatrix} -\{\mathbf{r}_{i,n+1}\}^T \\ \{\mathbf{s}_{i,n+1}^*\}^T \end{bmatrix} \Delta\gamma_{i,n+1} - \begin{bmatrix} \mathbf{R}_{3,n+1} \\ \mathbf{R}_{4,n+1} \end{bmatrix} \quad (\text{ix})$$

$$\{\Delta\mathbf{r}_{i,n+1}\} = \begin{bmatrix} \{\partial_{\sigma\sigma} g_i\} & \{\partial_{\sigma\alpha} g_i\} \end{bmatrix} \begin{bmatrix} \Delta\boldsymbol{\sigma}_{n+1} \\ \Delta\boldsymbol{\alpha}_{n+1} \end{bmatrix} - \{\mathbf{R}_{r,i,n+1}\} \quad (\text{x})$$

$$\Delta\mathbf{s}_{i,n+1}^* = \partial_{r_i} \tilde{\mathbf{s}}_i \Delta\mathbf{r}_{i,n+1} - \mathbf{R}_{s,i,n+1} \quad \forall \quad i \in \mathcal{J}_{act} \quad (\text{xi})$$

$$\Delta\boldsymbol{\varepsilon}_{n+1}^p = -\mathbb{C}^{-1} : \Delta\boldsymbol{\sigma}_{n+1} - \Delta\mathbf{R}_{\sigma,n+1} \quad (\text{xii})$$

Table 6.2: Dimension of variables and derivations

variable	one surface	RT surface	several surfaces
f_i	1×1	1×1	$m_{act} \times 1$
$\partial f_{i,\sigma}$	1×3	1×3	$m_{act} \times 3$
$\partial f_{i,\alpha}$	1×1	1×2	$m_{act} \times l$
$\partial g_{i,\sigma}$	1×3	1×3	$m_{act} \times 3$
$\partial g_{i,\sigma\sigma}$	3×3	3×3	$(3 \times 3) \times m_{act}$
$\partial g_{i,\sigma\alpha}$	3×1	3×2	$(3 \times l) \times m_{act}$
\mathbf{s}_i	1×1	2×1	$(l \times 1) \times m_{act}$
$\partial \mathbf{s}_{i,ri}$	1×3	2×3	$(l \times 3) \times m_{act}$
$\boldsymbol{\alpha}$	1×1	2×1	$(l \times 1) \times m_{act}$
γ	1×1	1×1	$m_{act} \times 1$

$i \in \mathcal{J}_{act}, \quad l = m_{act} + 1 \quad \text{if} \quad \text{RT} \in \mathcal{J}_{act} \quad \text{else} \quad l = m_{act}$

6.4 Corner-projection in multi-surface plasticity

The return mapping algorithm for trial states close to the intersection of yield surfaces, i.e. close to edges or corners, may result in a wrong projection. Two cases may occur, where an apparently correct projection leads to a wrong result. In Figure 6.4 the wrong projection and the correction with a new projection are pictorially indicated for both cases.

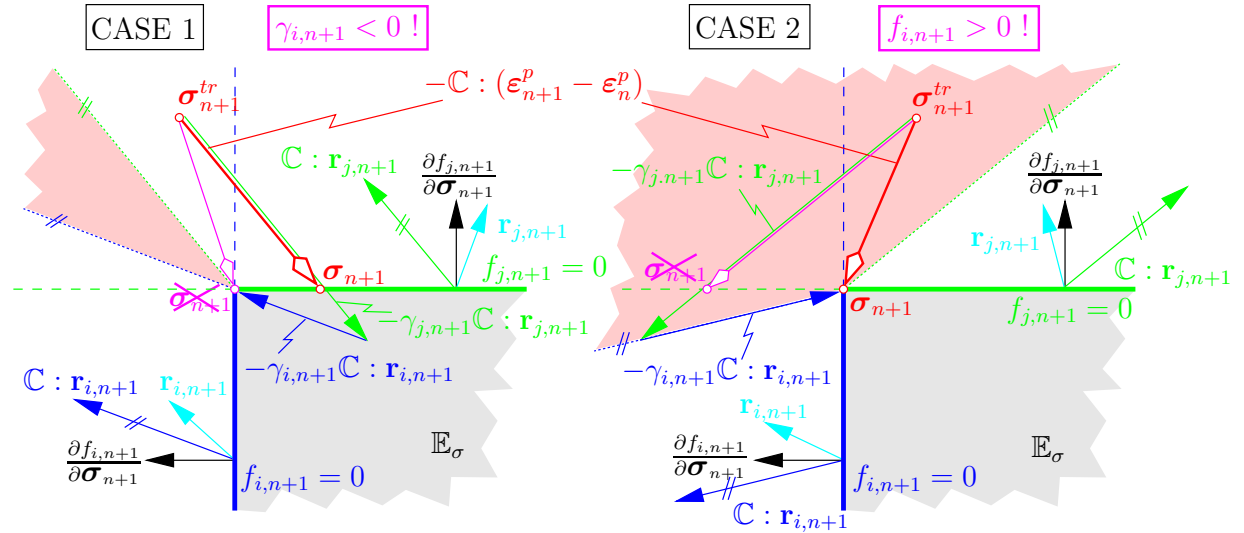


Figure 6.4: Geometric illustration of both cases in the corner projection of the return mapping algorithm.

Case 1

The first case is indicated by a state with $f_{i,n+1}^{tr} > 0$ and $f_{j,n+1}^{tr} > 0$, where $\mathcal{J}_{act} = \{i, j\}$. This leads to a projection of the stress point onto the intersection of the surfaces $f_{i,n+1}$ and

$f_{j,n+1}$, as both are active. During this projection a consistency parameter with $\gamma_{i,n+1} < 0$ occurs in equation (6.54). This is equivalent to a projection vector, that does not point toward the yield surfaces, if using the trial point as a reference. Because $\gamma_{i,n+1} < 0$ violates of the Kuhn-Tucker conditions (4.112) the projection is invalid, even though the projected solution σ_{n+1} satisfies the yield-conditions $f_{\alpha,n+1} = 0$.

Repeating this projection and setting the surface that led to the violation of the loading and unloading condition with $\gamma_{i,n+1} < 0$ inactive, i.e. $f_{i,n+1} = 0$, leads to a correct projection on the other surface f_j .

Case 2

In Case 2 only one yield surface is active $f_{j,n+1} > 0$ ($\mathcal{J}_{act} = \{j\}$) and also its consistency parameter $\gamma_{j,n+1} > 0$ does not violate the Kuhn-Tucker conditions. Nevertheless the converged projection result σ_{n+1} violates the yield-condition $f_{i,n+1} < 0$. This means the stress point is located in the non-admissible set and not, as required, on the border of the admissible set $\partial\mathbb{E}_\sigma$ (4.107). This means, that a yield surface f_j , which was not active before the projection is now active.

Setting the yield surface, which violated the yield condition after convergence, active with $f_{j,n+1} > 0$ for a new projection leads to the correct solution.

Algorithm for corner-projection

The general solution of this problem is an algorithm, that first computes a projection as predetermined by

$$\mathcal{J}_{act} = \{f_{i,n+1}^{tr} \geq 0\}. \quad (6.71)$$

After checking

$$\gamma_{i,n+1} > 0 \quad \text{and} \quad f_{i,n+1} < 0 \quad \forall \quad i \in \mathcal{J}_{act} \quad (6.72)$$

it computes a new projection if (6.72) was violated. For the second projection a new set of active yield surfaces according to

$$\mathcal{J}_{act}^{new} = \{i \in \mathcal{J}_{act} | \gamma_{i,n+1} \geq 0\} \cup \{j \notin \mathcal{J}_{act} | f_{j,n+1} > 0\} \quad (6.73)$$

is used. This algorithm needs to verify every projection, also if only one surface was active in the first projection.

6.5 Algorithmic tangent

With the back projection of a stress point, the state for a given time increment is known. In order to be able to compute the next displacement field of the structure a finite element program also needs the stiffness at this time-step. This stiffness at a time t_{n+1} is called the consistent algorithmic elasto-plastic tangent \mathbb{C}_{n+1}^{ep} . The elasto-plastic tangent has to be consistent with the integration algorithm (projection) in order to achieve quadratic convergence. Use of the continuum tangent \mathbb{C}^{ep} or an error in the matrix representation of tensors would not yield to quadratic convergence to a solution. The integration algorithm itself only assures a stable solution.

The consistent algorithmic elasto-plastic tangent is defined as the tensor operator that connects an finite small change in total strain $\boldsymbol{\varepsilon}_{n+1}$ with a finite small change in the projected stress $\boldsymbol{\sigma}_{n+1}$, i.e.

$$d\boldsymbol{\sigma}_{n+1} = \mathbb{C}_{n+1}^{ep} : d\boldsymbol{\varepsilon}_{n+1}. \quad (6.74)$$

Also the partitioned solution schemes in Sections 6.2 and 6.3 connect the total strain with the stress. Thus the closed solution of (6.27), i.e. the inversion of $D_q \mathbf{R}_{n+1}$ can be used to compute \mathbb{C}_{n+1}^{ep} .

At a converged solution for the projection the residuum $\mathbf{R}_{n+1} = \mathbf{0}$, hence also its differential $d\mathbf{R}_{n+1} = \mathbf{0}$. Setting $d\mathbf{R}_{n+1} = \mathbf{0}$ in (6.32) yields

$$d\mathbf{q}_{n+1} = -(D_q \mathbf{R}_{n+1})^{-1} \bullet D_\varepsilon \mathbf{R}_{n+1} : d\boldsymbol{\varepsilon}_{n+1} \quad (6.75)$$

with

$$D_\varepsilon \mathbf{R}_{n+1} = \{-\mathbb{I}, \mathbf{0}, \mathbf{0}, \mathbf{0}, \mathbf{0}, \mathbf{0}\}^T. \quad (6.76)$$

(6.76) is evident from the differential of (6.18)

$$d\mathbf{R}_\sigma = -d\boldsymbol{\varepsilon}_{n+1}, \quad (6.77)$$

as all other differentials of (6.19) to (6.23) are zero. Taking into account that the first entry of $d\mathbf{q}_{n+1}$ is $d\boldsymbol{\sigma}_{n+1}$ and comparing (6.75) with (6.74) makes clear that the first entry of $(D_q \mathbf{R}_{n+1})^{-1}$ is equal to the consistent tangent operator. Thus, a formula for the elasto-plastic stiffness at a given time increment can be written as

$$\mathbb{C}_{n+1}^{ep} = \{\mathbb{I} \mathbf{0} \mathbf{0} \mathbf{0} \mathbf{0} \mathbf{0}\} \bullet (D_q \mathbf{R}_{n+1})^{-1} \bullet \{\mathbb{I} \mathbf{0} \mathbf{0} \mathbf{0} \mathbf{0} \mathbf{0}\}^T. \quad (6.78)$$

As mentioned in Section 6.3 the algorithm described in Table 6.1 is exactly equal to the negative inverse of the first-order tangent operator. Thus one can introduce an analogy by comparing (6.29) with (6.75) that

- replaces the incremental correction Δ for each iteration (k) with an finite differential step d ,
- introduces a new residuum $\mathbf{R}_{n+1} = \{-d\boldsymbol{\varepsilon}_{n+1} \mathbf{0} \mathbf{0} \mathbf{0} \mathbf{0} \mathbf{0}\}^T$ and
- a new vector of unknowns $\mathbf{q}_{n+1} = \{d\boldsymbol{\sigma}_{n+1} \mathbf{0} \mathbf{0} \mathbf{0} \mathbf{0} \mathbf{0}\}^T$.

This analogy simply states that if one inputs a small change of $\boldsymbol{\varepsilon}^p$ into the newton algorithm and computes the change in $\boldsymbol{\sigma}$ the necessary computation steps must be equal to \mathbb{C}_{n+1}^{ep} . Applying this analogy to Table 6.1 leads to a closed formula for the consistent tangent operator for multiple state surfaces. Table 6.3 shows the computation of the consistent elasto-plastic tangent operator from this analogy.

Leaving out the summation and suppressing the subscripts i and j in the definition of \mathbb{F}_{n+1} leads to the tangent operator for a single surface. The matrix $\{A_{\gamma,ij}\}^{-1}$ degenerates to $1/A_{\gamma,n+1}$.

To ensure, that at the first plastic step the elasto-plastic tangent and not the elastic tangent is used, the yield condition should be checked with a negative tolerance value. This leads to a faster convergence.

Table 6.3: Computation of the consistent elasto-plastic tangent operator

- From the analogy (other components of \mathbf{R}_{n+1} and $\Delta \mathbf{q}_{n+1}$ are zero)

$$\mathbf{R}_{\sigma,n+1} = -d\boldsymbol{\varepsilon}_{n+1} \quad \text{and} \quad \Delta \boldsymbol{\sigma}_{n+1} = d\boldsymbol{\sigma}_{n+1} \quad (\text{i})$$

- Thus, from (i) in Table 6.1 yield the new right-hand sides

$$\mathbf{R}_{1,n+1} = \mathbf{0} \quad \{\mathbf{R}_{2,i,n+1}\} = \mathbf{0} \quad (\text{ii})$$

$$\begin{bmatrix} \mathbf{R}_{3,n+1} \\ \mathbf{R}_{4,n+1} \end{bmatrix} = \Xi_{n+1} \begin{bmatrix} -d\boldsymbol{\varepsilon}_{n+1} \\ \mathbf{0} \end{bmatrix} \quad (\text{iii})$$

$$\{R_{5,i,n+1}\} = \begin{bmatrix} \{\partial_\sigma f_i\} & \{\partial_\alpha f_i\} \end{bmatrix} \Xi_{n+1} \begin{bmatrix} -d\boldsymbol{\varepsilon}_{n+1} \\ \mathbf{0} \end{bmatrix} \quad (\text{iv})$$

- $d\gamma_j$ follows by multiplying (viii) in Table 6.1 with an inverse matrix $\{A_{\gamma,ji}\}^{-1}$ to

$$\{A_{\gamma,ki}\}^{-1} \{A_{\gamma,ij}\} \{d\gamma_{j,n+1}\} = \{\delta_{kj}\} \{d\gamma_{j,n+1}\} = \{A_{\gamma,ki}\}^{-1} \{R_{5,i,n+1}\} \quad (\text{v})$$

$$\{d\gamma_k\} = \{A_{\gamma,ki}\}^{-1} \{R_{5,i,n+1}\} \quad \text{with} \quad \{A_{\gamma,ik}\}^{-1} \{A_{\gamma,kj}\} = \{\delta_{ij}\} \quad (\text{vi})$$

- To compute $d\boldsymbol{\sigma}_{n+1}$ one may introduce a transformation matrix \mathbb{P} such that

$$d\boldsymbol{\sigma}_{n+1} = \mathbb{P} \begin{bmatrix} d\boldsymbol{\sigma}_{n+1} \\ d\boldsymbol{\alpha}_{n+1} \end{bmatrix} \quad \text{with} \quad \mathbb{P} = [\mathbb{I} \quad \mathbf{0}] \quad (\text{vii})$$

- Using (ix) from Table 6.1 with (iv) and (vi) yields

$$d\boldsymbol{\sigma}_{n+1} = \mathbb{P} : \Xi_{n+1} \begin{bmatrix} -\{\mathbf{r}_{i,n+1}\} \\ \{\mathbf{s}_{i,n+1}^*\} \end{bmatrix} \{A_{\gamma,ij}\}^{-1} \{R_{5,j,n+1}\} - \mathbb{P} : \Xi_{n+1} \begin{bmatrix} -d\boldsymbol{\varepsilon}_{n+1} \\ \mathbf{0} \end{bmatrix} \quad (\text{viii})$$

- Inserting (iv) into (viii) and prescind $d\boldsymbol{\varepsilon}_{n+1}$ leads to (subscript $n+1$ suppressed)

$$d\boldsymbol{\sigma} = \left(-\mathbb{P} : \Xi \begin{bmatrix} -\{\mathbf{r}_i\} \\ \{\mathbf{s}_i^*\} \end{bmatrix} \{A_{\gamma,ij}\}^{-1} \begin{bmatrix} \{\partial_\sigma f_i\} & \{\partial_\alpha f_i\} \end{bmatrix} \Xi : \mathbb{P}^T + \mathbb{P} : \Xi : \mathbb{P}^T \right) d\boldsymbol{\varepsilon} \quad (\text{ix})$$

- By definition (see (6.74)) the term in parentheses is the consistent tangent

$$\mathbb{C}_{n+1}^{ep} = \mathbb{P} : \Xi_{n+1} : \mathbb{P}^T - \mathbb{P} : \Xi_{n+1} \bullet \mathbb{F}_{n+1} \bullet \Xi_{n+1} : \mathbb{P}^T \quad \text{with} \quad (\text{x})$$

$$\mathbb{F}_{n+1} = \sum_{i \in \mathcal{I}_{act}} \sum_{j \in \mathcal{I}_{act}} \begin{bmatrix} -\mathbf{r}_{i,n+1} A_{\gamma,ij}^{-1} \partial_\sigma f_j & -\mathbf{r}_{i,n+1} A_{\gamma,ij}^{-1} \partial_\alpha f_j \\ \mathbf{s}_{i,n+1}^* A_{\gamma,ij}^{-1} \partial_\sigma f_j & \mathbf{s}_{i,n+1}^* A_{\gamma,ij}^{-1} \partial_\alpha f_j \end{bmatrix} \quad (\text{xi})$$

6.6 Approximation of the algorithmic tangent

An approximation for \mathbb{C}_{n+1}^{ep} can be computed in a much easier way and may be avail to check the results of the obtained formula for the elasto-plastic tangent.

The algorithmic tangent operator is defined by the gradient in a point of the plastic range of the stress-strain relationship. This definition can be used to write

$$\mathbb{C}_{n+1}^{ep} = \frac{d\boldsymbol{\sigma}_{n+1}}{d\boldsymbol{\varepsilon}_{n+1}} = \left[\frac{d\boldsymbol{\sigma}_{n+1}}{d\varepsilon_{LL,n+1}} \quad \frac{d\boldsymbol{\sigma}_{n+1}}{d\varepsilon_{RR,n+1}} \quad \frac{d\boldsymbol{\sigma}_{n+1}}{d\varepsilon_{LR,n+1}} \right], \quad (6.79)$$

i.e. a small change λ in $\boldsymbol{\varepsilon}_{n+1}$ when computing $\boldsymbol{\sigma}_{n+1}$ as described in 6.2 and 6.3 leads to the tangent operator.

The definition of the derivation

$$\frac{d\boldsymbol{\sigma}_{n+1}}{dx} = \lim_{\lambda \rightarrow 0} \frac{\boldsymbol{\sigma}_{n+1}(x + \lambda) - \boldsymbol{\sigma}_{n+1}(x)}{\lambda} \quad (6.80)$$

can be used to compute the i -th column of $\mathbb{C}_{n+1,approx}^{ep}$, from an incremental change λ of each component i of $\boldsymbol{\varepsilon}_{n+1}$. This incremental change leads to a small stress difference. Taking the limit of this increment toward zero leads to an infinitely small stress difference, thus

$$\mathbb{C}_{n+1,approx}^{ep} : \mathbf{M}_i = \lim_{\lambda \rightarrow 0} \frac{\boldsymbol{\sigma}_{n+1}(\boldsymbol{\varepsilon}_{n+1} + \lambda \mathbf{M}_i) - \boldsymbol{\sigma}_{n+1}(\boldsymbol{\varepsilon}_{n+1})}{\lambda} \quad i \in 1, 2, 3 \quad (6.81)$$

with

$$\mathbf{M}_1 = \mathbf{M}_L, \quad \mathbf{M}_2 = \mathbf{M}_R, \quad \text{and} \quad \mathbf{M}_3 = \mathbf{N}, \quad (6.82)$$

results in the i -th column of (6.79).

6.7 Residuum

The residuum given in Table 6.1 equation (i) is used to determine if the return mapping algorithm has reached the solution values, i.e. $\mathbf{R}_{n+1} = 0$. The different components of \mathbf{R}_{n+1} have different units. It may therefore be the case, that one component has a much higher influence, because its order of magnitude is higher. To prevent this, all components need to be dimensionless.

The last component $R_{f,n+1}$ is the only dimensionless value, due to the construction of the state surfaces given in Chapter 5. $\mathbf{R}_{\sigma,n+1}$, $\mathbf{R}_{\varepsilon,n+1}$ and $\mathbf{R}_{\alpha,n+1}$ are strain-like components with a dimension of stress over stiffness. The components $\mathbf{R}_{r,n+1}$ and $\mathbf{R}_{s,n+1}$ have a dimension of one over stress.

The dimensionless condition to determine, if the end of the return mapping algorithm is reached, reads

$$\|\mathbf{R}\| = \frac{E}{\beta^0} (\|\mathbf{R}_{\sigma}\| + \|\mathbf{R}_{\varepsilon}\| + \|\mathbf{R}_{\alpha}\|) + \beta^0 (\|\mathbf{R}_r\| + \|\mathbf{R}_s\|) + |R_f| = 0. \quad (6.83)$$

In the numerical implementation, (6.83) needs to be satisfied only in accordance with the numerical possibilities of the computer. The tolerance factor should be close to the possible accuracy of the machine.

The convergence check should be made with a relative tolerance for $\|\mathbf{R}_{n+1}\|/\|\mathbf{R}_{n+1}\|^{(0)}$, where $\|\mathbf{R}_{n+1}\|^{(0)}$ is the value at the start of the iteration. And also with an absolute tolerance, which is smaller than the relative one, for $\|\mathbf{R}_{n+1}\|$. The second inquiry with the absolute tolerance prevents a high or infinite number of iterations, when $\|\mathbf{R}_{n+1}\|^{(0)}$ is already very close to the computer accuracy.

6.8 Interdependency of return mapping algorithm and FE-computation

The numerical solution of a plane stress problem in orthotropic multi-surface plasticity requires two major computational components.

The first component deals with the material modeling itself and was elucidated in this chapter. The return mapping algorithm, which is standard for isotropic materials, was specified for multi-surface plasticity. A special framework to handle the orthotropic properties of wood was used to formulate the material model and its algorithmic implementation. This framework was given in Chapter 4.

The second component is the numerical computation of the actual problem. The solution for the deformation and stress states of a solid body, in general, requires numerical methods. Only in a few relatively easy problems a analytical solution exist. The numerical method used in this work is the finite-element method. *Finite* indicates, that the body is divided into elements with finite dimensions. Moreover, also the loading history is subdivided into finite time increments. Literature on the topic of finite element analysis is broad. A short introduction can be found in [34], whereas the books [2, 48] give a detailed discussion on the finite element method.

There are two possibilities for the computation of the local stresses and stiffness, which provide core information needed for any finite element analysis.

One can either use the strains $\boldsymbol{\varepsilon}^{12}$, given by the finite element program, and compute the stresses $\boldsymbol{\sigma}^{12}$ and stiffness \mathbb{C}^{12} with the return mapping algorithm in the coordinate system defined by \mathbf{e}_1 and \mathbf{e}_2 of the FE-program. In this case the algorithm needs to be programmed with the general structural tensors, which carry the information of the orientation of the grain direction, defined by the grain angle φ .

An other way is the compute the local solution of the return mapping algorithm in the material coordinates defined by \mathbf{A}_L and \mathbf{A}_R and transformed it back into the coordinate system of the finite element computation. In this case the formulation of the return mapping algorithm can be specified for the case that the material coordinate system is equal to the observer coordinate system, i.e. $\mathbf{A}_L = \mathbf{e}_1$ and $\mathbf{A}_R = \mathbf{e}_2$.

The strains from the FE-analysis need to be transformed into local material coordinates with

$$\boldsymbol{\varepsilon}^{LR} = \mathbf{T}\boldsymbol{\varepsilon}^{12}. \quad (6.84)$$

After convergence of the solution in the return mapping algorithm the stresses and stiffness must be transformed back into the coordinate system of the finite element program according to

$$\boldsymbol{\sigma}^{12} = \mathbf{T}^T \boldsymbol{\sigma}^{LR} \quad \text{and} \quad \mathbb{C}^{12} = \mathbf{T}^T \mathbb{C}^{LR} \mathbf{T}. \quad (6.85)$$

The transformation matrix \mathbf{T} is only depending on the grain angle φ and is given to

$$\mathbf{T} = \begin{bmatrix} \cos^2 \varphi & \sin^2 \varphi & \sin \varphi \cos \varphi \\ \sin^2 \varphi & \cos^2 \varphi & -\sin \varphi \cos \varphi \\ -2 \sin \varphi \cos \varphi & 2 \sin \varphi \cos \varphi & \cos^2 \varphi - \sin^2 \varphi \end{bmatrix}. \quad (6.86)$$

Stabilizing numerical algorithms for unstable cracks

The material model was implemented in a finite element program written for MATLAB. To control the different state surfaces, several examples were analyzed. For a standard implementation, examples that activated the softening behavior of a surface did not show quadratic convergence or any convergence at all. Moreover, some results did show stress states at levels much higher than any allowed state.

This behavior was found to originate from two different levels of the computational implementation: the local effect of the softening model, and the global structural level, both of which have to be considered separately. The model parameter characteristic length ℓ_c , which is connected to the description of cracks in this material model, is the main parameter influencing numerical problems due to softening behavior resulting from crack development.

In this chapter, the theoretical background for this numerical problem will be developed. Possible solution algorithms are laid out and convergence studies will demonstrate their effect. The first two subsections deal with the influence of the softening model included in the plasticity model described in Chapter 5, whereas the last subsection describes the structural influence on the convergence behavior.

7.1 Description of the problem for one dimension

All softening functions given in Chapter 5 used to describe the post-failure behavior of spruce wood for the observed failure modes are of the type

$$\beta(\alpha) = \beta^0 \exp(-k\alpha). \quad (7.1)$$

All these functions are based on an exponential decrease of the initial strength β^0 with respect either to the crack opening w or the strain-like parameter

$$\alpha := \frac{w}{\ell_c}, \quad (7.2)$$

where ℓ_c is the characteristic length. Figure 7.1 shows the softening behavior for these two representations.

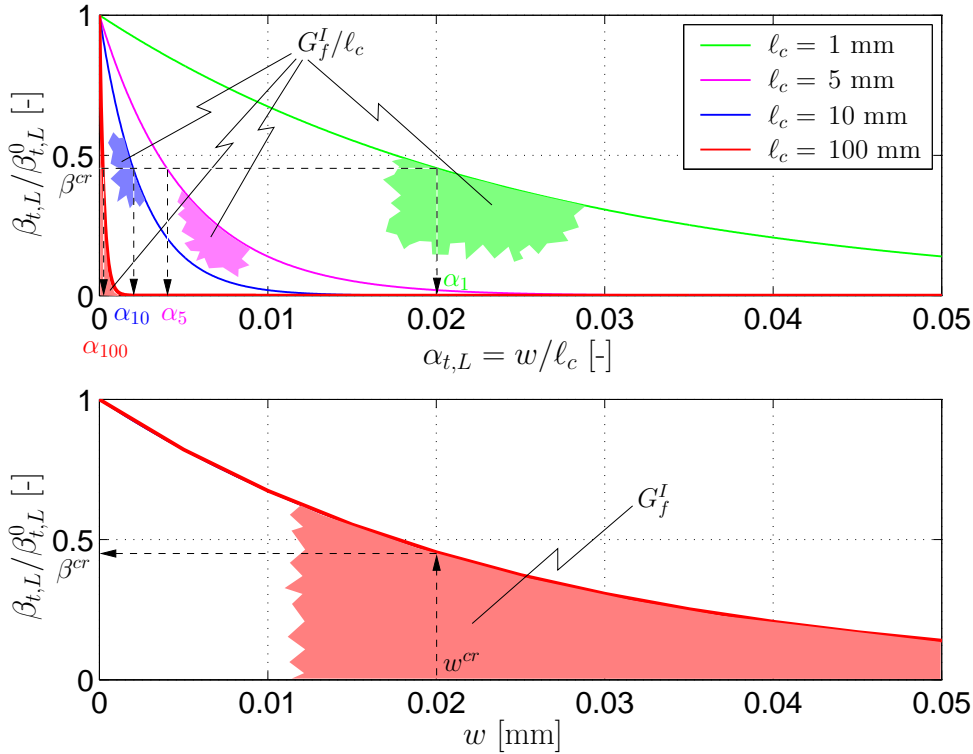


Figure 7.1: Strength softening model with respect to w and α .

Figure 7.1 and 7.3 show softening functions and stress-strain curves for the tensile strength in longitudinal direction, even though the validity of these graphs is general. The softening functions of the state surfaces only differ in the material parameters, which influence the position and curvature of the exponential function. For a given surface, the softening function is only influenced by ℓ_c .

To model a crack one has to find a way to deal with the numerical problems emanating from the discontinuity in the displacement field due to a crack. The characteristic length ℓ_c is the extension of a domain over which a crack opening w will be distributed as an equivalent strain ϵ^p in a smeared crack model. ℓ_c may be the length of a finite element perpendicular to the crack direction.

The interpretation of α is therefore depending on the chosen representative dimension of the finite element mesh. It can be interpreted as an equivalent crack strain. For a given crack opening w the corresponding value of α depends on the characteristic length and

therefore on the dimension of the used finite element mesh. Figure 7.2 shows the graphical interpretation of the relationship between the parameter α , the crack opening w and the average total strain ε for a representative volume at failure.

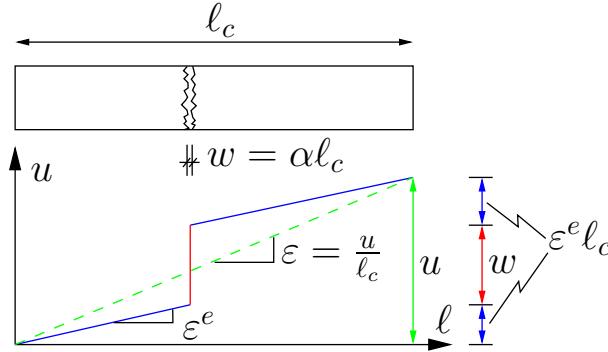


Figure 7.2: Representative volume (finite element) with crack opening.

The following derivations are shown only for one-dimensional problems in order to explicate problems that occur in the two-dimensional implementation of this softening model and to make them more comprehensible.

7.1.1 Determination of softening coefficient k

The softening coefficient k in (7.1) may be identified in terms of fracture mechanical properties. This will be outlined in this subsection. Using a one-dimensional yield-function

$$f(\sigma, \beta) = \sigma - \beta \leq 0 \quad (7.3)$$

and the before-mentioned general form of the softening function (7.1), one can compute the factor k in the exponent from energetic considerations.

Using a flow rule and a softening rule

$$\dot{\varepsilon}^p = \frac{\partial f}{\partial \sigma} \dot{\gamma} = \dot{\gamma} \quad \text{and} \quad \dot{\alpha} = |\dot{\varepsilon}^p| = \dot{\gamma}, \quad (7.4)$$

respectively, and the fact that at failure ($f = 0$) the stresses are equal to the strength of the material $\sigma = \beta(\alpha)$, the dissipation (4.80) can be written as

$$\mathcal{D} = \sigma \dot{\varepsilon}^p = \beta(\alpha) \dot{\gamma} = \beta(\alpha) \dot{\alpha}. \quad (7.5)$$

Dissipation is defined as the density of mechanical power converted into heat. Integration of the dissipation over the representative volume V of a continuum and over the process time t leads to the total dissipated energy \mathcal{E} during crack development as

$$\mathcal{E} = \int_V \int_0^\infty \mathcal{D} dt dV = \int_V \int_0^\infty \beta(\alpha) \dot{\alpha} dt dV = V \int_0^\infty \beta(\alpha) d\alpha. \quad (7.6)$$

For the last operation in (7.6) it is assumed that \mathcal{D} is constant in V . In fracture mechanics the energy release rate or fracture toughness G_f is introduced. It is a measure for the energy loss per area of a newly developed crack surface. Considering a fully developed crack through the element (see Fig. 7.2) with an area A , the dissipated energy follows as

$$\mathcal{E} = \int_A \int_0^\infty \sigma_n dw dA = AG_f \quad (7.7)$$

The work done by the plastic deformations in a continuum must be equivalent to the work done by a crack as described in fracture mechanics. \mathcal{E} for the continuum concept (equ. (7.6)) and \mathcal{E} for the fracture mechanics concept (equ. (7.7)) describes the same physical process and thus must be identical. This leads to

$$V \int_0^\infty \beta(\alpha) d\alpha = AG_f \quad \Rightarrow \quad \int_0^\infty \beta(\alpha) d\alpha = \frac{G_f}{V/A} = \frac{G_f}{\ell_c} \quad (7.8)$$

with characteristic length $\ell_c := V/A$. From equation (7.8) it is obvious that the area under the softening function in the upper graph in Figure 7.1 equals G_f/ℓ_c (or to G_f in the lower graph).

Using the definition of the softening function (7.1) in the second equation of (7.8) and performing the integration leads to a closed expression for the coefficient k as

$$\frac{G_f}{\ell_c} = \frac{1}{k} \int_0^\infty \beta^0 \exp(-k\alpha) d(k\alpha) \quad \Rightarrow \quad k = \frac{\beta^0 \ell_c}{G_f}. \quad (7.9)$$

The coefficient k determines how strong the softening effect is at the element level. A larger k leads to a stronger (faster) degeneration of strength as the crack opens. Therefore, a higher value for the ratio β^0/G_f and larger characteristic length ℓ_c , e.g. a coarser finite element mesh have the same impact on the softening behavior.

The influence of k in the behavior of the material model is illustrated in Figure 7.3 in a stress-strain diagram. Each graph is a representation of $f(\sigma) = 0$, i.e. for an active yield surface. The area left to this function indicates $f < 0$, the area to the right indicates $f > 0$. The latter therefore does not allow any stress points. After stress reaches the ultimate strength the strength decreases at an exponential rate. This is illustrated by Figure 7.3.

For sufficiently small values of k there is only one unique solution. For high values of k the solution becomes non-unique. In a numerical simulation, the first plastic iteration step found by the return mapping algorithm may be positioned on the wrong branch of the exponential function.

A non-unique stress-strain relationship occurs as k exceeds a critical value k_{crit} . As β^0/G_f is constant for a specific material, a critical characteristic length $\ell_{c,crit}$ corresponds with k_{crit} . For a given strain ε there exist up to three solutions for the stress σ . This leads to numerical problems as the solution is not unique in this regime. The typical observation related to this phenomenon is an alternation of the iterative procedure between two or three

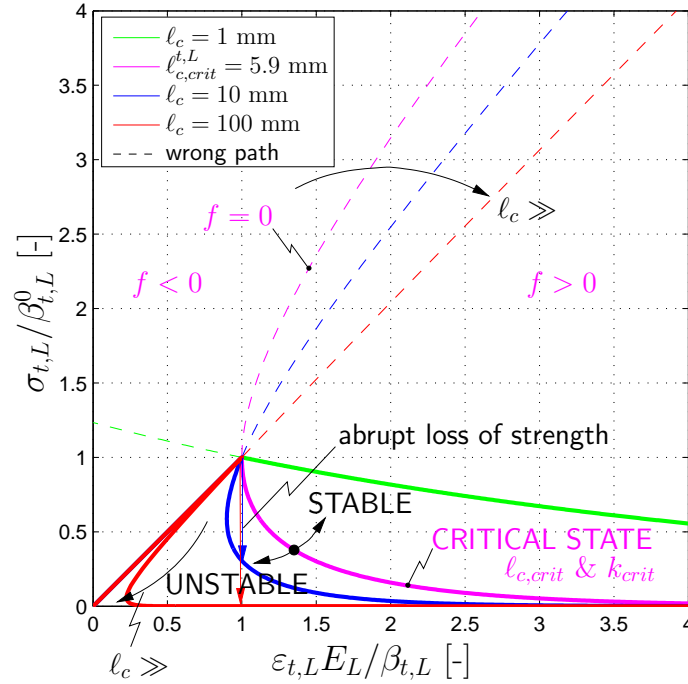


Figure 7.3: Stress-strain curve for different values of ℓ_c and therefore of k .

of the possible solutions. Section 7.2 describes two algorithms to eliminate this numerical problem.

As ℓ_c increases the range between different solutions grows larger until reaching the limit state of $\ell_c = \infty$, where only the elastic part of the curve in Figure 7.3 and the strain-axis remain (they define the asymptotes as $\ell_c \rightarrow \infty$).

The curve for $\ell_{c,crit}$ marks the limit state for the transition from stable to unstable crack propagation. States with $\ell_c > \ell_{c,crit}$ display an abrupt and immediate drop of strength at the first inelastic (plastic) step, whereas states with $\ell_c < \ell_{c,crit}$ show a continuous transition from elastic loading to plastic softening. The latter case allows a stable crack propagation, where cracks open slowly until they are fully developed. An unstable crack propagation leads to sudden opening of a crack and related drop of strength (see Fig. 7.3).

A characteristic length of zero would mean no strain softening behavior at all. This, however, is a limit which cannot be reached by a continuum based formulation. The corresponding stress-strain curve for $\ell_c = 0$ would be equal to an elastic-ideally plastic material behavior.

7.1.2 Critical characteristic length

Figure 7.4 shows the softening behavior according to (7.1) and the appertaining stress-strain relationship for an $\ell_c > \ell_{c,crit}$. To understand the connection between the two functions, the derivation of the stiffness is given in this subsection. Integration of these functions over α and ε , respectively, results in G_f/ℓ_c in both cases. This result shows that

the areas under both functions are identical. The gradient of the softening function in any

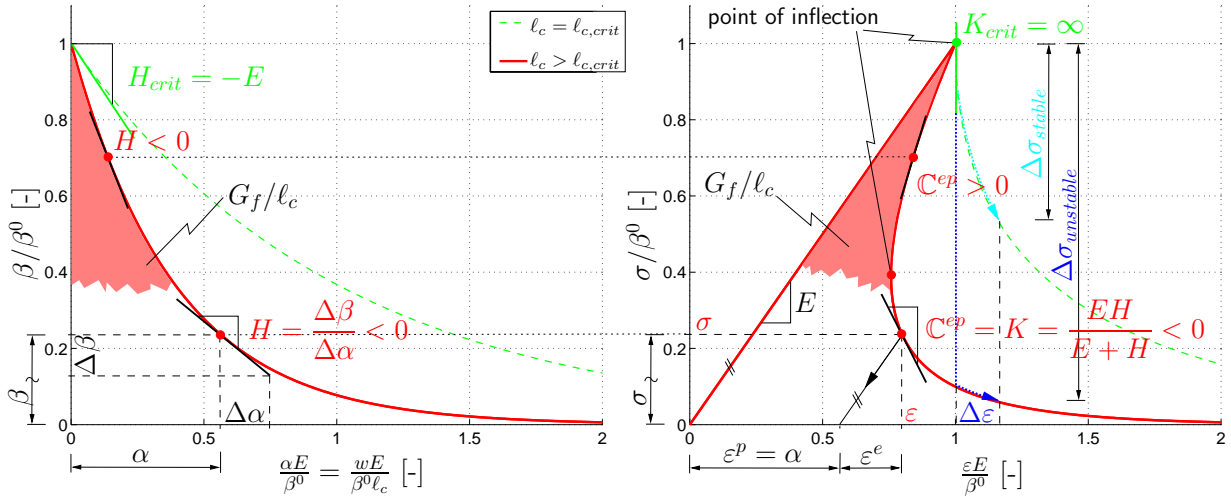


Figure 7.4: Softening function and corresponding stress-strain curve.

point α is smaller than zero and defines the hardening modulus to

$$H = \frac{\partial \beta(\alpha)}{\partial \alpha} = -k\beta^0 \exp(-k\alpha) = -k\beta(\alpha) \leq 0. \quad (7.10)$$

The softening modulus H can be written in terms of a incremental change in $\Delta w = \ell_c \Delta \alpha$ and a resulting incremental change or in differential values as

$$H = \lim_{\Delta w \rightarrow 0} \frac{\Delta \sigma}{\Delta w / \ell_c} = \frac{d\sigma}{dw / \ell_c}. \quad (7.11)$$

The elastic stiffness E (or \mathbb{C}) in the elastic regime changes to the elasto-plastic stiffness K (or \mathbb{C}^{ep}) after crack initiation. In the case of the non-unique solution domain, i.e. $\ell_c > \ell_{c,crit}$, \mathbb{C}^{ep} can be greater than zero and even reach infinity. The latter case occurs when exactly two solutions for σ are possible, which is the point of inflection on the stress-strain curve. Exactly *one* solution at the point of inflection indicates the critical state.

Looking at an element with length ℓ_c , the total strain

$$\varepsilon = \varepsilon^e + \varepsilon^p = \frac{u}{\ell_c} \quad (7.12)$$

or the strain differential

$$d\varepsilon = d\varepsilon^e + d\varepsilon^p = \frac{du}{\ell_c} \quad (7.13)$$

can be computed, where u is the displacement as shown in Figure 7.2 and du its differential change.

For $\varepsilon^p = 0$ and therefore $f < 0$, the elastic strain follows from Hooke's Law to

$$d\varepsilon^e = \frac{d\sigma}{E}. \quad (7.14)$$

From the definition (7.2) of the strain-like parameter α and from (7.4) one can write

$$d\varepsilon^p = \frac{dw}{\ell_c} \quad (7.15)$$

for the differential of plastic strain. Substituting (7.14) and (7.15) into equation (7.12) yield the differential strain under consideration of (7.11) as

$$d\varepsilon = \frac{du}{\ell_c} = \frac{d\sigma}{E} + \frac{dw}{\ell_c} = \left(\frac{1}{E} + \frac{1}{H} \right) d\sigma = \frac{E+H}{EH} d\sigma. \quad (7.16)$$

Writing equation (7.16) in the form of stiffness times deformation equals stress one obtains a formula for the one-dimensional elasto-plastic stiffness

$$d\sigma = \frac{EH}{E+H} d\varepsilon = \mathbb{C}^{ep} d\varepsilon \quad \forall \quad \varepsilon > \frac{\beta^0}{E}. \quad (7.17)$$

The critical value for ℓ_c is reached when the point of inflection of the stress-strain curve in Figure 7.4 complies with the last elastic point. At the point of inflection of the plastic regime the elasto-plastic stiffness reaches the limit value of infinity. It is evident from (7.17) that a hardening modulus equal to the negative Young's modulus yields to an infinite elasto-plastic stiffness.

The last state in the elastic regime and, for $\ell_c = \ell_{c,crit}$, the point of inflection are characterized by $\alpha = 0$. From (7.10) one can compute the hardening modulus for $\alpha = 0$ to

$$H(\alpha = 0) = -k\beta^0 < 0. \quad (7.18)$$

This negative ($k > 0, \beta^0 > 0$) “hardening modulus” is due to its sign a “softening modulus”. The critical characteristic length $\ell_{c,crit}$ is found from (7.18) and

$$H + E = 0 \quad \Rightarrow \quad k\beta^0 = E. \quad (7.19)$$

Using (7.9) and solving for ℓ_c leads to the critical characteristic length

$$\ell_{c,crit} = \frac{EG_f}{(\beta^0)^2}. \quad (7.20)$$

The effect of $\ell_c = \ell_{c,crit}$ is shown in Figure 7.4. The first inelastic strain increment $\Delta\varepsilon$ can result either in a stable crack propagation with $\Delta\sigma_{stable}$ or in an unstable one with $\Delta\sigma_{unstable}$, depending on the value of ℓ_c . $\Delta\sigma_{stable}$ and $\Delta\sigma_{unstable}$ are indicated in Fig. 7.4. The proper solution for α right after crack initiation is either $\alpha = 0$ in the case of a stable crack or $\alpha \gg 0$ for unstable crack propagation.

If the elastic energy stored in the element is bigger than the energy necessary to fully developed a crack, the crack opens abruptly. A small variation of strength in the material leads to immediate loss of strength. The resulting stress strain curve does not show a continuous softening behavior, but rather an abrupt loss of strength. A continuous softening curve can neither be achieved with stress-driven nor with strain-driven tests, due to two or three possible analytical solutions. Further loading leads to growth of the crack opening, as most strength was lost at crack initiation. A softening function with relatively high values for $\ell_{c,crit}$ triggers this behavior. Wood shows such a behavior in fiber and radial tension direction as described in Chapter 3.4.

7.1.3 Maximum softening

A fully developed crack and therefore the maximum possible softening state is important for algorithms that eliminate the numerical problems described in this section. Theoretically, a fully developed crack can never occur due to the exponential softening function. When 97 % of G_f are released, the error made by assuming a full crack, is considered acceptable small.

Before crack initialization, the deformation state in an element is characterized by

$$\Delta\varepsilon = \Delta\varepsilon^e = \frac{\Delta u}{\ell_c} \quad \text{and} \quad \Delta\varepsilon^p = \frac{\Delta w}{\ell_c} = 0. \quad (7.21)$$

An incremental displacement Δu leads to an increase in the total strain $\varepsilon_{n+1} = \varepsilon_n + \Delta\varepsilon$ with

$$\Delta\varepsilon = \Delta\varepsilon^e + \Delta\varepsilon^p = \frac{\Delta\sigma}{E} + \frac{\Delta w}{\ell_c} = \frac{\Delta u}{\ell_c}. \quad (7.22)$$

From (7.22) the increment of crack opening can be computed to

$$\Delta w = \Delta u - \Delta\varepsilon^e \ell_c. \quad (7.23)$$

At the fully developed crack the reversed elastic deformation adds to the total incremental strain $\Delta\varepsilon$, because the elastic unloading of the two separated parts of the element of length ℓ_c is no longer restricted. The crack opening for maximum softening therefore reads

$$\Delta w = \Delta u + \varepsilon_n^e \ell_c \quad \text{or} \quad \Delta\varepsilon^p = \Delta\varepsilon + \varepsilon_n^e, \quad (7.24)$$

with $\varepsilon_n^e = \mathbb{C}^{-1}\sigma_{n+1}$. With $\varepsilon_{n+1} = \varepsilon_n + \Delta\varepsilon$ and $\sigma_{n+1} = \mathbb{C}(\varepsilon_n - \varepsilon_n^p)$, (7.24) can be written as

$$\Delta\varepsilon^p = \varepsilon_{n+1} - \varepsilon_n + \mathbb{C}^{-1}\sigma_{n+1} = \varepsilon_{n+1} - \varepsilon_n + \mathbb{C}^{-1}\mathbb{C}(\varepsilon_n - \varepsilon_n^p) = \varepsilon_{n+1} - \varepsilon_n^p. \quad (7.25)$$

If the element is loaded after the crack is fully opened, an increase in displacement causes equal increase of the crack opening, i.e.

$$\Delta u = \Delta w. \quad (7.26)$$

7.2 Solution and implementation for biaxial stress states

7.2.1 Altering the start values of the return map algorithm

The critical point for numerical algorithms is to solve the non-linear problem of finding the correct solution for state variables α_{n+1} and ε_{n+1}^p even for high values of ℓ_c and the resulting abrupt loss of strength.

There are several possibilities to deal with the numerical difficulties in the projection algorithm:

- Using a quadratic newton algorithm to solve the equation $f_{n+1} = 0$ to determine a better start value for γ_{n+1} .

- Using an explicit Euler algorithm for the first iteration step to get a start value for γ_{n+1} closer to the true solution.
- Using the limit state of maximum softening, i.e. fully separated crack surfaces, to determine an upper limit for γ_{n+1} .

The key for all solutions is to find a better start value for the projection algorithm (return mapping algorithm). The standard start value for the consistency parameter, $\gamma_{n+1}^{(0)}$, is zero, i.e. the trial state. The trial state leads to a residuum vector $\mathbf{R}_{n+1}^{(0)}$ with only one non-zero entry, i.e. the yield function $f_{n+1}^{(0)}$. Modifying $\gamma_{n+1}^{(0)}$ means changing the state variable $\alpha_{n+1}^{(0)}$. With $\gamma_{n+1}^{(0)} > 0$ the values for $\mathbf{R}_\varepsilon^{(0)}$ according (6.19) and $\mathbf{R}_\alpha^{(0)}$ according (6.21) are no longer zero. The start value $\sigma_{n+1}^{(0)}$ is no longer the trial state. Therefore also $\mathbf{R}_\sigma^{(0)}$ according (6.18) is non-zero. $\mathbf{R}_r^{(0)}$ according (6.20) and $\mathbf{R}_s^{(0)}$ according (6.22) are dependent on the state variable α_{n+1} and thus change their values in dependency of the active failure surface.

The additional computational effort should be as small as possible, as this algorithm needs to be run for every gauss point in every iteration step of every time step. The least computational effort and also the easiest solution to implement is the last given above.

The limit state of maximum softening, as described in Section 7.1, can be written as

$$\Delta \varepsilon_{max}^p = \varepsilon_{n+1} - \varepsilon_n^p = \frac{\Delta w_{max}}{\ell_c}. \quad (7.27)$$

From this maximal possible plastic strain increment the start values for each failure surface can be computed. These values are closer to the solution and they are positioned on the correct softening path. In some cases of small ℓ_c , these start values may not be as good as $\gamma_{n+1}^{(0)} = 0$, but the algorithm still converges to the correct solution at a quadratic rate.

To determine, which characteristic length for each respective state surface is within the numerical stable range, the critical characteristic lengths are given in Table 7.1. These values are only valid if no more than one surface is active. For $\ell_{c,crit}$ of the fiber compression surface, $(\beta^0)^2$ in the denominator of equation (7.20) must be substituted by $Y_1 Y_0$. The other $\ell_{c,crit}$ follow from (7.20) and the material parameters from Table 5.1.

Table 7.1: Critical characteristic length for each state surfaces

Surface	$\ell_{c,crit}$ [mm]
Fiber tension	5.858
Fiber compression	1503.006
Radial tension - mode I	12.296
Radial tension - mode II	3.310
Radial compression	∞

For the fiber tension and the radial tension surfaces an algorithm is required to be able to use practical dimensions of ℓ_c . From Table 7.1, Figures 5.1, 5.10, and 5.11 it is obvious that values of $\ell_c > 5$ mm are not possible when solving without an additional

measure to eliminate stability problems as described in Section 7.1. Values for ℓ_c in the order of magnitude of a few millimeters would require a very fine finite element mesh when modeling bigger structures. Such fine meshes are hard to create and require huge computational resources.

The fiber compression surface does not show high sensitivity to ℓ_c , as the post-failure behavior in Figure 5.4 and the high critical characteristic length (see Table 7.1) showed. ℓ_c in the range of few decimeters is beyond limit state. Nevertheless, to eliminate any problem with ℓ_c the following algorithm will also be implemented for this surface.

The state surface for the radial compression mechanism does not contain softening behavior. The post-failure behavior (Figure 5.6) does not show any dependency of ℓ_c . Therefore the start values are not being altered for this surface.

7.2.2 Algorithm for fiber tension and compression

The algorithm for fiber tension and compression is given without the indices t and c , because it is valid for both.

The maximum increment $\Delta\alpha$ of the state variable $\alpha_{L,n+1}$ and the start value for $\alpha_{L,n+1}^{(0)}$ follows from (7.27) to

$$\Delta\alpha_{L,max}^{(0)} = \gamma_{n+1}^{(0)} s_{L,n+1}^{(0)} = \langle \pm \mathbf{M}_L \Delta \boldsymbol{\varepsilon}_{max}^p \rangle = |\Delta \varepsilon_{LL,max}^p| \quad (7.28)$$

and

$$\alpha_{n+1,max}^{(0)} = \alpha_n + \Delta\alpha_{L,max}^{(0)}. \quad (7.29)$$

The start value for $\boldsymbol{\sigma}_{n+1}$ changes from the trial stress tensor $\boldsymbol{\sigma}_{n+1}^{tr}$ because of $\gamma_{n+1}^{(0)} \neq 0$ to a new start value $\boldsymbol{\sigma}_{n+1}^{(0)}$ for the return mapping algorithm. From (6.5) in (6.7) and with consideration of the $\boldsymbol{\sigma}_{n+1}^{tr}$ ((6.15)) this start value follows to

$$\boldsymbol{\sigma}_{n+1}^{(0)} = \mathbb{C} : (\boldsymbol{\varepsilon}_{n+1} - \boldsymbol{\varepsilon}_n^p - \Delta \boldsymbol{\varepsilon}_{max}^p) = \boldsymbol{\sigma}_{n+1}^{tr} - \mathbb{C} : \Delta \boldsymbol{\varepsilon}_{max}^p. \quad (7.30)$$

With the altered start values $\boldsymbol{\sigma}_{n+1}^{(0)}$ and $\alpha_{L,n+1}^{(0)} = \alpha_{L,max}^{(0)}$, new values for $\mathbf{r}_{L,n+1}^{(0)}$ and $s_{L,n+1}^{(0)}$ can be computed from the according state surface, i.e. from the equations (5.30) and (5.35) or (5.47) and (5.54), respectively.

The new start value for the consistency parameter follows from (7.28), as $s_{L,n+1}^{(0)}$ is now known, to

$$\gamma_{n+1}^{(0)} = \frac{\Delta\alpha_{L,max}^{(0)}}{s_{L,n+1}^{(0)}}, \quad (7.31)$$

where $s_{L,n+1}^{(0)} > 0$, since the direction of the plastic flow $\mathbf{r}_{n+1}^{(0)}$ always points away from the surface and thus its components are positive.

(7.27) also defines the start value for the plastic strain as

$$\boldsymbol{\varepsilon}_{n+1}^{p(0)} = \boldsymbol{\varepsilon}_n^p + \Delta \boldsymbol{\varepsilon}_{max}^p = \boldsymbol{\varepsilon}_{n+1}. \quad (7.32)$$

After changing the usual start values for the iterative projection needed for the return mapping algorithm the iteration for $\mathbf{R}_{n+1} = 0$ starts normally.

7.2.3 Algorithm for radial tension - stress space

The radial tension surface incorporates also the shear invariant of stress. The respective surface consists of a hyperbola, only one arm of which is physically valid, as discussed in Chapter 5. Besides finding better start values for the return mapping algorithm, it is essential that the projected stress point lays always on the correct arm of the hyperbola. To ensure this, the start point must always be as close as possible to the correct solution branch. Two different approaches have been implemented. In the first approach the trial stress point is projected, in the stress space, on the hyperbola in the maximal softened state of the increment. The geometry of the projection was chosen in the stress space in a way to achieve a best possible approximation of the actual projection.

The start value for the state variables α_{n+1} must be edited in the same way as in the fiber direction surfaces (fiber tension and fiber compression). The incremental state variable in radial tension can be computed from the maximum possible incremental plastic strain (7.27) to

$$\Delta\alpha_{t,R,max}^{(0)} = \gamma_{n+1}s_{t,R,n+1} = \langle \mathbf{M}_R \Delta\epsilon_{max}^p \rangle = |\Delta\epsilon_{RR,max}^p|. \quad (7.33)$$

Also the incremental state variable for shear follows from the same equation

$$\Delta\alpha_{S,max}^{(0)} = \gamma_{n+1}s_{S,n+1} = \sqrt{\Delta\epsilon_{max}^p : \mathbb{M} : \Delta\epsilon_{max}^p} = |\Delta\gamma_{S,max}^p|. \quad (7.34)$$

With (7.33) and (7.34) the start value for the state variable is

$$\alpha_{n+1,max}^{(0)} = \left\{ \begin{array}{c} \alpha_{n,t,R,max} \\ \alpha_{n,S,max} \end{array} \right\} + \left\{ \begin{array}{c} \Delta\alpha_{t,R,max}^{(0)} \\ \Delta\alpha_{S,max}^{(0)} \end{array} \right\} = \alpha_n + \Delta\alpha_{t,RS,max}^{(0)}. \quad (7.35)$$

Knowing $\alpha_{n+1,max}^{(0)}$, the model parameters $\beta_{t,R}^{(0)}$ and $a^{(0)}$, which define the position and curvature of the hyperbola in the stress space for the maximum softening within this load step, can be computed from (5.112) and (5.113). With the unchanged trial value for the stress tensor σ_{n+1}^{tr} an intersection point σ_{n+1}^* of a chosen projection line and the maximal softened hyperbola can be determined. The projection is performed in a plane parallel to the $\sigma_{LL} = 0$ plane, therefore only the values of σ_{RR} and τ_{LR} change in σ_{n+1}^{tr} .

To achieve a good approximation of the correct projection, the plastic flow direction should be approximated by the chosen projection to achieve σ_{n+1}^* . Two different possibilities are elucidated at the end of this section.

From (7.30) an equation for $\Delta\epsilon^p$ can be converted to

$$\Delta\epsilon_{max}^p = \mathbb{C}^{-1} : (\sigma_{n+1}^{tr} - \sigma_{n+1}^{(0)}) = \mathbb{C}^{-1} : \mathbf{d}, \quad (7.36)$$

where $\sigma_{n+1}^{(0)} = \sigma_{n+1}^*$ is the, by the projection, given point on the state surface and \mathbf{d} is the vector of this projection. The first entry in \mathbf{d} is zero, because the projection is parallel to the $\sigma_{LL} = 0$ plane.

(7.36) can be used with $\Delta\epsilon_{max}^p = \gamma_{n+1}\mathbf{r}_{n+1}$ and the assumption $\gamma_{n+1} = 1$, to compute a plastic flow

$$\mathbf{r}_{n+1}^{*,(0)} = \mathbb{C}^{-1} : \mathbf{d}, \quad (7.37)$$

This measure is necessary, because for small $\|\mathbf{d}\|$ the direction \mathbf{d} can not be computed accurate enough any more. The tolerance should be smaller than $a/2$ to ensure that also for a surface close to the maximal softened state, the stress point is closer to the physical relevant branch. Such a surface is characterized by a very small a .

The theoretical limit for a is zero, as this represents the residual state of this surface. To prevent numerical problems at the tip of the friction cone a limit for a slightly higher than zero was set in the algorithm. Therefore the tip is always rounded. This measurement does not influence the accuracy of this model.

The consistency parameter follows from the ratio of the plastic flow, resulting from the transformation of the vector \mathbf{d} , and the length of the plastic flow in the intersection point

$$\gamma_{n+1}^{(0)} = \frac{\mathbf{r}_{n+1}^{\star,(0)}}{\mathbf{r}_{n+1}^{(0)}} = \frac{\mathbf{r}_{n+1}^{\star,(0)}}{\partial g / \partial \boldsymbol{\sigma}_{n+1}^{\star}}, \quad (7.40)$$

to ensure a correct, with $\mathbf{r}_{n+1}^{(0)}$ concurrent, value.

The start values for the softening rule $\mathbf{s}_{n+1}^{(0)}$ follow from (5.136) with the computed plastic flow $\mathbf{r}_{n+1}^{(0)}$.

With the values for $\gamma_{n+1}^{(0)}$ and $\mathbf{r}_{n+1}^{(0)}$ the start value for the stress tensor results from

$$\boldsymbol{\sigma}_{n+1}^{(0)} = \boldsymbol{\sigma}_{n+1}^{tr} - \gamma_{n+1}^{(0)} \mathbb{C} : \mathbf{r}_{n+1}^{(0)} \quad (7.41)$$

and (7.32) is valid for the plastic strain.

The projection can be accomplished in many ways. Besides using the hyperbola itself as the projection aim, also a tangent to the hyperbola could be used. Leading to a slightly easier computation of the intersection of two straight lines. In this case it must be ensured, that the gradients of the surface and the tangent plane in the projection point are equal.

The formulation of the state surface for radial tension (5.77) can be easily transformed into a general equation of a hyperbola

$$\frac{x^2}{a^2} - \frac{y^2}{b^2} = 1 \quad (7.42)$$

with

$$x = \sigma_{RR} - \beta_{t,R} - a, \quad y = \tau_{LR} \quad \text{and} \quad b = a \tan(\phi). \quad (7.43)$$

Projection

The definition of a tangent plane to a function $f(\mathbf{x})$ in point $\tilde{\mathbf{x}}$ is

$$f(\tilde{\mathbf{x}}) + Df|_{\tilde{\mathbf{x}}} \Delta \mathbf{x} = 0 \quad (7.44)$$

The differential of (7.42) reads

$$df = \frac{\partial f}{\partial x} dx + \frac{\partial f}{\partial y} dy = -\frac{2\tilde{x}}{a^2} dx + \frac{2\tilde{y}}{b^2} dy = 0 \quad (7.45)$$

with

$$dx = \Delta x = x - \tilde{x} \quad \text{and} \quad dy = \Delta y = y - \tilde{y} \quad (7.46)$$

and with (7.42) evaluated at $\tilde{\mathbf{x}}$ the equation for the tangent plane follows to

$$-\frac{\tilde{x}}{a^2}x + \frac{\tilde{y}}{b^2}y + 1 = 0. \quad (7.47)$$

Using the tangent plane for the projection, i.e. as a new state surfaces for the first projection, does not give the optimal start value for the projection.

Using an intersection directly with the hyperbola leads to better results. Two different intersections with the hyperbola are being mentioned here. For the first possibility the projection is assumed normal to the asymptote for angles $\alpha > \phi$, where

$$\alpha = \tan^{-1} \frac{\tau_{LR}^{tr}}{\sigma_R^{tr} - \sigma_{\phi,R}} \quad (7.48)$$

is the angle of the line between the two stress points and the τ_{LR} -axis (see Fig. 7.5). For angles $\alpha < \phi$ the projection was directed to the point of curvature of the physical relevant branch of the hyperbola. Better results were achieved by changing the projection for stress points with $\sigma_{RR} > \sigma_{\phi,R}$ to a parallel line to the σ_{RR} -axis.

From the geometry of the hyperbola given in Figure 5.9, the R -component of the curvature point of the right arm of the hyperbola, follows to

$$\sigma_{\phi,R} = \beta_{t,R} - a \tan^2(\phi). \quad (7.49)$$

The L and LR -coordinates are equal to zero, so that $\boldsymbol{\sigma}_{\phi} = [0, \sigma_{\phi,R}, 0]^T$.

The equation of a line through the curvature point and an arbitrary point, i.e. the trail state, reads

$$y = (\sigma_R^{tr} - \sigma_{\phi,R}) \tan \alpha = kx + y_0 \quad (7.50)$$

with

$$k = \tan \alpha \quad \text{and} \quad y_0 = a \frac{\tan \alpha}{\cos^2 \phi}. \quad (7.51)$$

and $\sigma_R^{tr} = x + \beta_{t,R} + a$ as the R -component of $\boldsymbol{\sigma}_{n+1}^{tr}$.

Computing the intersection of this line with the hyperbola, by insertion of (7.50) in (7.42) leads to

$$\tilde{x}_{1,2} = \frac{-ky_0 \pm \tan \phi \sqrt{a^2(\tan^2 \phi - k^2) + y_0^2}}{k^2 - \tan^2 \phi}, \quad (7.52)$$

where the correct intersection point is the one with the higher x -coordinate. This solution is valid for angles $\alpha \leq \frac{\pi}{2} - \phi$. In special case of $\alpha = \phi$, the denominator of (7.52) vanishes and the quadratic equation reduces to a linear equation with

$$\tilde{x} = -\frac{y_0^2 + a^2 \tan^2 \phi}{2ky_0} = -\frac{a}{2 \cos^2 \phi} - \frac{a \cos^2 \phi}{2} \quad (7.53)$$

as the solution.

The line equation for $\alpha > \frac{\pi}{2} - \phi$, which describes a normal line on the asymptote, is equal to (7.50) with $\alpha = \frac{\pi}{2} - \phi$. The slop k and y_0 follow therefore to

$$k = \frac{1}{\tan \alpha} = \tan \left(\frac{\pi}{2} - \phi \right) \quad \text{and} \quad y_0 = a \frac{1}{\cos \phi \sin \phi}. \quad (7.54)$$

The x -coordinate of the intersection point for this case is

$$\tilde{x}_{1,2} = \frac{-a/\cos^2 \phi \pm a\sqrt{2}\tan^3 \phi/\cos \phi}{1 - \tan^4 \phi}. \quad (7.55)$$

The y -coordinate of the intersection \tilde{y} in all cases can be computed by back insertion in the equation of the straight line (7.50).

This projection does not give an accurate enough starting point for the return mapping algorithm and is therefore not used. The results implied a better approximation to the correct projection, which is controlled by the plastic flow direction. Hence the plastic flow direction was used to approximate the projection. For associative plasticity the plastic flow direction is perpendicular to the state surface. The non-associative flow rule used for the radial tension surface leads to a plastic flow $\tilde{\mathbf{r}}_{t,RS}$ normal to the surface for $\tau_{LR} = 0$. For negative values of σ_{RR} the plastic flow is parallel to the $\sigma_{RR} = 0$ plane. Between those values $\tilde{\mathbf{r}}_{t,RS}$ is shifted from one direction to the other according to the function κ according to (5.88). The plastic flow directions in a plane with $\sigma_{LL} = 0$ are shown in Figure 7.5.

The intersection of a line parallel to the τ_{LR} -axis is trivial, as the line is defined by a constant value of x . The y -coordinate of the intersection point follows from (7.42). The coordinates of the projection point for trial states with $\sigma_R^{tr} < \sigma_{\varrho,R}$ are therefore

$$\tilde{x} = \sigma_R^{tr} \quad \text{and} \quad \tilde{y} = b\sqrt{\left(\frac{\tilde{x}}{a}\right)^2 - 1} \operatorname{sign} \tau_{LR}^{tr}, \quad (7.56)$$

where the sign-function ensures the correct position of the projected stress point.

7.2.4 Algorithm for radial tension - strain space

The second approach, to ensure, that the starting point is close enough to the correct arm of the hyperbola, does not deal with a projection in the stress space. It rather formulates the intersection of the projection with the hyperbola in the strain space, leading to a quadratic equation for the consistency parameter γ_{n+1} . Problems with points, that are very close to the surface, do not occur with this solution.

The computation of the maximum state variable for a full crack $\boldsymbol{\alpha}_{n+1,max}^{(0)}$ according to (7.35) is equal to the previous approach.

The tensors \mathbf{a} and \mathbf{b} of the corresponding hyperbola follow from (5.81), (5.82) and (5.83) in dependency from $\boldsymbol{\alpha}_{n+1,max}^{(0)}$. Also the position of the curvature point $\boldsymbol{\sigma}_{\varrho}$ is dependent on the state variable and was given above in (7.49).

The vector of the projection, defined in the stress space, will be defined in the same way as explained above, according to the non-associative plastic flow direction. For stress points with $\sigma_{RR} > \sigma_{\varrho,R}$ the projection line is defined by the trial stress and the curvature point of the physical relevant branch of the hyperbola as

$$\bar{\mathbf{r}}_{n+1} = \mathbb{P} : \boldsymbol{\sigma}_{n+1}^{tr} - \boldsymbol{\sigma}_{\varrho} \quad \text{with} \quad \mathbb{P} = \begin{bmatrix} 0 & 0 & 0 \\ 0 & 1 & 0 \\ 0 & 0 & 1 \end{bmatrix}. \quad (7.57)$$

The projection is parallel to the $\sigma_{LL} = 0$ plane, as can be seen from the assembly of \mathbb{P} . If a trial stress point is positioned, such that $\sigma_{RR} < \sigma_{\varrho,R}$, the point will be projected parallel to the τ_{LR} -axis. That means the vector $\bar{\mathbf{r}}_{n+1}$ must be edited to

$$\bar{\mathbf{r}}_{n+1} = \bar{\mathbf{r}}_{n+1} - \mathbf{M}_R(\mathbf{M}_R : \bar{\mathbf{r}}_{n+1}). \quad (7.58)$$

The searched intersection point can be written with $\Delta\boldsymbol{\varepsilon}_{max}^p = \bar{\gamma}_{n+1}\bar{\mathbf{r}}_{n+1}$ and (7.30) as

$$\boldsymbol{\sigma}_{n+1}^{(0)} = \boldsymbol{\sigma}_{n+1}^{tr} - \mathbb{C} : \bar{\mathbf{r}}_{n+1}\bar{\gamma}_{n+1}, \quad (7.59)$$

where the term $\mathbb{C} : \bar{\mathbf{r}}_{n+1}$ stands for the direction of the projection and $\bar{\gamma}_{n+1}$ for the distance to the surface.

Using the definition of the generic yield function (5.8) with $q = 0$ and (7.59) leads to a quadratic equation (indices $n + 1$ suppressed)

$$\underbrace{\mathbf{a} : \boldsymbol{\sigma}^{tr} + \boldsymbol{\sigma}^{tr} : \mathbf{b} : \boldsymbol{\sigma}^{tr} - Y}_{f^{tr}} + (-2\boldsymbol{\sigma}^{tr} : \mathbf{b} : \mathbb{C} : \bar{\mathbf{r}} - \mathbf{a} : \mathbb{C} : \bar{\mathbf{r}})\bar{\gamma} + \bar{\mathbf{r}} : \mathbb{C} : \mathbf{b} : \mathbb{C} : \bar{\mathbf{r}}\bar{\gamma}^2 = 0. \quad (7.60)$$

The equality in (7.60) is used because a point *on* the surface is needed. The first part of (7.60) is equal to the value of the yield function of the trial state f^{tr} . This quadratic equation is equivalent to a intersection of a straight line (projection) with an hyperbola (failure surface). The solutions of (7.60) are given by

$$\bar{\gamma}_{n+1}^{1,2} = \frac{B \pm \sqrt{B^2 - 4AC}}{2A} \quad (7.61)$$

with

$$A = \bar{\mathbf{r}}_{n+1} : \mathbb{C} : \mathbf{b} : \mathbb{C} : \bar{\mathbf{r}}_{n+1}, \quad B = 2\boldsymbol{\sigma}_{n+1}^{tr} : \mathbf{b} : \mathbb{C} : \bar{\mathbf{r}}_{n+1} + \mathbf{a} : \mathbb{C} : \bar{\mathbf{r}}_{n+1} \quad \text{and} \quad C = f^{tr}. \quad (7.62)$$

Five different possibilities for the solution exist. Figure 7.6 shows the according projection lines. In the first case, both solutions of $\bar{\gamma}_{n+1}$ are positive and the smaller one is the correct value of $\bar{\gamma}_{n+1}$, because the vector $\bar{\mathbf{r}}_{n+1}$ points from the trial state point to the left arm of the hyperbola. Therefore the shorter vector points to the correct intersection point.

The second case is similar to the first, but the vector $\bar{\mathbf{r}}_{n+1}$ needs to be changed according to (7.58), leading to a projection that does not intersect the curvature point.

In the case of a positive and a negative value (case three in Figure 7.6), the positive is the correct value for $\bar{\gamma}_{n+1}$, because the vector $\bar{\mathbf{r}}_{n+1}$ must point to the left branch of the hyperbola.

The solutions of (7.61) in case four are also both positive (as in case one), but the trial stress point is within the right branch of the hyperbola, which means $f^{tr} < 0$. The larger of the two $\bar{\gamma}_{n+1}$ points to the correct projection point. To eliminate problems with the inquiry at the border of $f^{tr} = 0$ with the tolerance, both solutions should be checked for their position.

If the projection is parallel to the asymptote, as in case five, the term A is equal to zero and (7.61) simplifies to $\bar{\gamma}_{n+1} = -C/B$ with only one solution for $\bar{\gamma}_{n+1}$.

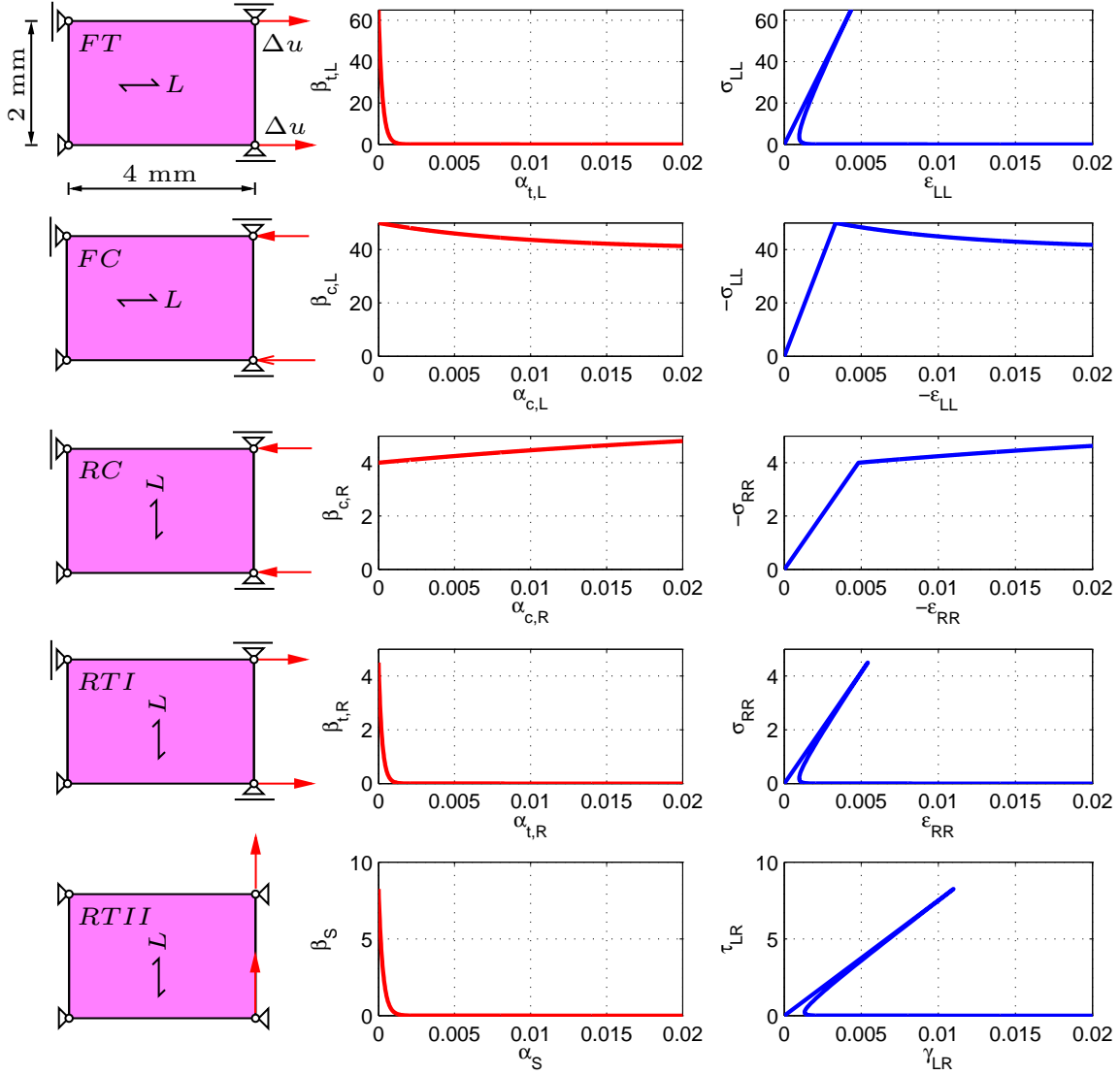


Figure 7.7: Example to show convergence, softening behavior and stress-strain relationship for each surface with $\ell_c = 100$ mm.

A single finite element with a length of 4 mm and a width of 2 mm was loaded with nodal displacements as shown in Figure 7.7 for each state surface. The softening behavior, with an underlying characteristic length of $\ell_c = 100$ mm, are also shown in this figure, as are the stress-strain relationships of all surfaces. For the radial tension surface mode I and mode II are considered individually to be able to distinguish between the effects on tension in radial direction and pure shear.

Tables 7.2 to 7.4 show the convergence behavior of the iteration for the time steps and

for the return mapping algorithm, i.e. the projection in the stress space. The number of integration steps for a time step is abbreviated with IS . Whereas PS stands for the number of iteration steps for a projection. For each integration point on a finite element (gauss-point) one projection has to be computed per iteration of the time step. If more than one number is given for a time step, this means that a different amount of steps was needed during the iteration. Obviously the number of the projection can only be given for plastic load steps. The computation was evaluated for very high values of t , i.e. α and ε to see if the algorithm works also for a completely softened state. The large strains are to high, for the validation in this model, which was developed for small deformations.

Table 7.2: Fiber tension model with $\ell_c = 100$ mm

	FT with algorithm			FT without algorithm		
u	$\sigma_{t,L}$	PS	IS	$\sigma_{t,L}$	PS	IS
[mm]	[N/mm ²]	[-]	[-]	[N/mm ²]	[-]	[-]
0.0100	37.5	-	2	37.5	-	2
0.017333	65.0	-	2	65.0	-	2
0.017334	2.5e-6	1-3	5	65.0	2	4
0.0200	2.5e-7	1	3	75.6	4	4
0.0220	2.5e-8	1	3	83.5	4	4
0.0250	1.32e-9	1	3	95.3	4	4
0.0300	9.5e-12	1	2	114.7	4	4
0.0350	0	1	2	134.0	4	4
0.0400	0	1	2	153.3	4	4
0.0500	0	1	2	191.6	4	4
0.0750	0	1	2	286.9	5	4
0.1000	0	1	2	381.8	4	4
0.1500	0	1	2	570.8	5	4
0.2000	0	1	2	759.4	4	4
0.3000	0	1	2	1136.0	5	4
0.4000	0	1	2	1512.0	4	3
0.5000	0	1	2	1888.0	4	4

To show the effect of the algorithm for large ℓ_c , the fiber tension surface was once computed without and once with the algorithm. Both results are shown in Table 7.2. The solutions for the stress in fiber direction increase after the ultimate strength and follow the wrong branch of the stress-strain relationship (see Fig. 7.3) if the algorithm is not used. With the implementation of the algorithm, the correct branch can be reached by the projection. The brittle behavior in fiber tensile direction leads to an immediate total loss of strength after reaching the ultimate strength and a crack occurs. The convergence of the iteration in the load step, as well as in the return mapping algorithm is better than without the algorithm. For the first plastic step a few more iteration steps for the projection were needed. For high strains, i.e. values of α , the computation accuracy is reached because the softening follows an exponential function, which reaches exactly zero for $\alpha \rightarrow \infty$.

Table 7.3: Fiber compression model with $\ell_c = 100$ mm and radial compression model

FC				RC			
u	$-\sigma_{c,L}$	PS	IS	u	$-\sigma_{c,R}$	PS	IS
[mm]	[N/mm ²]	[-]	[-]	[mm]	[N/mm ²]	[-]	[-]
0.0100	37.5	-	2	0.0100	2	-	2
0.013306	49.9	-	2	0.0150	3.11	-	2
0.013307	49.8	3	4	0.0170	3.53	-	2
0.0150	49.5	3	4	0.019277	4.00	2	2
0.0170	48.9	3	4	0.019278	4.00	1,3	3
0.0200	48.3	3	4	0.0200	4.01	1,3	3
0.0220	47.8	3	4	0.0220	4.03	1,3	3
0.0250	47.2	3	4	0.0250	4.06	1,3	3
0.0300	46.2	3	4	0.0300	4.13	1,3	3
0.0350	45.5	3	4	0.0350	4.19	1,3	3
0.0400	44.9	3	4	0.0400	4.25	1,3	3
0.0500	43.7	3	4	0.0500	4.20	1,3	3
0.0750	41.9	3	4	0.0750	4.50	1,3	3
0.1000	40.9	3	4	0.1000	4.79	1,3	3
0.1500	40.1	3	4	0.1500	5.10	1,3	3
0.2000	40.0	3	4	0.2000	5.31	1,3	3
0.3000	39.9	2,3	4	0.3000	5.57	1,3	3
0.4000	39.9	2	3	0.4000	5.60	1,3	3
0.5000	39.9	2	3	0.5000	5.70	1,3	3

Table 7.3 shows the results for compression behavior in both, fiber and radial direction. The fiber compressive behavior only incorporates a minor softening. A ℓ_c of 100 mm is small enough to not cause numerical problems if the algorithm is not used. Even with the large strains used in this example, the densification in the post failure behavior is not reached. An indicator that this range is only of importance for large strains, which are not considered in the material model. The convergence is quadratic in both iterations and reaches the correct solution in a few steps.

The hardening of compression loading in radial direction is shown in 7.3. Because of the independency from ℓ_c there is no problem with the convergence.

Finding the correct solution in a projection onto the Weihe-Kroeplin fiber tension and mixed mode surface is most problematic. This is due to its construction as an hyperbolic surface in stress space. Projections on the correct branch of this hyperboloid need special procedures as laid out earlier in this section.

The method discussed in Subsection 7.2.3 was used to accomplish the results in Table 7.4. As in the fiber tension direction, the tensile strength is immediately lost after reaching the ultimate strength. Also here the computation accuracy reaches its limits for large strains. Besides a slightly higher number for the first plastic projection, all iterations

Table 7.4: Radial tension model for mode I and II with $\ell_c = 100$ mm

RT mode I				RT mode II			
u	$\sigma_{t,L}$	PS	IS	u	τ_S	PS	IS
[mm]	[N/mm ²]	[-]	[-]	[mm]	[N/mm ²]	[-]	[-]
0.0100	2.2	-	2	0.0100	1.88	-	2
0.021686	4.5	-	2	0.0200	3.75	-	2
0.021687	1.33e-3	5	4	0.0300	5.63	-	2
0.0220	1.18e-3	3,4	3	0.0400	7.51	-	2
0.0250	3.82e-4	3,4	3	0.043942	8.25	-	2
0.0300	5.85e-5	3,4	3	0.043942	3.32e-11	19	2
0.0350	2.73e-6	3,4	3	0.0450	3.32e-11	1	2
0.0400	1.38e-6	2,4	3	0.0500	3.27e-11	1,4	2
0.0500	3.20e-8	2,4	3	0.0600	3.25e-11	1,4	2
0.0750	2.7e-12	1,4	3	0.0750	3.25e-11	1,4	2
0.1000	0	1,4	2	0.1000	3.25e-11	1,4	2
0.1500	0	2,4	2	0.1500	3.25e-11	1,4	2
0.2000	0	1,4	2	0.2000	3.25e-11	1,5	2
0.3000	0	1,3	2	0.3000	3.25e-11	1,5	2
0.4000	0	1,3	2	0.4000	3.25e-11	1,5	2
0.5000	0	1,3	2	0.5000	3.25e-11	1,5	2

show the same magnitude as in the other calculations.

The shear strength is also lost abruptly after crack initialization. The computation does not reach zero for large strains in this case, because the theoretical limit of $a = 0$ and therefore $\tau_{LR} = 0$, was not permitted in the numerical implementation. This led to a residual τ_{LR} according to a_{min} and a minor error, which is negligible.

Due to the boundary conditions for the pure shear example and hence the known deformation state of the element, no iteration is necessary for the load steps. The number of iteration for the first plastic projection is very high. The reason for this unknown, but the solution is correct and further steps do not show this anomaly.

7.2.6 Mixed mode example

Tensile loading of an element in radial direction with a minor shear loading leads to mixed mode loading. Mode I and II of the radial tension surface interact. The projection algorithm for this case could not reach results for a value $\ell_c = 100$ mm. Even though a better starting point is computed the iteration starts to alternated. For values of $\ell_c = 20$ mm or smaller the iteration does not alternated, but a quadratic convergence can not be reached. The return mapping algorithm converges to the correct solution, but the iteration in the time step does not converge.

Because of the importance of the shear interaction for all surfaces, a computation of a general structure with this material model is not yet possible.

Figure 7.8 shows the return mapping algorithm for an element loaded in radial tensile

direction, as shown in Fig. 7.7. The grain angle to the loading direction was $\varphi = 45^\circ$. This led to a mixed mode loading. For $\ell_c = 10$ mm and $\ell_c = 20$ mm the trial, start and converged states are shown for the first iteration of the return mapping algorithm of the first integration point.

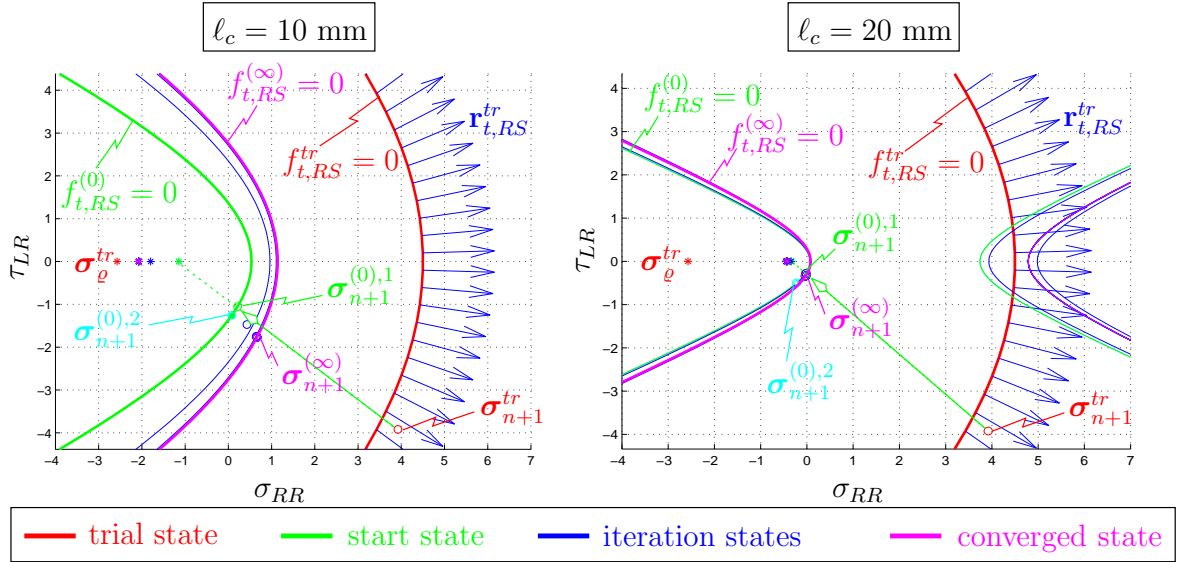


Figure 7.8: Mixed mode convergence for $\ell_c = 10$ mm and $\ell_c = 20$ mm with $\varphi = 45^\circ$.

The computation was performed with both algorithms suggested for the radial tension surface in Sections 7.2.3 and 7.2.4. The same solution was reached in both cases. The figure shows the iteration states for the algorithm of Section 7.2.3. It is obvious that for the trail state and during the iteration the stress point is not on the yield surface. The yield condition $f = 0$ must only hold for the converged state.

The start values of both algorithms are indicated by $\sigma_{n+1}^{(0),1}$ for the algorithm of Section 7.2.3 and $\sigma_{n+1}^{(0),2}$ for Section 7.2.4. The projection for the start value is shown by an arrow for the first algorithm.

For $\ell_c = 20$ mm the right branch of the hyperbola is already closer to the trial state than the correct one. Thus the solution would converge to this branch of the hyperbola.

In both examples the converged state is between the trial and the start state. This is consistent with the fact that the start state is the state of maximal softening for this increment. The softening behavior is much stronger for $\ell_c = 20$ mm. The radial tensile strength $\beta_{t,R}$ has already reached zero, whereas with $\ell_c = 10$ mm a residual strength of about 1 N/mm² is still existing.

7.2.7 Start values for return mapping algorithm in edges and corners

The starting values for each surface are changed by the algorithms described above, for each surface individually. This is no problem for the variables of the residual vector \mathbf{R}_{n+1} ,

$\alpha_{i,n+1}$, $s_{i,n+1}$, $\mathbf{r}_{i,n+1}$ and $\gamma_{i,n+1}$, which describe the state of the failure surface $i \in \mathcal{J}_{act}$ and exist for each surface. $\alpha_{i,n+1}$ and $s_{i,n+1}$ are combined into vectors $\boldsymbol{\alpha}_{n+1}$ and \mathbf{s}_{n+1}^* , respectively. For $\mathbf{r}_{i,n+1}$ and $\gamma_{i,n+1}$ an equation was formulated for each surface individually (see Chapter 6).

The other unknowns of a state are the stress tensor $\boldsymbol{\sigma}_{n+1}$ and the plastic strain tensor $\boldsymbol{\varepsilon}_{n+1}^p$. For each surface the start values $\boldsymbol{\sigma}_{i,n+1}^{(0)}$ and $\boldsymbol{\varepsilon}_{i,n+1}^{p(0)}$ are computed individually, therefore collective values $\boldsymbol{\sigma}_{n+1}^{(0)}$ and $\boldsymbol{\varepsilon}_{n+1}^{p,(0)}$ need to be found to perform a projection to a corner.

Computing a combined strain tensor $\Delta\boldsymbol{\varepsilon}^p$ and from this the stress point

$$\boldsymbol{\sigma}_{n+1}^{(0)} = \mathbb{C} : \left(\boldsymbol{\varepsilon}_{n+1} - \boldsymbol{\varepsilon}_n^p - \sum_{i \in \mathcal{J}_{act}} \gamma_{i,n+1}^{(0)} \mathbf{r}_{i,n+1}^{(0)} \right) \quad (7.64)$$

gives good start values, if the active yield-surfaces are perpendicular to each other. For small angles between the the surfaces, the resulting stress point may be far off the correct solution.

A better value for the stress tensor is the vectorial midpoint in the stress space, defined by

$$\boldsymbol{\sigma}_{n+1}^{(0)} = \frac{\sum_{i \in \mathcal{J}_{act}} \boldsymbol{\sigma}_{i,n+1}^{(0)}}{m_{act}}, \quad (7.65)$$

where m_{act} is the number of active yield surfaces $i \in \mathcal{J}_{act}$. The corresponding plastic strain is given by

$$\boldsymbol{\varepsilon}_{n+1}^p = \boldsymbol{\varepsilon}_{n+1} - \mathbb{C}^{-1} : \boldsymbol{\sigma}_{n+1}^{(0)}. \quad (7.66)$$

7.3 Problem on structural-level

The numerical difficulties with high values of the characteristic length described in Section 7.1 and the solutions given in Section 7.2 for the gauss-point level, show the problem on a local element level. Another effect on the global or structural level appears when several finite elements are connected to model a structure. The same characteristic length ℓ_c can lead to problems in the convergence of the iteration in a time step depending on the ratio of the maximum elastic load to the according displacement, i.e. the elastic stiffness of the structure.

7.3.1 One-dimensional example

To clarify the numerical problem on a global level it is first shown in a one-dimensional example.

Figure 7.9 shows three rod elements where the middle one comprises a softening behavior after reaching the elastic limit and the two outer elements are elastic until infinity. The stiffnesses are therefore given by EA/ℓ in the elastic range and KA/ℓ after failure, where $E = \mathbb{C}$ is the elastic stiffness, $K = \mathbb{C}^{ep}$ is the elasto-plastic stiffness, A the area of the cross-section of the rod and ℓ the length of the element.

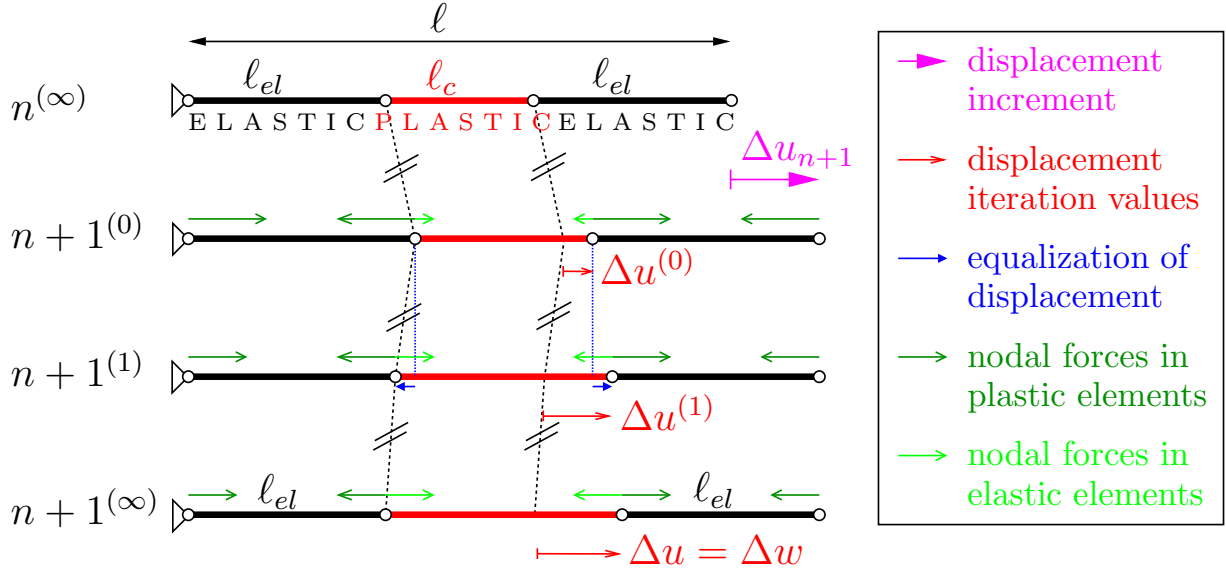


Figure 7.9: One dimensional example to show structural influence.

The first picture in Figure 7.9 represents the last step in the elastic range. The first and second iteration step for the solution of this system after applying a incremental displacement Δu_{n+1} on the global structure is shown in the other sketches. The node forces, i.e. the internal stresses, and the resulting nodal displacements, i.e. the internal strains, are included in the sketches to indicate the iteration process. The (0)-iteration assumes an elastic behavior that results in higher nodal forces in the elastic elements than in the middle element, as this reaches its ultimate strength. To reach an equilibrium at the nodes, the forces must become smaller, which is only possible by elongation of the inner element (equivalent to a crack opening) and a shortening of the outer elements (equivalent to an elastic unloading). This results in a drop of the global force, that accords with the projection onto the softening curve. This iteration step will be continued until an equilibrium state for the structure is reached ($n+1^{(0)}$). At this state the displacement increment, i.e. the whole crack opening, is being added to the middle element and the elastic elements are fully unloaded, assuming a fully developed crack.

Different force-displacement curves for structures with the same ℓ_c are shown in Figure 7.10. The different elastic structure stiffnesses and therefore the different displacements where plastic deformations occur, are visible. The transition from a stable structural performance with relative high elastic stiffnesses to a unstable performance with lower stiffnesses is visible. For the same characteristical length the softening behavior of the structures is not equal for all. They differ in a most basic way, with a huge influence in the structural behavior.

The problem for a certain elastic structure stiffness, is in the projection from the incorrect elastic solution to the correct solution on the softening curve, as this curve has two possible solutions. One of this solutions is on the wrong branch of the exponential softening curve and may be closer to the correct one, depending on its curvature. This is visible in Figure 7.10, as the wrong path of the force-displacement curve gets closer to the

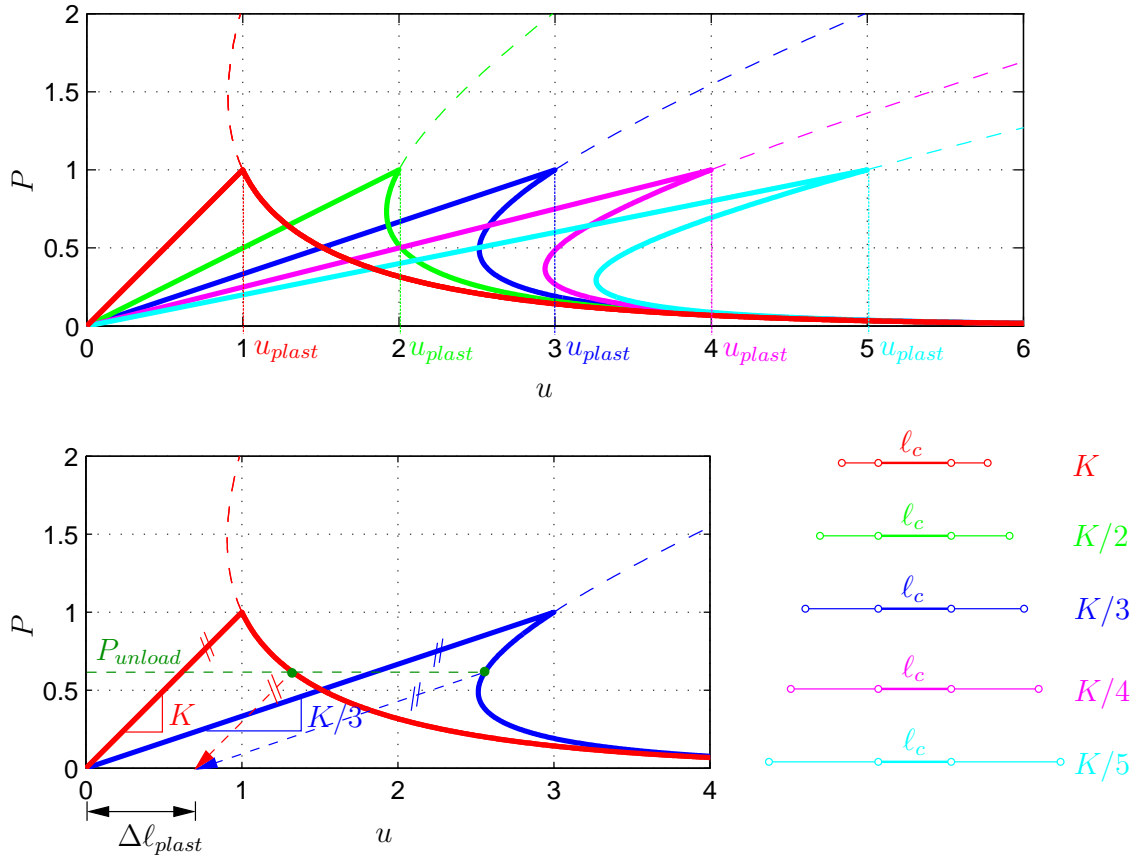


Figure 7.10: Force-displacement curves of structures with equal ℓ_c .

last elastic state ($u_{plastic}$), with decreasing elastic stiffness. After unloading, the permanent plastic deformation for a system with equal length of the elements with elasto-plastic properties ($=\ell_c$) must be the same for all, as indicated in the lower picture of Figure 7.10.

The stiffness matrix for a structure as shown in Fig. 7.9 in the plastic state (i.e. after failure) is given to

$$\mathbf{K}_T = \frac{A}{\ell_{el}} \begin{bmatrix} E & -E & 0 & 0 \\ -E & E + K \frac{\ell_{el}}{\ell_c} & -K \frac{\ell_{el}}{\ell_c} & 0 \\ 0 & -K \frac{\ell_{el}}{\ell_c} & E + K \frac{\ell_{el}}{\ell_c} & -E \\ 0 & 0 & -E & E \end{bmatrix}. \quad (7.67)$$

The first row and the first column can be neglected because of the boundary condition in the left node $u = 0$. For the limit state with $K \rightarrow 0$, i.e. no residual elasto-plastic stiffness after a full crack, the stiffness of the structure can be written

$$\mathbf{K}_T = \frac{EA}{\ell_{el}} \begin{bmatrix} 1 & 0 & 0 \\ 0 & 1 & -1 \\ 0 & -1 & 1 \end{bmatrix}. \quad (7.68)$$

To find the deformation state of the structure the set of equations

$$\mathbf{K}_T \mathbf{u} = \mathbf{f} \quad (7.69)$$

must be solved, where \mathbf{u} is the vector of nodal displacements and \mathbf{f} is the vector of nodal forces. A solution of (7.69) is not possible if \mathbf{K}_T is singular, i.e. $\det \mathbf{K}_T = 0$. Also if a submatrix of \mathbf{K}_T is singular a convergence to a solution is impossible. K is the only value comprising the softening parameters ℓ_c , G_f , and β^0 . To find the critical crack opening ($\det \mathbf{K}_T = 0$), the determinant of the submatrix with entries of K must be set equal to zero. The sub-matrix with the second and third row and column of \mathbf{K}_T in (7.67) leads to the determination equation for the critical plastic stiffness

$$\left(E + K \frac{\ell_{el}}{\ell_c}\right)^2 - \left(-K \frac{\ell_{el}}{\ell_c}\right)^2 = 0 \quad \text{or} \quad E^2 + 2EK \frac{\ell_{el}}{\ell_c} = 0. \quad (7.70)$$

The critical plastic stiffness K_{crit} can be computed from this equation to

$$K_{crit} = -\frac{E\ell_c}{2\ell_{el}}. \quad (7.71)$$

From (7.17) with (7.10) follows

$$K = \mathbb{C}^{ep} = -\frac{Ek\beta}{E - k\beta} \quad (7.72)$$

and setting $K_{crit} = K$ with the (7.1) leads to

$$\frac{\ell_c E}{k\beta^0} = (2\ell_{el} + \ell_c) \exp(-k\alpha). \quad (7.73)$$

With $\ell = 2\ell_{el} + \ell_c$ and the definition of k from (7.9) the critical crack opening can be written

$$w_{crit} = \frac{G_f}{\beta^0} \ln \left(\frac{\ell(\beta^0)^2}{EG_f} \right). \quad (7.74)$$

Notice that the total length ℓ influences the critical state on structural level and not ℓ_c alone. Setting the critical crack opening equal to zero leads to the same equation for ℓ_{crit} as for $\ell_{c,crit}$ according to (7.20). This is due to the construction of this example, that behaves for a full crack like a single element.

7.3.2 Convergence study for a biaxial stress state

To show the effect of different elastic stiffnesses for biaxial stress states, a simple example was computed with the material model described in this work.

The algorithms elucidated in Section 7.2 were used to eliminate problems in the convergence on the gauss-point level. The example is shown in Figure 7.11. The dimensions ℓ_c and ℓ_{el} were changed according to Table 7.5 with all possible combinations.

The loading in the examples is tension in fiber direction. The computation has therefore only been carried out with the fiber tension surface. The other three surfaces of the material

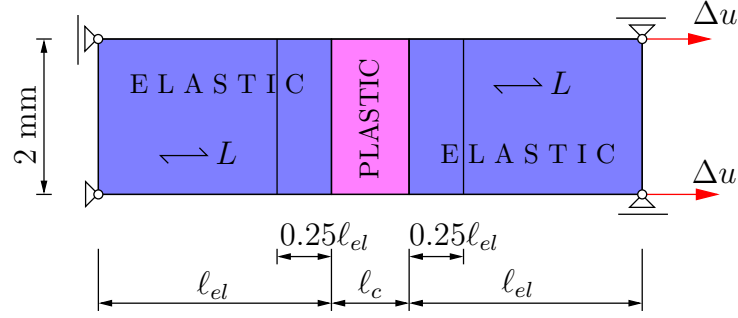


Figure 7.11: Example to show structural behavior effects.

model were deactivated. Three of the four failure surfaces, including the fiber tension surface, comprehend the softening behavior, which is the subject matter of this chapter.

The displacement increment history was constructed by a combination of all displacements u_{plast} . This results in some increments of about one tenth of a micrometer or less. The first step at which plastic deformations occur was set only one hundredth of a millimeter or less higher than the analytical value.

Table 7.5: Values for the model dimensions ℓ_c and ℓ_{el}

ℓ_c [mm]	1	2	3	4	5	6
ℓ_{el} [mm]	0.1	0.5	1	2	3	4

The results of the convergence study with 36 finite element analyses are given in Table 7.6. For each of the six different characteristic length ℓ_c the total length ℓ of the example, the displacement u_{plast} , the critical crack opening w_{crit} and the number of iteration steps of the first plastic step are shown. From ℓ one can compute the displacement

$$u_{plast} = \ell \frac{\beta^0}{E}, \quad (7.75)$$

where plastic deformations occur. For w_{crit} the equation of the one-dimensional example was used. The validation of these values is therefore limited and they are only given for comparison.

An 'x' stands for a computation where alteration occurred after ten iteration steps. This alteration either results in no solution or in the solution on the wrong path in the force-displacement diagram. A solution on the wrong branch would be equivalent to a hardening effect instead of a softening of the structure. In some cases the solution found in the first plastic step was very close to the correct one and the solutions of subsequent steps were on the correct softening path. These cases showed nearly quadratic convergence and slower convergence at the first steps. These results were also marked not converged, due to the alteration in the first step and the missing quadratic convergence. This occurred in examples close to the last converged example with small ℓ_{el} .

Table 7.6: Convergence study results

ℓ_c	1 mm				2 mm				3 mm			
ℓ_{el}	ℓ	u_{plast}	w_{crit}	IS	ℓ	u_{plast}	w_{crit}	IS	ℓ	u_{plast}	w_{crit}	IS
[mm]	[mm]	[μm]	[μm]	[-]	[mm]	[μm]	[μm]	[-]	[mm]	[μm]	[μm]	[-]
0	1	4.33	-44.9	4	2	8.67	-27.3	4	3	13.00	-17.0	4
0.1	1.2	5.20	-40.2	4	2.2	9.53	-24.9	4	3.2	13.87	-15.3	4
0.5	2	8.67	-27.3	4	3	13.00	-17.0	5	4	17.33	-9.7	5
1	3	13.00	-17.0	5	4	17.33	-9.7	5	5	21.67	-4.0	5
2	5	21.67	-4.0	5	6	26.00	0.6	x	7	30.33	4.5	x
3	7	30.33	4.5	x	8	34.67	7.9	x	9	39.00	10.9	x
4	9	39.00	10.9	x	10	43.33	13.6	x	11	47.67	16.0	x

ℓ_c	4 mm				5 mm				6 mm			
ℓ_{el}	ℓ	u_{plast}	w_{crit}	IS	ℓ	u_{plast}	w_{crit}	IS	ℓ	u_{plast}	w_{crit}	IS
[mm]	[mm]	[μm]	[μm]	[-]	[mm]	[μm]	[μm]	[-]	[mm]	[μm]	[μm]	[-]
0	4	17.33	-9.7	4	5	21.67	-4.0	4	6	26.00	0.6	5
0.1	4.2	18.20	-8.4	5	5.2	22.53	-3.0	5	6.2	26.87	1.4	7
0.5	5	21.67	-4.0	5	6	26.00	0.6	x	7	30.33	4.5	x
1	6	26.00	0.6	x	7	30.33	4.5	x	8	34.67	7.9	x
2	8	34.67	7.9	x	9	39.00	10.9	x	10	43.33	13.6	x
3	10	43.33	13.6	x	11	47.67	16.0	x	12	52.00	18.2	x
4	12	52.00	18.2	x	13	56.33	20.2	x	14	60.67	22.1	x

IS ... number of integration steps

x ... no quadratic solution

For all different characteristic lengths the examples show an alternation at the same total length ℓ . This length indicates the critical length ℓ_{crit} between a unique and non-unique solution. Also a critical plastic deformation $u_{plast,crit}$ can be specified.

From Table 7.6 one can see that the critical total length must be smaller than 6 mm or the critical plastic deformation must be smaller than 2.6 mm. To narrow the range of the values, more examples were computed for $\ell_c = 1$ mm, with elastic length between 2 and 3 mm. At $\ell_{el} = 2.45$ mm the projection did not converge. This corresponds to a critical total length $\ell_{crit} = 5.8$ mm and a critical plastic displacement $u_{plast,crit} = 0.0256$ mm.

Using the equations derived for the one-dimensional case is a good approximation for most of these examples. With the material parameters from Table 5.1 for the fiber tension surface the critical total length yields $\ell_{crit} = 5.858$ mm with a corresponding plastic displacement of $u_{plast,crit} = 0.0254$ mm. This analytical results coincide perfectly with the results from the computations.

The critical crack opening w_{crit} vanishes at the critical state with ℓ_{crit} . A correct, stable solution is characterized by $w_{crit} < 0$, whereas a negative w_{crit} results in an alteration of the projection algorithm or in a wrong solution. The distance between the correct solution and the starting value of the iteration increases with the critical crack opening.

This example reveals the general problem, but only for a special case. A general, more

complicated structure follows different rules, even though a critical state, where numerical difficulties occur, will also exist.

Computing this example with geometric nonlinearity can lead to error in the results. This is due to the fact, that large deformations occur, when the crack is opened very wide, to verify the stability of the algorithm. The deformations in the elements that are subject to plastic strains, are much higher than in elastic elements. This leads to a distorted computation of the stress, which can lead to stress values in the elastic elements, that are higher than the initial strength. This hardening effect can be avoided if the geometric nonlinearity is formulated with the second Piola-Kirchhoff stress tensor. For small deformations, geometric nonlinearity formulated with the first Piola-Kirchhoff stress tensor is applicable, because the difference in the solutions is marginal.

Summary and conclusions

8.1 Summary

This thesis presented a multi-surface plasticity model for the description the pre- and post-failure behavior of clear spruce wood under plane stress conditions. The mathematical background and the algorithms for the numerical implementation in a finite element program of a multi-surface model by Mackenzie-Helnwein [30], were reviewed. The four failure surfaces of this model were described using orthotropic tensor functions. The non-linear softening behavior was analyzed and discussed. Both, the surface and its motion due to softening or hardening, respectively, were graphically shown in the stress space.

For failure due to fiber tension, a tension cut-off surface to model fiber rupture was defined. It assumed same maximum strength for small variations of the grain angles. Combined tensile and shear failure in planes parallel to grain were modeled using a formulation by Weihe [44, 45]. An open parabolic failure surface for fiber compression was fit to the single-surface model of Tsai and Wu [42] based on the parameters identified by Eberhardsteiner [7]. Compressive failure in for radial direction was modeled by a surface suggested by Helnwein et al. [29], even though parameters were recalibrated.

Some problems regarding numerical instability of the solution algorithm for the softening behavior at larger characteristic length ℓ_c and larger time steps were solved. The modeling parameter characteristic length ℓ_c was identified as crucial for the convergence behavior at a local gauss point level. Its effect and thus the effect of the finite element discretization on the model with regard to the development of a stable or unstable crack was analyzed. A critical characteristic length $\ell_{c,crit}$ was identified and a solution strategy for the return mapping algorithm at large characteristic length for was presented. The implementation of this algorithm for those three surfaces showing softening behavior was laid out, including a special algorithm for the radial tension failure surface. Convergence studies at large characteristic lengths showed the improvements achieved by the proposed algorithms.

On a structural or global level, convergence problems with an unstable crack propaga-

tion were identified and explained for one dimensional examples. Calculations for 36 plane stress examples using the fiber tension failure surface confirmed the results in a convergence study.

8.2 Conclusions

The convergence problems observed for coarse finite element meshes could be eliminated at a local level both for the tension and the compression surfaces in fiber direction. The numerical stability of the radial tension model in the post-failure regime could be enhanced, but not stabilized without limitations. Even though the convergence behavior for radial tension and pure shear could be enhanced for large characteristic lengths, mixed mode loading still leads to difficulties with the convergence behavior. The possible maximum values for the characteristic length could be increased for mixed mode loading, but not to a level which would allow a discretization of larger structures without limitations. Very fine finite element meshes with very small elements would lead to excessive need for hardware resources and computation time. Thus, the solution of this remaining problem is essential for the full utilization of this material model.

The difficulties in modeling the initialization of an unstable crack in a structure were specified, but not solved. The effects could be confined to the global structural level. This structural level can not be influenced by the material model alone. The problem must be addressed at the global level of a finite element analysis. Use of the generalized arc-length method [6, 37, 36, 46] may help solving this problem but has not been investigated in this work.

8.3 Future developments

Future enhancement of this multi-surface failure model for wood should focus on the remaining issue with the local stability of the model. The general stability of the whole model depends on improvements of the behavior under mixed mode loading. Therefore, the first step in future developments should be algorithmic enhancements for the radial tension failure surface.

The back-calculation of biaxial tests showing unstable crack development, is a good verification of the post-failure behavior of the multi-surface wood model. If the structural convergence problems cannot be controlled by local stability alone, a solution at global level of the finite element analysis must be found. This may require incorporation of more sophisticated path following techniques.

Interdependency of the different failure-surfaces and their strength functions is another source of potential improvements. Inelastic (plastic) deformations in one direction may reduce the strength in other material directions. Incorporating these effects in the model may lead to higher accuracy of the predicted material behavior.

Due to the occurrence of large strains perpendicular to grain, the model should be extended to accommodate finite strains.

Bibliography

- [1] C. Adalian and P. Morlier. “Wood Model” for the dynamic behaviour of wood in multiaxial compression. *Holz als Roh- und Werkstoff*, 60(6):433–439, 2002.
- [2] K.-J. Bathe. *Finite element procedures*. Prentice-Hall, Englewood Cliffs, New Jersey, USA, 1996.
- [3] J. Betten. *Tensorrechnung für Ingenieure*. Teubner, 1987.
- [4] J. Betten. *Kontinuumsmechanik – Elasto-, Plasto- und Kriechmechanik*. Springer, 1993.
- [5] J.P. Boehler. *Applications of Tensor Functions in Solid Mechanics*, volume 292 of *CISM courses and lectures*, chapter 1–7. Springer, 1987.
- [6] M.A. Crisfield. An arc-length method including line searches and accelerations. *International Journal for Numerical Methods in Engineering*, 19:1269–1289, 1983.
- [7] J. Eberhardsteiner. *Mechanisches Verhalten von Fichtenholz – Experimentelle Bestimmung der biaxialen Festigkeitseigenschaften*. Springer, Vienna, 2002.
- [8] J. Eberhardsteiner, M. Gingerl, and L. Ondris. Experimental investigation of the strength of solid wood under biaxial loading oblique to the grain direction. In P. Morlier and G. Valentin, editors, *COST Action E8: Workshop Damage in Wood*, Bordeaux, France, May 27–28, 1999.
- [9] J. Eberhardsteiner, F. Pulay, and H.A. Mang. Zur Frage der Lasteinleitung bei experimentellen Festigkeitsuntersuchungen von zweiaxial beanspruchtem Holz. *Österreichische Ingenieur- und Architekten-Zeitschrift*, 136(6):265–272, 1991.
- [10] J. Ehlbeck and K. Hemmer. Erfassung, systematische Auswertung und Ermittlung von Grundlagen über das Zusammenwirken von Längs, Quer- und Schubspannungen bei fehlerfreiem und fehlerbehaftetem Nadelholz. Technical report, Stuttgart: IRB Verlag, 1986.
- [11] C. Faessel, P. Navi, and M. Jirasek. 2D anisotropic damage model for wood in tension. In P. Morlier and G. Valentin, editors, *COST Action E8: Workshop Damage in Wood*, pages 21–37, Bordeaux, France, May 27–28, 1999.

- [12] D. Fengel and G. Grosser. Holz, Morphologie und Eigenschaften. In F. Ullmann, editor, *Ullmanns Encyklopedie der technischen Chemie*, pages 669–679, Weinheim, 1976. Verlag Chemie.
- [13] D. Fengel and M. Stoll. Über die Veränderung des Zellquerschnitts, der Dicke der Zellwand und der Wandschichten von Fichtentracheiden innerhalb eines Jahrringes. *Holzforschung*, 27:1–7, 1973.
- [14] D. Fengel and G. Wegener. *Wood. Chemistry, Ultrastructure, Reactions*. Verlag Kessel, Remagen, 2003.
- [15] P. François and P. Morlier. Plasticité du bois en compression simple. *Matériaux et Techniques*, 81(12):5–14, 1993.
- [16] L.J. Gibson and F. Ashby. *Cellular solids, Structure and properties – 2nd edition*. Cambridge University Press, 1997.
- [17] M. Gingerl. *Realisierung eines optischen Deformationsmeßsystems zur experimentellen Untersuchung des orthotropen Materialverhaltens von Holz bei biaxialer Beanspruchung*. Österreichischer Kunst- und Kulturverlag, 1998. In German.
- [18] P. Helnwein. Some remarks on the compressed matrix representation of symmetric second-order and fourth-order tensors. *Computer Methods in Applied Mechanics and Engineering*, 190:2753–2770, 2001.
- [19] P. Helnwein, J. Eberhardsteiner, and A. Hanhijärvi. Constitutive model for the short-term failure analysis of wood under multiaxial states of stress: Effect of radial compression. In *Proceedings of the First International Conference of the European Society for Wood Mechanics*, Lausanne, Switzerland, April 19–21 2001. Building Material Laboratory, Materials Science and Engineering Department, Swiss Federal Institute of Technology Lausanne (EPFL).
- [20] K. Hemmer. *Versagensarten des Holzes der Weißtanne unter mehrachsiger Beanspruchung*. Doctoral thesis, Technical University of Karlsruhe, Germany, 1986.
- [21] H.F. Jakob. *Nanostructure of natural cellulose and cellulose composites*. Doctoral thesis, University of Vienna, Vienna, Austria, 1996.
- [22] J. Keckes, I. Burgert, K. Fruehmann, M. Mueller, K. Koelln, M. Hamilton, M. Burghammer, S.V. Roth, S. Stanzl-Tschegg, and P. Fratzl. Cell-wall recovery after irreversible deformation of wood. *Nature Materials*, 2:810–813, 2003.
- [23] F. Kollmann. *Technologie des Holzes und der Holzwerkstoffe*, volume 1. Berlin Heidelberg New York: Springer-Verlag, Berlin, 2nd edition, 1982.
- [24] B. Kröplin and S. Weihe. Constitutive and geometrical aspects of fracture induced anisotropy. In T.J.R. Owen, E. Oñate, and E. Hinton, editors, *International Conference on Computational Plasticity, COMPLAS 5*, pages 255–279, Barcelona, Spain, 1997.

- [25] H. Lichtenegger. *The composite architecture of the wood cell wall*. Doctoral thesis, University of Vienna, Vienna, Austria, 1999.
- [26] H. Lichtenegger, A. Reiterer, S.E. Stanzl-Tschegg, and P. Fratzl. Variation of cellulose microfibril angles in softwoods and hardwoods – a possible strategy of mechanical optimization. *Journal of Structural Biology*, 128:257–269, 1999.
- [27] J. Lubliner. *Plasticity Theory*. Macmillan Publishing Company, New York, 1990.
- [28] J. Lucena-Simon, B.H. Kröplin, G. Dill-Langer, and S. Aicher. A fictitious crack approach for the anisotropic degradation of wood. In *Proceedings of the International Conference on Wood and Wood Fiber Composites*, pages 229–240, University of Stuttgart, Germany, 13.–15. April 2000. COST Action E8, Otto-Graf-Institute.
- [29] P. Mackenzie-Helnwein, J. Eberhardsteiner, and H.A. Mang. Short-term mechanical behavior of biaxially stressed wood: Experimental observations and constitutive modeling as an orthotropic multi-surface elasto-plastic material. In *Proceedings of the 14th US National Congress on Theoretical and Applied Mechanics, USNCTAM14*, pages 290–291, Blacksburg, VA, USA, June 23–28, 2002.
- [30] P. Mackenzie-Helnwein, J. Eberhardsteiner, and H.A. Mang. A multi-surface plasticity model for clear wood and its application to the finite element analysis of structural details. *Computational Mechanics*, 31(1–2):204–218, 2003.
- [31] P. Mackenzie-Helnwein, J. Eberhardsteiner, and H.A. Mang. Multi-surface plasticity of clear spruce wood. In E. Oñate and D.R.J. Owen, editors, *Proceedings of the VII International Conference on Computational Plasticity, COMPLAS 2003*, Barcelona, Spain, 2003. CIMNE.
- [32] L.E. Malvern. *Introduction to the Mechanics of a Continuous Medium*. Series in Engineering of the Physical Sciences. Prentice-Hall, 1969.
- [33] H.A. Mang, J. Eberhardsteiner, R. Lackner, P. Mackenzie-Helnwein, and Pichler Ch. Constitutive modeling and computational mechanics of wood and cement-based materials. In *CD-ROM Proceedings of the 9th International Conference on Numerical Methods in Continuum Mechanics, NCMCM 2003*, Zilina, Slovak Republic, 2003.
- [34] H.A. Mang and G. Hofstetter. *Festigkeitslehre*. Springer, Vienna, 2000.
- [35] H.W. Müllner. Konstitutives Modellieren von Fichtenholz unter biaxialer Beanspruchung mittels eines orthotropen Einflächenmodells unter Berücksichtigung von Ver- und Entfestigung. Dipl.-ing.-thesis, Vienna University of Technology, Vienna, Austria, 2003.
- [36] E. Ramm. Strategies for tracing the nonlinear response near limit points. In W. Wunderlich, E. Stein, and K.-J. Bathe, editors, *Nonlinear Finite Element Analysis in Structural Mechanics*, pages 63–89. Springer, New York, 1981.

- [37] K.H. Schweizerhof and P. Wriggers. Consistent linearization for path following methods in nonlinear FE analysis. *Computer Methods in Applied Mechanics and Engineering*, 59:261–279, 1986.
- [38] J.C. Simo and T.J.R. Hughes. *Computational Inelasticity*. Interdisciplinary Applied Mathematics. Springer, Berlin, 1998.
- [39] J.C. Simo and R.L. Taylor. Consistent tangent operators for rate independent elasto-plasticity. *Computer Methods in Applied Mechanics and Engineering*, 48:101–118, 1985.
- [40] M. Sippola and S. Koponen. Fracture behaviour of clear softwood; Tests and FEM models. In *COST E8, Damage in Wood*, pages 27–28, Bordeaux, France, May 27–28, 1999.
- [41] R. Spengler. Festigkeitsverhalten von Brettelelementen aus Fichte unter zweiachsiger Beanspruchung; Ergebnisse aus experimentellen Untersuchungen. Technical report, Munich University of Technology, Institut für Bauingenieurwesen II, 1986.
- [42] S.W. Tsai and E.M. Wu. A general theory of strength for anisotropic materials. *Journal of Composite Materials*, 5:58–80, 1971.
- [43] R. Wagenführ and C. Schreiber. *Holzatlas*. VEB Fachbuchverlag, Leipzig, 1974.
- [44] S. Weihe. *Modelle der fiktiven Rissbildung zur Berechnung der Initiierung und Ausbreitung von Rissen: ein Ansatz zur Klassifizierung*. PhD thesis, University of Stuttgart, Germany, 1995.
- [45] S. Weihe. Failure induced anisotropy in the framework of multi-surface plasticity. In T.J.R. Owen, E. Oñate, and E. Hinton, editors, *Computational Plasticity, Fundamentals and Applications*, pages 1049–1056, Barcelona, Spain, 1997. CIMNE.
- [46] G.A. Wempner. Discrete approximations related to non-linear theories of solids. *International Journal for Solids and Structures*, 7:1581–1599, 1971.
- [47] Q.-S. Zheng. Theory of Representations for Tensor Functions – Unified Invariant Approach to Constitutive Equations. *Applied Mechanics Review*, 47(11):545–587, 1994.
- [48] O.C. Zienkiewicz and R.L. Taylor. *The Finite Element Method*, volume 1 & 2. McGraw-Hill, London, England, 4. edition, 1994.

List of Figures

2.1	Cross-section of spruce wood tracheids: (a) two annual rings, (b) annual ring border, (c) earlywood tracheids with bordered pits and (d) latewood tracheids [25].	8
3.1	Uniaxial strength of wood [23] and biaxial strain state [7].	13
3.2	Spruce wood specimen in biaxial testing device [7].	14
3.3	Cruciform specimen with applied displacements [7] and coordinate system $\{1;2\}$ and material coordinate system $\{L;R\}$	15
3.4	Biaxial stress-strain curves and failure positions for fiber directions $\varphi = 0^\circ$ and $\varphi = 45^\circ$ [7].	18
3.5	Elliptic failure envelopes and stress-strain curves with fracture type for characteristic loading types [30, 31].	19
3.6	Tensile and compression failure modes in fiber direction.	20
3.7	Failure mode for radial compression.	22
4.1	Effect of orthotropy in elasticity-theory.	24
4.2	Illustration of the mathematical definition of isotropy and orthotropy. . . .	25
4.3	Symmetry transformations for 2D orthotropy.	26
4.4	Definition of the material vectors aligned to the directions of the tree [30].	28
5.1	Post-failure behavior for uniaxial tension according to the fiber tension model (5.25)	52
5.2	Motion of the fiber tension surface in the cross-sections (a) $\sigma_{RR} = 0$ and (b) $\tau_{RL} = 0$ for $\ell_c = 1$ mm.	52
5.3	Parameters for strength function and hardening stress	55
5.4	Post-failure behavior according to the fiber compression model (5.41). . . .	56
5.5	Motion of the fiber compression surface in the cross-sections (a) $\sigma_{RR} = 0$ and (b) $\tau_{RL} = 0$ for $\ell_c = 100$ mm.	57
5.6	Definition of parameters for the strength- and densification functions. . . .	59
5.7	Post-failure behavior of the radial compression model (5.56).	60
5.8	Motion of the radial compression surface in the cross-section $\sigma_{LL} = 0$ (ℓ_c without influence).	60
5.9	Failure surface of the radial tension model for a plane with $\sigma_{LL} = \text{const.}$. .	63
5.10	Modeled post-failure behavior for radial tension σ_{RR} (mode I).	67
5.11	Modeled post-failure behavior for shear τ_{LR} (mode II).	68
5.12	Strength degradation for mixed mode loading and $\ell_c = 1, 10$ and 100 mm.	68

5.13	Motion of the radial tension surface in the cross-section $\sigma_{LL} = 0$ for $\ell_c = 1$ mm (only mode I: dashed lines, only mode II: solid lines).	71
5.14	Multi-surface model in its initial state (failure envelope).	73
5.15	Cross-sections through planes (a) $\sigma_{RR} = 0$ and (b) $\tau_{RL} = 0$	74
5.16	Cross-section through plane $\sigma_{LL} = 0$,	75
5.17	Possible motion of state surfaces in the plane $\tau_{RL} = 0$	75
5.18	Uniaxial strength of clear spruce wood in dependency of the grain angle φ computed with different failure models [30].	76
6.1	Geometrical interpretation of θ	79
6.2	Geometric illustration of the concept of closest point projection and the return mapping algorithm, for an yield surface with isotropic and kinematic hardening.	86
6.3	Combined projection of the trial stress onto active surfaces	87
6.4	Geometric illustration of both cases in the corner projection of the return mapping algorithm.	91
7.1	Strength softening model with respect to w and α	99
7.2	Representative volume (finite element) with crack opening.	100
7.3	Stress-strain curve for different values of ℓ_c and therefore of k	102
7.4	Softening function and corresponding stress-strain curve.	103
7.5	Projection onto the radial tension state surface in the σ_{LL} plane.	109
7.6	Graphical interpretation of the solutions of (7.61).	114
7.7	Example to show convergence, softening behavior and stress-strain relationship for each surface with $\ell_c = 100$ mm.	115
7.8	Mixed mode convergence for $\ell_c = 10$ mm and $\ell_c = 20$ mm with $\varphi = 45^\circ$. . .	119
7.9	One dimensional example to show structural influence.	121
7.10	Force-displacement curves of structures with equal ℓ_c	122
7.11	Example to show structural behavior effects.	124

List of Tables

2.1	Average thickness and percentage of the cell wall layers of spruce wood (<i>Picea abies</i>) tracheids [13].	11
4.1	Matrix representation of symmetry transformations for two dimensional orthotropy for the special coordinate-system $\mathbf{A}_1 = \mathbf{e}_1$ and $\mathbf{A}_2 = \mathbf{e}_2$	27
4.2	Coordinate representation of material vectors and structural tensors for different angles θ	29
4.3	Number of independent invariants and material parameters for isotropic and orthotropic materials.	37
4.4	Possible combinations of f , \dot{f} and γ and their loading state equivalence. . .	41
5.1	Material parameters for the multi-surface plasticity model	73
6.1	Partitioned solution scheme for stress projection	90
6.2	Dimension of variables and derivations	91
6.3	Computation of the consistent elasto-plastic tangent operator	94
7.1	Critical characteristical length for each state surfaces	106
7.2	Fiber tension model with $\ell_c = 100$ mm	116
7.3	Fiber compression model with $\ell_c = 100$ mm and radial compression model	117
7.4	Radial tension model for mode I and II with $\ell_c = 100$ mm	118
7.5	Values for the model dimensions ℓ_c and ℓ_{el}	124
7.6	Convergence study results	125